University of Alberta

Nonlinear State Estimation and Modeling of a Helicopter UAV

by

Martin Barczyk

A thesis submitted to the Faculty of Graduate Studies and Research
in partial fulfillment of the requirements for the degree of

Doctor of Philosophy

in

Control Systems

Department of Electrical and Computer Engineering

Spring 2012
Edmonton, Alberta

Abstract

Experimentally-validated nonlinear flight control of a helicopter UAV has two necessary conditions: an estimate of the vehicle's states from noisy multirate output measurements, and a nonlinear dynamics model with minimum complexity, physically controllable inputs and experimentally identified parameter values. This thesis addresses both these objectives for the Applied Nonlinear Controls Lab (ANCL)'s helicopter UAV project. A magnetometer-plus-GPS aided Inertial Navigation System (INS) for outdoor flight as well as an Attitude and Heading Reference System (AHRS) for indoor testing are designed, implemented and experimentally validated employing an Extended Kalman Filter (EKF), using a novel calibration technique for the magnetometer aiding sensor added to remove the limitations of an earlier GPS-only aiding design. Next the recently-developed nonlinear observer design methodology of invariant observers is adapted to the aided INS and AHRS examples, employing a rotation matrix representation for the state manifold to obtain designs amenable to global stability analysis, obtaining a direct nonlinear design for gains of the AHRS observer, modifying the previously-proposed Invariant EKF systematic method for computing gains, and culminating in simulation and experimental validation of the observers. Lastly a nonlinear control-oriented model of the helicopter UAV is derived from first principles, using a rigid-body dynamics formulation augmented with models of the on-board subsystems: main rotor forces and blade flapping dynamics, the Bell-Hiller system and flybar flapping dynamics, tail rotor forces, tail gyro unit, engine and rotor speed, servo operation, fuselage drag, and tail stabilizer forces. The parameter values in the resulting models are identified experimentally. Using these the model is further simplified to be tractable for model-based control design.

Table of Contents

1 Introduction **1**
- 1.1 Background . . . 1
  - 1.1.1 Motivation of Research . . . 3
- 1.2 Literature Survey . . . 4
  - 1.2.1 Aided Navigation . . . 4
  - 1.2.2 Invariant Observers . . . 4
  - 1.2.3 Helicopter Modeling and Identification . . . 5
- 1.3 Outline of Thesis . . . 5
  - 1.3.1 Statement of Contributions . . . 6

2 Mathematical Preliminaries **8**
- 2.1 Rotation Matrices . . . 8
- 2.2 Cross-Product and Skew-Symmetric Matrices . . . 10
- 2.3 Rotation Kinematics . . . 11
- 2.4 Navigation Dynamics . . . 13
- 2.5 Parameterizing the Rotation Matrix . . . 15
- 2.6 Euler Angles Parametrization . . . 18
- 2.7 Quaternions . . . 22
- 2.8 Earth's Magnetic Field . . . 28
  - 2.8.1 Computing Yaw . . . 30
- 2.9 Magnetometer Calibration . . . 31

3 Extended Kalman Filter Design for Aided Navigation **35**
- 3.1 Overview of EKF . . . 35
- 3.2 EKF Design . . . 36
  - 3.2.1 Complementary Filter Topology . . . 36
  - 3.2.2 Sensor Models . . . 38
  - 3.2.3 Dynamics and Output Equations . . . 39
  - 3.2.4 Numerical Integration . . . 40
  - 3.2.5 Linearized Error Dynamics . . . 42
  - 3.2.6 Observability Analysis . . . 45
  - 3.2.7 Discretization . . . 48
  - 3.2.8 Kalman Filter . . . 51
  - 3.2.9 Extended Kalman Filter . . . 52
  - 3.2.10 EKF Implementation . . . 52
  - 3.2.11 Initialization . . . 54
- 3.3 AHRS Testing . . . 56

3.3.1 Simulation Results . . . 56
3.3.2 Experimental Results . . . 57
3.4 Aided INS Testing . . . 58
3.4.1 Simulation Results . . . 58
3.4.2 Experimental Ground Test Results . . . 61
3.4.3 Experimental Flight Results . . . 64

4 Invariant Observer Design for Aided Navigation 69
4.1 Overview . . . 69
4.2 Motivating Example . . . 70
4.3 System Symmetries . . . 72
4.3.1 Lie Group Actions . . . 74
4.4 AHRS symmetries . . . 75
4.4.1 Ground frame symmetries . . . 75
4.4.2 Combined symmetries . . . 76
4.5 Aided INS Symmetries . . . 78
4.6 Invariant Observer Theory . . . 82
4.6.1 Invariants and Moving Frame . . . 82
4.6.2 Invariant Frame . . . 85
4.6.3 Invariant Observer, Invariant Output Error . . . 87
4.7 Invariant Observer Design . . . 91
4.7.1 Invariant AHRS Design . . . 91
4.7.2 Invariant Aided INS Design . . . 97
4.8 Nonlinear Observer Gain Design . . . 104
4.9 Invariant Extended Kalman Filter . . . 106
4.9.1 Invariant EKF Overview . . . 107
4.9.2 Invariant AHRS EKF design . . . 108
4.9.3 Invariant Aided INS EKF design . . . 113
4.10 Invariant AHRS testing . . . 121
4.10.1 Implementation Details . . . 121
4.10.2 Simulation Results . . . 123
4.10.3 Experimental Results . . . 126
4.11 Invariant Aided INS testing . . . 130
4.11.1 Implementation details . . . 130
4.11.2 Simulation results . . . 132
4.11.3 Experimental results . . . 135

5 Nonlinear Model of a Helicopter UAV 139
5.1 Overview . . . 139
5.2 Rigid-Body Model . . . 139
5.2.1 Torsional Pendulum . . . 144
5.2.2 Extended Moment Equation . . . 146
5.3 Aerodynamics and Subsystem Modeling . . . 148
5.3.1 Main Rotor . . . 148
5.3.2 Rotor Head . . . 168
5.3.3 Tail Rotor . . . 176
5.3.4 Rotor Speed and Engine . . . 181
5.3.5 Servo Commands . . . 182

5.3.6 Fuselage Drag 184
5.3.7 Tail Stabilizers 185
5.4 Dynamics Model Summary 188
5.4.1 Hover Model 189
5.5 Identified Parameter Values 191

6 Conclusions **194**
6.1 Review of Results 194
6.1.1 Magnetometer Integration 194
6.1.2 Invariant Observers 194
6.1.3 Modeling and Identification 195
6.2 Future Work 196
6.2.1 Engine-on Noise Characteristics 196
6.2.2 Nonlinear Gain Design for Invariant Aided INS Observer . . 197
6.2.3 Experimental Testing of Nonlinear Model 197

Bibliography **198**

List of Tables

2.1 Magnetometer Calibration Constants 34

3.1 Identified Noise Parameters – Engine Off [75] 38
3.2 Modified Noise Parameters – Engine On 65

4.1 Engine-on Invariant Aided INS observer parameters 137

List of Figures

1.1 ANCL helicopter UAV in flight [75]; note the underslung avionics enclosure and tail-mounted GPS antenna 2

2.1 Three-frame schematic; frame origins offset for clarity 10
2.2 Rigid Body Rotation About Fixed Origin 12
2.3 Body, Navigation and ECEF frames 14
2.4 Elementary rotations about n_1, n_2 and n_3 18
2.5 Roll-Pitch-Yaw sequence of rotations, $\phi = -\pi/2$, $\theta = \pi/2$, $\psi = \pi$ . . 21
2.6 Alternative Roll-Pitch-Yaw sequence of rotations, $\phi = -\pi$, $\theta = \pi/2$, $\psi = \pi/2$ 21
2.7 Earth's Magnetic Field 29
2.8 Magnetometer Calibration, Engine Off: Raw Sensor Readings, Hard-Iron Compensated, Fully Compensated 33

3.1 Topology of AHRS; signal rate inversely proportional to dot spacing 37
3.2 Topology of Aided INS; signal rate inversely proportional to dot spacing 37
3.3 AHRS simulation: estimated states (—), reference states (- - -). . . . 56
3.4 AHRS simulation: error between estimated and reference attitude angles 57
3.5 AHRS experiment: estimated states (—), Vicon attitudes (- - -). . . . 57
3.6 AHRS experiment: error between AHRS and Vicon attitudes; $\|\tilde{y}_a\|$. 58
3.7 State Estimates: Simulated Hover 59
3.8 State Estimates: Simulated Hover, GPS-only Aiding 59
3.9 State Estimates: Simulated figure-8 60
3.10 State Estimates: Simulated figure-8, GPS-only Aiding 61
3.11 State Estimation Errors: Simulated figure-8, Mag-plus-GPS vs GPS-only Aiding 61
3.12 State Estimates: Ground Test, 3-Axis Mag Aiding 62
3.13 State Estimates: Ground Test, Yaw-Only Mag Aiding 63
3.14 Magnetometer Calibration Comparison, Ground Test, Yaw-Only Mag Aiding: Overhead Position; Yaw Angle 64
3.15 State Estimates: Flight Test, 3-Axis Mag Aiding 65
3.16 State Estimates: Flight Test, Yaw-Only Mag Aiding 66
3.17 Magnetometer Calibration Comparison, Flight Test, 3-Axis Mag Aiding: Estimated Attitude 67

4.1 Orbits of $SO(2)$ on $\mathbb{R}^2$ and cross-section K 84

4.2 Invariant AHRS Simulation: Body-Frame Symmetry Observer (4.15) using gains from nonlinear design (left); Invariant EKF (right) . . . 124
4.3 Invariant AHRS Simulation: Ground-Frame Symmetry Observer (4.16) using gains from nonlinear design (left); Invariant EKF (right) . . . 125
4.4 Invariant AHRS Simulation: Comparison of estimation errors 126
4.5 Invariant AHRS Experiment: Body-Frame Symmetry Observer (4.15) using gains from nonlinear design (left); Invariant EKF (right) . . . 127
4.6 Invariant AHRS Experiment: Ground-Frame Symmetry Observer (4.16) using gains from nonlinear design (left); Invariant EKF (right) . . . 128
4.7 Invariant AHRS Experiment: Comparison of attitude estimation errors 129
4.8 Body-Frame Invariant Aided INS: Simulated Hover 133
4.9 Ground-Frame Invariant Aided INS: Simulated Hover 133
4.10 Body-Frame Invariant Aided INS: Simulated Figure-8 flight 134
4.11 Ground-Frame Invariant Aided INS: Simulated Figure-8 flight 134
4.12 Invariant Aided INS: Simulated Figure-8 flight estimation errors: Body-frame symmetry; Ground-frame symmetry 134
4.13 Body-Frame Invariant Aided INS: Experimental engine-off walk . . . 135
4.14 Ground-Frame Invariant Aided INS: Experimental engine-off walk . 135
4.15 Invariant Aided INS: Experimental engine-off walk comparison: Body-frame symmetry; Ground-frame symmetry 136
4.16 Body-Frame Invariant Aided INS: Experimental engine-on hover . . 137
4.17 Ground-Frame Invariant Aided INS: Experimental engine-on hover . 138
4.18 Invariant Aided INS: Pre-takeoff estimated position zoom-in view . . 138

5.1 Helicopter Model: Overall View [59] 140
5.2 Navigation and Body Frames on Helicopter 140
5.3 Helicopter UAV with identified CM location 144
5.4 Torsional pendulum schematic 144
5.5 Geometry of support cable; disk rotated by θ 145
5.6 Experimental measurement of J using a torsional pendulum [53]: pitch axis, roll axis. 146
5.7 Rigid body with body frame fixed at arbitrary point o 147
5.8 Rotor inflow in hover 149
5.9 Rotor inflow in fast forward flight 150
5.10 Rotor inflow in general flight 151
5.11 Blade cross-section 152
5.12 NACA 0014 data from JavaFoil: Coefficients of lift and drag vs angle of attack 153
5.13 Main Rotor: Blade free-body diagram 154
5.14 Blade flapping kinematics 155
5.15 Main rotor k_β identification: experiment setup; restoring torque τ versus flapping angle β 168
5.16 Bell-Hiller system schematic [76] for $\psi = 0$, $\psi_f = 90°$; δ_c omitted for clarity. 168
5.17 Flybar ratio K_F identification: experiment setup; blade pitch Θ versus flybar tilt β_f 170
5.18 Flybar Kinematics 171
5.19 Rotor head system diagram — roll channel 176

5.20 Helicopter tail: Side view (left), Overhead view (right) 177
5.21 Throttle-pitch curves: Stock (left), Full-payload (right) 182
5.22 Duty Cycles Δ_c, Δ_r for collective and roll stick sweeps 184
5.23 Tail zoom-in; note main blades overhang horizontal stabilizer 186
5.24 Topology of helicopter dynamics model 188

Chapter 1

Introduction

1.1 Background

The helicopter (rotary-wing vehicle) platform offers a number of advantages over the airplane (fixed-wing vehicle) one, namely in-place hover, low-speed flight in any direction and vertical take-off and landing[1], in addition to fast forward flight capability. The price is much greater complexity in the piloting, mechanical design and maintenance, as well as dynamics modeling in the rotary-wing configuration in comparison to the fixed-wing case. This explains why helicopters were introduced much later than airplanes: the first production helicopter using the single main rotor configuration was the Sikorsky R-4 delivered to the US Army in May 1942 [44, p. 108], while the first radio-controlled helicopter was the fixed-pitch Bell Huey Cobra successfully flown in April 1970 [121, p. 8].

Academic interest in autonomous helicopter flight control can be traced back to 1991, the first year of the International Aerial Robotics Competition created by Prof. Robert Michelson from Georgia Tech. The competition consists of a pre-specified "mission" which must be executed in a fully autonomous fashion. The first mission required moving a metal disk between two designated locations separated by a three-foot high central barrier on an outdoor field, and was successfully completed in 1995 by a team from Stanford University [133]. As of 2011 the competition is on its sixth mission, which requires entering a building, swapping a USB flash drive on a desk with a replica and leaving with the original, all the while avoiding detection from walking guards and surveillance equipment at the site.

The University of Alberta's Applied Nonlinear Controls Lab (ANCL) helicopter UAV project began with the work of [75] who designed and built an avionics suite for a stock radio-controlled Bergen Industrial Twin helicopter, popular for aerial cinematography due to its considerable payload capacity (9.1 kg) and flight endurance (30 min). A picture of the UAV in flight is shown in Figure 1.1. The avionics consist of an Ampro ReadyBoard 800 single-board computer equipped with a Pentium M 1.4 GHz CPU and 512 MB of RAM running the QNX real-time operating system; a Microhard VIP2400 2.4 GHz radio modem providing Ethernet and RS-232 communication with the ground station; a Microstrain 3DM-GX1 Inertial Measurement Unit (IMU) providing triaxial magnetometer, accelerometer and rate gyro measurements at up to 333 Hz; a NovAtel OEM4-G2 carrier phase differential GPS

[1] Available to a very small subset of fixed-wing vehicles such as the Harrier and F-35.

capable of centimeter-level accuracy position measurements at 10 Hz; two Measurement Computing CTR10HD counter/timer boards used to respectively log RC pilot inputs and control the helicopter's servos; and a takeover board used to switch between manual and autonomous flight control. A GPS-aided inertial navigation system (INS) was implemented and experimentally validated on this system. This UAV platform has motivated research work presented in this thesis, further detailed in Section 1.1.1.

Figure 1.1: ANCL helicopter UAV in flight [75]; note the underslung avionics enclosure and tail-mounted GPS antenna

The current trend among UAV research groups seems to be the small electric quadrotor vehicle, e.g. [68, 102, 66]. However an outdoor heavy-lift helicopter remains the best choice for applications such as powerline inspection, a current joint research project between ANCL and BC Hydro [85, 128], which requires carrying infrared and ultraviolet cameras used to detect existing or imminent damage in high-voltage transmission lines. Employing a UAV for this task is dramatically less risky for the inspection crews as exemplified by the following anecdote from [44, p. 244]:

> Five years earlier I rode in a small helicopter while an electrician on board worked on a live transmission line in Pennsylvania. We were eighty feet off the ground, and pilot Mark Campolong had to hold his machine next to a thumb-thick aluminum-steel cable carrying 230,000 volts of electricity. His job, simply stated, was to keep electrician Jeff Pigott close enough to the cable to do his work, but not so close as to tangle his ship with the line. New pilots need a football field or larger when learning to maneuver; Campolong had no more than sixteen inches of tolerable error (In such a situation, the pilot is conscious of two risks in particular: an engine failure or accidentally bringing the tail rotor against the cable. Either would lead to a crash). I watched his gloved hands cope with the light and variable winds: his hand on the cyclic was as economical of motion as a bicyclist who is cruising down the street. After we banked and flew back to the fueling truck, he said that his mother-in-law asked why his work was so tiring. In her opinion, all he did was sit around all day.

1.1.1 Motivation of Research

There are two necessary though not sufficient conditions to achieve experimentally-validated nonlinear autonomous flight control on a UAV: an observer to estimate the state of the vehicle from noisy, multi-rate measurements; and a dynamics model with minimum complexity, physically controllable inputs and experimentally-identified parameter values. These two goals have motivated and been successfully achieved with the research work presented in this thesis.

The earliest stage of work involved adding magnetometer readings as an aiding measurement to the existing GPS-only aided INS [75] which had been found to give incorrect heading angle estimates in hover but correct ones in forward flight experiments. It turns out the heading angle in a GPS-aided INS is only observable if the vehicle has non-zero lateral acceleration, i.e. is manoeuvering; of course adding a direct measurement of this angle resolves this issue. The work is reported in Chapter 3 including the mathematical derivation, hardware implementation and extensive simulation and experimental validation of the resulting system. Using experience acquired during this work, an Attitude and Heading Reference System (AHRS) was also designed and implemented. In contrast to the Aided INS' position, velocity and attitude estimates the AHRS provides only attitude information, however it does not use GPS aiding and hence is useful for prototyping attitude-stabilization algorithms in our indoor laboratory. The AHRS derivation, implementation and testing is provided alongside the Aided INS in Chapter 3.

Aided navigation, with Mag-plus-GPS Aided INS and AHRS as specific examples, is fundamentally a nonlinear observer design problem due to the presence of rigid-body attitude dynamics (c.f. Section 2.4). The conventional design approach to this class of systems is the Extended Kalman Filter (EKF), which is based on re-linearization of the system about its latest estimate. This method is universally used in the aerospace industry c.f. [49, 51] and works very well in practice as demonstrated in Chapter 3. However, a direct nonlinear observer design is of interest for at least two reasons other than its intrinsic elegance: first, the EKF is unable to guarantee global stability due to its reliance on (re)linearization of the system equations; and second, the EKF algorithm is computationally expensive due to its requirements of linearizing the system and propagating the estimation error covariance matrix at every aiding measurement. The research focused on the Invariant (Symmetry-Preserving) Observer method [27, 28] due to its novelty and successful application to aided navigation examples [25, 91] whose dynamics possess the necessary symmetries (formally defined in Section 4.3). This work is documented in Chapter 4, using the AHRS and Aided INS examples from Chapter 3, with successful validation of the results in simulation and experiment. This part of the research required a substantial investment of time to learn the tools of differential geometry, and made full use of the experience gained from designing the conventional EKF systems.

Accurate estimates of vehicle's state enable non-model based control — namely PID — but a dynamic model is required for more sophisticated control schemes, both those based on linearization (e.g. $\mathcal{H}_\infty$ [46]) and nonlinear methods (e.g. MPC [5]). Since the model is used for control, it must possess the following characteristics: system equations of sufficiently low order and complexity to be usable yet which adequately capture the physics of the vehicle; physically controllable inputs, which requires modeling of the mechanization of the helicopter controls including servo

operation, the Bell-Hiller system and the tail gyro unit; and parameter values identified specifically for our UAV platform, i.e. not available from the literature. Such a model is developed throughout Chapter 5 using a first-principles approach to explain which assumptions are being made, and making extensive use of simplifications based on identified parameter values, e.g. neglecting servo dynamics based on their measured performance c.f. Section 5.3.5. The result is a nonlinear model of the helicopter capturing the full flight envelope (hover, climb and fast forward flight) and its simplification to the case of hover useful for a first version of model-based control design.

We mention the highly simplified model introduced in [79] popularly used for simulation studies of nonlinear helicopter control e.g. [80, 87, 56, 71, 86, 57, 89]. The model itself is unsuitable for experimental implementation due to a number of unrealistic assumptions (c.f. [59, p. 56]): instantaneous control of main and tail rotor thrusts and rotor disc tilt angles, whose amplitudes are unaffected by the system's state and cannot saturate; ignoring the mappings between servo inputs and the above actuation mechanisms, which are non-trivial due to the Bell-Hiller mechanism and tail gyro unit equipped on UAV helicopters; and neglecting state feedback effects such as translational lift, fuselage drag and rotor-fuselage coupling which strongly affect the performance of real helicopters. It is hoped the model developed and identified in Chapter 5, in particular the simplified hover model mentioned above, can act as a bridge between the nonlinear control techniques developed in the literature and experimentally-validated designs.

1.2 Literature Survey

1.2.1 Aided Navigation

A comprehensive survey of algorithms which have been employed for experimentally-validated aided navigation is provided in [49] including the Extended Kalman Filter, $\mathcal{H}_\infty$ methods, unscented filters, particle filters, as well as a selection of nonlinear observers. The EKF method, first employed in the early 1960's by NASA for the Apollo lunar landing program [97], remains the most widely-used tool for aided navigation design [51, 119]; textbook references to the EKF method include [34, 123, 48]. In particular research groups employing outdoor UAV helicopters [122, 74, 45, 59, 132, 21, 3, 134] have all used the EKF for state estimation.

1.2.2 Invariant Observers

Invariant Observers, also known as Symmetry-Preserving Observers are a novel approach to nonlinear observer design. The method is described in [27, 28] with preliminary versions having appeared in [30, 25, 26]. It provides a systematic method to build a nonlinear observer structure which possesses the same symmetries (formally defined in Section 4.3) as the original system, guaranteeing a reduced-complexity estimation error dynamics (c.f. Section 4.6.3) which simplifies gain selection and stability analysis. The existence of symmetries in dynamical system under state feedback was previously studied in [129, 63] and for the observer case in [64]. Exploiting system symmetries for design first appeared in the context of tracking controllers [120], continued in [90] and more recently [47]; using symmetries for observer

design was first seen in [10, 11]. The invariant observer design method was applied to aided navigation examples in [91, 93, 92, 94, 95].

1.2.3 Helicopter Modeling and Identification

References for full-sized helicopter modeling include [61, 72, 126, 115, 113, 33]. Radio-controlled (RC) helicopters [121] such as the Bergen Industrial Twin employed by the ANCL UAV project operate on the same principles, but have a number of characteristics which distinguish them from the full-sized versions [101, Chap. 5] including much higher thrust-to-weight ratios and head speeds, hingeless blades, and the inclusion of a Bell-Hiller mechanism and tail gyro to ease pilot workload. Modeling specific to RC helicopters includes [60, 76, 81, 101, 21, 36, 116]. Highly simplified models used for simulation of nonlinear control methods (c.f. Section 1.1.1) are developed in [80, 131, 37].

Model identification is a broad subject. Frequency-domain system identification of full-sized helicopters is treated in [127] and the references therein. Application of frequency-domain methods to UAV-sized helicopters is found in [122, 81, 101]. Such approaches necessarily provide linear models which are valid around the operating point where the identification data was collected. An alternative time-domain method is used in [7, 6, 5] which combines nonlinear rigid-body dynamics together with simple linear parameterizations of force and moment components as functions of system state and pilot inputs. These parameters are identified using logged flight data and a least-squares minimization between measured and predicted accelerations. The third approach is to identify a model's parameters using direct measurements and experimental tests as done by [59, 21, 77]. This approach may require further tuning of the parameters to match the simulated and experimental data [65, 22] but provides a single nonlinear model for the full flight envelope of the helicopter. This is the approach taken in this thesis, and the specific methods employed for parameter identification will be referenced throughout Chapter 5.

1.3 Outline of Thesis

This Chapter provided a background of the ANCL helicopter UAV project and the motivations for undertaking the research presented in this thesis, followed by a survey of existing literature. An itemized statement of contributions will be provided in Section 1.3.1.

Chapter 2 is a collection of mathematical results used throughout the rest of the thesis. We first review rotation matrices, their use for changing basis vectors and measuring the attitude of a vehicle, then the $\mathbb{R}^3$ cross-product and its relation to skew-symmetric matrices. These are used to obtain rotational kinematics, the nonlinear dynamics of rotation matrices resp. vehicle attitude. We use these tools to derive the system equations of aided inertial navigation. Next we cover the parametrization of rotation matrices using in turn axis-angle, Euler angles and unit quaternions. Finally we review the Earth's magnetic field, the calculation of heading angle using the measurements from a triaxial magnetometer, and the problem of magnetometer calibration whose importance will become clear at the end of Chapter 3, specifically Sections 3.4.2 and 3.4.3 describing experimental testing of the aided inertial navigation system.

In Chapter 3 we cover the design of the Extended Kalman Filter (EKF), the conventional approach to designing observers for aided navigation problems. We perform the design steps using two examples relevant to our project, an Attitude and Heading Reference System (AHRS) and a Magnetometer-plus-GPS-aided Inertial Navigation System (Aided INS): models of sensor signals, bias and noise; nonlinear system equations and their numerical integration; linearized error dynamics used by the Kalman observer and their observability properties; discretization; the Kalman Filter and its adaptation to nonlinear systems, the Extended Kalman Filter; and implementation details including initialization and aiding criteria. The resulting AHRS and Aided INS designs are then extensively tested and validated in simulation and experiment, demonstrating excellent performance and showing how the deficiencies of the previous GPS-only Aided INS have been resolved.

Chapter 4 treats Invariant (Symmetry-Preserving) Observers, a novel approach to nonlinear observer design. Using the AHRS example we intuitively demonstrate the existence of system symmetries. These are then formally defined using the coordinate-free language of differential geometry, and their existence in the AHRS and Aided INS examples in Chapter 3 is shown. We review the method of invariant observer design including the proofs of key results, then apply the method to design invariant observers for the two examples above. For the AHRS observer, a nonlinear gain design is found which guarantees almost-global stability, although not for the (more complicated) Aided INS case. For this reason we employ the Invariant EKF [23, 29], a systematic approach to design the gains of the invariant observer based on re-linearizing its invariant estimation error dynamics. This method is applied to both the AHRS and Aided INS systems. Finally a comprehensive simulation and experimental evaluation of the AHRS and Aided INS invariant observers is made including comparing the performance of the nonlinear gain design versus the Invariant EKF method.

Chapter 5 develops a nonlinear model of the helicopter UAV and experimentally identifies its parameter values. The aim of the model is to be of sufficiently low order and complexity to be tractable, yet to accurately model the real helicopter e.g. the mechanization of the control inputs. We first derive the rigid-body dynamics of the helicopter using tools from Chapter 2, then perform subsystem-by-subsystem modeling of its components: the main rotor and blade flapping dynamics, rotor head construction and the Bell-Hiller mechanism, tail rotor and the tail gyro unit, rotor speed and engine, servos, fuselage drag and tail stabilizers. The resulting nonlinear model is also simplified to the case of hover, c.f. Section 1.1.1. The parameter values of the nonlinear model are experimentally identified throughout and are summarized together at the end of this chapter.

Chapter 6 summarizes the work done in the thesis and the resulting findings. Possible future research tasks which build on the present thesis are discussed.

1.3.1 Statement of Contributions

The following items are claimed as research contributions of this thesis (listed in order of appearance):

- Integrating the magnetometer calibration proposed in [54] (described in Section 2.9) into the Aided INS design and experimentally demonstrating the

resulting improvement in performance over the conventional (hard-iron calibration) method and the uncompensated case, as well as resolving the shortcomings of the previous GPS-only version of the aided navigation system [75, Chap. 5]. This work was reported in conference proceedings [15] and journal paper [17].

- Implementing an AHRS system for indoor testing of attitude-stabilization algorithms. The design inherits features developed for the Aided INS design including magnetometer calibration, an orthogonality-preserving attitude update (c.f. Section 3.2.5) and accurately-identified sensor noise and bias characteristics (c.f. Section 3.2.2). The design was experimentally validated using an indoor motion-capture system as described in Section 3.3.2. The work was reported in conference proceedings [16].

- Design and validation of invariant observers for the AHRS and Aided INS examples. Specific contributions are: designing the observers in terms of $R \in SO(3)$ making them amenable to global stability analysis, c.f. [38]; finding a set of gains for the invariant AHRS guaranteeing almost-global stability (Section 4.8); improving the Invariant EKF method [23, 29] by removing the requirement for invariant noise and rendering the Aided INS invariant observer case tractable, c.f. Section 4.9.1; and validating the designs in both simulation and experiment. The Aided INS invariant observer was published in conference proceedings [18] while the AHRS invariant observer was submitted as journal publication [19].

- Developing an identified nonlinear dynamics model of the helicopter UAV from first principles for the purpose of control. Specific contributions include an elegant derivation of the rigid-body and flapping dynamics in the style of [105]; simplification of the main rotor and flybar flapping dynamics based on experimentally identified parameter values, c.f. Sections 5.3.1.4 and 5.3.2.1, the latter including a mathematical analysis of the Bell-Hiller mechanism as a derivative action stability augmentation system; a simplified version of the nonlinear model to the case of hover provided in Section 5.4.1 which removes the need for an iterative solution of induced velocity v_i (c.f. Section 5.3.1.5) and analytically explains the rotor-fuselage coupling characteristic of helicopter UAVs [101, 59, 127]; and obtaining the numerical values of the model parameters, tabulated in Section 5.5 with identification details provided throughout the chapter.

Chapter 2

Mathematical Preliminaries

This chapter presents a number of mathematical results used throughout the rest of the thesis. Derivations are included in order to make the thesis self-contained.

2.1 Rotation Matrices

We typically make use of two coordinate frames (a set of orthonormal vectors spanning $\mathbb{R}^3$): a ground-fixed *navigation frame* with basis vectors $\{n_1, n_2, n_3\}$, and a body-fixed *body frame* using basis vectors $\{b_1, b_2, b_3\}$. The basis vectors for both frames are orthonormal and follow the right-handed convention, i.e. $n_1 \times n_2 = n_3$ and $b_1 \times b_2 = b_3$ where $\times$ denotes the $\mathbb{R}^3$ cross-product. Note that the navigation frame is stationary, making it an inertial frame where Newton's Laws can be applied. By contrast, the body-fixed frame moves with the body which may be accelerating and/or rotating, making the body frame a non-inertial frame.

In order to describe the orientation of the body with respect to the ground, we express the body frame basis vectors in the navigation frame basis. Using the dot product $\cdot$ for projection, we have

$$b_i = (b_i \cdot n_1)n_1 + (b_i \cdot n_2)n_2 + (b_i \cdot n_3)n_3, \qquad i = 1, 2, 3.$$

For a given point p we define $p_B = [p_{B,1} \quad p_{B,2} \quad p_{B,3}]^T \in \mathbb{R}^3$ as its coordinates in the body frame and $p_N = [p_{N,1} \quad p_{N,2} \quad p_{N,3}]^T \in \mathbb{R}^3$ in the navigation frame. The coordinates are related as follows:

$$\begin{aligned}
p &= p_{B,1}b_1 + p_{B,2}b_2 + p_{B,3}b_3 \\
&= p_{B,1}\big[(b_1 \cdot n_1)n_1 + (b_1 \cdot n_2)n_2 + (b_1 \cdot n_3)n_3\big] \\
&+ p_{B,2}\big[(b_2 \cdot n_1)n_1 + (b_2 \cdot n_2)n_2 + (b_2 \cdot n_3)n_3\big] \\
&+ p_{B,3}\big[(b_3 \cdot n_1)n_1 + (b_3 \cdot n_2)n_2 + (b_3 \cdot n_3)n_3\big] \\
&= \big[p_{B,1}(b_1 \cdot n_1) + p_{B,2}(b_2 \cdot n_1) + p_{B,3}(b_3 \cdot n_1)\big]n_1 \\
&+ \big[p_{B,1}(b_1 \cdot n_2) + p_{B,2}(b_2 \cdot n_2) + p_{B,3}(b_3 \cdot n_2)\big]n_2 \\
&+ \big[p_{B,1}(b_1 \cdot n_3) + p_{B,2}(b_2 \cdot n_3) + p_{B,3}(b_3 \cdot n_3)\big]n_3 \\
&= p_{N,1}n_1 + p_{N,2}n_2 + p_{N,3}n_3.
\end{aligned}$$

The above can be written as

$$\underbrace{\begin{bmatrix} p_{N,1} \\ p_{N,2} \\ p_{N,3} \end{bmatrix}}_{p_N} = \underbrace{\begin{bmatrix} b_1 \cdot n_1 & b_2 \cdot n_1 & b_3 \cdot n_1 \\ b_1 \cdot n_2 & b_2 \cdot n_2 & b_3 \cdot n_2 \\ b_1 \cdot n_3 & b_2 \cdot n_3 & b_3 \cdot n_3 \end{bmatrix}}_{R} \underbrace{\begin{bmatrix} p_{B,1} \\ p_{B,2} \\ p_{B,3} \end{bmatrix}}_{p_B},$$

where R is known as the *rotation matrix*. By construction, the columns of R represent the coordinates of each b_i in the navigation frame. Since $\{b_1, b_2, b_3\}$ are orthonormal, the columns of R are automatically orthonormal as well, making R an orthogonal matrix, i.e. $R^{-1} = R^T$ and $|R| = \pm 1$. Further, $\{b_1, b_2, b_3\}$ obey the right-handed convention, from which it follows that $|R| = +1$. This subset of orthogonal matrices generates the *special orthogonal* group $SO(3)$, to which all rotation matrices belong to:

$$R \in SO(3) \Longrightarrow R \in \mathbb{R}^{3\times 3}, RR^T = R^T R = I, |R| = 1.$$

The rotation matrix measures the orientation of the body relative to the ground. In general motion, as the body rotates, the entries of R change with time which we denote as $R = R(t)$.

The above ideas can be applied to the case of three or more frames, leading to the composition of rotations. Consider again the fixed point p and the frames N, B and C, illustrated in Figure 2.1 with offset origins for clarity (i.e. there is no translation between the frames, only rotation). There exist three possible changes of coordinates between the frames:

$$p_N = R_N^B p_B \tag{2.1a}$$

$$p_B = R_B^C p_C \tag{2.1b}$$

$$p_N = R_N^C p_C, \tag{2.1c}$$

with, for instance, R_N^B denoting a transformation from frame B to the frame N. It can also be interpreted as the rotation of frame B with respect to the base frame N. Substituting (2.1b) into (2.1a) and comparing with (2.1c), we see that

$$p_N = R_N^B R_B^C p_C,$$

i.e. the $C \to N$ transformation can be performed in two steps, $C \to B$ then $B \to N$, *in that order*. The composition of rotations will be used extensively in Section 2.6.

Consider the inverse transformation case. From (2.1a) above,

$$p_N = R_N^B p_B \Longrightarrow p_B = \left(R_N^B\right)^T p_N,$$

and so

$$\left(R_N^B\right)^T = R_B^N,$$

the transformation from frame N to frame B.

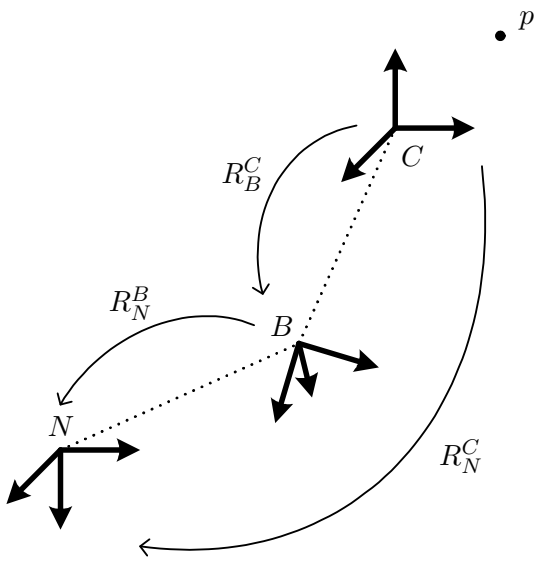

Figure 2.1: Three-frame schematic; frame origins offset for clarity

2.2 Cross-Product and Skew-Symmetric Matrices

Let $x = \begin{bmatrix} x_1 & x_2 & x_3 \end{bmatrix}^T$ and $y = \begin{bmatrix} y_1 & y_2 & y_3 \end{bmatrix}^T$ be two vectors in $\mathbb{R}^3$. By definition of the cross-product,

$$x \times y = \begin{bmatrix} x_2 y_3 - x_3 y_2 \\ x_3 y_1 - x_1 y_3 \\ x_1 y_2 - x_2 y_1 \end{bmatrix},$$

$\times$ being an anti-commutative, homogenous, distributive and non-associative operation. The cross-product can be expressed as a matrix multiplication:

$$x \times y = \underbrace{\begin{bmatrix} 0 & -x_3 & x_2 \\ x_3 & 0 & -x_1 \\ -x_2 & x_1 & 0 \end{bmatrix}}_{S(x)} \underbrace{\begin{bmatrix} y_1 \\ y_2 \\ y_3 \end{bmatrix}}_{y}. \tag{2.2}$$

Remark that $S(x)$ is a skew-symmetric matrix, i.e. $S(x)^T = -S(x)$. All $\mathbb{R}^{3\times3}$ skew-symmetric matrices can be parameterized using three scalars, or equivalently $S(x), x \in \mathbb{R}^3$ generates all possible skew-symmetric matrices within $\mathbb{R}^{3\times3}$.

We show that $S(x)S(y) - S(y)S(x) = S(x \times y)$ by expanding the left-hand side:

$$
\begin{aligned}
&= \begin{bmatrix} 0 & -x_3 & x_2 \\ x_3 & 0 & -x_1 \\ -x_2 & x_1 & 0 \end{bmatrix} \begin{bmatrix} 0 & -y_3 & y_2 \\ y_3 & 0 & -y_1 \\ -y_2 & y_1 & 0 \end{bmatrix} - \begin{bmatrix} 0 & -y_3 & y_2 \\ y_3 & 0 & -y_1 \\ -y_2 & y_1 & 0 \end{bmatrix} \begin{bmatrix} 0 & -x_3 & x_2 \\ x_3 & 0 & -x_1 \\ -x_2 & x_1 & 0 \end{bmatrix} \\
&= \begin{bmatrix} -x_3y_3 - x_2y_2 & x_2y_1 & x_3y_1 \\ x_1y_2 & -x_3y_3 - x_1y_1 & x_3y_2 \\ x_1y_3 & x_2y_3 & -x_2y_2 + x_1y_1 \end{bmatrix} \\
&- \begin{bmatrix} -x_3y_3 - x_2y_2 & x_1y_2 & x_1y_3 \\ x_2y_1 & -x_3y_3 - x_1y_1 & x_2y_3 \\ x_3y_1 & x_3y_2 & -x_2y_2 + x_1y_1 \end{bmatrix} \\
&= \begin{bmatrix} 0 & x_2y_1 - x_1y_2 & x_3y_1 - x_1y_3 \\ x_1y_2 - x_2y_1 & 0 & x_3y_2 - x_2y_3 \\ x_1y_3 - x_3y_1 & x_2y_3 - x_3y_2 & 0 \end{bmatrix} \\
&= S(x_2y_3 - x_3y_2, x_3y_1 - x_1y_3, x_1y_2 - x_2y_1) = S(x \times y).
\end{aligned}
$$

Next we develop a property of $R \in SO(3)$ and the cross-product. Recall that the columns of R are the coordinates of the body frame basis vectors b_i in the navigation frame, i.e.

$$R = \begin{bmatrix} b_{1N} & b_{2N} & b_{3N} \end{bmatrix},$$

with $b_{iN} \in \mathbb{R}^3$, $i = 1, 2, 3$ orthonormal and obeying the right-handed convention $b_{1N} \times b_{2N} = b_{3N}$. We compute:

$$
\begin{aligned}
Rx \times Ry &= (x_1 b_{1N} + x_2 b_{2N} + x_3 b_{3N}) \times (y_1 b_{1N} + y_2 b_{2N} + y_3 b_{3N}) \\
&= x_1y_1 b_{1N} \times b_{1N} + x_1y_2 b_{1N} \times b_{2N} + x_1y_3 b_{1N} \times b_{3N} \\
&+ x_2y_1 b_{2N} \times b_{1N} + x_2y_2 b_{2N} \times b_{2N} + x_2y_3 b_{2N} \times b_{3N} \\
&+ x_3y_1 b_{3N} \times b_{1N} + x_3y_2 b_{3N} \times b_{2N} + x_3y_3 b_{3N} \times b_{3N} \\
&= (x_1y_2 - x_2y_1) b_{3N} + (x_1y_3 - x_3y_1) b_{2N} + (x_2y_3 - x_3y_2) b_{1N} = R(x \times y),
\end{aligned}
$$

proving that $R(x \times y) = Rx \times Ry, R \in SO(3)$. Note this property does *not* hold for general $\mathbb{R}^{3\times3}$ matrices.

The last property to be established involves R and S and makes use of all the results developed above. Note that $R^T \in SO(3)$ because $SO(3)$ is a group.

$$
\begin{aligned}
R^T S(x) R y &= R^T [x \times Ry] \\
&= R^T x \times y \\
&= S(R^T x) y,
\end{aligned}
$$

hence $R^T S(x) R = S(R^T x)$.

2.3 Rotation Kinematics

Consider a point p fixed to a rigid body rotating in space, shown schematically in Figure 2.2. The basis vectors $\{b_1, b_2, b_3\}$ are attached to the body, and their origin coincides with the fixed $\{n_1, n_2, n_3\}$ basis vectors' origin at all times. In other words, the rigid body is free to rotate about an axis which may change orientation, but

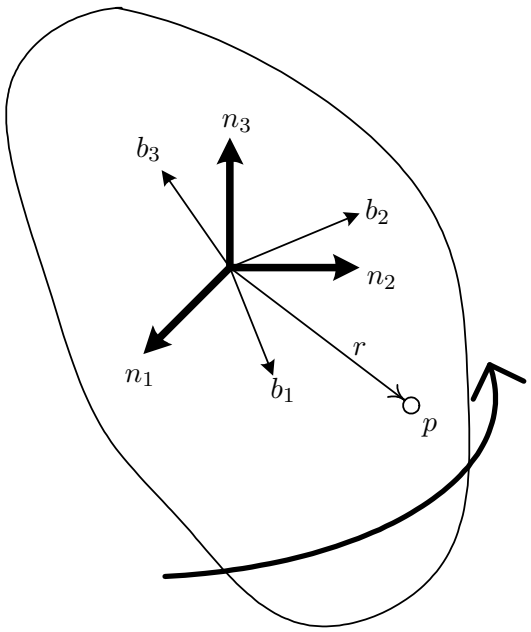

Figure 2.2: Rigid Body Rotation About Fixed Origin

always passes through the common origin. Consider the vector r from the origin to the point p; the coordinates of this vector in the body frame are r_B whose entries are constant with time since both the b_i basis vectors and the point p are rigidly attached to the body. As the body rotates, the point p moves in space, and so the coordinates of vector r in the navigation frame $r_N(t)$ are a function of time. The two coordinates are related by

$$r_N(t) = R(t)r_B.$$

Differentiating with respect to time,

$$\dot{r}_N(t) := v_N(t) = \dot{R}(t)r_B$$

where $v_N(t)$, mathematically defined as the rate of change of coordinates of p in frame N, are the coordinates of the *velocity* v of point p, where v is an absolute velocity vector (as opposed to a relative velocity vector) since its components were measured w.r.t. a stationary origin.

In order to obtain an expression for $\dot{R}(t)$ we time differentiate the identity $R(t)R^T(t) = I$, which gives

$$\dot{R}(t)R^T(t) + R(t)\dot{R}^T(t) = 0 \Longrightarrow \dot{R}(t)R^T(t) = -R(t)\dot{R}^T(t) = -(\dot{R}(t)R^T(t))^T,$$

i.e. $\dot{R}(t)R^T(t)$ is a skew-symmetric matrix. We can parameterize this last term using $S(\omega(t))$, where $\omega(t) \in \mathbb{R}^3$ has a physical interpretation which we will see shortly. Using this parametrization gives

$$\dot{R}(t)R^T(t) = S(\omega(t)) \Longrightarrow \dot{R}(t) = S(\omega(t))R(t),$$

and we obtain

$$v_N(t) = \dot{R}(t)r_B = S(\omega(t))R(t)r_B = S(\omega(t))r_N(t) = \omega(t) \times r_N(t).$$

This last expression gives the velocity vector $v_N(t)$ of a point located by the position vector $r_N(t)$ on a rigid body undergoing a purely rotational motion. From mechanics we now see that the parameterizing vector $\omega(t)$ is $\omega_N(t)$, the navigation frame coordinates of the rigid body's angular velocity vector ω, which measures the rate of rotation of the body w.r.t. frame N and is an absolute angular velocity since frame N is non-rotating. The expression for $\dot{R}(t)$ is thus

$$\dot{R}(t) = S(\omega_N(t))R(t), \tag{2.3}$$

the rotational kinematics equation of a rigid body for an angular velocity vector expressed in navigation frame coordinates.

The kinematic equation (2.3) has an alternative form, which we now develop by taking advantage of the last property developed in Section 2.2:

$$\begin{aligned}
\dot{R}(t) &= S(\omega_N(t))R(t) \\
&= R(t)R^T(t)S(\omega_N(t))R(t) \\
&= R(t)S(R^T\omega_N(t)) \\
\dot{R}(t) &= R(t)S(\omega_B(t))
\end{aligned} \tag{2.4}$$

where $\omega_B(t) = R^T(t)\omega_N(t)$ is the absolute angular velocity vector of the rigid body expressed in body frame coordinates. The components of $\omega_B(t)$ can be directly measured using a set of three rate gyros, each fixed to the rigid body and aligned with its corresponding body frame axis b_i. This class of sensors, known as *inertial*, measures absolute quantities (here, angular velocity) despite being mounted on a rotating/accelerating body.

2.4 Navigation Dynamics

We now derive the navigation dynamics equations used for Aided Inertial Navigation System (Aided INS) design in Chapters 3 and 4 using the tools in Sections 2.1–2.3. The navigation problem makes use of three coordinate frames schematically illustrated in Figure 2.3:

- Body-fixed frame B: Origin rigidly attached to Helicopter's centre of mass (CM), with b_1 and b_2 aligned with longitudinal and lateral axes, and b_3 pointing down. The on-board Inertial Measurement Unit (IMU) provides accelerometer, rate gyro and magnetometer measurements in this frame.
- Navigation frame N: Origin is fixed at an arbitrary geographic location, with n_1, n_2 and n_3 pointing in the North, East and Down directions, respectively. The navigation system outputs its estimates in this frame.
- Earth-Centered, Earth-Fixed (ECEF) frame E: Origin is fixed at the Earth's centre of mass, with axes pointing towards $(0°\text{N}, 0°\text{E})$, $(0°\text{N}, 90°\text{E})$ and $90°\text{N}$ geodetic coordinates, respectively. The GPS receiver reports position p_E in the ECEF frame.

We neglect the rotation of the Earth, such that E and N frames are inertial. This assumption is due to the available resolution of the rate gyros as well as the back-and-forth flying patterns which nullify the Coriolis effect.

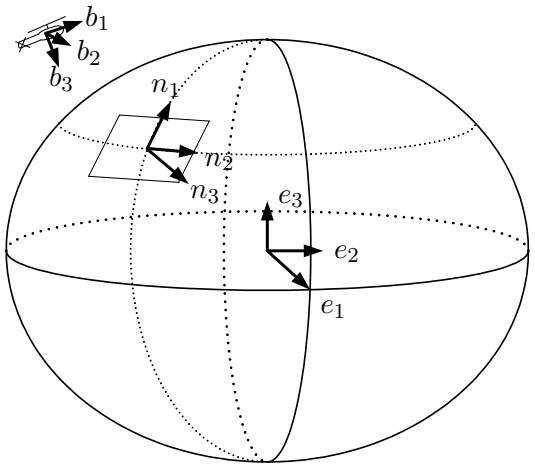

Figure 2.3: Body, Navigation and ECEF frames

Let p denote the position vector of the helicopter's CM with respect to the navigation frame origin, with $p_N(t)$ the vector's coordinates in the navigation frame. As in Section 2.3 we have $(d/dt)p_N(t) = v_N(t)$, an absolute velocity since its components are measured w.r.t. the stationary origin of frame N, and so Newton's second law applies directly:

$$\frac{d}{dt}(mv_N(t)) = F_N(t) \Longrightarrow ma_N(t) = F_N(t)$$

where $(d/dt)v_N(t) = a_N(t)$ is the acceleration of the helicopter's CM w.r.t. the origin of frame N and $F_N(t)$ is the net external force vector acting on the helicopter expressed in N frame coordinates; this last term includes the gravity force mg_N where $g_N = [0 \quad 0 \quad 9.81]^T$ is a constant. The expression above becomes

$$\begin{aligned} m\dot{v}_N(t) &= F_N(t) - mg_N + mg_N \\ \dot{v}_N(t) &= a_N(t) - g_N + g_N \\ \dot{v}_N(t) &= R_N^B(t)\left(a_B(t) - g_B(t)\right) + g_N \end{aligned}$$

where $R_N^B(t) := R(t)$ measures the attitude of the helicopter w.r.t. the navigation frame and $a_B(t) - g_B(t) := f_B(t)$, the difference between inertial and gravity accelerations known as specific force f, is directly measurable using a triaxial accelerometer fixed to the helicopter and aligned with the B frame axes. Remark an accelerometer which is stationary outputs $f_B = -g_B$ as its measurement, while in a free-fall condition the output will be $f_B = 0$. The dynamics of attitude $R(t)$ are governed by (2.4)

$$\dot{R}(t) = R(t)S(\omega_B(t))$$

where ω_B is directly measured by the IMU's triaxial rate gyro. The dynamics of the navigation system are thus

$$\begin{aligned} \dot{p}_N &= v_N \\ \dot{v}_N &= Rf_B + g_N \\ \dot{R} &= RS(\omega_B) \end{aligned} \tag{2.5}$$

with state $x = [p_N \quad v_N \quad R]$ and inputs $u = [f_B \quad \omega_B]$. The outputs of the system are taken as the IMU magnetometer measurement $m_B(t) = R^T(t)m_N$, where m_N is the Earth's magnetic field in the navigation frame, to be discussed in Section 2.8; and the GPS receiver measurement $r_E(t) = r_E^o + p_E(t)$, where r and r^o are position vectors from the E frame origin (Earth's CM) to the vehicle and N frame origin, respectively. The r_E^o value can be measured directly using the GPS receiver, either at a fixed location or by taking the helicopter's pre-takeoff location as the N frame origin. The $p_E(t)$ value is written in terms of system state x as $p_E(t) = R_E^N p_N(t)$ where rotation matrix R_E^N is computed by [51, p. 43]

$$R_E^N = \begin{bmatrix} -\sin\lambda\cos\varphi & -\sin\varphi & -\cos\lambda\cos\varphi \\ -\sin\lambda\sin\varphi & \cos\varphi & -\cos\lambda\sin\varphi \\ \cos\lambda & 0 & -\sin\lambda \end{bmatrix} \tag{2.6}$$

where (λ, φ) are the geodetic (latitude, longitude) coordinates of the N frame origin. These are obtained from $r_E^o = [X \quad Y \quad Z]$ using the closed-form solution [32]

$$\begin{aligned} \upsilon &= \arctan \frac{bZ}{ap}\left(1 + e'\frac{b}{R}\right) \\ \lambda &= \arctan \frac{Z + e'b\sin^3\upsilon}{p - e^2 a\cos^3\upsilon} \\ \varphi &= \text{atan2}(Y, X), \end{aligned} \tag{2.7}$$

where $p = \sqrt{X^2 + Y^2}$, $R = \sqrt{X^2 + Y^2 + Z^2}$, and a, b, e^2, e' are respectively semi-major axis, semi-minor axis, first eccentricity squared and second eccentricity of the ellipsoid used to approximate the shape of the earth's surface. The most commonly used ellipsoid model is WGS84 [1, Sec. 3] which defines these values as $a = 6378137.0$ m, $b = 6356752.3142$ m, $e = 6.69437999014 \times 10^{-3}$ and $e' = 8.2094437949696 \times 10^{-2}$. In summary the navigation system outputs $y = [y_m \quad y_p]$ are written as functions of state x as

$$\begin{aligned} y_m &= R^T m_N \\ y_p &= r_E^o + R_E^N p_N \end{aligned} \tag{2.8}$$

A navigation system estimates $x = [p_N \quad v_N \quad R]$ from sensor inputs $u = [f_B \quad \omega_B]$ and aiding measurements $y = [y_m \quad y_p]$ — a nonlinear observer design problem due to the form of (2.5).

2.5 Parameterizing the Rotation Matrix

Up to now, the orientation of the helicopter with respect to the ground was described by the nine-element matrix R. We now show it is possible to parameterize the rotation matrix using a smaller set of numbers. This can be intuitively seen from the fact that any rotation matrix has orthonormal columns and a determinant of $+1$, so the nine entries of R *cannot* be independent of each other.

Consider the matrix exponential of a skew-symmetric matrix,

$$e^{S(x)\theta}$$

where $x \in \mathbb{R}^3$ as before and $\theta \in \mathbb{R}$ is a scalar whose physical significance will become clear soon. We have

$$\left(e^{S(x)\theta}\right)^{-1} = e^{-S(x)\theta} = e^{S(x)^T\theta} = \left(e^{S(x)\theta}\right)^T,$$

i.e. $e^{S(x)\theta}$ is an orthogonal matrix hence

$$\left|e^{S(x)\theta}\right| = \pm 1.$$

Note that for $\theta = 0$, $|e^0| = |I| = 1$, and because both the matrix exponential and the determinant are continuous functions $|e^{S(x)\theta}| = 1$. Therefore $e^{S(x)\theta} \in SO(3)$ for $x \in \mathbb{R}^3$, $\theta \in \mathbb{R}$ — a candidate 4-element parametrization of R, but only if it can be shown to be surjective onto $SO(3)$.

Before proving surjectivity, we need a formula for calculating $e^{S(x)\theta}$. By definition,

$$e^{S(x)\theta} = I + S(x)\theta + \frac{S(x)^2\theta^2}{2!} + \frac{S(x)^3\theta^3}{3!} + \cdots$$

By direct computation, we have:

$$\begin{aligned}
S(x) &= \begin{bmatrix} 0 & -x_3 & x_2 \\ x_3 & 0 & -x_1 \\ -x_2 & x_1 & 0 \end{bmatrix}, \\
S(x)^2 &= \begin{bmatrix} -x_2^2 - x_3^2 & x_1x_2 & x_1x_3 \\ x_1x_2 & -x_1^2 - x_3^2 & x_2x_3 \\ x_1x_3 & x_2x_3 & -x_1^2 - x_2^2 \end{bmatrix}, \\
S(x)^3 &= \begin{bmatrix} 0 & x_1^2x_3 + x_2^2x_3 + x_3^3 & -x_1^2x_2 - x_2^3 - x_1^2x_2 \\ -x_1^2x_3 - x_2^2x_3 - x_3^3 & 0 & x_1^3 + x_1x_2^2 + x_1x_3^2 \\ x_1^2x_2 + x_2^3 + x_1^2x_2 & -x_1^3 - x_1x_2^2 - x_1x_3^2 & 0 \end{bmatrix} \\
&= -(x_1^2 + x_2^2 + x_3^2) \begin{bmatrix} 0 & -x_3 & x_2 \\ x_3 & 0 & -x_1 \\ -x_2 & x_1 & 0 \end{bmatrix} = -\|x\|^2 S(x).
\end{aligned}$$

We see that

$$\begin{aligned}
S(x)^4 &= -\|x\|^2 S(x)^2, \\
S(x)^5 &= \left(-\|x\|^2\right)^2 S(x),
\end{aligned}$$

and by induction,

$$\begin{aligned}
S(x)^{2k} &= (-1)^{k-1}\left(\|x\|^2\right)^{k-1} S(x)^2, \quad k = 1, 2, \ldots \\
S(x)^{2k+1} &= (-1)^k\left(\|x\|^2\right)^k S(x), \quad k = 0, 1, \ldots
\end{aligned}$$

Returning to the matrix exponential definition,

$$\begin{aligned}
e^{S(x)\theta} &= I + \left(S(x)\theta + \frac{S(x)^3\theta^3}{3!} + \cdots\right) + \left(\frac{S(x)^2\theta^2}{2!} + \frac{S(x)^4\theta^4}{4!} + \cdots\right) \\
&= I + \left(S(x)\theta - \frac{\|x\|^2 S(x)\theta^3}{3!} + \cdots\right) + \left(\frac{S(x)^2\theta^2}{2!} - \frac{\|x\|^2 S(x)^2\theta^4}{4!} + \cdots\right) \\
&= I + \frac{S(x)}{\|x\|}\left(\|x\|\theta - \frac{\|x\|^3\theta^3}{3!} + \cdots\right) + \frac{S(x)^2}{\|x\|^2}\left(\frac{\|x\|^2\theta^2}{2!} - \frac{\|x\|^4\theta^4}{4!} + \cdots\right) \\
e^{S(x)\theta} &= I + \frac{S(x)}{\|x\|}\sin(\|x\|\theta) + \frac{S(x)^2}{\|x\|^2}\left(1 - \cos(\|x\|\theta)\right), \qquad (2.9)
\end{aligned}$$

known as Rodrigues' formula. We will use the normalized version of x, $a = x/\|x\|$, such that Rodrigues' formula takes the form

$$e^{S(a)\theta} = I + S(a)\sin\theta + S(a)^2(1 - \cos\theta), \quad \|a\| = 1. \qquad (2.10)$$

Note that (2.10) is still a 4-element (candidate) parametrization of $SO(3)$, because a is constructed of three independent entries, then normalized. To prove surjectivity, start with an arbitrary $R \in SO(3)$. Expanding (2.10), we obtain

$$\underbrace{\begin{bmatrix} 1-(a_2^2+a_3^2)v_\theta & -a_3 s_\theta + a_1 a_2 v_\theta & a_2 s_\theta + a_1 a_3 v_\theta \\ a_3 s_\theta + a_1 a_2 v_\theta & 1-(a_1^2+a_3^2)v_\theta & -a_1 s_\theta + a_2 a_3 v_\theta \\ -a_2 s_\theta + a_1 a_3 v_\theta & a_1 s_\theta + a_2 a_3 v_\theta & 1-(a_1^2+a_2^2)v_\theta \end{bmatrix}}_{e^{S(a)\theta}} = \underbrace{\begin{bmatrix} r_{11} & r_{12} & r_{13} \\ r_{21} & r_{22} & r_{23} \\ r_{31} & r_{32} & r_{33} \end{bmatrix}}_{R}, \qquad (2.11)$$

where $a = [a_1 \quad a_2 \quad a_3]^T$, $s_\theta = \sin\theta$ and $v_\theta = 1 - \cos\theta$, the versine function. Equating traces,

$$3 - 2(1-\cos\theta)\underbrace{(a_1^2 + a_2^2 + a_3^2)}_{\|a\|^2=1} = \underbrace{r_{11} + r_{22} + r_{33}}_{\mathrm{tr}(R)} \Longrightarrow \theta = \arccos\left(\frac{\mathrm{tr}(R) - 1}{2}\right) \qquad (2.12)$$

A property of all rotation matrices, i.e. members of $SO(3)$, is that they possess one eigenvalue at $+1$, and the remaining two eigenvalues are complex conjugates with magnitude 1. Also, the trace of any matrix equals the sum of its eigenvalues. We conclude $-1 \leq \mathrm{tr}(R) \leq 3$, and the domain of arccos in (2.12) is $[-1, 1]$, so θ exists for any $\{r_{11}, r_{22}, r_{33}\} \in R$. Strictly speaking, the solution of (2.12) is $\pm\theta$, because cos is an even function; we can remove this ambiguity by the restriction $\theta \geq 0$, however. Equating the remaining entries in (2.11), we have

$$\begin{aligned}
r_{32} - r_{23} &= 2a_1 \sin\theta, \\
r_{13} - r_{31} &= 2a_2 \sin\theta, \\
r_{21} - r_{12} &= 2a_3 \sin\theta,
\end{aligned}$$

from which, provided $\theta \neq 0$,

$$\begin{bmatrix} a_1 \\ a_2 \\ a_3 \end{bmatrix} = \frac{1}{2\sin\theta}\begin{bmatrix} r_{32} - r_{23} \\ r_{13} - r_{31} \\ r_{21} - r_{12} \end{bmatrix},$$

which proves the existence of a for any $\{r_{12}, r_{13}, r_{21}, r_{23}, r_{31}, r_{32}\}$ entries of R provided $\theta \neq 0$. Consider the $\theta = 0$ case, which only occurs when $\mathrm{tr}(R) = 3$ in (2.12). Since R has orthonormal columns, this is only possible for $R = I$. Returning to (2.11), we have

$$\begin{bmatrix} 1-(a_2^2+a_3^2)0 & -a_30+a_1a_20 & a_20+a_1a_30 \\ a_30+a_1a_20 & 1-(a_1^2+a_3^2)0 & -a_10+a_2a_30 \\ -a_20+a_1a_30 & a_10+a_2a_30 & 1-(a_1^2+a_2^2)0 \end{bmatrix} = \begin{bmatrix} 1 & 0 & 0 \\ 0 & 1 & 0 \\ 0 & 0 & 1 \end{bmatrix},$$

which is obviously satisfied for *any* a, meaning $R = I$ is in the range of $e^{S(a)\theta}$ as well. This completes the proof of surjectivity, and we have shown that $e^{S(a)\theta}$ fully parameterizes $SO(3)$. Comparing this result with Euler's Rotation Theorem, we see that a physically represents the (normalized) axis of rotation and θ the angle through which the object is rotated. $\theta = 0$ is the no-rotation case, in which case any rotation axis a can be used in the exponential. From the proof, we see that a given R configuration yields a unique $\{a, \theta\}$ pair (as long as $\theta > 0$ is assumed, otherwise both $\{\theta, a\}$ and $\{-\theta, -a\}$ are solutions), except at $R = I$, where an infinity of solutions exist. This effect is known as a *singularity* of the parametrization, because it destroys the continuous nature of the inverse problem (finding the set of parameters given an orientation R). Singularities are also discussed in Section 2.6.

Consider the matrix exponential $e^{S(x)}$, where $x \in \mathbb{R}^3$ is not necessarily of unit length. Clearly,

$$e^{S(x)} = e^{S(x/\|x\|)\,\|x\|}.$$

By rotating x (changing its entries while keeping $\|x\|$ constant), it is possible for $x/\|x\|$ to span the entire set $a \in \mathbb{R}^3, \|a\| = 1$; this is true for any choice of $\|x\| \in \mathbb{R}$. In this way, $e^{S(x)}$ can be made equal to $e^{S(a)\theta}$, $\|a\| = 1$, $\theta \in \mathbb{R}$, which was shown to be surjective onto $SO(3)$. Since $x \in \mathbb{R}^3$, we conclude it is possible to surjectively parameterize SO(3) with only three parameters.

2.6 Euler Angles Parametrization

Having shown that $R \in SO(3)$ can be parameterized using only three numbers, we now develop a concrete case, Euler angles. We will compose three rotations, each described by one angle, to produce the final orientation R. The composition of rotations was discussed in Section 2.1.

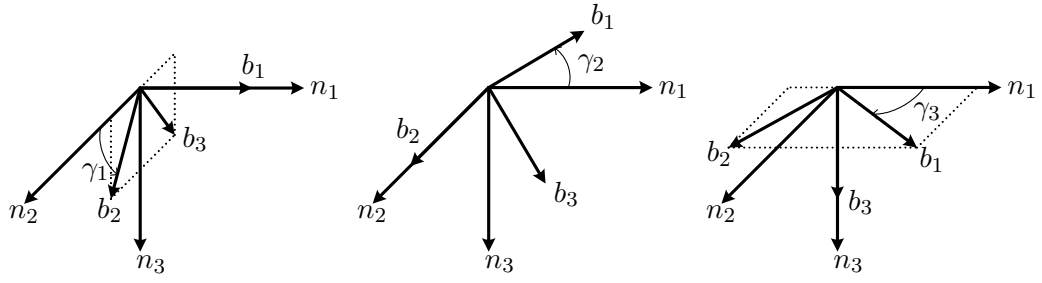

Figure 2.4: Elementary rotations about n_1, n_2 and n_3

We first derive the rotation matrices about the three basis axes, illustrated in Figure 2.4. Note that *unlike* Section 2.1, all three rotations are made with respect

to the same frame N instead of using the previous frame as the "datum". This will be reflected in the physical interpretation of Euler Angles below — however, the composition of rotations still holds because R measures only the rotation between two frames, so composing three rotations relative to N is mathematically identical to the case in Section 2.1. Using the definition of R from Section 2.1,

$$R_N^B = \begin{bmatrix} b_1 \cdot n_1 & b_2 \cdot n_1 & b_3 \cdot n_1 \\ b_1 \cdot n_2 & b_2 \cdot n_2 & b_3 \cdot n_2 \\ b_1 \cdot n_3 & b_2 \cdot n_3 & b_3 \cdot n_3 \end{bmatrix},$$

we work out the rotations about n_1, n_2 and n_3 as

$$R_1(\gamma_1) = \begin{bmatrix} 1 & 0 & 0 \\ 0 & \cos\gamma_1 & \cos(\pi/2+\gamma_1) \\ 0 & \cos(\pi/2-\gamma_1) & \cos\gamma_1 \end{bmatrix} = \begin{bmatrix} 1 & 0 & 0 \\ 0 & \cos\gamma_1 & -\sin\gamma_1 \\ 0 & \sin\gamma_1 & \cos\gamma_1 \end{bmatrix}, \quad (2.13a)$$

$$R_2(\gamma_2) = \begin{bmatrix} \cos\gamma_2 & 0 & \cos(\pi/2-\gamma_2) \\ 0 & 1 & 0 \\ \cos(\pi/2+\gamma_2) & 0 & \cos\gamma_2 \end{bmatrix} = \begin{bmatrix} \cos\gamma_2 & 0 & \sin\gamma_2 \\ 0 & 1 & 0 \\ -\sin\gamma_2 & 0 & \cos\gamma_2 \end{bmatrix}, \quad (2.13b)$$

$$R_3(\gamma_3) = \begin{bmatrix} \cos\gamma_3 & \cos(\pi/2+\gamma_3) & 0 \\ \cos(\pi/2-\gamma_3) & \cos\gamma_3 & 0 \\ 0 & 0 & 1 \end{bmatrix} = \begin{bmatrix} \cos\gamma_3 & -\sin\gamma_3 & 0 \\ \sin\gamma_3 & \cos\gamma_3 & 0 \\ 0 & 0 & 1 \end{bmatrix}. \quad (2.13c)$$

It's easy to directly verify that each matrix in (2.13) belongs to $SO(3)$.

As seen in Section 2.1 composing rotations corresponds to matrix multiplication, hence the order is not commutative. Any three-part sequence is valid provided adjacent rotations are not made about the same axis, which gives $3 \times 2 \times 2 = 12$ possible parameterizations. We choose to use the so-called roll-pitch-yaw sequence, the most widely used in aerospace literature. This sequence is defined by

$$R_N^B = R_3(\psi)R_2(\theta)R_1(\phi), \quad (2.14)$$

where roll ϕ, pitch θ and yaw ψ are defined as rotations about the x, y and z axes, respectively. Substituting (2.13) into (2.14) and performing matrix multiplication gives

$$R_N^B = \begin{bmatrix} c_\theta c_\psi & s_\phi s_\theta c_\psi - c_\phi s_\psi & c_\phi s_\theta c_\psi + s_\phi s_\psi \\ c_\theta s_\psi & s_\phi s_\theta s_\psi + c_\phi c_\psi & c_\phi s_\theta s_\psi - s_\phi c_\psi \\ -s_\theta & s_\phi c_\theta & c_\phi c_\theta \end{bmatrix}, \quad (2.15)$$

where $c_\phi = \cos\phi$, etc. Since $R_k \in SO(3)$ we know $R_N^B \in SO(3)$. As will be shown below, roll-pitch-yaw is surjective *but not* injective onto $SO(3)$.

Physically, the composition (2.14) represents an ordered sequence of rotations of the helicopter body frame with respect to the ground. As seen in Figure 2.4, R_1, R_2 and R_3 represent rotations with respect to the N frame, so (2.14) corresponds to the following rotation sequence, starting from a level flight configuration (frames N and B aligned, $R = I$):

1. Rotate the helicopter about n_1 by ϕ (roll)
2. Rotate about n_2 by θ (pitch)
3. Rotate about n_3 by ψ (yaw).

It is also possible to interpret the angles ϕ, θ, ψ from a body-frame point of view. Starting from $R = I$, the rotations are made with respect to b_1, b_2 and b_3, requiring the transpose version of (2.13) because $R_N^B = (R_B^N)^T$ as shown in Section 2.1. Note the base frame B gets rotated at each step, but once again the mathematical form of composing rotations remains the same. For reasons that will become clear soon the rotation sequence is done "backwards" from the one above:

1. Rotate the helicopter about b_3 by ψ (yaw)
2. Rotate about b_2 by θ (pitch)
3. Rotate about b_1 by ϕ (roll)

This sequence of rotations composes to

$$R_B^N = R_1(\phi)^T R_2(\theta)^T R_3(\psi)^T$$

and transposing both sides gives

$$R_N^B = R_3(\psi) R_2(\theta) R_1(\phi),$$

which is identical to (2.14) above. In this sense, roll-pitch-yaw represents both the ground-fixed rotation sequence

$$\text{Roll } \phi \text{ around } n_1 \Longrightarrow \text{Pitch } \theta \text{ around } n_2 \Longrightarrow \text{Yaw } \psi \text{ around } n_3,$$

and the body-fixed rotation sequence

$$\text{Yaw } \psi \text{ around } b_3 \Longrightarrow \text{Pitch } \theta \text{ around } b_2 \Longrightarrow \text{Roll } \phi \text{ around } b_1.$$

Consider the numerical example $\{\phi = -\pi/2,\ \theta = \pi/2,\ \psi = \pi\}$. This sequence can be executed in either the ground-fixed or body-fixed order, giving the same final configuration as illustrated in Figure 2.5. Remark that the body frame axes b_k are rotated at each step.

Consider the inverse problem of calculating the sequence $\{\phi, \theta, \psi\}$ given an orientation R. Starting from (2.15),

$$R = \begin{bmatrix} c_\theta c_\psi & s_\phi s_\theta c_\psi - c_\phi s_\psi & c_\phi s_\theta c_\psi + s_\phi s_\psi \\ c_\theta s_\psi & s_\phi s_\theta s_\psi + c_\phi c_\psi & c_\phi s_\theta s_\psi - s_\phi c_\psi \\ -s_\theta & s_\phi c_\theta & c_\phi c_\theta \end{bmatrix} = \begin{bmatrix} r_{11} & r_{12} & r_{13} \\ r_{21} & r_{22} & r_{23} \\ r_{31} & r_{32} & r_{33} \end{bmatrix}. \tag{2.16}$$

By inspection, $\theta = -\arcsin r_{31}$. Since $R \in SO(3)$ the matrices (2.16) are orthonormal. It follows that $|r_{31}| \leq 1$ and so $-\pi/2 \leq \theta \leq \pi/2$. Consider first the case $|\theta| < \pi/2$, from which $c_\theta \neq 0$ and thus

$$\tan\phi = \frac{r_{32}}{r_{33}} \Longrightarrow \phi = \text{atan2}(r_{32}, r_{33})$$
$$\tan\psi = \frac{r_{21}}{r_{11}} \Longrightarrow \psi = \text{atan2}(r_{21}, r_{11})$$

where atan2 is the "smart" arctan function which assigns the correct quadrant and handles the case of division by zero. Since arcsin and arctan are injective functions and the entire range of R is in their domain, roll-pitch-yaw is a bijective

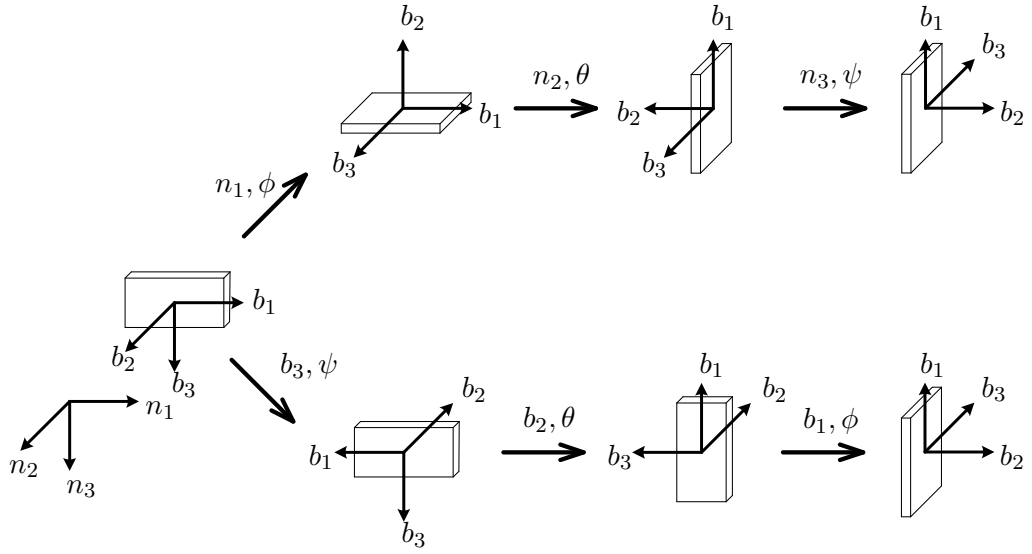

Figure 2.5: Roll-Pitch-Yaw sequence of rotations, $\phi = -\pi/2$, $\theta = \pi/2$, $\psi = \pi$

parametrization of $SO(3)$ *provided* $\theta \neq \pm\theta/2$. This last condition is a *singularity* of Euler angles, discussed next.

Consider the case where $r_{31} = \pm 1 \Longrightarrow \theta = \mp\pi/2$. From orthonormality, $r_{11} = r_{21} = 0$ necessarily, and $r_{33} = r_{32} = 0$ since $R^T \in SO(3)$ as well. Equation (2.16) reduces to

$$\begin{bmatrix} 0 & r_{12} & r_{13} \\ 0 & r_{22} & r_{23} \\ \pm 1 & 0 & 0 \end{bmatrix} = \begin{bmatrix} 0 & \mp\sin(\phi \pm \psi) & \mp\cos(\phi \pm \psi) \\ 0 & \cos(\phi \pm \psi) & -\sin(\phi \pm \psi) \\ \pm 1 & 0 & 0 \end{bmatrix}.$$

We see injectivity has been lost for $\theta = \mp\pi/2$ because two different roll-pitch-yaw sequences with the same $\phi \pm \psi$ will map to the same R. This loss of injectivity is a singularity of the roll-pitch-yaw parametrization, just like $R = I$ for axis-angle in Section 2.5. As an example consider Figure 2.5 again, which used a (singular) sequence $\phi = -\pi/2$, $\theta = \pi/2$, $\psi = \pi$. A different sequence with $\theta = \pi/2$ and $\phi - \psi = -\pi/2 - \pi = -3\pi/2$, for instance $\phi = -\pi$, $\psi = \pi/2$, will give the same final orientation. This is shown in Figure 2.6 using the body-fixed rotation convention.

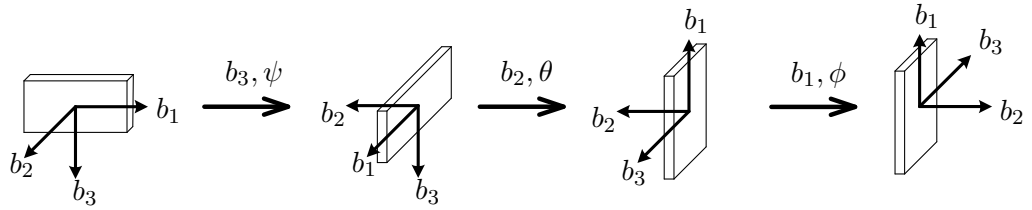

Figure 2.6: Alternative Roll-Pitch-Yaw sequence of rotations, $\phi = -\pi$, $\theta = \pi/2$, $\psi = \pi/2$

Euler angles can be used to parameterize the rotation kinematics developed in Section 2.3. Consider the body-frame version (2.4)

$$\dot{R}(t) = R(t)S(\omega_B(t)),$$

We use R from (2.15), compute $\dot{R}$ and solve the above for $\{\dot{\phi}, \dot{\theta}, \dot{\psi}\}$. Since the $\dot{R}$ expression is quite long, we first group terms on the left side then perform the matrix multiplication in e.g. Mathematica:

$$R^T \dot{R} = S(\omega_B)$$

$$\begin{bmatrix} 0 & s_\phi \dot{\theta} - c_\phi c_\theta \dot{\psi} & c_\phi \dot{\theta} + s_\phi c_\theta \dot{\psi} \\ -s_\phi \dot{\theta} + c_\phi c_\theta \dot{\psi} & 0 & -\dot{\phi} + s_\theta \dot{\psi} \\ -c_\phi \dot{\theta} - s_\phi c_\theta \dot{\psi} & \dot{\phi} - s_\theta \dot{\psi} & 0 \end{bmatrix} = \begin{bmatrix} 0 & -\omega_{B,3} & \omega_{B,2} \\ \omega_{B,3} & 0 & -\omega_{B,1} \\ -\omega_{B,2} & \omega_{B,1} & 0 \end{bmatrix}.$$

Isolating ω_B,

$$\begin{bmatrix} \omega_{B,1} \\ \omega_{B,2} \\ \omega_{B,3} \end{bmatrix} = \begin{bmatrix} \dot{\phi} - s_\theta \dot{\psi} \\ c_\phi \dot{\theta} + s_\phi c_\theta \dot{\psi} \\ -s_\phi \dot{\theta} + c_\phi c_\theta \dot{\psi} \end{bmatrix} = \begin{bmatrix} 1 & 0 & -s_\theta \\ 0 & c_\phi & s_\phi c_\theta \\ 0 & -s_\phi & c_\phi c_\theta \end{bmatrix} \begin{bmatrix} \dot{\phi} \\ \dot{\theta} \\ \dot{\psi} \end{bmatrix}$$

Inverting, we obtain

$$\begin{bmatrix} \dot{\phi} \\ \dot{\theta} \\ \dot{\psi} \end{bmatrix} = \begin{bmatrix} 1 & \sin\phi \tan\theta & \cos\phi \tan\theta \\ 0 & \cos\phi & -\sin\phi \\ 0 & \sin\phi \sec\theta & \cos\phi \sec\theta \end{bmatrix} \begin{bmatrix} \omega_{B,1} \\ \omega_{B,2} \\ \omega_{B,3} \end{bmatrix},$$

or equivalently

$$\begin{aligned} \dot{\phi} &= \omega_{B,1} + \sin\phi \tan\theta\, \omega_{B,2} + \cos\phi \tan\theta\, \omega_{B,3} \\ \dot{\theta} &= \cos\phi\, \omega_{B,2} - \sin\phi\, \omega_{B,3} \\ \dot{\psi} &= \sin\phi \sec\theta\, \omega_{B,2} + \cos\phi \sec\theta\, \omega_{B,3} \end{aligned} \tag{2.17}$$

Equations (2.17) are the dynamics of the roll-pitch-yaw Euler angle parametrization. Remark the dynamics involve trig functions and become undefined at the parametrization singularity $\theta = \pm\pi/2$, making them a poor choice for numerical implementation.

As mentioned previously, roll-pitch-yaw is just one of twelve possible Euler Angle parameterizations. It can be verified that all exhibit singularities, and in more general terms it can be shown that *any* three-element parametrization of $SO(3)$ will possess singularities [125]. A practical solution is avoiding configurations which are singular, e.g. never pitching the helicopter straight up or down. A more elegant solution is to use a parametrization with > 3 elements which does not contain singularities, specifically unit quaternions discussed in the next section.

2.7 Quaternions

Quaternions were first introduced by Hamilton as a generalization of complex numbers. Just as complex numbers on the unit circle can represent planar rotations via $e^{i\theta}$, unit-length quaternions can represent three-dimensional rotations.

A quaternion $r \in \mathbb{H}$ is defined as

$$r = r_0 + r_1 \boldsymbol{i} + r_2 \boldsymbol{j} + r_3 \boldsymbol{k}$$

where $(r_0, r_1, r_2, r_3) \in \mathbb{R}^4$ and $\mathbb{H}$ is a four-dimensional vector space over the reals with basis vectors $\{1, \boldsymbol{i}, \boldsymbol{j}, \boldsymbol{k}\} \in \mathbb{H}$. A quaternion can be written as $r = (r_0, \vec{r})$

where $r_0 \in \mathbb{R}$ is the "scalar" component and $\vec{r} := (r_1, r_2, r_3) \in \mathbb{R}^3$ is the "vector" component. A quaternion with $r_0 = 0$ is known as a "pure" quaternion.

Quaternion multiplication $*$ is defined by

$$\boldsymbol{i} * \boldsymbol{i} = \boldsymbol{j} * \boldsymbol{j} = \boldsymbol{k} * \boldsymbol{k} = \boldsymbol{i} * \boldsymbol{j} * \boldsymbol{k} = -1,$$

a bilinear, distributive, *non-commutative* operation. Left and right–multiplying the above yields

$$\begin{aligned} \boldsymbol{i} * \boldsymbol{j} &= \boldsymbol{k} & \boldsymbol{j} * \boldsymbol{k} &= \boldsymbol{i} & \boldsymbol{k} * \boldsymbol{i} &= \boldsymbol{j}, \\ \boldsymbol{j} * \boldsymbol{i} &= -\boldsymbol{k} & \boldsymbol{k} * \boldsymbol{j} &= -\boldsymbol{i} & \boldsymbol{i} * \boldsymbol{k} &= -\boldsymbol{j}. \end{aligned}$$

The multiplication of quaternions $r = (r_0, \vec{r})$ and $s = (s_0, \vec{s})$ is written out as

$$\begin{aligned} r * s =& (r_0 + r_1\boldsymbol{i} + r_2\boldsymbol{j} + r_3\boldsymbol{k}) * (s_0 + s_1\boldsymbol{i} + s_2\boldsymbol{j} + s_3\boldsymbol{k}) \\ =& r_0 s_0 + r_0 s_1 \boldsymbol{i} + r_0 s_2 \boldsymbol{j} + r_0 s_3 \boldsymbol{k} \\ &+ r_1 s_0 \boldsymbol{i} + r_1 s_1 \boldsymbol{i} * \boldsymbol{i} + r_1 s_2 \boldsymbol{i} * \boldsymbol{j} + r_1 s_3 \boldsymbol{i} * \boldsymbol{k} \\ &+ r_2 s_0 \boldsymbol{j} + r_2 s_1 \boldsymbol{j} * \boldsymbol{i} + r_2 s_2 \boldsymbol{j} * \boldsymbol{j} + r_2 s_3 \boldsymbol{j} * \boldsymbol{k} \\ &+ r_3 s_0 \boldsymbol{k} + r_3 s_1 \boldsymbol{k} * \boldsymbol{i} + r_3 s_2 \boldsymbol{k} * \boldsymbol{j} + r_3 s_3 \boldsymbol{k} * \boldsymbol{k} \\ =& (r_0 s_0 - r_1 s_1 - r_2 s_2 - r_3 s_3) \\ &+ r_0 s_1 \boldsymbol{i} + r_0 s_2 \boldsymbol{j} + r_0 s_3 \boldsymbol{k} \\ &+ r_1 s_0 \boldsymbol{i} + r_2 s_0 \boldsymbol{j} + r_3 s_0 \boldsymbol{k} \\ &+ (r_2 s_3 - r_3 s_2)\boldsymbol{i} + (r_3 s_1 - r_1 s_3)\boldsymbol{j} + (r_1 s_2 - r_2 s_1)\boldsymbol{k} \\ =& (r_0 s_0 - \vec{r} \cdot \vec{s}, r_0 \vec{s} + s_0 \vec{r} + \vec{r} \times \vec{s}), \end{aligned}$$

where $\cdot$ and $\times$ are the $\mathbb{R}^3$ inner and cross-product, respectively. Note that quaternion multiplication is *not* commutative. By inspection the above can be written as a matrix multiplication, better suited for numerical implementation (note there are two possible forms):

$$r * s = \begin{bmatrix} r_0 & -r_1 & -r_2 & -r_3 \\ r_1 & r_0 & -r_3 & r_2 \\ r_2 & r_3 & r_0 & -r_1 \\ r_3 & -r_2 & r_1 & r_0 \end{bmatrix} \begin{bmatrix} s_0 \\ s_1 \\ s_2 \\ s_3 \end{bmatrix} = \begin{bmatrix} s_0 & -s_1 & -s_2 & -s_3 \\ s_1 & s_0 & s_3 & -s_2 \\ s_2 & -s_3 & s_0 & s_1 \\ s_3 & s_2 & -s_1 & s_0 \end{bmatrix} \begin{bmatrix} r_0 \\ r_1 \\ r_2 \\ r_3 \end{bmatrix}.$$

We define the quaternion conjugate as $r^* = (r_0, -\vec{r})$, and the norm as

$$\|r\| = \sqrt{r * r^*} = \sqrt{r_0^2 + r_1^2 + r_2^2 + r_3^2}.$$

The identity element for quaternion multiplication is $(1, \vec{0})$, and the inverse of a quaternion is given by $r^{-1} = r^*/\|r\|^2$. In this way, quaternions form a (non-Abelian) group under multiplication. Consider the conjugate of quaternion multiplication

$$(r * s)^* = (r_0 s_0 - \vec{r} \cdot \vec{s}, -r_0 \vec{s} - s_0 \vec{r} - \vec{r} \times \vec{s}),$$

and now note that

$$\begin{aligned} s^* * r^* &= (s_0, -\vec{s}) * (r_0, -\vec{r}) \\ &= \big(s_0 r_0 - (-\vec{s}) \cdot (-\vec{r}), s_0(-\vec{r}) + r_0(-\vec{s}) + (-\vec{s}) \times (-\vec{r})\big) \\ &= (r_0 s_0 - \vec{r} \cdot \vec{s}, -r_0 \vec{s} - s_0 \vec{r} - \vec{r} \times \vec{s}) \\ &= (r * s)^*, \end{aligned}$$

analogous to matrix multiplication; this property will be used shortly.

In Section 2.5, we have shown that $R \in SO(3)$ can be surjectively parameterized by a rotation axis a, $\|a\| = 1$ and angle θ via the matrix exponential. Define the associated quaternion

$$q = (\cos(\theta/2), a\sin(\theta/2)). \tag{2.18}$$

Remark that $\|q\| = 1$ by construction. We now show that (2.18) is also *surjective* onto unit quaternions

$$q = (q_0, \vec{q}), \quad q_0^2 + \|\vec{q}\|^2 = 1.$$

For the scalar part,

$$\cos(\theta/2) = q_0 \Longrightarrow \theta = 2\arccos q_0,$$

and since $|q_0| \leq 1$ for a unit quaternion, θ can always be found. For the vector part, consider first the case $\theta \neq 0$:

$$a\sin(\theta/2) = \vec{q} \Longrightarrow a = \frac{1}{\sqrt{1-q_0^2}} \begin{bmatrix} q_1 \\ q_2 \\ q_3 \end{bmatrix} = \frac{\vec{q}}{\|\vec{q}\|},$$

i.e. a unit rotation axis a can be found for any values of $\vec{q}$. Now consider the case $\theta = 0$:

$$\theta = 0 \Longrightarrow q_0 = 1 \Longrightarrow \vec{q} = \vec{0},$$

and the axis is

$$a\sin 0 = \vec{0} \Longrightarrow a \in \mathbb{R}^3 \Longrightarrow a = \vec{0};$$

i.e. we have *chosen* $a = \vec{0}$ when $\theta = 0$. Note in this case, $\|a\| \neq 1$ in Equation (2.18); however, $q = (1, \vec{0})$, still a unit quaternion. We conclude that (2.18) is a surjective parametrization of unit quaternions.

We now relate unit quaternions q written as (2.18) to $R \in SO(3)$. For the case $\theta \neq 0$, $\|a\| = 1$ and we use Rodrigues' formula (2.10):

$$\begin{aligned}
R &= I + S\left(\frac{\vec{q}}{\sqrt{1-q_0^2}}\right)\sin(2\arccos q_0) + S\left(\frac{\vec{q}}{\sqrt{1-q_0^2}}\right)^2 (1 - \cos(2\arccos q_0)) \\
&= I + S(\vec{q})\frac{2q_0\sqrt{1-q_0^2}}{\sqrt{1-q_0^2}} + S(\vec{q})^2\frac{2(1-q_0^2)}{1-q_0^2} \\
&= \begin{bmatrix} 1 & 0 & 0 \\ 0 & 1 & 0 \\ 0 & 0 & 1 \end{bmatrix} + 2q_0 \begin{bmatrix} 0 & -q_3 & q_2 \\ q_3 & 0 & -q_1 \\ -q_2 & q_1 & 0 \end{bmatrix} + 2\begin{bmatrix} -q_2^2 - q_3^2 & q_1q_2 & q_1q_3 \\ q_1q_2 & -q_1^2 - q_3^2 & q_2q_3 \\ q_1q_3 & q_2q_3 & -q_1^2 - q_2^2 \end{bmatrix} \\
&= \begin{bmatrix} 1 - 2(q_2^2 + q_3^2) & 2q_1q_2 - 2q_0q_3 & 2q_1q_3 + 2q_0q_2 \\ 2q_1q_2 + 2q_0q_3 & 1 - 2(q_1^2 + q_3^2) & 2q_2q_3 - 2q_0q_1 \\ 2q_1q_3 - 2q_0q_2 & 2q_2q_3 + 2q_0q_1 & 1 - 2(q_1^2 + q_2^2) \end{bmatrix}.
\end{aligned}$$

For $\theta = 0$, $q = (1, \vec{0})$, which gives $R = I$ above, which is consistent because $\theta = 0$ denotes the no-rotation case. We conclude the matrix above, equivalently written as

$$R = \begin{bmatrix} q_0^2 + q_1^2 - q_2^2 - q_3^2 & 2(q_1q_2 - q_0q_3) & 2(q_1q_3 + q_0q_2) \\ 2(q_1q_2 + q_0q_3) & q_0^2 - q_1^2 + q_2^2 - q_3^2 & 2(q_2q_3 - q_0q_1) \\ 2(q_1q_3 - q_0q_2) & 2(q_2q_3 + q_0q_1) & q_0^2 - q_1^2 - q_2^2 + q_3^2 \end{bmatrix}, \tag{2.19}$$

is the rotation matrix corresponding to the unit quaternion q. An immediate benefit of quaternion parametrization is that (2.19) does not use trig functions, as compared to e.g. roll-pitch-yaw in (2.15).

Using parametrization (2.19), we can investigate the injectivity of q onto $SO(3)$. As with Euler angles, begin by equating (2.19) to an arbitrary $R \in SO(3)$,

$$\begin{bmatrix} q_0^2+q_1^2-q_2^2-q_3^2 & 2(q_1q_2-q_0q_3) & 2(q_1q_3+q_0q_2) \\ 2(q_1q_2+q_0q_3) & q_0^2-q_1^2+q_2^2-q_3^2 & 2(q_2q_3-q_0q_1) \\ 2(q_1q_3-q_0q_2) & 2(q_2q_3+q_0q_1) & q_0^2-q_1^2-q_2^2+q_3^2 \end{bmatrix} = \begin{bmatrix} r_{11} & r_{12} & r_{13} \\ r_{21} & r_{22} & r_{23} \\ r_{31} & r_{32} & r_{33} \end{bmatrix}. \tag{2.20}$$

Equating traces, and using the fact that $\|q\| = 1 \Longrightarrow q_0^2+q_1^2+q_2^2+q_3^2 = 1$,

$$\begin{aligned} 3q_0^2 - (q_1^2+q_2^2+q_3^2) &= r_{11}+r_{22}+r_{33} \\ 4q_0^2 - 1 &= r_{11}+r_{22}+r_{33} \\ q_0 &= \pm\frac{1}{2}\sqrt{1+r_{11}+r_{22}+r_{33}}. \end{aligned}$$

As shown in Section 2.5, $-1 \leq \mathrm{tr}(R) \leq 3$, so $q_0 \in \mathbb{R}$, $|q_0| \leq 1$ as expected. Also note there are two possible solutions to q_0 — this will be discussed below. From (2.20) we also have

$$\begin{aligned} 4q_0q_1 &= r_{32}-r_{23} \\ 4q_0q_2 &= r_{13}-r_{31} \\ 4q_0q_3 &= r_{21}-r_{12}, \end{aligned}$$

so

$$q_1 = \frac{r_{32}-r_{23}}{4q_0}, \qquad q_2 = \frac{r_{13}-r_{31}}{4q_0}, \qquad q_3 = \frac{r_{21}-r_{12}}{4q_0}.$$

Since the q_0 sign choice is arbitrary, it follows that both q and $-q$ map to the *same* R, i.e. unit quaternions provide a two-to-one covering of $SO(3)$. From (2.18) this is equivalent to saying (θ, a) and $(-\theta, -a)$ produce the same rotation. This issue is easily resolved by always picking the $q_0 \geq 0$ value when converting R to q. The other ambiguity is the $q_0 = 0$ case, which occurs if $\theta = \pm\pi$ in (2.18). We investigate the limit

$$\lim_{q_0 \to 0} q_1 = \lim_{q_0 \to 0} \frac{r_{32}-r_{23}}{4q_0}.$$

Using (2.19), this can be rewritten as

$$\lim_{q_0 \to 0} \frac{2q_2q_3+2q_0q_1-2q_2q_3+2q_0q_1}{4q_0} = \lim_{q_0 \to 0} \frac{q_0q_1}{q_0},$$

and by using l'Hôpital's rule,

$$\lim_{q_0 \to 0} q_1 = q_1,$$

i.e. a (unique) limit exists. The analogous result holds for q_2 and q_3, which completes the proof that quaternions form a two-to-one covering of $SO(3)$.

Although we have proven the limit to exist, numerical problems will appear as $q_0 \to 0$ in the formulas above. To resolve this issue, we return to Equation (2.20)

and arrange the diagonal entries as one of:

$$\begin{aligned}\mathcal{B} &= r_{11} - r_{22} - r_{33} = 3q_1^2 - (q_0^2 + q_2^2 + q_3^2)\\ \mathcal{C} &= -r_{11} + r_{22} - r_{33} = 3q_2^2 - (q_0^2 + q_1^2 + q_3^2)\\ \mathcal{D} &= -r_{11} - r_{22} + r_{33} = 3q_3^2 - (q_0^2 + q_1^2 + q_2^2),\end{aligned}$$

which result in

$$q_1 = \frac{\pm\sqrt{1+\mathcal{B}}}{2}, \qquad q_2 = \frac{\pm\sqrt{1+\mathcal{C}}}{2}, \qquad q_3 = \frac{\pm\sqrt{1+\mathcal{D}}}{2},$$

respectively. Clearly if $\mathcal{A} = r_{11}+r_{22}+r_{33} = 0$, then $\mathcal{B}, \mathcal{C}, \mathcal{D} \neq 0$ and one of the above q_k solutions can be used to find the remaining three entries of q. Since q_k will be used in the denominator of the remaining entries, we use "option" $\max\{\mathcal{A}, \mathcal{B}, \mathcal{C}, \mathcal{D}\}$ to reduce numerical problems. The conversion formulas for each option are provided below:

$\mathcal{A}$:	$\mathcal{B}$:	$\mathcal{C}$:	$\mathcal{D}$:
$q_0 = \frac{\sqrt{1+\mathcal{A}}}{2}$	$q_0 = \frac{r_{32}-r_{23}}{2\sqrt{1+\mathcal{B}}}$	$q_0 = \frac{r_{13}-r_{31}}{2\sqrt{1+\mathcal{C}}}$	$q_0 = \frac{r_{21}-r_{12}}{2\sqrt{1+\mathcal{D}}}$
$q_1 = \frac{r_{32}-r_{23}}{2\sqrt{1+\mathcal{A}}}$	$q_1 = \frac{\sqrt{1+\mathcal{B}}}{2}$	$q_1 = \frac{r_{12}+r_{21}}{2\sqrt{1+\mathcal{C}}}$	$q_1 = \frac{r_{13}+r_{31}}{2\sqrt{1+\mathcal{D}}}$
$q_2 = \frac{r_{13}-r_{31}}{2\sqrt{1+\mathcal{A}}}$	$q_2 = \frac{r_{12}+r_{21}}{2\sqrt{1+\mathcal{B}}}$	$q_2 = \frac{\sqrt{1+\mathcal{C}}}{2}$	$q_2 = \frac{r_{23}+r_{32}}{2\sqrt{1+\mathcal{D}}}$
$q_3 = \frac{r_{21}-r_{12}}{2\sqrt{1+\mathcal{A}}}$	$q_3 = \frac{r_{13}+r_{31}}{2\sqrt{1+\mathcal{B}}}$	$q_3 = \frac{r_{23}+r_{32}}{2\sqrt{1+\mathcal{C}}}$	$q_3 = \frac{\sqrt{1+\mathcal{D}}}{2}$

We develop two useful properties of unit quaternions. Consider a rotation matrix acting on a vector:

$$\vec{v}\,' = R\vec{v}, \qquad R \in SO(3); \vec{v}, \vec{v}\,' \in \mathbb{R}^3.$$

Let $v = (0, \vec{v})$ and $v' = (0, \vec{v}\,')$ be two pure non-unit quaternions. We will show that for the unit quaternion q parameterizing R above,

$$v' = q * v * q^{-1} = q * v * q^*.$$

Using the angle-axis form (2.18) of q and assuming $\theta \neq 0$ so that $\|a\| = 1$,

$$\begin{aligned}
&q * v * q^* \\
&= (c_{\theta/2}, as_{\theta/2}) * (0, \vec{v}) * (c_{\theta/2}, -as_{\theta/2}) \\
&= \big(c_{\theta/2}, as_{\theta/2}\big) * \big(\vec{v} \cdot as_{\theta/2}, \vec{v}c_{\theta/2} + (a \times \vec{v})s_{\theta/2}\big) \\
&= \big(\underbrace{-a \cdot (a \times \vec{v})}_{0} s^2_{\theta/2}, c^2_{\theta/2}\vec{v} + 2c_{\theta/2}s_{\theta/2}(a \times \vec{v}) + s^2_{\theta/2}a(\vec{v} \cdot a) + s^2_{\theta/2}a \times (a \times \vec{v})\big) \\
&= \big(0, (1 - s^2_{\theta/2})\vec{v} + s_\theta(a \times \vec{v}) + s^2_{\theta/2}a(a \cdot \vec{v}) + s^2_{\theta/2}a \times (a \times \vec{v})\big) \\
&= \big(0, \vec{v} + s^2_{\theta/2} \underbrace{\big(a(a \cdot \vec{v}) - \vec{v}\underbrace{(a \cdot a)}_{\|a\|^2=1}\big)}_{a \times (a \times \vec{v})} + s_\theta(a \times \vec{v}) + s^2_{\theta/2}a \times (a \times \vec{v})\big) \\
&= \big(0, \vec{v} + 2s^2_{\theta/2}a \times (a \times \vec{v}) + s_\theta(a \times \vec{v})\big) \\
&= \big(0, \vec{v} + (1 - c_\theta)S(a)(S(a)\vec{v}) + s_\theta S(a)\vec{v}\big) \\
&= \big(0, (I + s_\theta S(a) + (1 - c_\theta)S(a)^2)\vec{v}\big) \\
&= \big(0, e^{S(a)\theta}\vec{v}\big) \\
&= \big(0, R\vec{v}\big) \\
&= v'.
\end{aligned}$$

If $\theta = 0$, $q = (1, \vec{0}) = q^*$, and $v' = v$, which is correct since $\theta = 0$ corresponds to $R = I$.

The above leads to another property of unit quaternions. Composing rotations as in Section 2.1, assume we have

$$\vec{v}' = R_1\vec{v},\ \vec{v}'' = R_2\vec{v}'; \qquad \vec{v}, \vec{v}', \vec{v}'' \in \mathbb{R}^3, \quad R_1, R_2 \in SO(3).$$

It follows that

$$\vec{v}'' = R_2R_1\vec{v}.$$

Using pure quaternions, the above are equivalent to

$$v' = q_1 * v * q_1^*, \quad v'' = q_2 * v' * q_2^*,$$

and by substitution,

$$\begin{aligned}
v'' &= q_2 * q_1 * v * q_1^* * q_2^* \\
&= (q_2 * q_1) * v * (q_2 * q_1)^*.
\end{aligned}$$

It follows that $q_2 * q_1$ corresponds to the composed rotation R_2R_1 and so $q_2 * q_1$ is a unit quaternion. This means that unit quaternions form a subgroup of $\mathbb{H}$ whose group operation $*$ composes rotations just as in the $SO(3)$ group.

We will now use unit quaternions q to parameterize the rotation dynamics (2.4) $\dot{R} = RS(\omega_B)$ obtained in Section 2.3. Expanding $R^T\dot{R} = S(\omega_B)$ using (2.19) we obtain four equations:

$$2\begin{bmatrix} q_0\dot{q}_0 + q_1\dot{q}_1 + q_2\dot{q}_2 + q_3\dot{q}_3 \\ -q_1\dot{q}_0 + q_0\dot{q}_1 + q_3\dot{q}_2 - q_2\dot{q}_3 \\ -q_2\dot{q}_0 - q_3\dot{q}_1 + q_0\dot{q}_2 + q_1\dot{q}_3 \\ -q_3\dot{q}_0 + q_2\dot{q}_1 - q_1\dot{q}_2 + q_0\dot{q}_3 \end{bmatrix} = \begin{bmatrix} 0 \\ \omega_{B,1} \\ \omega_{B,2} \\ \omega_{B,3} \end{bmatrix},$$

equivalent to

$$\begin{bmatrix} q_0 & q_1 & q_2 & q_3 \\ -q_1 & q_0 & q_3 & -q_2 \\ -q_2 & -q_3 & q_0 & q_1 \\ -q_3 & q_2 & -q_1 & q_0 \end{bmatrix} \begin{bmatrix} \dot{q}_0 \\ \dot{q}_1 \\ \dot{q}_2 \\ \dot{q}_3 \end{bmatrix} = \frac{1}{2} \begin{bmatrix} 0 \\ \omega_{B,1} \\ \omega_{B,2} \\ \omega_{B,3} \end{bmatrix}.$$

Inverting,

$$\begin{bmatrix} \dot{q}_0 \\ \dot{q}_1 \\ \dot{q}_2 \\ \dot{q}_3 \end{bmatrix} = \frac{1}{2} \begin{bmatrix} q_0 & -q_1 & -q_2 & -q_3 \\ q_1 & q_0 & -q_3 & q_2 \\ q_2 & q_3 & q_0 & -q_1 \\ q_3 & -q_2 & q_1 & q_0 \end{bmatrix} \begin{bmatrix} 0 \\ \omega_{B,1} \\ \omega_{B,2} \\ \omega_{B,3} \end{bmatrix},$$

the matrix form of the quaternion multiplication

$$\dot{q} = \frac{1}{2} q * (0, \vec{\omega}_B) \tag{2.21}$$

which can also be expressed as

$$\begin{bmatrix} \dot{q}_0 \\ \dot{q}_1 \\ \dot{q}_2 \\ \dot{q}_3 \end{bmatrix} = \frac{1}{2} \begin{bmatrix} 0 & -\omega_{B,1} & -\omega_{B,2} & -\omega_{B,3} \\ \omega_{B,1} & 0 & \omega_{B,3} & -\omega_{B,2} \\ \omega_{B,2} & -\omega_{B,3} & 0 & \omega_{B,1} \\ \omega_{B,3} & \omega_{B,2} & -\omega_{B,1} & 0 \end{bmatrix} \begin{bmatrix} q_0 \\ q_1 \\ q_2 \\ q_3 \end{bmatrix}.$$

Similarly for (2.3) we have $\dot{R}R^T = S(\omega_N)$ and obtain

$$2 \begin{bmatrix} q_0\dot{q}_0 + q_1\dot{q}_1 + q_2\dot{q}_2 + q_3\dot{q}_3 \\ -q_1\dot{q}_0 + q_0\dot{q}_1 - q_3\dot{q}_2 + q_2\dot{q}_3 \\ -q_2\dot{q}_0 + q_3\dot{q}_1 + q_0\dot{q}_2 - q_1\dot{q}_3 \\ -q_3\dot{q}_0 - q_2\dot{q}_1 + q_1\dot{q}_2 + q_0\dot{q}_3 \end{bmatrix} = \begin{bmatrix} 0 \\ \omega_{N,1} \\ \omega_{N,2} \\ \omega_{N,3} \end{bmatrix}$$

$$\begin{bmatrix} q_0 & q_1 & q_2 & q_3 \\ -q_1 & q_0 & -q_3 & q_2 \\ -q_2 & q_3 & q_0 & -q_1 \\ -q_3 & -q_2 & q_1 & q_0 \end{bmatrix} \begin{bmatrix} \dot{q}_0 \\ \dot{q}_1 \\ \dot{q}_2 \\ \dot{q}_3 \end{bmatrix} = \frac{1}{2} \begin{bmatrix} 0 \\ \omega_{N,1} \\ \omega_{N,2} \\ \omega_{N,3} \end{bmatrix}$$

$$\begin{bmatrix} \dot{q}_0 \\ \dot{q}_1 \\ \dot{q}_2 \\ \dot{q}_3 \end{bmatrix} = \frac{1}{2} \begin{bmatrix} q_0 & -q_1 & -q_2 & -q_3 \\ q_1 & q_0 & q_3 & -q_2 \\ q_2 & -q_3 & q_0 & q_1 \\ q_3 & q_2 & -q_1 & q_0 \end{bmatrix} \begin{bmatrix} 0 \\ \omega_{N,1} \\ \omega_{N,2} \\ \omega_{N,3} \end{bmatrix}$$

$$= \frac{1}{2} \begin{bmatrix} 0 & -\omega_{N,1} & -\omega_{N,2} & -\omega_{N,3} \\ \omega_{N,1} & 0 & -\omega_{N,3} & \omega_{N,2} \\ \omega_{N,2} & \omega_{N,3} & 0 & -\omega_{N,1} \\ \omega_{N,3} & -\omega_{N,2} & \omega_{N,1} & 0 \end{bmatrix} \begin{bmatrix} q_0 \\ q_1 \\ q_2 \\ q_3 \end{bmatrix}$$

$$\implies \dot{q} = \frac{1}{2}(0, \vec{\omega}_N) * q \tag{2.22}$$

2.8 Earth's Magnetic Field

The Earth's magnetic field m can be visualized by modeling the Earth as a magnetic dipole, with magnetic field lines emanating vertically from the southern magnetic

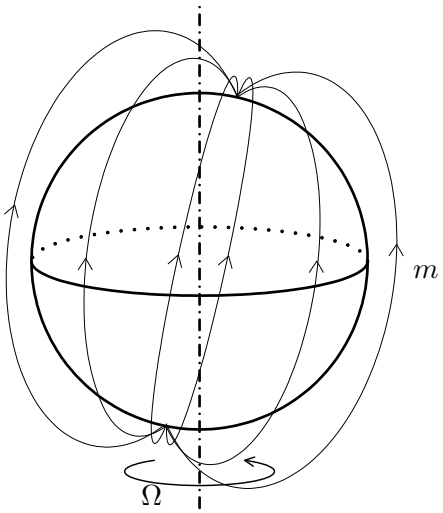

Figure 2.7: Earth's Magnetic Field

pole, running nearly parallel to the surface near the equator, and sinking vertically into the north magnetic pole as illustrated in Figure 2.7.

We distinguish between magnetic and geographic ("true") north: the magnetic north is defined as the geographic location where the magnetic field lines point vertically down into the ground, while geographic north is defined by the location of the Earth's rotation axis which also defines latitude 90° N. The magnetic north is not fixed; for instance in 2010 it was located at 84.97° N, 132.35° W, drifting North-West at approximately 55 km/year. For this reason geographic north is always used for navigation, and the N frame's n_1 and n_2 axes (c.f. Section 2.4) are defined as pointing respectively in geographic north and east directions. A hand-held compass measures the direction of magnetic north and its reading must be corrected by the declination angle λ between true and magnetic north at a given geographic location. In Edmonton $\lambda > 0$ indicates magnetic north is east relative to geographic north.

The SI unit for the magnetic field is the Tesla. A 1 T field is extremely strong so a more common unit is the Gauss where 1 T $= 1 \times 10^4$ G. The magnetic field vector m varies in magnitude and direction over the surface of the Earth, but can be taken as constant for a given geographic location. The on-board IMU's triaxial magnetometer directly measures m_B with a range of ± 1.2 G and a resolution of 0.2 mG on each axis. The reference magnetic field vector coordinates m_N as well as declination angle λ can be computed for a given location and date using the International Geomagnetic Reference Field (IGRF) [2] or World Magnetic Model (WMM) [98] models[1]. For instance the ERCHA flight field located at 53°25′12" N, 113°23′58" W, alt = 712.2 m has the magnetic field value

$$m_N = \begin{bmatrix} 0.1404 & 0.0386 & 0.5578 \end{bmatrix}^T \text{ G}, \qquad \lambda = 15.38^\circ$$

for September 1, 2011 using the IGRF model.

[1] An online calculator is available at `http://www.ngdc.noaa.gov/geomagmodels/IGRFWMM.jsp`.

2.8.1 Computing Yaw

During the navigation system's initialization phase, the magnetometer is used to calculate the yaw angle ψ of the helicopter w.r.t. the ground-fixed frame N, i.e. the angle of the longitudinal body-fixed axis b_1 relative to geographic north direction n_1. Together with roll ϕ and pitch θ angles, this is used to compute the initial attitude $R_0 \in SO(3)$ of the vehicle.

The roll and pitch angles ϕ_0 and θ_0 of the helicopter during initialization can typically be taken as zero since the helicopter starts out level on its landing skids. More generally these angles can be computed from the accelerometer: as discussed in Section 2.4 a *stationary* accelerometer outputs $\bar{f}_B = -g_B$ where $g_B = R^T g_N$, $g_N = [0 \quad 0 \quad g]^T$ and using (2.15),

$$\begin{bmatrix} \bar{f}_{B,1} \\ \bar{f}_{B,2} \\ \bar{f}_{B,3} \end{bmatrix} = - \begin{bmatrix} c_\theta c_\psi & c_\theta s_\psi & -s_\theta \\ s_\phi s_\theta c_\psi - c_\phi s_\psi & s_\phi s_\theta s_\psi + c_\phi c_\psi & s_\phi c_\theta \\ c_\phi s_\theta c_\psi + s_\phi s_\psi & c_\phi s_\theta s_\psi - s_\phi c_\psi & c_\phi c_\theta \end{bmatrix} \begin{bmatrix} 0 \\ 0 \\ g \end{bmatrix} = \begin{bmatrix} s_\theta \\ -s_\phi c_\theta \\ -c_\phi c_\theta \end{bmatrix} g$$

such that

$$\phi_0 = \arctan\left(\frac{\bar{f}_{B,2}}{\bar{f}_{B,3}}\right) \qquad \text{and} \qquad \theta_0 = \arcsin\left(\frac{\bar{f}_{B,1}}{g}\right)$$

are the initialization roll and pitch angles of the vehicle provided it is stationary. Remark the range of both arctan and arcsin is $[-\pi/2, \pi/2]$ but the helicopter is not expected to exceed this range during initialization.

Once initialization roll and pitch angles ϕ_0, θ_0 are available, the yaw angle ψ_0 can be computed from the magnetometer. Let $m_N := [B_x \quad B_y \quad B_z]^T$ be the (known) reference magnetic field in the navigation frame. We directly measure $\bar{m}_B = R^T m_N$ and from (2.14) and (2.13) we have

$$\begin{aligned} R_1(\phi)^T R_2(\theta)^T R_3(\psi)^T m_N &= \bar{m}_B \\ R_3(\psi)^T m_N &= R_2(\theta) R_1(\phi) \bar{m}_B \\ \begin{bmatrix} c_\psi & s_\psi & 0 \\ -s_\psi & c_\psi & 0 \\ 0 & 0 & 1 \end{bmatrix} \begin{bmatrix} B_x \\ B_y \\ B_z \end{bmatrix} &= \begin{bmatrix} c_\theta & 0 & s_\theta \\ 0 & 1 & 0 \\ -s_\theta & 0 & c_\theta \end{bmatrix} \begin{bmatrix} 1 & 0 & 0 \\ 0 & c_\phi & -s_\phi \\ 0 & s_\phi & c_\phi \end{bmatrix} \begin{bmatrix} \bar{m}_{B,1} \\ \bar{m}_{B,2} \\ \bar{m}_{B,3} \end{bmatrix} \\ \begin{bmatrix} c_\psi B_x + s_\psi B_y \\ -s_\psi B_x + c_\psi B_y \\ B_z \end{bmatrix} &= \begin{bmatrix} c_\theta & s_\theta s_\phi & s_\theta c_\phi \\ 0 & c_\phi & -s_\phi \\ -s_\theta & c_\theta s_\phi & c_\theta c_\phi \end{bmatrix} \begin{bmatrix} \bar{m}_{B,1} \\ \bar{m}_{B,2} \\ \bar{m}_{B,3} \end{bmatrix} \end{aligned}$$

The first two vector entries give

$$\begin{aligned} c_\psi B_x + s_\psi B_y &= c_\theta \bar{m}_{B,1} + s_\phi s_\theta \bar{m}_{B,2} + c_\phi s_\theta \bar{m}_{B,3} = \mathcal{X} \\ -s_\psi B_x + c_\psi B_y &= c_\phi \bar{m}_{B,2} - s_\phi \bar{m}_{B,3} = \mathcal{Y} \end{aligned}$$

Combining the above two equations leads to:

$$\begin{aligned} \mathcal{X} B_y - \mathcal{Y} B_x &= s_\psi (B_y^2 + B_x^2) \\ \mathcal{X} B_x + \mathcal{Y} B_y &= c_\psi (B_x^2 + B_y^2) \end{aligned}$$

And so

$$\tan\psi = \frac{\mathcal{X} B_y - \mathcal{Y} B_x}{\mathcal{X} B_x + \mathcal{Y} B_y} \Longrightarrow \psi = \text{atan2}(\mathcal{X} B_y - \mathcal{Y} B_x, \mathcal{X} B_x + \mathcal{Y} B_y),$$

or written out explicitly,

$$\psi = \operatorname{atan2}\Bigg(B_y\Big[c_\theta \bar{m}_{B,1} + s_\phi s_\theta \bar{m}_{B,2} + c_\phi s_\theta \bar{m}_{B,3}\Big] - B_x\Big[c_\phi \bar{m}_{B,2} - s_\phi \bar{m}_{B,3}\Big], \\ B_x\Big[c_\theta \bar{m}_{B,1} + s_\phi s_\theta \bar{m}_{B,2} + c_\phi s_\theta \bar{m}_{B,3}\Big] + B_y\Big[c_\phi \bar{m}_{B,2} - s_\phi \bar{m}_{B,3}\Big]\Bigg) \tag{2.23}$$

Equation (2.23) provides a direct calculation for ψ, the yaw angle relative to true north. The disadvantage is the reliance on m_N which is calculated from a theoretical world magnetic model and may be different in experiment due to warping of the local magnetic field by things such as ferromagnetic building materials or active magnetic field sources such as power lines. We will revisit this point in Section 2.9.

An alternative approach to computing yaw is to consider a different ground-fixed frame whose first axis points in the direction of *magnetic* north. We denote this as the magnetic frame M where m_3 points vertically down just like in the navigation frame such that m_2 points in the direction of magnetic east. The magnetic field m expressed in M frame coordinates becomes $m_M := [B_H \quad 0 \quad B_V]^T$ where B_H and B_V are the horizontal and vertical components of the magnetic field vector. The vehicle's yaw with respect to the magnetic north is known as the azimuth ψ^m. The azimuth can be converted to navigation frame yaw ψ by $\psi = \psi_m + \lambda$ where λ is the local declination angle as discussed in Section 2.8. The advantage of using ψ^m instead of ψ is that (2.23) simplifies considerably for m_M:

$$\psi^m = \operatorname{atan2}\left(-c_\phi \bar{m}_{B,2} + s_\phi \bar{m}_{B,3}, c_\theta \bar{m}_{B,1} + s_\phi s_\theta \bar{m}_{B,2} + c_\phi s_\theta \bar{m}_{B,3}\right), \tag{2.24}$$

which does not employ the reference value of m. In addition to ψ^m we compute the value of the m_M reference field using ϕ_0, θ_0 and $\bar{m}_B$: from (2.15),

$$m_M = \begin{bmatrix} B_H \\ 0 \\ B_V \end{bmatrix} = \begin{bmatrix} * & * & * \\ * & * & * \\ -s_\theta & s_\phi c_\theta & c_\phi c_\theta \end{bmatrix} \begin{bmatrix} \bar{m}_{B,1} \\ \bar{m}_{B,2} \\ \bar{m}_{B,3} \end{bmatrix}$$

and so

$$\begin{aligned} B_V &= -\sin\theta_0\, \bar{m}_{B,1} + \sin\phi_0 \cos\theta_0\, \bar{m}_{B,2} + \cos\phi_0 \cos\theta_0\, \bar{m}_{B,3} \\ B_H &= \sqrt{\bar{m}_{B,1}^2 + \bar{m}_{B,2}^2 + \bar{m}_{B,3}^2 - B_V^2} \end{aligned} \tag{2.25}$$

2.9 Magnetometer Calibration

The measurements made by a magnetometer sensor are affected by the surrounding environment (e.g. structural steel in buildings, power lines) as well as the vehicle itself (e.g. ferrous metal parts, engine magneto). Since the earth's magnetic field is very weak, uncompensated magnetometer readings cannot be trusted.

Field distortions present in the environment, e.g. inside a building, have an unknown spatially-varying nature and cannot be compensated for in practice. For instance, we have observed the measured magnetic field inside a lab shift by 90 degrees just from moving the sensor close to the wall. For this reason all indoor testing is done in a prescribed section of the lab where magnetic interference has

been verified to be minimal, and the magnetic frame M is used as the ground-fixed frame to remove the need for a theoretical magnetic field value. Conversely, outdoor testing is conducted on a flying field situated far from buildings such that the reference magnetic field value m_N is reliable and the navigation frame N can be employed. This is important for GPS-aided navigation because the R_E^N matrix in (2.8) specifically requires the use of the N frame.

Field distortions caused by the vehicle body are fixed w.r.t. the magnetometer sensor, and can be quantified and removed from subsequent sensor readings by a calibration procedure. The simplest approach is to collect a set of sensor readings $\{\tilde{m}\}$ while sequentially rotating the vehicle about the body-fixed axes b_1, b_2 and b_3, each aligned with the magnetic East-West line. Since the theoretical magnetic field vector m is constant, the collected data points should trace out a 3-D sphere centered at zero with radius $|m|$. As shown in Figure 2.8 below, the actual sensor readings will trace out a warped, offset sphere, whose center $b_m = \text{mean}(\{\tilde{m}\})$ can be computed and used to correct future measurements by $\tilde{m} - b_m$. This method is commonly known as Hard-Iron Calibration and is often found as a firmware feature on commercial magnetometers, including the IMU used in our helicopter UAV. It has the advantage of a simple calculation and not requiring knowledge of the local magnetic field amplitude. Its disadvantage is the inability to compensate for field distortions which show up as a warping of the spherical shape.

A novel compensation approach is proposed in [54]. The magnetometer sensor model is taken as

$$\tilde{m} = \begin{bmatrix} \varepsilon_1 & 0 & 0 \\ \varepsilon_2 \sin\rho_1 & \varepsilon_2 \cos\rho_1 & 0 \\ \varepsilon_3 \sin\rho_2 \cos\rho_3 & \varepsilon_3 \sin\rho_3 & \varepsilon_3 \cos\rho_2 \cos\rho_3 \end{bmatrix} m + \begin{bmatrix} \zeta_1 \\ \zeta_2 \\ \zeta_3 \end{bmatrix} = K_m m + b_m, \quad (2.26)$$

where ε_k represent the sensor scaling errors, ρ_k the sensor misalignment angles, and ζ_k the sensor offsets of the individual magnetometer axes, $1 \leq k \leq 3$. Physically (2.26) models the following sources of magnetometer error: scale factor, misalignment, null shift (sensor bias), hard-iron and soft-iron errors [54]. Remark that (2.26) reduces to the Hard-Iron Calibration model by taking $\varepsilon_k = 1$ and $\rho_k = 0$ resp. $K_m = I$.

Equation (2.26) is inverted to $m = K_m^{-1}(\tilde{m} - b_m)$ and substituted into $m_1^2 + m_2^2 + m_3^2 = |m|^2$ where $|m|$ is known and constant, c.f. Section 2.8, resulting in

$$C_1\tilde{m}_1^2 + C_2\tilde{m}_1\tilde{m}_2 + C_3\tilde{m}_1\tilde{m}_3 + C_4\tilde{m}_2^2 + C_5\tilde{m}_2\tilde{m}_3 + C_6\tilde{m}_3^2 + C_7\tilde{m}_1 + C_8\tilde{m}_2 + C_9\tilde{m}_3 = C_{10} \quad (2.27)$$

where the coefficients C_l are nonlinear functions of ε, ρ, ζ and $|m|$. Assume a magnetometer calibration data set $\{\tilde{m}\}$ has been collected, consisting of N data points for which (2.27) holds. The system is rewritten as

$$\begin{bmatrix} \tilde{m}_{1,1}^2 & \tilde{m}_{1,1}\tilde{m}_{2,1} & \cdots & \tilde{m}_{3,1} \\ \vdots & \vdots & \ddots & \vdots \\ \tilde{m}_{1,N}^2 & \tilde{m}_{1,N}\tilde{m}_{2,N} & \cdots & \tilde{m}_{3,N} \end{bmatrix} \begin{bmatrix} C_1/C_{10} \\ \vdots \\ C_9/C_{10} \end{bmatrix} = \begin{bmatrix} 1 \\ \vdots \\ 1 \end{bmatrix}, \quad (2.28)$$

from which a least-squares solution for the numerical values of $C_1/C_{10} \ldots C_9/C_{10}$ is performed. This produces a system of nine nonlinear equations in nine unknowns ε,

ρ, ζ, which can be solved numerically. Using $\varepsilon = 1$, $\rho = 0$, $\zeta = 0$ as initial guesses, the solution converges rapidly. The calibration constants are then substituted back into (2.26), and future sensor readings are corrected as $K_m^{-1}(\tilde{m} - b_m) := A_c\tilde{m} + b_c$, a linear mapping.

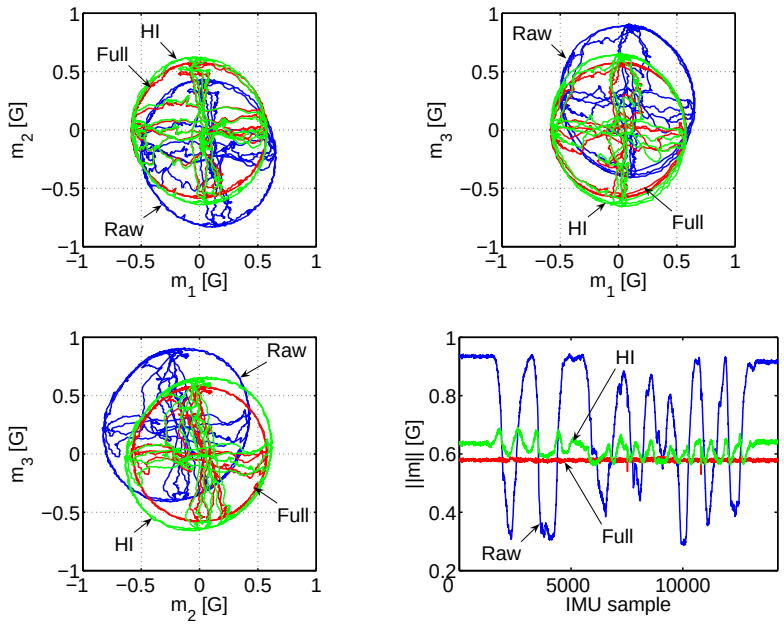

Figure 2.8: Magnetometer Calibration, Engine Off: Raw Sensor Readings, Hard-Iron Compensated, Fully Compensated

The data collected during engine-off calibration is plotted alongside its hard-iron and fully-compensated versions in Figure 2.8. Observe the original data's offset centre is corrected by both methods, but only the full compensation (2.26) corrects the elliptical distortion. The magnitude plot in the bottom-right corner confirms the improvement in accuracy. The impact of magnetometer calibration on the experimental performance of an aided inertial navigation system will be covered in Section 3.4.2.

Running the helicopter's engine creates substantial distortions in the measured magnetic field. For this reason, a separate engine-on calibration data set is collected and the calculations above are repeated. The two sets of constants are given in Table 2.1. The change in parameters is pronounced, confirming that the running engine has a significant impact on the sensed magnetic field. This will be shown through flight experiments in Section 3.4.3.

Table 2.1: Magnetometer Calibration Constants

	ε	ρ	ζ
Engine Off	1.0044	$-3.292°$	0.0795
	1.0884	$-3.934°$	-0.1978
	1.1423	$6.242°$	0.2412
Engine On	1.0373	$4.211°$	0.0616
	1.2658	$-6.862°$	0.0149
	1.3635	$-12.380°$	0.0020

Chapter 3

Extended Kalman Filter Design for Aided Navigation

As mentioned in Section 1.2.1 the Extended Kalman Filter (EKF) is the conventional method of choice for aided navigation design. We apply this method to two examples used for our helicopter UAV project: an Attitude and Heading Reference System (AHRS) and a Magnetometer-plus-GPS Aided Inertial Navigation System (Aided INS). The resulting designs are implemented and validated in experiment and provide a foundation for the invariant observer design in Chapter 4.

3.1 Overview of EKF

The method of the Extended Kalman Filter is to linearize the system dynamics around a nominal trajectory and use the resulting model in a Kalman filter, an optimal linear time-varying observer used to estimate the state of the linearized system from sensor and aiding measurement signals corrupted by noise. The resulting estimates are then added to the nominal trajectory to obtain state estimates for the nonlinear system. A nonlinear system with noise inputs is written as

$$\begin{aligned} \dot{x} &= f(x, u, w) \\ y &= h(x, v) \end{aligned} \tag{3.1}$$

where x and y are the state and output (aiding measurements) vectors, u is the input (sensors) vector, and w, v are process and measurement Gaussian white noise vectors with zero mean and known covariance. Let $(\hat{x}, u, 0, 0)$ represent a nominal (noise-free) trajectory of (3.1), i.e. one which satisfies

$$\begin{aligned} \dot{\hat{x}} &= f(\hat{x}, u, 0) \\ \hat{y} &= h(\hat{x}, 0) \end{aligned} \tag{3.2}$$

where $\hat{y}$ is the nominal output. Linearizing (3.1) about the nominal trajectory we obtain

$$\begin{aligned} \dot{x} &= f(\hat{x}, u, 0) + \left.\frac{\partial f}{\partial x}\right|_{\hat{x},u,0} (x - \hat{x}) + \left.\frac{\partial f}{\partial u}\right|_{\hat{x},u,0} (u - u) + \left.\frac{\partial f}{\partial w}\right|_{\hat{x},u,0} (w - 0) \\ y &= h(\hat{x}, 0) + \left.\frac{\partial h}{\partial x}\right|_{\hat{x},0} (x - \hat{x}) + \left.\frac{\partial h}{\partial v}\right|_{\hat{x},0} (v - 0), \end{aligned}$$

and after defining $\delta x = x - \hat{x}$, $\delta y = y - \hat{y}$ and the Jacobian matrices $F(t) = (\partial f/\partial x)(\hat{x}, u)$, $G(t) = (\partial f/\partial w)(\hat{x}, u)$, $H(t) = (\partial h/\partial x)(\hat{x})$ and $L(t) = (\partial h/\partial v)(\hat{x})$, we obtain the LTV system

$$\begin{aligned} \delta\dot{x} &= F(t)\delta x + G(t)w \\ \delta y &= H(t)\delta x + L(t)v \end{aligned} \tag{3.3}$$

The nominal trajectory $\hat{x}$ can be either computed ahead of time as $\hat{x} = \hat{x}^*$, a design known as the Linearized Kalman Filter (LKF); or $\hat{x}$ can be taken as the estimated state of (3.1) itself, equivalent to re-linearizing the system about its latest estimate, which is known as the Extended Kalman Filter. We use the latter approach since the motions of the vehicle cannot be predicted a priori. The EKF is an ad-hoc design because the convergence properties of the observer depend on the trajectories of the nonlinear system and we cannot formally prove non-local stability. Nevertheless the EKF works well in practice due to its inherent robustness to sensor noise and tolerance of aiding measurement drop-outs. We will revisit the issue of observer stability in Chapter 4.

3.2 EKF Design

3.2.1 Complementary Filter Topology

For Aided INS designs, the EKF is used inside a complementary filter topology [34, Chap. 10]: the nominal system dynamics (3.2) are numerically integrated using high-rate, low-accuracy sensor signals u to produce the (roughly) estimated state $\hat{x} =: \hat{x}^-$ of the nonlinear system (3.1). Whenever a low-rate, high-accuracy aiding measurement is available, $\hat{x}^-$ is used to obtain the linearized model (3.3), used by the Kalman Filter together with u and y to estimate $\delta\hat{x}$, which corrects the nonlinear system state as $\hat{x}^- + \delta\hat{x} = \hat{x}^+$. The updated state $\hat{x}^+$ is output to the user and becomes the IC for the next integration of (3.2). Conversely if an aiding measurement is not available at the current time, $\hat{x}^-$ is output directly and used for the next (3.2) integration.

The complementary filter setup is ideal for Aided INS applications because of the multirate nature of the on-board sensors: in our system, the IMU provides accelerometer, rate gyro and magnetometer information at 100 Hz whereas GPS information is available at 10 Hz and is subject to service drop-outs due to environmental conditions. For the AHRS, all sensor signals are available at 100 Hz, however the aiding rate may be set lower to conserve CPU cycles since the numerical integration is computationally much less expensive than the Kalman update. This is particularly useful for implementation on low-power embedded systems.

3.2.1.1 AHRS

The topology of the AHRS is shown in Figure 3.1. The task of the system is to estimate the attitude of the vehicle, measured by the rotation matrix $R \in SO(3)$ of the body-fixed frame relative to the ground-fixed magnetic frame (c.f. Section 2.9). The name AHRS comes from aviation where "attitude" means the roll and pitch angles of the vehicle i.e. its attitude w.r.t the horizon while "heading" is its yaw angle to magnetic north [9, p. 3-22]. The design is a complementary filter consisting of

high-rate integration of a rate gyro signal $\tilde{\omega}$ from the IMU and low-rate correction of the resulting estimates using magnetometer and accelerometer aiding measurements via the Extended Kalman Filter.

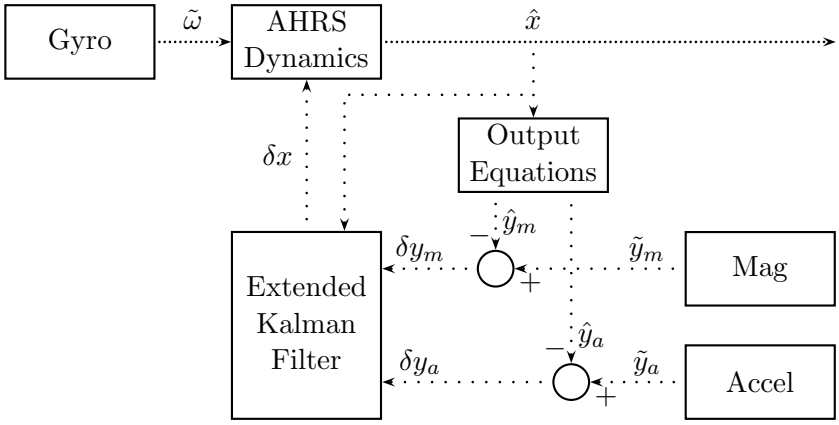

Figure 3.1: Topology of AHRS; signal rate inversely proportional to dot spacing

3.2.1.2 Aided INS

The Mag-plus-GPS aided INS topology is shown in Figure 3.2. The system provides estimates of the position, velocity and attitude of the vehicle relative to the ground-fixed navigation frame. The high-rate signals are the accelerometer $\tilde{f}$ and rate gyro $\tilde{\omega}$ measurements provided by the IMU. The low-rate aiding measurements are obtained from the on-board magnetometer and GPS receiver. Remark that unlike Figure 3.1 the system's EKF employs input (sensor) signals u in addition to aiding measurements y.

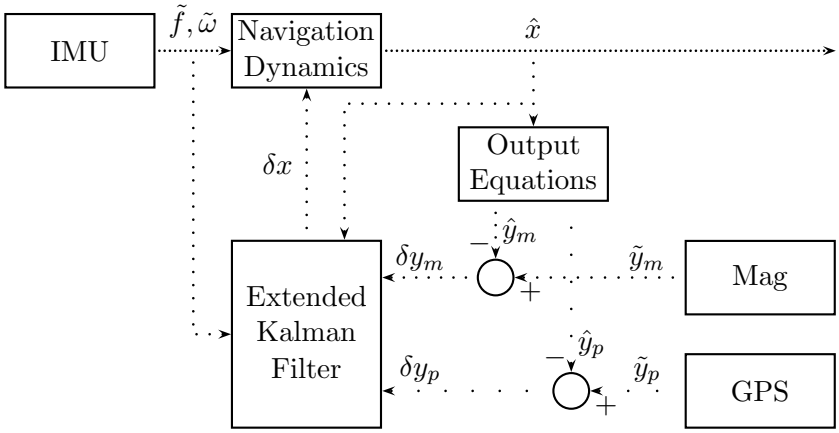

Figure 3.2: Topology of Aided INS; signal rate inversely proportional to dot spacing

Table 3.1: Identified Noise Parameters – Engine Off [75]

σ_f [m/s$^{3/2}$]	σ_ω [rad/$\sqrt{\text{s}}$]	β_f [1/s]	σ_{bf} [m/s^2]	β_ω [1/s]	$\sigma_{b\omega}$ [rad/s]	σ_m [G$\sqrt{\text{s}}$]
0.0079	0.0017	1.89/178	0.0042	1.89/562	0.00029	0.00058
0.0074	0.0017	1.89/562	0.0020	1.89/562	0.00038	0.00051
0.0090	0.0021	1.89/562	0.0016	1.89/562	0.00032	0.00051

3.2.2 Sensor Models

The on-board IMU is equipped with a triaxial accelerometer, rate gyro and magnetometer, respectively measuring specific force $f_B = \ddot{p}_B - g_B$, angular velocity ω_B and the Earth's magnetic field $m_B = R^T m_G$ at a rate of 100 Hz where $m_G = m_M$ or m_N is the magnetic field vector in the ground-fixed frame coordinates, taken as known and constant as discussed in Section 2.8. The measured data exhibits significant bias and noise effects, which must be accounted for. The proposed sensor models with frame subscripts omitted are

$$\begin{aligned} \tilde{f} &= f + b_f + \nu_f \\ \tilde{\omega} &= \omega + b_\omega + \nu_\omega \\ \tilde{m} &= K_m m + b_m + \nu_m \end{aligned} \tag{3.4}$$

where each ν represents a Gaussian white noise vector with zero mean and diagonal covariance matrix entries σ^2. The noise properties of the accelerometer and rate gyro sensors were analyzed using the method of Allan Variance [12] by [75, Chap. 4], who proposed modeling both bias terms as $b = b_0 + b_t$ where b_0 is the constant turn-on bias to be computed during initialization, and b_t is the time-varying part described as a Gauss-Markov random process

$$\dot{b}_t = -\beta b_t + \sqrt{2\beta}\nu_b$$

where $1/\beta$ is the time constant of the process and ν_b is a Gaussian white noise vector as before.

The $K_m \in \mathbb{R}^{3\times 3}$ and $b_m \in \mathbb{R}^3$ in (3.4) are constant terms used to model the warping of the magnetic field, found by performing a calibration as described in Section 2.9. For later convenience the magnetometer signal is rewritten as

$$m = \underbrace{K_m^{-1}(\tilde{m} - b_m)}_{\tilde{y}_m^c} - \underbrace{K_m^{-1}\nu_m}_{\nu_m^c} \Longrightarrow \tilde{y}_m^c = m + \nu_m^c,$$

where as in Section 2.9

$$\tilde{y}_m^c = A_c\tilde{m} + b_c, \qquad A_c := K_m^{-1}, \quad b_c := -K_m^{-1}b_m$$

is the compensated magnetometer measurement, and $\nu_m^c := A_c\nu_m$ is still a Gaussian white noise vector due to the linear transformation [123, p. 60], with covariance $(\sigma_m^c)^2 = E\langle\nu_m^c(\nu_m^c)^T\rangle = A_c\sigma_m^2(A_c)^T$. The identified noise parameters for the engine-off case are provided in Table 3.1.

A GPS receiver measures the position of the antenna mounted on the tail of the vehicle w.r.t. the ECEF frame origin r_E^a where by Section 2.4 $r_E^a = r_E^o + R_E^N p_N^a$

with r_E^o, R_E^N constant terms computed during initialization. The GPS receiver runs its own Kalman filter, which provides position measurements $\tilde{y}_p = r^a + \nu_p$ along with their estimated standard deviations σ_p and diagnostic information at 10 Hz. Using carrier-phase differential GPS the receiver is capable of providing up to 2 cm circular error probable precision, however atmospheric conditions may cause periods of decreased accuracy or measurement drop-outs which will be addressed in Section 3.2.10.2.

The accelerometer measures the difference between the vehicle's inertial acceleration and gravity, known as the specific force $f = a - g$. The standard practice in AHRS design is to use the accelerometer as a tilt sensor by assuming $a = 0$, which holds if the body is stationary. This assumption also holds for a stationary engine-on vehicle exhibiting vibrations due to $E\langle a \rangle = 0$. Clearly, this assumption is violated under any vehicle manoeuvres. For reasons explained in Section 3.2.6.1, in the AHRS design we take the accelerometer bias model as $b_f = b_{f0}$ where b_{f0} is the constant turn-on bias which is found during initialization. The accelerometer output measurement (for the AHRS case) is thus written as

$$f \approx -g \Longrightarrow \underbrace{\tilde{f} - b_{f0}}_{\tilde{y}_a} - \nu_f \approx -g \Longrightarrow \tilde{y}_a \approx -g + \nu_f,$$

where $\approx$ is used to emphasize the $a = 0$ assumption does not always hold.

3.2.3 Dynamics and Output Equations

3.2.3.1 AHRS

The AHRS is described using states R and b_ω measuring attitude and rate gyro bias, respectively. Employing the body-frame rotational kinematics (2.4) with sensor models (3.4) the AHRS dynamics are

$$\begin{aligned} \dot{R} &= RS(\tilde{\omega} - b_\omega - \nu_\omega) \\ \dot{b}_\omega &= -\beta_\omega(b_\omega - b_{\omega 0}) + \sqrt{2\beta_\omega}\nu_{b\omega} \end{aligned} \tag{3.5}$$

The measured outputs are written as functions of state

$$\begin{aligned} \tilde{y}_m^c &= R^T m_M + \nu_m^c \\ \tilde{y}_a &= -R^T g_M + \nu_f \end{aligned} \tag{3.6}$$

where m_M, g_M are respectively the magnetic and gravity field vectors in magnetic frame coordinates. The nominal (noise-free) trajectory $\hat{x}$ dynamics are

$$\begin{aligned} \dot{\hat{R}} &= \hat{R}S(\tilde{\omega} - \hat{b}_\omega) \\ \dot{\hat{b}}_\omega &= -\beta_\omega(\hat{b}_\omega - b_{\omega 0}) \end{aligned} \tag{3.7}$$

with corresponding output

$$\begin{aligned} \hat{y}_m &= \hat{R}^T m_M \\ \hat{y}_a &= -\hat{R}^T g_M \end{aligned} \tag{3.8}$$

As discussed in Section 3.2.2, the y_a model implicitly assumes zero vehicle acceleration, which may be violated. The rate gyro constant turn-on bias $b_{\omega 0}$ is computed during initialization.

3.2.3.2 Aided INS

The IMU is assumed to be located sufficiently close to the vehicle's centre of mass to directly measure its acceleration. Using sensor models from Section 3.2.2 with navigation dynamics (2.5) from Section 2.4 gives

$$\begin{aligned}
\dot{p}_N &= v_N \\
\dot{v}_N &= R(\tilde{f} - b_f - \nu_f) + g_N \\
\dot{R} &= RS(\tilde{\omega} - b_\omega - \nu_\omega) \\
\dot{b}_f &= -\beta_f(b_f - b_{f0}) + \sqrt{2\beta_f}\nu_{bf} \\
\dot{b}_\omega &= -\beta_\omega(b_\omega - b_{\omega 0}) + \sqrt{2\beta_\omega}\nu_{b\omega}
\end{aligned} \tag{3.9}$$

The nominal dynamics of the system are the noise-free version of (3.9)

$$\begin{aligned}
\dot{\hat{p}}_N &= \hat{v}_N \\
\dot{\hat{v}}_N &= \hat{R}(\tilde{f} - \hat{b}_f) + g_N \\
\dot{\hat{R}} &= \hat{R}S(\tilde{\omega} - \hat{b}_\omega) \\
\dot{\hat{b}}_f &= -\beta_f(\hat{b}_f - b_{f0}) \\
\dot{\hat{b}}_\omega &= -\beta_\omega(\hat{b}_\omega - b_{\omega 0})
\end{aligned} \tag{3.10}$$

As in the AHRS the constant turn-on bias terms b_{f0} and $b_{\omega 0}$ will be computed during the system's initialization.

The output (aiding) measurements of the system are the position of the tail-mounted GPS antenna reported in E frame coordinates and the compensated magnetometer output in the B frame. From Section 3.2.2

$$\begin{aligned}
\tilde{y}_p &= r_E^o + R_E^N\,(p_N + Rl_B) + \nu_p \\
\tilde{y}_m^c &= R^T m_N + \nu_m^c
\end{aligned} \tag{3.11}$$

where r_E^o is the position vector of the navigation frame origin w.r.t. the ECEF frame origin, R_E^N is the rotation matrix between N and E, l_B is the position vector of the GPS antenna w.r.t. the body frame origin, and m_N is the reference magnetic field in the navigation frame. The terms r_E^o and R_E^N are computed during the initialization period, c.f. Section 2.4. The lever-arm term l_B is measured directly from the vehicle's geometry. The value of m_N is available from a magnetic reference model as discussed in Section 2.8. The corresponding nominal output equations are

$$\begin{aligned}
\hat{y}_p &= r_E^o + R_E^N\left(\hat{p}_N + \hat{R}l_B\right) \\
\hat{y}_m &= \hat{R}^T m_N
\end{aligned} \tag{3.12}$$

3.2.4 Numerical Integration

The AHRS and Aided INS nominal dynamics (3.7) and (3.10) in Section 3.2.3 are numerically integrated at the IMU sampling rate of 100 Hz. As discussed in Section 3.2.1 the resulting estimated state $\hat{x}^-$ is periodically updated using the high-precision, low-rate aiding measurements via the Extended Kalman Filter.

Instead of directly numerically integrating the equations using e.g. Runge-Kutta, we solve them analytically then apply numerical quadrature if required. For $\hat{b}_\omega$ dynamics in (3.7) and $\hat{b}_f$, $\hat{b}_\omega$ dynamics in (3.10) we left-multiply by the integrating factor

$$e^{\int_{t_0}^{t} \beta ds} = e^{\beta(t-t_0)},$$

then integrate the result between $t = t_0$ and $t = t_1$. This gives:

$$\begin{aligned}
e^{\beta(t-t_0)}\dot{\hat{b}}(t) + e^{\beta(t-t_0)}\beta\hat{b}(t) &= e^{\beta(t-t_0)}\beta b_0 \\
\frac{d}{dt}\left(e^{\beta(t-t_0)}\hat{b}(t)\right) &= e^{\beta(t-t_0)}\beta b_0 \\
\int_{t_0}^{t_1} \frac{d}{dt}\left(e^{\beta(t-t_0)}\hat{b}(t)\right) dt &= \int_{t_0}^{t_1} e^{\beta(t-t_0)}\beta dt b_0 \\
e^{\beta(t_1-t_0)}\hat{b}(t_1) - e^{\beta(t_0-t_0)}\hat{b}(t_0) &= \left(e^{\beta(t_1-t_0)} - e^{\beta(t_0-t_0)}\right) b_0 \\
\hat{b}(t_1) &= e^{-\beta(t_1-t_0)}\left(\hat{b}(t_0) - b_0\right) + b_0
\end{aligned}$$

For $\hat{R}$ dynamics in (3.7), (3.10) we right-multiply by the integrating factor

$$e^{-\int_{t_0}^{t} S(\hat{\omega}(s))ds}$$

where $\hat{\omega}(t) := \tilde{\omega}(t) - \hat{b}_\omega(t)$, then integrate the result between $t = t_0$ and $t = t_1$:

$$\begin{aligned}
\dot{\hat{R}}(t)e^{-\int_{t_0}^{t} S(\hat{\omega}(s))ds} - \hat{R}(t)S(\hat{\omega}(s))e^{-\int_{t_0}^{t} S(\hat{\omega}(s))ds} &= 0 \\
\frac{d}{dt}\left(\hat{R}(t)e^{-\int_{t_0}^{t} S(\hat{\omega}(s))ds}\right) &= 0 \\
\int_{t_0}^{t_1} \frac{d}{dt}\left(\hat{R}(t)e^{-\int_{t_0}^{t} S(\hat{\omega}(s))ds}\right) dt &= \int_{t_0}^{t_1} 0\, dt \\
\hat{R}(t_1)e^{-\int_{t_0}^{t_1} S(\hat{\omega}(s))ds} &= \hat{R}(t_0)e^{-\int_{t_0}^{t_0} S(\hat{\omega}(s))ds} \\
\hat{R}(t_1) &= \hat{R}(t_0)e^{\int_{t_0}^{t_1} S(\hat{\omega}(s))ds}
\end{aligned}$$

where we used the matrix exponential properties $d/dt(e^{At}) = Ae^{At} = e^{At}A$, $e^{-At} = (e^{At})^{-1}$ and $e^{0_{3\times3}} = I$. We evaluate the integral using the trapezoidal rule

$$\int_a^b f(x)dx \approx (b-a)\frac{f(a)+f(b)}{2}$$

so that the update equation is

$$\hat{R}(t_1) = \hat{R}(t_0)\exp\left(\frac{(t_1-t_0)}{2}S\left[\tilde{\omega}(t_0) - \hat{b}_\omega(t_0) + \tilde{\omega}(t_1) - \hat{b}_\omega(t_1)\right]\right)$$

Alternatively, define $\xi \in \mathbb{R}^3$ as

$$\xi := \frac{(t_1-t_0)}{2}\left[\tilde{\omega}(t_0) - \hat{b}_\omega(t_0) + \tilde{\omega}(t_1) - \hat{b}_\omega(t_1)\right] \approx \int_{t_0}^{t_1} \hat{\omega}(s)ds$$

and use Rodrigues' formula (2.9) from Section 2.5 to express the exponential of a skew-symmetric matrix:

$$\hat{R}(t_1) = \hat{R}(t_0)e^{S(\xi)} = \hat{R}(t_0)\left(I + \frac{S(\xi)}{\|\xi\|}\sin\|\xi\| + \frac{S(\xi)^2}{\|\xi\|^2}(1-\cos\|\xi\|)\right)$$

which is equivalent to the previous numerical update but does not require computing a matrix exponential.

The $\hat{v}_N$ and $\hat{p}_N$ dynamics in (3.10) are directly solved by integrating both sides. The trapezoidal rule then gives

$$\hat{v}_N(t_1) = \hat{v}_N(t_0) + \frac{(t_1 - t_0)}{2}\left[\hat{R}(t_0)\left(\tilde{f}(t_0) - \hat{b}_f(t_0)\right) + \hat{R}(t_1)\left(\tilde{f}(t_1) - \hat{b}_f(t_1)\right) + 2g_N\right]$$

and

$$\hat{p}_N(t_1) = \hat{p}_N(t_0) + \frac{(t_1 - t_0)}{2}\left[\hat{v}_N(t_0) + \hat{v}_N(t_1)\right]$$

3.2.5 Linearized Error Dynamics

The EKF requires a linearized system model (3.3) with state $\delta x = x - \hat{x}$ for the error between the true and nominal system trajectories. In order to handle the terms $R - \hat{R}$ we use the following standard approach [51, 59]: use the ground-frame rotation kinematics (2.3) $\dot{R} = S(\omega_N)R$ and define $\omega_N =: d\gamma/dt$ where $\gamma \in \mathbb{R}^3$ is a vector which will be used to measure attitude error; remark γ is expressed in navigation frame coordinates. Multiplying the above by dt and taking the approximations $dR \approx R - \hat{R}$, $d\gamma \approx \gamma - \hat{\gamma} = \delta\gamma$ gives

$$R - \hat{R} \approx S(\delta\gamma)R$$

which is left-multiplied by $\hat{R}^T$ and right-multiplied by R^T, giving

$$\hat{R}^T - R^T \approx \hat{R}^T S(\delta\gamma)$$

Transposing both sides then gives

$$\hat{R} - R \approx -S(\delta\gamma)\hat{R} \quad \text{or equivalently} \quad R \approx \hat{R} + S(\delta\gamma)\hat{R} \tag{3.13}$$

where we used the fact that S is a skew-symmetric matrix. The term $\delta\gamma$ will be used to represent the error between R and $\hat{R}$; the remaining states will use the default $\delta x = x - \hat{x}$ definition. The reason for redefining the attitude error is that as mentioned in Section 2.5, the 9 entries of $R \in SO(3)$ are not independent of each other and so using $R - \hat{R}$ as the error state would lead to a singular covariance matrix P (c.f. Section 3.2.8) in the EKF which is numerically difficult to maintain [84, Sec. VIII].

The EKF is an observer which estimates the state δx of the linearized system (3.3) using sensor (input) signals $\tilde{u}$ and aiding (output) measurements $\tilde{y}$. The estimate $\delta\gamma \subset \delta x$ is used to update $\hat{R}$ to R; however, using the approximation (3.13) for this purpose causes $\hat{R}$ to lose orthogonality, creating significant problems in the algorithm *unless* the resulting matrix is numerically re-orthogonalized after each update, typically using SVD [51, p. 469]. A more elegant solution is to use an attitude update which preserves orthogonality [17, 59]: for (2.3) $\dot{R} = S(\omega_N)R$ the integrating factor is

$$e^{-\int_{t_0}^{t} S(\omega_N(s))ds}$$

which left-multiplies the rotational kinematics (in contrast to Section 3.2.3):

$$\begin{aligned}
e^{-\int_{t_0}^{t} S(\omega_N(s))ds}\dot{R}(t) - e^{-\int_{t_0}^{t} S(\omega_N(s))ds}S(\omega_N(t))R(t) &= 0 \\
\frac{d}{dt}\left(e^{-\int_{t_0}^{t} S(\omega_N(s))ds}R(t)\right) &= 0 \\
\int_{t_0}^{t_1}\frac{d}{dt}\left(e^{-\int_{t_0}^{t} S(\omega_N(s))ds}R(t)\right)dt &= \int_{t_0}^{t_1} 0\,dt \\
e^{-\int_{t_0}^{t_1} S(\omega_N(s))ds}R(t_1) &= e^{-\int_{t_0}^{t_0} S(\omega_N(s))ds}R(t_0) \\
R(t_1) &= e^{\int_{t_0}^{t_1} S(\omega_N(s))ds}R(t_0)
\end{aligned}$$

Using $\omega_N(s) = d\gamma/ds$ as before with $R(t_0) = \hat{R}$, $R(t_1) = R$ we have

$$R = e^{\int_{t_0}^{t_1} S(d\gamma/ds)ds}\hat{R} = e^{S(\gamma-\hat{\gamma})}\hat{R} = e^{S(\delta\gamma)}\hat{R} \tag{3.14}$$

an attitude update which preserves orthogonality:

$$RR^T = e^{S(\delta\gamma)}\hat{R}\hat{R}^T e^{-S(\delta\gamma)} = e^{S(\delta\gamma)(1-1)} = I$$

where we have used the identities $(e^A)^T = e^{A^T}$ and $e^{At_1}e^{At_2} = e^{A(t_1+t_2)}$. Equation (3.14) is used with $\delta\gamma$ from the EKF to correct the state $\hat{R}$ obtained from numerical integration of the nominal dynamics. The remaining states are corrected directly from the definition of δx as

$$x = \hat{x} + \delta x$$

We now work out the linearized error dynamics and outputs for the AHRS and Aided INS dynamics in Sections 3.2.3.1 and 3.2.3.2, respectively. For attitude errors $R - \hat{R}$, starting from (3.13), we have

$$\begin{aligned}
\dot{R} - \dot{\hat{R}} &= S(\delta\dot{\gamma})\hat{R} + S(\delta\gamma)\dot{\hat{R}} \\
RS(\tilde{\omega} - b_\omega - \nu_\omega) &= \hat{R}S(\tilde{\omega} - \hat{b}_\omega) + S(\delta\dot{\gamma})\hat{R} \\
&\quad + S(\delta\gamma)\hat{R}S(\tilde{\omega} - \hat{b}_\omega) \\
\left(\hat{R} + S(\delta\gamma)\hat{R}\right)S(\tilde{\omega} - b_\omega - \nu_\omega) &= \left(\hat{R} + S(\delta\gamma)\hat{R}\right)S(\tilde{\omega} - \hat{b}_\omega) + S(\delta\dot{\gamma})\hat{R} \\
\left(\hat{R} + S(\delta\gamma)\hat{R}\right)S(\tilde{\omega} - (\hat{b}_\omega + \delta b_\omega) - \nu_\omega) &= \left(\hat{R} + S(\delta\gamma)\hat{R}\right)S(\tilde{\omega} - \hat{b}_\omega) + S(\delta\dot{\gamma})\hat{R} \\
\left(\hat{R} + S(\delta\gamma)\hat{R}\right)S(-\delta b_\omega - \nu_\omega) &= S(\delta\dot{\gamma})\hat{R} \\
\hat{R}S(-\delta b_\omega - \nu_\omega) + \underbrace{S(\delta\gamma)\hat{R}S(-\delta b_\omega - \nu_\omega)}_{\approx 0} &= S(\delta\dot{\gamma})\hat{R} \\
S(-\delta b_\omega - \nu_\omega) &= \hat{R}^T S(\delta\dot{\gamma})\hat{R} = S(\hat{R}^T\delta\dot{\gamma}) \\
-\delta b_\omega - \nu_\omega &= \hat{R}^T\delta\dot{\gamma} \\
\delta\dot{\gamma} &= -\hat{R}\delta b_\omega - \hat{R}\nu_\omega
\end{aligned}$$

where the neglected expression consists of quadratic (i.e. non-linear) terms. For bias errors $\delta b = b - \hat{b}$, we have

$$\begin{aligned}
\delta\dot{b} &= \dot{b} - \dot{\hat{b}} \\
&= -\beta(b - b_0) + \sqrt{2\beta}\nu_b + \beta(\hat{b} - b_0) \\
&= -\beta(b - \hat{b}) + \sqrt{2\beta}\nu_b \\
\delta\dot{b} &= -\beta\delta b + \sqrt{2\beta}\nu_b
\end{aligned}$$

an exact expression since the bias dynamics model is linear, c.f. Section 3.2.2. For Aided INS, the velocity error $\delta v = v - \hat{v}$ dynamics are

$$\begin{aligned}
\delta\dot{v} &= R(\tilde{f} - b_f - \nu_f) + g_N - \hat{R}(\tilde{f} - \hat{b}_f) - g_N \\
&= R(\tilde{f} - b_f - \nu_f) - R(\tilde{f} - \hat{b}_f) + R(\tilde{f} - \hat{b}_f) - \hat{R}(\tilde{f} - \hat{b}_f) \\
&= -R\delta b_f - R\nu_f + (R - \hat{R})(\tilde{f} - \hat{b}_f) \\
&= -\hat{R}\delta b_f - \underbrace{S(\delta\gamma)\hat{R}\delta b_f}_{\approx 0} - \hat{R}\nu_f - \underbrace{S(\delta\gamma)\hat{R}\nu_f}_{\approx 0} + S(\delta\gamma)\hat{R}(\tilde{f} - \hat{b}_f) \\
&= -\hat{R}\delta b_f - \hat{R}\nu_f + \delta\gamma \times \left(\hat{R}(\tilde{f} - \hat{b}_f)\right) = -\hat{R}\delta b_f - \hat{R}\nu_f - \left(\hat{R}(\tilde{f} - \hat{b}_f)\right) \times \delta\gamma \\
\delta\dot{v} &= -S\left(\hat{R}(\tilde{f} - \hat{b}_f)\right)\delta\gamma - \hat{R}\delta b_f - \hat{R}\nu_f
\end{aligned}$$

and for position error $\delta p = p - \hat{p}$ the dynamics are

$$\delta\dot{p} = v - \hat{v} = \delta v$$

The magnetometer output error is

$$\begin{aligned}
\delta y_m &= \tilde{y}_m^c - \hat{y}_m \\
&= R^T m_G + \nu_m^c - \hat{R}^T m_G \\
&= (R - \hat{R})^T m_G + \nu_m^c \\
&= \left(S(\delta\gamma)\hat{R}\right)^T m_G + \nu_m^c \\
&= -\hat{R}^T S(\delta\gamma) m_G + \nu_m^c \\
&= -\hat{R}^T (\delta\gamma \times m_G) + \nu_m^c \\
&= \hat{R}^T (m_G \times \delta\gamma) + \nu_m^c \\
\delta y_m &= \hat{R}^T S(m_G)\delta\gamma + \nu_m^c
\end{aligned}$$

where $m_G = m_M$ for AHRS and $m_G = m_N$ for Aided INS. The AHRS accelerometer output error δy_a is obtained simply by replacing m_G by $-g_M$ and ν_m^c by ν_f in the last line above:

$$\delta y_a = -\hat{R}^T S(g_M)\delta\gamma + \nu_f$$

For Aided INS the GPS output error δy_p is

$$\begin{aligned}
\delta y_p &= \tilde{y}_p - \hat{y}_p \\
&= r_E^o + R_E^N(p_N + R\, l_B) + \nu_p - r_E^o - R_E^N(\hat{p}_N + \hat{R}\, l_B) \\
&= R_E^N\left(\delta p + S(\delta\gamma)\hat{R}\, l_B\right) + \nu_p \\
&= R_E^N \delta p - R_E^N S(\hat{R}\, l_B)\delta\gamma + \nu_p
\end{aligned}$$

In each case the linearized error dynamics form the continuous-time LTV system (c.f. Section 3.1)

$$\begin{aligned} \delta\dot{x} &= F(t)\delta x + G(t)w \\ \delta y &= H(t)\delta x + v, \end{aligned} \tag{3.15}$$

where the entries of $F(t)$, $G(t)$ and $H(t)$ are read off the expressions above. The resulting linearized error dynamics are summarized in Sections 3.2.5.1 and 3.2.5.2.

3.2.5.1 AHRS

The error system (3.15) is

$$\begin{aligned} \begin{bmatrix} \delta\dot{\gamma} \\ \delta\dot{b}_\omega \end{bmatrix} &= \begin{bmatrix} 0 & -\hat{R} \\ 0 & -\beta_\omega \end{bmatrix} \begin{bmatrix} \delta\gamma \\ \delta b_\omega \end{bmatrix} + \begin{bmatrix} -\hat{R} & 0 \\ 0 & \sqrt{2\beta_\omega} \end{bmatrix} \begin{bmatrix} \nu_\omega \\ \nu_{b\omega} \end{bmatrix} \\ \begin{bmatrix} \delta y_m^c \\ \delta y_a \end{bmatrix} &= \begin{bmatrix} \hat{R}^T S(m_M) & 0 \\ -\hat{R}^T S(g_M) & 0 \end{bmatrix} \begin{bmatrix} \delta\gamma \\ \delta b_\omega \end{bmatrix} + \begin{bmatrix} \nu_m^c \\ \nu_f \end{bmatrix} \end{aligned} \tag{3.16}$$

and the process and measurement noise vectors w and v are characterized by the covariance matrices $Q = E\langle ww^T\rangle = \mathrm{diag}(\sigma_\omega^2, \sigma_{b\omega}^2)$ and $R = E\langle vv^T\rangle = \mathrm{diag}((\sigma_m^c)^2, \sigma_f^2)$.

3.2.5.2 Aided INS

The error system (3.15) is

$$\begin{aligned} \begin{bmatrix} \delta\dot{p} \\ \delta\dot{v} \\ \delta\dot{\gamma} \\ \delta\dot{b}_f \\ \delta\dot{b}_\omega \end{bmatrix} &= \begin{bmatrix} 0 & I & 0 & 0 & 0 \\ 0 & 0 & -S(\hat{R}(\tilde{f} - \hat{b}_f)) & -\hat{R} & 0 \\ 0 & 0 & 0 & 0 & -\hat{R} \\ 0 & 0 & 0 & -\beta_f & 0 \\ 0 & 0 & 0 & 0 & -\beta_\omega \end{bmatrix} \begin{bmatrix} \delta p \\ \delta v \\ \delta\gamma \\ \delta b_f \\ \delta b_\omega \end{bmatrix} \\ &\quad + \begin{bmatrix} 0 & 0 & 0 & 0 \\ -\hat{R} & 0 & 0 & 0 \\ 0 & -\hat{R} & 0 & 0 \\ 0 & 0 & \sqrt{2\beta_f} & 0 \\ 0 & 0 & 0 & \sqrt{2\beta_\omega} \end{bmatrix} \begin{bmatrix} \nu_f \\ \nu_\omega \\ \nu_{bf} \\ \nu_{b\omega} \end{bmatrix} \\ \begin{bmatrix} \delta y_p \\ \delta y_m \end{bmatrix} &= \begin{bmatrix} R_E^N & 0 & -R_E^N S(\hat{R}\, l_B) & 0 & 0 \\ 0 & 0 & \hat{R}^T S(m_N) & 0 & 0 \end{bmatrix} \begin{bmatrix} \delta p \\ \delta v \\ \delta\gamma \\ \delta b_f \\ \delta b_\omega \end{bmatrix} + \begin{bmatrix} \nu_p \\ \nu_m^c \end{bmatrix} \end{aligned} \tag{3.17}$$

The process and measurement noise vectors w and v are characterized by the covariance matrices $Q = E\langle ww^T\rangle = \mathrm{diag}(\sigma_f^2, \sigma_\omega^2, \sigma_{bf}^2, \sigma_{b\omega}^2)$ and $R = E\langle vv^T\rangle = \mathrm{diag}\left(\sigma_p^2, (\sigma_m^c)^2\right)$.

3.2.6 Observability Analysis

As mentioned in Section 3.2.5, the LTV systems (3.16), (3.17) are used to the design the EKF, an observer which estimates the state δx from inputs u and outputs y where u represents sensor signals which enter the Jacobians $F(t)$, $G(t)$, $H(t)$ and y represents aiding measurements. We first verify the observability of these systems.

3.2.6.1 AHRS

Following [40, Theorem 6.O12], for a LTV system with state dimension n we define the observability matrix

$$\mathcal{O}(t) = \begin{bmatrix} N_0(t) \\ N_1(t) \\ \vdots \\ N_{n-1}(t) \end{bmatrix}$$

where

$$\begin{aligned} N_0(t) &= H(t) \\ N_{m+1}(t) &= N_m(t)F(t) + (d/dt)N_m(t), \qquad m = 0, \ldots, n-2 \end{aligned}$$

where $F(t)$ and $H(t)$ are the state and output matrices. For system (3.16), $n = 6$ and we would need to compute terms up to $N_5(t)$. We have

$$N_0(t) = H(t) = \begin{bmatrix} \hat{R}^T S(m_M) & 0 \\ -\hat{R}^T S(g_M) & 0 \end{bmatrix}$$

and by (3.7), $\dot{\hat{R}} = \hat{R}S(\tilde{\omega} - \hat{b}_\omega) \Longrightarrow \dot{\hat{R}}^T = -S(\tilde{\omega} - \hat{b}_\omega)\hat{R}^T$. We now compute

$$\begin{aligned} N_1(t) &= N_0(t)F(t) + \dot{N}_0(t) \\ &= \begin{bmatrix} \hat{R}^T S(m_M) & 0 \\ -\hat{R}^T S(g_M) & 0 \end{bmatrix} \begin{bmatrix} 0 & -\hat{R} \\ 0 & -\beta_\omega \end{bmatrix} + \begin{bmatrix} -S(\tilde{\omega} - \hat{b}_\omega)\hat{R}^T S(m_M) & 0 \\ S(\tilde{\omega} - \hat{b}_\omega)\hat{R}^T S(g_M) & 0 \end{bmatrix} \\ &= \begin{bmatrix} 0 & -\hat{R}^T S(m_M)\hat{R} \\ 0 & \hat{R}^T S(g_M)\hat{R} \end{bmatrix} + \begin{bmatrix} -S(\tilde{\omega} - \hat{b}_\omega)\hat{R}^T S(m_M) & 0 \\ S(\tilde{\omega} - \hat{b}_\omega)\hat{R}^T S(g_M) & 0 \end{bmatrix} \\ &= \begin{bmatrix} -S(\tilde{\omega} - \hat{b}_\omega)\hat{R}^T S(m_M) & -\hat{R}^T S(m_M)\hat{R} \\ S(\tilde{\omega} - \hat{b}_\omega)\hat{R}^T S(g_M) & \hat{R}^T S(g_M)\hat{R} \end{bmatrix} \end{aligned}$$

The observability matrix $\mathcal{O}(t)$ has the structure

$$\begin{bmatrix} N_0(t) \\ N_1(t) \\ * \end{bmatrix} = \begin{bmatrix} \hat{R}^T S(m_M) & 0 \\ -\hat{R}^T S(g_M) & 0 \\ -S(\tilde{\omega} - \hat{b}_\omega)\hat{R}^T S(m_M) & -\hat{R}^T S(m_M)\hat{R} \\ S(\tilde{\omega} - \hat{b}_\omega)\hat{R}^T S(g_M) & \hat{R}^T S(g_M)\hat{R} \\ * & * \end{bmatrix}$$

Consider the left half of the $N_0(t)$ line, written as

$$\begin{bmatrix} \hat{R}^T S(m_M) \\ -\hat{R}^T S(g_M) \end{bmatrix} = \begin{bmatrix} \hat{R}^T & 0 \\ 0 & \hat{R}^T \end{bmatrix} \begin{bmatrix} S(m_M) \\ -S(g_M) \end{bmatrix}$$

Since $\hat{R} \in SO(3)$ is always invertible, we have

$$\operatorname{rank} \begin{bmatrix} \hat{R}^T S(m_M) \\ -\hat{R}^T S(g_M) \end{bmatrix} = \operatorname{rank} \begin{bmatrix} S(m_M) \\ -S(g_M) \end{bmatrix}$$

The magnetic and gravity field vectors are respectively $m_M = [B_H \quad 0 \quad B_V]^T$ and $g_M = [0 \quad 0 \quad g]^T$ and so the term above expands to

$$\operatorname{rank}\begin{bmatrix} S(m_M) \\ -S(g_M) \end{bmatrix} = \operatorname{rank}\begin{bmatrix} 0 & -B_V & 0 \\ B_V & 0 & -B_H \\ 0 & B_H & 0 \\ 0 & g & 0 \\ -g & 0 & 0 \\ 0 & 0 & 0 \end{bmatrix} = 3$$

Next, consider the right half of the $N_1(t)$ line, written as

$$\begin{bmatrix} -\hat{R}^T S(m_M)\hat{R} \\ \hat{R}^T S(g_M)\hat{R} \end{bmatrix} = \begin{bmatrix} \hat{R}^T & 0 \\ 0 & \hat{R}^T \end{bmatrix} \begin{bmatrix} -S(m_M)\hat{R} \\ S(g_M)\hat{R} \end{bmatrix} = \begin{bmatrix} \hat{R}^T & 0 \\ 0 & \hat{R}^T \end{bmatrix} \begin{bmatrix} -S(m_M) \\ S(g_M) \end{bmatrix} \begin{bmatrix} \hat{R} \end{bmatrix}$$

and with $\hat{R} \in SO(3)$ always invertible, we have

$$\operatorname{rank}\begin{bmatrix} -\hat{R}^T S(m_M)\hat{R} \\ \hat{R}^T S(g_M)\hat{R} \end{bmatrix} = \operatorname{rank}\begin{bmatrix} -S(m_M) \\ S(g_M) \end{bmatrix} = 3,$$

since the expanded form is just a sign change of the earlier term. Due to the lower-triangular form of the $N_0(t)$ and $N_1(t)$ lines in $\mathcal{O}(t)$, we know (e.g. [67, p. 25])

$$\operatorname{rank}\begin{bmatrix} N_0(t) \\ N_1(t) \end{bmatrix} \geq 3 + 3 \Longrightarrow \operatorname{rank}\begin{bmatrix} N_0(t) \\ N_1(t) \end{bmatrix} = 6 \Longrightarrow \operatorname{rank}\mathcal{O}(t) = 6,$$

i.e. the observability matrix $\mathcal{O}(t)$ is *always* full rank. The LTV system (3.16) representing the AHRS linearized error dynamics is therefore observable at any time $t \in (-\infty, \infty)$, and so is said to be instantaneously observable [39, p. 187].

The AHRS system in Section 3.2.3.1 could be expanded by including accelerometer bias as a dynamic state, i.e. adding

$$\dot{b}_f = -\beta_f(b_f - b_{f0}) + \sqrt{2\beta_f}\nu_{bf}$$

to (3.5) and using $\tilde{y}_a = \tilde{f} - \hat{b}_f$ in place of the current $\tilde{y}_a = \tilde{f} - b_{f0}$. In this case the LTV error system (3.16) increases its dimension to 9 and an observability analysis reveals the system is not observable *unless* it is rotating [51, p. 369]. We chose to include the rate gyro bias b_ω rather than accelerometer bias b_f as a state because the former is used to integrate the rotation kinematics, hence a detailed model of b_ω is more important than b_f for accuracy of the AHRS.

3.2.6.2 Aided INS

The original implementation of a navigation filter for our helicopter UAV [75] used the GPS position $\tilde{y}_p$ as the sole aiding measurement, which was found to provide reliable yaw estimates for trajectory flying but not in hover. An observability analysis of the LTV system (3.17) using δy_p as the only output reveals the $\delta\gamma_3$ state is unobservable unless the vehicle is manoeuvering [117], meaning ψ will remain uncorrected and slowly diverge in hover. This can be shown intuitively as follows: the only coefficient of $\delta\gamma$ in (3.17) is $S(\hat{R}(\tilde{f} - \hat{b}_f)) := S(\hat{f}_N)$ where $\hat{f}_N$ denotes the bias-corrected

accelerometer measurement expressed in the navigation frame. Expanding $S(\hat{f}_N)$ via (2.2) we see the coefficients of $\delta\gamma_3$ will vanish when $\hat{f}_{N,1} = \hat{f}_{N,2} = 0$, i.e. zero lateral acceleration. Thus, unless the vehicle is manoeuvering, $\delta\gamma_3$ cannot be observable; the $\delta\gamma$ term in δy_p cannot be distinguished from δp and does not alter this behaviour.

This effect can be eliminated by adding an aiding sensor which provides $\delta\gamma_3$ observability, e.g. a magnetometer. The output equation δy_m in (3.17) contains $S(m_N)\delta\gamma$ and gives non-zero $\delta\gamma_3$ coefficients provided $m_N \neq [0 \quad 0 \quad \pm|m|]^T$, which would only occur at the magnetic north or south poles. A different source of $\delta\gamma_3$ information such as a two-antenna GPS receiver [135] could also be employed.

The triaxial magnetometer part of the output matrix in (3.17) generally provides correction information for all three components of $\delta\gamma$, i.e. it provides updates for the roll and pitch axes in addition to the yaw axis. This is due to $S(m_N)\delta\gamma = m_N \times \delta\gamma$ in (3.17) providing observability for the part of $\delta\gamma$ which is not parallel to m_N. This is why $\delta\gamma_3$ becomes unobservable at the magnetic poles and why $\delta\gamma_1$ and $\delta\gamma_2$ are observable from δy_m as long as the rotation axis is not parallel to m_N. However in some situations the magnetometer should only be used to provide information about the yaw error state $\delta\gamma_3$ [50, p. 28]; this will be further discussed in Sections 3.4.2 and 3.4.3.

The yaw-only aiding equation is obtained as follows: starting from $y - \hat{y} = R^T m_N + \nu_m^c - \hat{R}^T m_N$, assume that roll and pitch are perfectly estimated by the navigation filter, i.e. $\phi = \hat{\phi}$ and $\theta = \hat{\theta}$. By (2.14) we have

$$R - \hat{R} = R_3(\psi)R_2(\hat{\theta})R_1(\hat{\phi}) - R_3(\hat{\psi})R_2(\hat{\theta})R_1(\hat{\phi})$$

and from (3.13)

$$R_3(\psi) - R_3(\hat{\psi}) \approx S([0, 0, \delta\gamma_3]^T)R_3(\hat{\psi})$$

Using these expressions, we obtain the yaw-only magnetometer output equation

$$\delta y_m = \hat{R}^T S(m_N)[0, 0, \delta\gamma_3]^T + \nu_m^c, \tag{3.18}$$

which clearly provides observability of only $\delta\gamma_3$.

3.2.7 Discretization

Since the aiding measurements are sampled, we use the discrete-time formulation of the Kalman Filter, which requires a discretized version of the linearized error system (3.15). The details of how the resulting model is used by the EKF algorithm will be covered in Section 3.2.8.

Let t_k, t_{k+1} denote successive sampling times with $\tau = t_{k+1} - t_k$ and $\hat{x}_k$ be the state estimate at $t = t_k$, then evaluate (3.15) at $\hat{x}_k$ to obtain $F_k = F(\hat{x}_k)$, $G_k = G(\hat{x}_k)$, $H_k = H(\hat{x}_k)$ which are assumed constant on $t \in [t_k, t_{k+1}]$. The resulting LTI system is then solved as

$$\begin{aligned}
\delta x_{k+1} &= e^{F_k\tau}\delta x_k + \int_{t_k}^{t_{k+1}} e^{F_k(t_{k+1}-t)}G_k w(t)dt = \Phi_k \delta x_k + w_k \\
\delta y_k &= H_k \delta x_k + v_k
\end{aligned}$$

where w_k represents a white sequence whose covariance is given by

$$\begin{aligned}
Q_k &= E\left\langle w_k w_k^T \right\rangle \\
&= E\left\langle \int_{t_k}^{t_{k+1}} e^{F_k(t_{k+1}-t)} G_k w(t) dt \int_{t_k}^{t_{k+1}} w^T(s) G_k^T e^{F_k^T(t_{k+1}-s)} ds \right\rangle \\
&= E\left\langle \int_{t_k}^{t_{k+1}} \int_{t_k}^{t_{k+1}} e^{F_k(t_{k+1}-t)} G_k w(t) w^T(s) G_k^T e^{F_k^T(t_{k+1}-s)} dt\, ds \right\rangle \\
&= \int_{t_k}^{t_{k+1}} \int_{t_k}^{t_{k+1}} e^{F_k(t_{k+1}-t)} G_k \underbrace{E\left\langle w(t) w^T(s) \right\rangle}_{Q\delta(s-t)} G_k^T dt\, e^{F_k^T(t_{k+1}-s)} ds \\
Q_k &= \int_{t_k}^{t_{k+1}} e^{F_k(t_{k+1}-s)} G_k Q G_k^T e^{F_k^T(t_{k+1}-s)} ds
\end{aligned} \tag{3.19}$$

where we used the definition of continuous-time white noise [34, p. 92] as a stationary random process with autocorrelation $E\langle \nu(t)\nu(t+s)\rangle = \sigma^2\delta(s)$ where δ denotes the Dirac delta function. The Q_k term (3.19) can be numerically evaluated using the following method adapted from [130]: form the matrix

$$M = \begin{bmatrix} A_1 & B_1 \\ 0 & A_2 \end{bmatrix}$$

where A_1, A_2 and B_1 are square matrices with the same dimensions. Due to its upper block-triangular structure, the matrix exponential of M takes the form

$$e^{Mt} = \begin{bmatrix} C_1(t) & D_1(t) \\ 0 & C_2(t) \end{bmatrix}$$

Since $(d/dt)e^{Mt} = Me^{Mt}$ and $e^0 = I$, we obtain the set of matrix differential equations

$$\begin{aligned}
\dot{C}_1(t) &= A_1 C_1(t) & C_1(0) &= I \\
\dot{C}_2(t) &= A_2 C_2(t) & C_2(0) &= I \\
\dot{D}_1(t) &= A_1 D_1(t) + B_1 C_2(t) & D_1(0) &= 0
\end{aligned}$$

whose solution is

$$\begin{aligned}
C_1(t) &= e^{A_1 t} \\
C_2(t) &= e^{A_2 t} \\
D_1(t) &= \int_0^t e^{A_1(t-s)} B_1 e^{A_2 s} ds
\end{aligned}$$

where $D_1(t)$ is found using the integrating factor approach employed in Section 3.2.4. To evaluate (3.19), form the matrix

$$M = \begin{bmatrix} -F_k & G_k Q G_k^T \\ 0 & F_k^T \end{bmatrix}$$

and recall $\tau = t_{k+1} - t_k$. Evaluating the matrix exponential $e^{M\tau}$ then gives

$$e^{M\tau} = \begin{bmatrix} N_1 & N_2 \\ 0 & N_3 \end{bmatrix} = \begin{bmatrix} e^{-F_k\tau} & \int_0^\tau e^{-F_k(\tau-s)} G_k Q G_k^T e^{F_k^T s} ds \\ 0 & e^{F_k^T \tau} \end{bmatrix}$$

Using the change of variables $s = t_{k+1} - t$,

$$\begin{aligned} N_2 &= e^{-F_k\tau} \int_0^\tau e^{F_k s} G_k Q G_k^T e^{F_k^T s} ds \\ &= \left(e^{F_k\tau}\right)^{-1} \int_{t_k}^{t_{k+1}} e^{F_k(t_{k+1}-t)} G_k Q G_k^T e^{F_k^T(t_{k+1}-t)} dt \end{aligned}$$

and referring to (3.19),

$$Q_k = (N_3)^T N_2$$

Remark that $(N_3)^T = e^{F_k\tau} = \Phi_k$, the transition matrix of the DT system.

The covariance of v_k, the measurement noise white sequence, is found as follows: first consider a continuous-time signal $f(t)$ with Fourier transform $F_c(\omega)$ and sample it with a period of T. The discrete-time Fourier transform $F_d(\Omega)$ of the resulting signal $f[k]$ can be shown to be [82, p. 636]

$$F_d(\Omega) = \frac{1}{T} F_c\left(\frac{\Omega}{T}\right)$$

where $F_d(\Omega)$ has a period of 2π; this relationship holds irrespective of whether $f(t)$ is bandlimited or whether it is sampled above its Nyquist rate. A continuous-time white noise term ν is defined by its autocorrelation $R(\tau) = E\left\langle \nu(t)\nu(t+\tau)\right\rangle = \sigma^2\delta(\tau)$ or equivalently by its power spectral density function

$$S_c(\omega) = \mathcal{F}_c\left(R(\tau)\right) = \int_{-\infty}^{\infty} \sigma^2\delta(\tau) e^{-j\omega\tau} d\tau = \sigma^2$$

The sampled version of ν is the discrete-time white sequence $v[k]$, defined by the autocorrelation $R_d[\kappa] = E\langle v[k]v[k+\kappa]\rangle = \sigma_d^2\delta_\kappa$ or equivalently the power spectral density function

$$S_d(\Omega) = \mathcal{F}_d\left(R_d[\kappa]\right) = \sum_{\kappa=-\infty}^{\kappa=\infty} \sigma_d^2\delta_\kappa e^{-j\Omega\kappa} = \sigma_d^2$$

By the above we have

$$S_d(\Omega) = \frac{1}{T} S_c\left(\frac{\Omega}{T}\right) = \frac{\sigma^2}{T}$$

and so the sampled version of ν possesses the discrete-time covariance $\sigma_d^2 = \sigma^2/T$. For the measurement white sequence v_k, this means

$$R_k = \left(\frac{1}{\tau}\right) R$$

In summary we have converted (3.15) into the discrete-time LTV system

$$\begin{aligned} \delta x_{k+1} &= \Phi_k \delta x_k + w_k & E\langle w_k w_k^T\rangle &= Q_k \\ \delta y_k &= H_k \delta x_k + v_k & E\langle v_k v_k^T\rangle &= R_k \end{aligned} \tag{3.20}$$

where Φ_k, H_k, Q_k and R_k are calculated as above using the current state $\hat{x}_k = \hat{x}(t_k)$ and interval between aiding measurements $\tau = t_{k+1} - t_k$.

3.2.8 Kalman Filter

The Kalman Filter applies to linear, discrete-time systems of the form (3.20) where w_k, v_k are white sequences with known covariances Q_k, R_k, respectively. We also assume that

$$E\left\langle w_k v_l^T \right\rangle = 0 \qquad \forall k, l$$

The reason for this assumption will become clear in the derivation below; physically, this means the process and measurement noise are uncorrelated with each other. This is a reasonable assumption as seen from (3.16) and (3.17) where the process w and measurement v noise vectors are composed from different sensors. Note the Kalman Filter can be modified to allow w_k and v_k to be correlated, c.f. [34, Sec. 9.2].

Define the pre-update estimate of the linearized system state δx_k as $\delta\hat{x}_k^-$ and the associated estimation error as $e_k^- = \delta x_k - \delta\hat{x}_k^-$ with covariance $P_k^- = E\left\langle (e_k^-)(e_k^-)^T \right\rangle$. The Kalman filter is the linear observer

$$\delta\hat{x}_k = \delta\hat{x}_k^- + K_k(\delta y_k - H_k\delta\hat{x}_k^-), \tag{3.21}$$

where K_k is chosen to minimize the trace of $P_k = E\left\langle (\delta x_k - \delta\hat{x}_k)(\delta x_k - \delta\hat{x}_k)^T \right\rangle = E\left\langle e_k\, e_k^T \right\rangle$, the post-update error covariance. This last condition is the cost function to be minimized, representing the sum of the variances of the individual entries of e_k, the estimation error vector. Substituting (3.21) into P_k and expanding via (3.20),

$$\begin{aligned}
P_k &= E\left\langle \left(\delta x_k - \delta\hat{x}_k^- - K_k(\delta y_k - H_k\delta\hat{x}_k^-)\right)\left(\delta x_k - \delta\hat{x}_k^- - K_k(\delta y_k - H_k\delta\hat{x}_k^-)\right)^T \right\rangle \\
&= E\left\langle \left(e_k^- - K_k(H_k e_k^- + v_k)\right)\left(e_k^- - K_k(H_k e_k^- + v_k)\right)^T \right\rangle \\
P_k &= (I - K_k H_k)P_k^-(I - K_k H_k)^T + K_k R_k K_k^T,
\end{aligned} \tag{3.22}$$

where we took $E\left\langle e_k^- v_k \right\rangle = E\left\langle e_k^- \right\rangle E\left\langle v_k \right\rangle = 0$ due to the assumption that v_k and w_k are uncorrelated. Equation (3.22) gives P_k as a quadratic function of K_k. Using the matrix differentiation formulas $d\left(\mathrm{tr}(AB)\right)/dA = B^T$, $d\left(\mathrm{tr}(ACA^T)\right)/dA = 2AC$, we compute $d\left(\mathrm{tr}P_k\right)/dK_k$ and find its minima:

$$\begin{aligned}
&\frac{d\left(\mathrm{tr}P_k\right)}{dK_k} = -2(H_k P_k^-)^T + 2K_k(H_k P_k^- H_k^T + R_k) = 0 \\
&\implies K_k = P_k^- H_k^T (H_k P_k^- H_k^T + R_k)^{-1},
\end{aligned} \tag{3.23}$$

where K_k is the optimal observer gain in (3.21). Using this value, we update the estimate $\delta\hat{x}_k^-$ using (3.21) and find the post-update error covariance of $\delta\hat{x}_k$ using (3.22). Finally, we propagate the post-update $\delta\hat{x}_k$ in time using (3.20) as

$$\delta\hat{x}_{k+1}^- = \Phi_k\delta\hat{x}_k \tag{3.24}$$

and the covariance P_k as

$$\begin{aligned}
P_{k+1}^- &= E\left\langle (\delta x_{k+1} - \delta\hat{x}_{k+1}^-)(\delta x_{k+1} - \delta\hat{x}_{k+1}^-)^T \right\rangle \\
&= E\left\langle (\Phi_k(\delta x_k - \delta\hat{x}_k) + w_k)(\Phi_k(\delta x_k - \delta\hat{x}_k) + w_k)^T \right\rangle \\
P_{k+1}^- &= \Phi_k P_k \Phi_k^T + Q_k,
\end{aligned} \tag{3.25}$$

where $E\left\langle e_k w_k \right\rangle = E\left\langle e_k \right\rangle E\left\langle w_k \right\rangle = 0$ because w_k is the process noise during the propagation interval $\left(\delta\hat{x}_k, \delta\hat{x}_{k+1}^-\right]$ and hence uncorrelated with e_k. The $\delta\hat{x}_{k+1}^-$ and P_{k+1}^- terms are used on the next Kalman Filter pass as $\delta\hat{x}_k^-$ and P_k^-, respectively, making it a recursive algorithm well-suited for computer implementation.

3.2.9 Extended Kalman Filter

As explained in Section 3.1, the Extended Kalman Filter re-linearizes the nonlinear system (3.1) about its latest nominal state $\hat{x}$ and output $\hat{y}$. The standard Kalman Filter algorithm in Section 3.2.8 is thus modified as described below.

Whenever an aiding measurement is available, the latest nominal state and output are obtained from integration of (3.2) as $\hat{x}_k^-$ and $\hat{y}_k^-$, respectively, where the superscript $^-$ is used to denote pre-correction quantities. The states of the linearized error system (3.20) are then $\delta x_k = x_k - \hat{x}_k^-$ and $\delta y_k = y_k - \hat{y}_k^-$, the estimated Kalman states are $\delta\hat{x}_k = \hat{x}_k - \hat{x}_k^-$ and $\delta\hat{x}_k^- = \hat{x}_k^- - \hat{x}_k^- = 0$, and so the update step (3.21) simplifies to

$$\hat{x}_k = \hat{x}_k^- + K_k\left(y_k - \hat{y}_k^-\right) \tag{3.26}$$

where K_k is computed by (3.23) and P_k is updated by (3.22) as in the conventional Kalman Filter. After update (3.26) is performed, the updated state $\hat{x}_k$ immediately becomes the linearization trajectory, so $\delta x_k = x_k - \hat{x}_k$ and $\delta\hat{x}_k = \hat{x}_k - \hat{x}_k = 0$. This means the estimated state propagation (3.24) becomes trivial and is *omitted*. The covariance matrix propagation step (3.25) still requires Φ_k and Q_k, which are calculated by the method in Section 3.2.7 using the just-updated state $\hat{x}_k$.

An important point for implementation is that the aiding measurements may be aperiodic, and so the EKF should not propagate P_k forwards in time. Instead, after performing the update (3.26), we save a copy of the updated state estimate $\hat{x}_k$, the error covariance P_k obtained from (3.22) and the current aiding time t_a. The next time an aiding measurement is available and the EKF is entered, we use the saved state as $\hat{x}_{k-1}$ to build F_{k-1}, G_{k-1}, compute $\tau = t - t_a$, calculate Φ_{k-1}, Q_{k-1} and use these to propagate the saved P_{k-1} to P_k^- by (3.25). This works because the calculation method for Φ_k and Q_k in Section 3.2.7 is time-invariant and requires only the elapsed time τ.

In summary, the EKF algorithm consists of the following sequence of operations, executed whenever an external aiding measurement is available:

1. Propagate previous covariance matrix: $P_k^- = \Phi_{k-1}P_{k-1}\Phi_{k-1}^T + Q_{k-1}$
2. Compute Kalman gain: $K_k = P_k^- H_k^T (H_k P_k^- H_k^T + R_k)^{-1}$
3. Update estimate: $\hat{x} = \hat{x}^- + K_k(y_k - \hat{y}_k^-)$
4. Compute covariance of updated estimate: $P_k = (I - K_k H_k)P_k^-(I - K_k H_k)^T + K_k R_k K_k^T$

Following the above, the terms $\hat{x}$ and P_k are retained. On the next EKF pass, the saved $\hat{x}$ is used as $\hat{x}_{k-1}$ to build F_{k-1}, G_{k-1} to calculate Φ_{k-1}, Q_{k-1}, and the saved P_k as P_{k-1} in step 1 above. To initialize the (recursive) EKF algorithm, $\hat{x}_{k-1}$ is assigned as the vehicle's initial state estimate $\hat{x}(0)$, computed during an initialization period discussed in Section 3.2.11. The P_{k-1} is assigned as a zero matrix, which results in sub-optimal estimates for the first few EKF passes but is numerically safer than over-estimating the entries [34, p. 261].

3.2.10 EKF Implementation

The EKF algorithm from Section 3.2.9 is implemented for the AHRS and Aided INS as a Simulink S-Function block written in C, using the open-source GNU Scientific

Library (GSL) for vector and matrix operations. The same code block is used for both offline and real-time operation.

The magnetometer compensation terms K_m, b_m resp. A_c, b_c (c.f. Section 3.2.2) are computed by (2.26) in Section 2.9 using parameters from Table 2.1. The entries of the continuous-time process and measurement noise covariance matrices Q, R in (3.16) and (3.17) are taken from Table 3.1 in Section 3.2.2, and are then discretized to Q_k and R_k as covered in Section 3.2.7.

3.2.10.1 AHRS

As mentioned in Section 3.2.9, the EKF algorithm can handle aperiodic aiding measurements by keeping track of the time elapsed since the previous update. We use this fact to allow the magnetometer and accelerometer aiding to be performed at independent, user-selectable intervals T_m and T_a, where $T_m, T_a \geq 0.01$ s, the IMU sampling period. The main reason for this is that the Kalman correction step is computationally much more expensive than the numerical integration step (c.f. Section 3.2.4), so if the hardware cannot maintain real-time performance due to e.g. a low-power processor or an expensive control algorithm such as MPC, the user can lengthen the aiding period(s). In practice, we have never encountered a problem due to the tremendous computational power provided by the on-board Ampro ReadyBoard 800, however this tuning capability may be useful in the future as more complex control algorithms are implemented.

Dual-rate aiding uses the DT model (3.20) with partitioned output matrix $H_k = [H_k^m; H_k^a]$ and measurement noise covariance matrix $R_k = \text{diag}(R_k^m, R_k^a)$. The variable τ is (still) used to measure the time elapsed since the previous Kalman update, whose type is irrelevant, and the EKF algorithm described in Section 3.2.9 is run using the stored $\hat{x}$ and P_k and the (H_k, R_k) pair for the current aiding measurement. Note that if both aiding measurements are available at a given time, the second EKF pass sees $\tau = 0$ in which case the propagation step becomes trivial: the stored P_k is used as P_k^-, so step 1 of the EKF algorithm is omitted.

The ability of the EKF to handle aperiodic aiding measurements is useful in another way. As discussed in Section 3.2.2, we assume the accelerometer measures only gravity, which is incorrect under acceleration. We test each aiding measurement by computing $\|\tilde{y}_a\|$ and comparing it to $\|g\| = 9.81$ m/s^2, considering it as reliable if

$$\frac{|\|\tilde{y}_a\| - 9.81|}{9.81} \leq \text{tol}$$

where tol ≥ 0 is the accelerometer tolerance factor selected by the user. An overly low tolerance will not work well in experiment due to noise and time-varying bias affecting the measurement; we have found tol $= 0.5$ performs well in practice. If $\tilde{y}_a$ is outside the prescribed tolerance the accelerometer aiding step is skipped such that the next EKF pass will use a larger τ value. Conversely $\tilde{y}_a$ aiding is re-established once the unit ceases to accelerate.

3.2.10.2 Aided INS

The dual-rate aiding discussed in Section 3.2.10.1 is used for Aided INS by partitioning the output matrix of the DT model (3.20) as $H_k = [H_k^p; H_k^m]$ and measurement noise covariance matrix as $R_k = \text{diag}(R_k^p, R_k^m)$. This allows using the magnetometer

at a user-specified aiding period $T_m \geq 0.01$ s corresponding to the IMU's 100 Hz measurement rate. The magnetometer aiding can also be disabled altogether.

As mentioned in Section 3.2.2 the GPS receiver reports the standard deviation σ_p and solution status of every measurement, nominally available at a period of $T_p = 0.1$ s (10 Hz rate). The reported standard deviation is used to build the discrete-time covariance matrix as $R_k^p = \text{diag}(\sigma_p^2)$. The solution status is a metric of the accuracy of the position measurement [108, Tbl. 47]; we employ solutions with floating narrow-lane ambiguity or better for aiding and discard others [75, p. 95].

3.2.11 Initialization

Both the AHRS and Aided INS designs employ an initialization period during which the vehicle is known to be stationary with given roll and pitch angles ϕ_0 and θ_0. Throughout initialization we compute a running average of the (compensated) magnetometer, accelerometer and rate gyro measurements, as well as GPS measurements in the Aided INS case. For a sampled signal y_k, the running average is computed as [123, p. 90]

$$\overline{y}_k = \frac{1}{k}\left[(k-1)\overline{y}_{k-1} + y_k\right]$$

When the user switches out of initialization mode the vectors $\overline{m}$, $\overline{f}$, $\overline{\omega}$ and $\overline{r}^a$ contain the averaged sensor readings for this period. These are used as follows:

3.2.11.1 AHRS

The magnetometer average $\overline{m}$ is used to calculate initial magnetic frame yaw ψ_0^m as (2.24)

$$\psi_0^m = \text{atan2}\left(-\cos\phi_0\,\overline{m}_2 + \sin\phi_0\,\overline{m}_3, \cos\theta_0\,\overline{m}_1 + \sin\phi_0\sin\theta_0\,\overline{m}_2 + \cos\phi_0\sin\theta_0\,\overline{m}_3\right)$$

The set $(\phi_0, \theta_0, \psi_0^m)$ gives the initial attitude (2.15)

$$R_0 = \begin{bmatrix} c_\theta c_\psi & s_\phi s_\theta c_\psi - c_\phi s_\psi & c_\phi s_\theta c_\psi + s_\phi s_\psi \\ c_\theta s_\psi & s_\phi s_\theta s_\psi + c_\phi c_\psi & c_\phi s_\theta s_\psi - s_\phi c_\psi \\ -s_\theta & s_\phi c_\theta & c_\phi c_\theta \end{bmatrix}$$

Using $\overline{m}$ we calculate the reference magnetic field $m_M = [B_H \quad 0 \quad B_V]^T$ as (2.25)

$$\begin{aligned} B_V &= -\sin\theta_0\,\overline{m}_1 + \sin\phi_0\cos\theta_0\,\overline{m}_2 + \cos\phi_0\cos\theta_0\,\overline{m}_3 \\ B_H &= \sqrt{\overline{m}_1^2 + \overline{m}_2^2 + \overline{m}_3^2 - B_V^2} \end{aligned}$$

The vector $\overline{f}$ gives (c.f. Section 3.2.2)

$$\overline{f} = E\langle\tilde{f}\rangle = E\left\langle a_0 - g_0 + b_{f0} + b_{ft} + \nu_f\right\rangle = -g_0 + b_{f0}$$

where

$$g_0 := R_0^T g_M = \begin{bmatrix} * & * & -s_\theta \\ * & * & s_\phi c_\theta \\ * & * & c_\phi c_\theta \end{bmatrix} \begin{bmatrix} 0 \\ 0 \\ g \end{bmatrix} = \begin{bmatrix} -\sin\theta_0 \\ \sin\phi_0\cos\theta_0 \\ \cos\phi_0\cos\theta_0 \end{bmatrix} g$$

such that $b_{f0} = \overline{f} + g_0$ is the constant turn-on accelerometer bias. The vector $\overline{\omega}$ gives

$$\overline{\omega} = E\langle \omega_0 + b_{\omega 0} + b_{\omega t} \rangle = b_{\omega 0},$$

the constant turn-on rate gyro bias. The initial state of nominal dynamics (3.2) is

$$\hat{x}(0) = \begin{bmatrix} \hat{R}(0) & \hat{b}_\omega(0) \end{bmatrix} = \begin{bmatrix} R_0 & b_{\omega 0} \end{bmatrix}$$

also used to initialize the EKF as discussed in Section 3.2.9.

3.2.11.2 Aided INS

We have the initialization conditions $p_0 = v_0 = 0$. As discussed in Section 2.8 the reference magnetic field $m_N = [B_x \quad B_y \quad B_z]^T$ is known. We calculate the initial navigation frame yaw ψ_0 as (2.23)

$$\psi_0 = \text{atan2}\Bigg(B_y \Big[c_{\theta_0} \overline{m}_1 + s_{\phi_0} s_{\theta_0} \overline{m}_2 + c_{\phi_0} s_{\theta_0} \overline{m}_3 \Big] - B_x \Big[c_{\phi_0} \overline{m}_2 - s_{\phi_0} \overline{m}_3 \Big], \\ B_x \Big[c_{\theta_0} \overline{m}_1 + s_{\phi_0} s_{\theta_0} \overline{m}_2 + c_{\phi_0} s_{\theta_0} \overline{m}_3 \Big] + B_y \Big[c_{\phi_0} \overline{m}_2 - s_{\phi_0} \overline{m}_3 \Big] \Bigg)$$

then use $(\phi_0, \theta_0, \psi_0)$ to build the initial attitude matrix (2.15)

$$R_0 = \begin{bmatrix} c_\theta c_\psi & s_\phi s_\theta c_\psi - c_\phi s_\psi & c_\phi s_\theta c_\psi + s_\phi s_\psi \\ c_\theta s_\psi & s_\phi s_\theta s_\psi + c_\phi c_\psi & c_\phi s_\theta s_\psi - s_\phi c_\psi \\ -s_\theta & s_\phi c_\theta & c_\phi c_\theta \end{bmatrix}$$

As in Section 3.2.11.1 we have $b_{f0} = \overline{f} + g_0$ and $b_{\omega 0} = \overline{\omega}$ where

$$g_0 = \begin{bmatrix} -\sin\theta_0 \\ \sin\phi_0 \cos\theta_0 \\ \cos\phi_0 \cos\theta_0 \end{bmatrix} g$$

and the initial state of nominal dynamics (3.2) is

$$\hat{x}(0) = \begin{bmatrix} \hat{p}(0) & \hat{v}(0) & \hat{R}(0) & \hat{b}_f(0) & \hat{b}_\omega(0) \end{bmatrix} = \begin{bmatrix} 0 & 0 & R_0 & b_{f0} & b_{\omega 0} \end{bmatrix}$$

also used to initialize the EKF in Section 3.2.9.

The antenna position $\overline{r}^a$ is converted from ECEF to geodetic coordinates (λ^a, φ^a) using (2.7) in Section 2.4. The resulting coordinates are used to compute the antenna-centered rotation matrix $(R_E^N)^a$ by (2.6) from which

$$\overline{r}^a - (R_E^N)^a R_0 \, l_B = r_E^o$$

i.e. the helicopter's centre of mass is used as the navigation frame origin whose position vector w.r.t. the ECEF frame origin is r_E^o. We then convert r_E^o to (λ, φ) by (2.7) and use (2.6) to obtain R_E^N, the rotation matrix between ECEF and navigation frame.

3.3 AHRS Testing

3.3.1 Simulation Results

The desired reference trajectory is generated and converted into m, f and ω signals, which are then corrupted by simulated white noise and time-varying bias employing the engine-off noise parameters in Table 3.1. We generate the following trajectory: the system is initialized for 5 s with $(\phi_0 = 0, \theta_0 = 0, \psi_0^m = 45^\circ)$ attitude. Next, the system is transitioned to $(\phi_1 = 90^\circ, \theta_1 = 60^\circ, \psi_1^m = 90^\circ)$, $(\phi_2 = -90^\circ, \theta_2 = -60^\circ, \psi_2^m = 0)$, $(\phi_3 = 0, \theta_3 = 0, \psi_3^m = 0)$ at times $t_1 = 10$ s, $t_2 = 15$ s, $t_3 = 20$ s, respectively. Adjacent segments are connected using three-point splines in order to reflect the smooth transition between motions in a real experiment. The attitude at $t = t_3$ is held constant during a 5 s interval while the system is shaken along its three axes, described by the acceleration profile $a_k = A_k \sin(\omega_k t)$ where $A_k \in (4, 8, 6)$ m/s^2 and $\omega_k \in (2.5, 2.5, 3.3)$ Hz; these values were experimentally identified from an IMU sensor data log collected while the unit was violently shaken by hand. The shaking is then terminated and the system is left at rest for 5 s to allow the estimates to re-converge.

As per Section 3.2.10 the process and measurement noise covariance matrices Q and R are (also) taken from Table 3.1. The magnetometer compensation terms are taken as $K_m = I$, $b_m = 0$ since we did not warp the sensed magnetic field in the simulated data. The aiding intervals are selected as $T_m = 0.04$ s and $T_a = 0.02$ s, i.e. magnetometer and accelerometer aiding rates of 25 Hz and 50 Hz respectively, and the latter's tolerance factor is set to tol $= 0.5$. The resulting state estimates are plotted versus their reference trajectories in Figure 3.3.

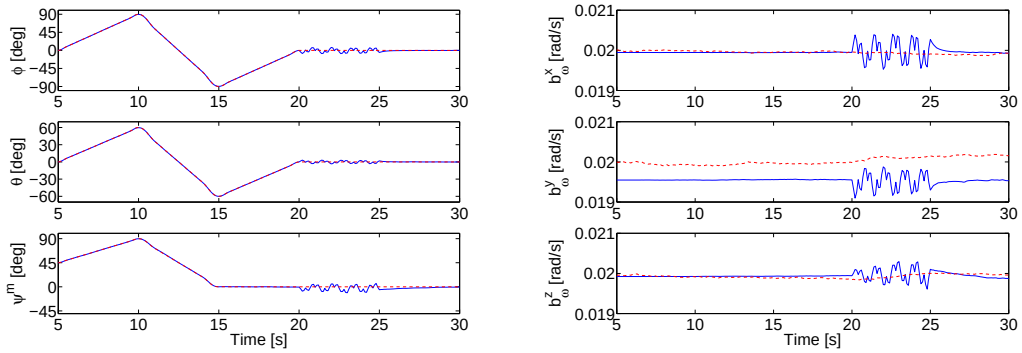

Figure 3.3: AHRS simulation: estimated states (—), reference states (- - -).

For the post-initialization, pre-shaking interval $5 \leq t \leq 20$ s the states estimated by the AHRS follow their reference values quite closely. The shaking phase on $20 < t \leq 25$ s exhibits a much larger discrepancy due to violating the $a = 0$ assumption in Section 3.2.2; the error is partially rectified by using the accelerometer tolerance factor tol. Once the shaking is stopped, the estimates re-converge on $25 < t \leq 30$ s.

The error between estimated and reference attitudes is plotted in Figure 3.4. The AHRS provides sub-degree precision under normal operation and bounds the errors to below 10° during the shaking period. The estimates re-converge once the unit is stationary on $t \geq 25$ s; remark the roll and pitch errors re-converge faster

than yaw due to the lower aiding rate of the magnetometer.

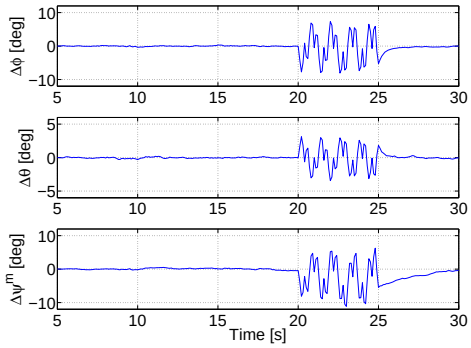

Figure 3.4: AHRS simulation: error between estimated and reference attitude angles

3.3.2 Experimental Results

The AHRS is now run experimentally in an indoor lab equipped with a Vicon motion-capture system. Using a set of passive optical markers attached to the vehicle, this system provides high-precision attitude and position measurements at up to 240 Hz. We set the Vicon output rate at 100 Hz and use the attitude measurements as a comparison for our estimates. Since the Vicon system uses the starting vehicle position as its $\phi = \theta = \psi = 0$ datum, we report AHRS yaw as $\psi = \psi^m - \psi_0^m$ where ψ_0^m is found in initialization, c.f. Section 3.2.11.1.

The experimental procedure is very similar to Section 3.3.1: after an initialization period where the unit is level, it is picked up by hand and maintained level. Next, a set of positive and negative roll, positive and negative pitch and negative and positive yaw motions are sequentially executed, returning to the level configuration after each one. After this the unit is violently shaken by hand and then set down. The AHRS system parameters are identical to those used in Section 3.3.1, except for using magnetometer compensation K_m, b_m resp. A_c, b_c factors found by performing a (full) calibration a priori, c.f. Sections 2.9 and 3.2.2.

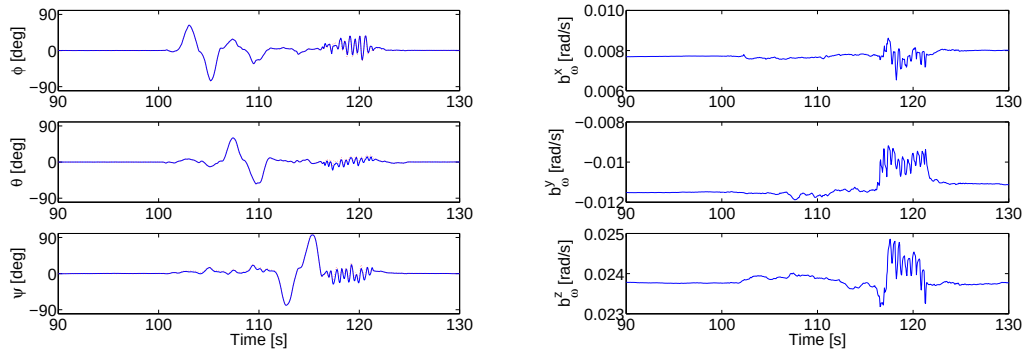

Figure 3.5: AHRS experiment: estimated states (—), Vicon attitudes (- - -).

The experimental AHRS state estimates and Vicon outputs are shown in Figure 3.5. Using the Vicon data as a reference we see very good attitude estimation

performance from the AHRS, in most cases achieving sub-degree accuracy and with peak errors of about 2° in the ϕ and θ and about 3° in ψ data outside the shaking period which occurs at $116 \leq t \leq 122$ s. This is more clearly seen in Figure 3.6 which plots the errors between attitude angles from both systems, as well as $\|\tilde{y}_a\|$ used to pinpoint the shaking interval. The AHRS bias estimates in Figure 3.5 do not have a reference trajectory, but we see the estimates are nearly constant throughout the experiment except during the shaking interval, after which they re-converge. This is consistent with the simulated results in Figure 3.3.

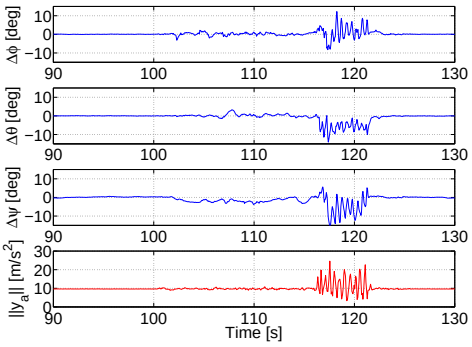

Figure 3.6: AHRS experiment: error between AHRS and Vicon attitudes; $\|\tilde{y}_a\|$

3.4 Aided INS Testing

3.4.1 Simulation Results

The Aided INS is first tested in simulation by generating a reference trajectory in the navigation frame described by smooth position p_N and Euler angles (ϕ, θ, ψ) functions of time. These are analytically differentiated and converted to IMU m_B, f_B, ω_B and GPS r_E^a signals using lever arm $l_B = [-0.8 \quad 0 \quad -0.5]^T$ for the antenna position[1]. A 45 s initialization period is added to the start of the trajectory, and the generated signals are then corrupted with simulated noise using the parameters provided in Table 3.1.

The EKF filter's process and measurement noise covariance matrices Q and R and bias decay constants β are (also) taken from Table 3.1. The reference magnetic field value m_N was provided in Section 2.8, and we perform magnetometer aiding at a period of $T_m = 0.02$ s. In order to validate Section 3.2.6.2, a GPS-only version of Aided INS is also employed by disabling magnetometer aiding as discussed in Section 3.2.10.2. As in Section 3.3.1 we do not warp the magnetic field in simulation such that $K_m = I$ and $b_m = 0$; the effect of magnetometer calibration on Aided INS performance will be comprehensively studied in experiment in Sections 3.4.2 and 3.4.3.

[1]This has been measured directly from the helicopter UAV.

3.4.1.1 Hover Simulation

The first case deals with an idealized hover. The vehicle starts out on the ground facing geographic East ($\psi_0 = 90°$). It then flies vertically up by 5 m, executes a 180° counter-clockwise turn and hovers facing geographic West, each stage taking 5 s with the vehicle stationary in-between; this is achieved using quintic and cubic splines to respectively transition the position and attitude between the given points [75, p. 102]. The resulting state estimates are shown in Figure 3.7, and the case with magnetometer aiding disabled is shown in Figure 3.8.

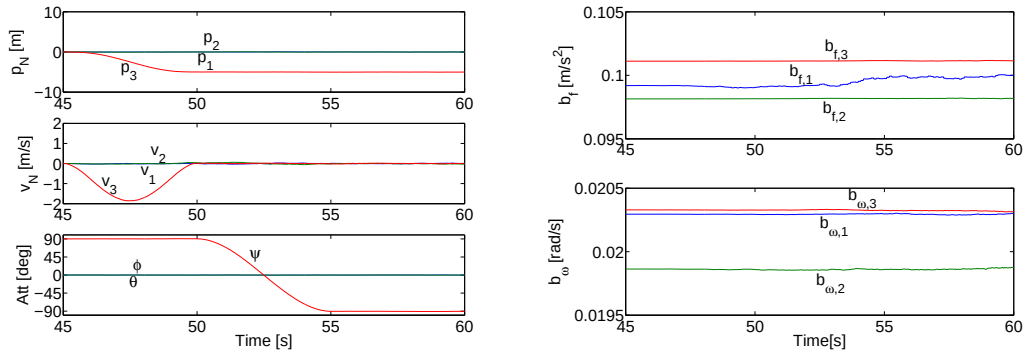

Figure 3.7: State Estimates: Simulated Hover

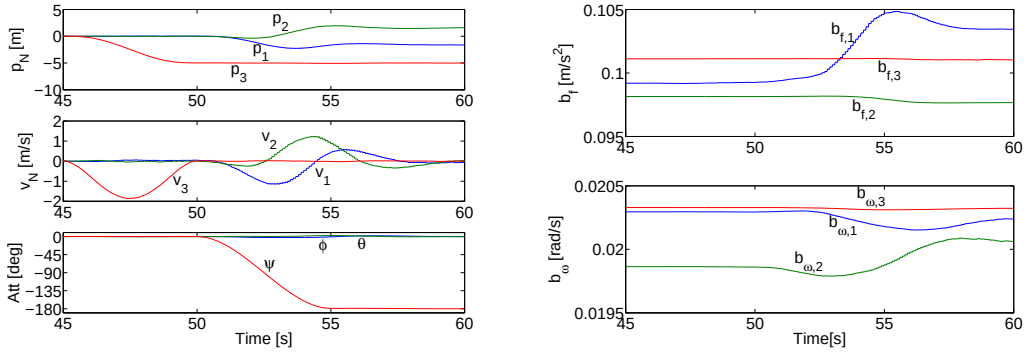

Figure 3.8: State Estimates: Simulated Hover, GPS-only Aiding

The simulated hover using magnetometer aiding (Figure 3.7) shows essentially perfect estimation with $\hat{p}_1 = \hat{p}_2 = 0$ and $\hat{\phi} = \hat{\theta} = 0$ as the vehicle climbs 5 m and yaws 180° counter-clockwise from the starting $\hat{\psi} = 90°$. The bias estimates $\hat{b}_f$ and $\hat{b}_\omega$ are nearly constant throughout. By contrast Figure 3.8 with GPS-only aiding (magnetometer disabled) shows markedly worse performance. The system incorrectly assumes $\psi_0 = 0$ due to the lack of the initial yaw calculation (2.23) and ψ remains uncorrected during the climb interval $45 \leq t \leq 50$ s since it is unobservable to the EKF. Integrating the nominal dynamics (3.10) using the rate gyro signal ω correctly identifies the $-180°$ change in ψ, however the error in the actual ψ value leads to errors in $\hat{p}$ and $\hat{v}$ estimates due to the lever-arm l_B of the GPS antenna creating errors in y_p aiding measurements. Although the velocity estimates re-converge to the correct $v = 0$ value on the stationary hover period $55 \leq t \leq 60$ s,

the $\hat{p}_1$ and $\hat{p}_2$ estimates each exhibit a steady-state error of almost 2 m. The bias estimates $\hat{b}_{f,1}$ and $\hat{b}_{\omega,1}, \hat{b}_{\omega,2}$ are (incorrectly) perturbed at $t \geq 50$ s, the start of the turn manoeuver, although the relative importance of this error is smaller than that for position, velocity and attitude estimates.

3.4.1.2 Trajectory Simulation

We now consider a more complicated flying trajectory: a three-dimensional figure-8, requiring motion in all six degrees of freedom and producing significant lateral accelerations due to banking turns. The trajectory is described as a parametric curve in the navigation frame,

$$\begin{aligned} x(t) &= M \sin(2\pi t/T) + x_0 \\ y(t) &= (m/2) \sin(4\pi t/T) + y_0 \\ z(t) &= (-H/2) \sin(\pi t/T) + z_0 \end{aligned} \tag{3.27}$$

where $M = 50$ m, $m = 25$ m represent the major and minor diameters of each lobe, respectively, $H = 10$ m is the total vertical height of the trajectory, $T = 50$ s is the period of one complete figure-8 circuit and $(x_0, y_0, z_0) = (0, 0, -15)$ m are the NED coordinates of the geometric center of the trajectory. We define the associated attitude such that the yaw corresponds to direction of travel, pitch is proportional to rate of climb, and roll to the turning rate:

$$\begin{aligned} \psi(t) &= \text{atan2}(y'(t), x'(t)) \\ \theta(t) &= -\alpha z'(t) \\ \phi(t) &= \beta \psi'(t), \end{aligned} \tag{3.28}$$

where $\alpha = 1$, $\beta = 1$ are the pitching and banking coefficients, which should be set proportional to the speed of the trajectory, which in turn is inversely proportional to T. The complete trajectory consists of the initialization period with $\psi_0 = 90°$, followed by a 10 s transition to the $t = 0$ point of (3.27), (3.28) using splines to generate a smooth transition trajectory as in Section 3.4.1.1, and a 200 s interval of flying a three-dimensional figure-8 pattern. As in Section 3.4.1.1 we employ magnetometer aiding at $T_m = 0.02$ s and for comparison consider a GPS-only aided design i.e. where magnetometer aiding is disabled.

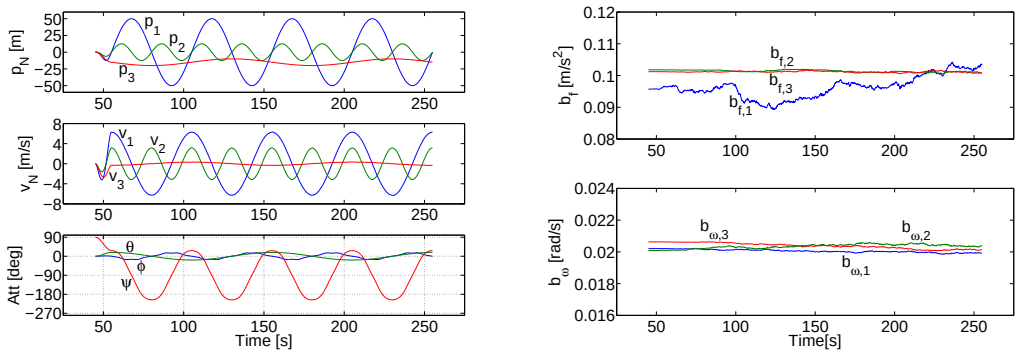

Figure 3.9: State Estimates: Simulated figure-8

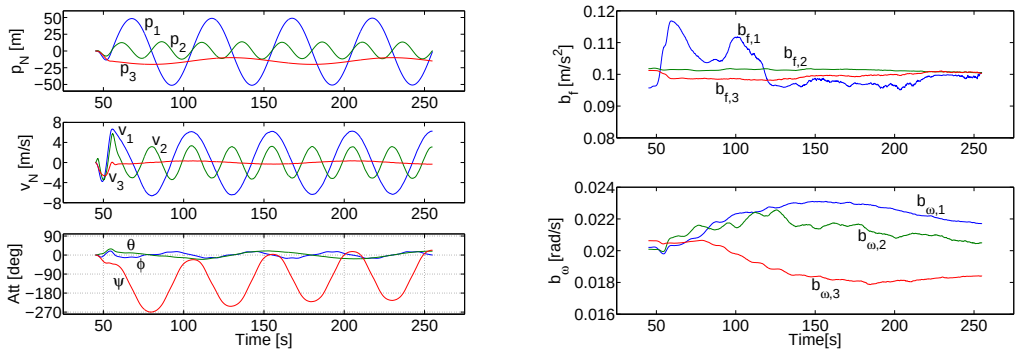

Figure 3.10: State Estimates: Simulated figure-8, GPS-only Aiding

The figure-8 trajectory estimation results are shown in Figure 3.9 for the mag-plus-GPS aided INS case and in Figure 3.10 for the GPS-only case. The clearest difference between the plots is the $\hat{\psi}$ estimate, which is initially 90° in error in the GPS-only case but slowly converges to the same trajectory as the mag-aided case due to the lateral accelerations providing observability of $\delta\gamma_3$ as discussed in Section 3.2.6.2. The magnetometer-aided case provides superior estimation performance. This is clearly seen in Figure 3.11 where the errors of all 15 estimated states from their reference trajectories are shown for both designs.

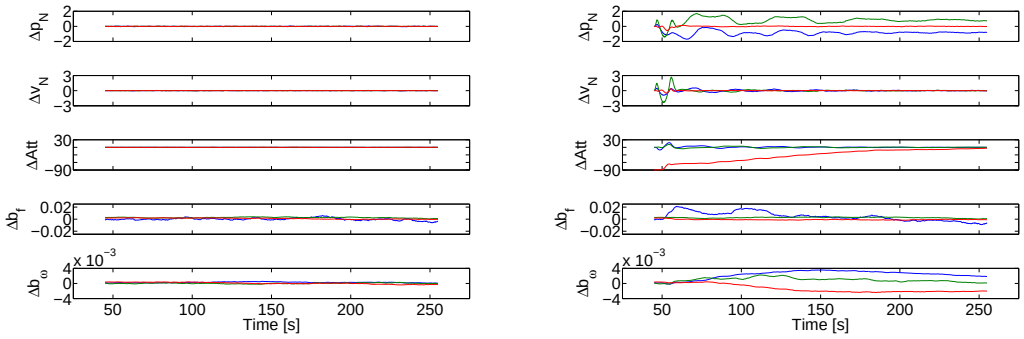

Figure 3.11: State Estimation Errors: Simulated figure-8, Mag-plus-GPS vs GPS-only Aiding

3.4.2 Experimental Ground Test Results

We now turn our attention to experimental results. In the first test, the engine-off helicopter was manually carried around the perimeter of a rectangular landing pad set up at the ERCHA flight field mentioned in Section 2.8. The vehicle was picked up at the southern-most corner of the pad, kept pointed in the direction of travel, executed a stop and 90° counter-clockwise turn at each corner, and was set down at the start point after two complete circuits. The sensor readings from the IMU, magnetometer and GPS were logged to disk and input into the Aided INS using the engine-off magnetometer calibration constants in Table 2.1 and the data in Table 3.1 as the EKF parameters.

3.4.2.1 Full versus Yaw-only Magnetometer Aiding

In our initial experiments, we used 3-axis magnetometer readings, compensated using the parameters in Table 2.1, as an aiding measurement via the linearized error system's output matrix H in (3.17). The resulting state estimates are plotted in Figure 3.12. The position estimates are qualitatively correct: a plot of p_2 vs p_1 traces out the rectangular shape of the landing pad, while p_3 correctly identifies the pickup and put-down events. Similarly, the estimated roll and pitch ϕ, θ are held close to zero, with oscillations created by the gait of the operator carrying the helicopter, while the estimated yaw ψ increases by $\pi/2$ at each corner. However, we see problems in the velocity estimates, which incorrectly estimate a non-zero velocity before and after the helicopter is carried.

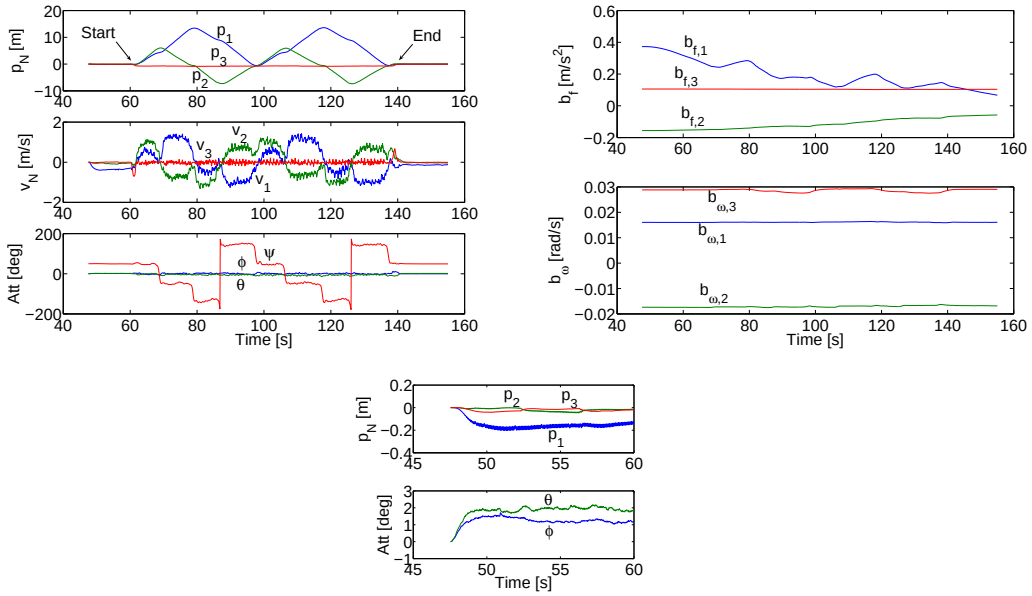

Figure 3.12: State Estimates: Ground Test, 3-Axis Mag Aiding

The incorrect velocity estimation problem was diagnosed by zooming in on the pre-pickup estimated states, $t \leq 60$ s, shown in the bottom plot of Figure 3.12. The position estimate p_1 is seen to be affected by the incorrect v_1 estimate, however this is mitigated by the EKF, evidenced by the 10 Hz "sawtooth" pattern created by the aiding measurements from the GPS receiver. This bounds the error in the position estimates. The estimated roll and pitch angles are updated from zero to $\phi \approx 1^\circ$, $\theta \approx 2^\circ$, which is incorrect since the helicopter remains level. Under the initial yaw angle $\psi \approx 50^\circ$, the helicopter is estimated to be tilting southwards, causing negative growth of v_1 due to the $\hat{R}$ term in nominal dynamics (3.10). As seen in Figure 3.12, the growth of v_1 is bounded due to GPS updates, however it creates jitter in the position estimates and affects the accelerometer bias estimates $b_{f,1}$, $b_{f,2}$, which will affect the accuracy of the integration of nominal dynamics (3.10). This chain of events is caused by the updates of roll and pitch during the pre-pickup stage, created by errors in magnetometer measurements remaining after compensation. As discussed in Section 3.2.6.2, the triaxial magnetometer output equation provides direct observability of roll and pitch via $\delta\gamma_1$ and $\delta\gamma_2$, respectively, which cause the

residual sensor errors to feed through into ϕ and θ.

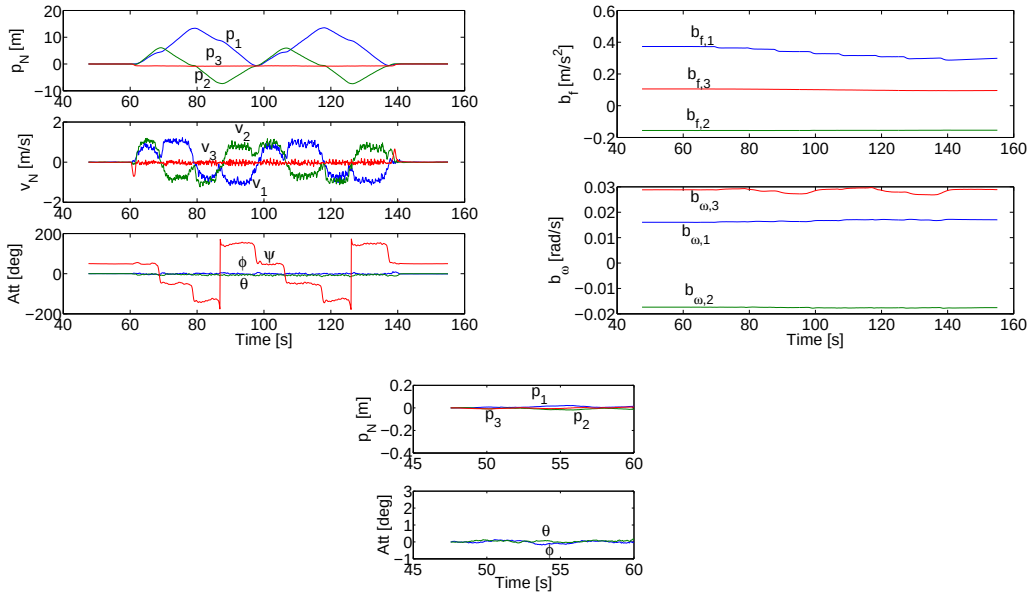

Figure 3.13: State Estimates: Ground Test, Yaw-Only Mag Aiding

The above discussion motivates the switch to a yaw-only magnetometer update by replacing the 3-axis δy_m in (3.17) with the yaw-only δy_m (3.18). The resulting state estimates are shown in Figure 3.13. We remark the estimated velocities in the pre- and post-carry phases are correct and that the accelerometer bias estimates change much less. The zoom-in view at the bottom of Figure 3.13 confirms the roll and pitch angles are not corrected, and exhibits smoother position estimates; the same conclusion was made in [50, p. 36]. We have found the opposite effect in flight testing, however, which will be covered in Section 3.4.3.

3.4.2.2 Comparison of Calibration Methods

We now compare the performance of calibration methods discussed in Section 2.9 in the yaw-only magnetometer updates version of the filter. Using the logged sensor data from the ground test, we compensate the magnetometer readings using in turn the full model (2.26) with engine-off parameters from Table 2.1, hard-iron compensation, uncompensated (raw) sensor data, and with magnetometer updates disabled. The overhead position and yaw angle estimates for each of the four cases are plotted in Figure 3.14. The dimensions of the landing pad and angle w.r.t. true north were measured directly and used to generate the reference trajectory. The reference yaw angle was generated by using the measured yaw angle of the first vertex and adding $\pi/2$ at every corner turn.

The full compensation case gives good navigation filter performance, with the estimated yaw and overhead positions tracking the reference trajectory fairly closely. A part of the tracking error is caused by imperfect alignment of the helicopter with the edges of the landing pad during the carry. The hard-iron compensation case shows good performance as well, although the yaw estimates differ from the full compensation case, visible in the start and end configurations. Since the same

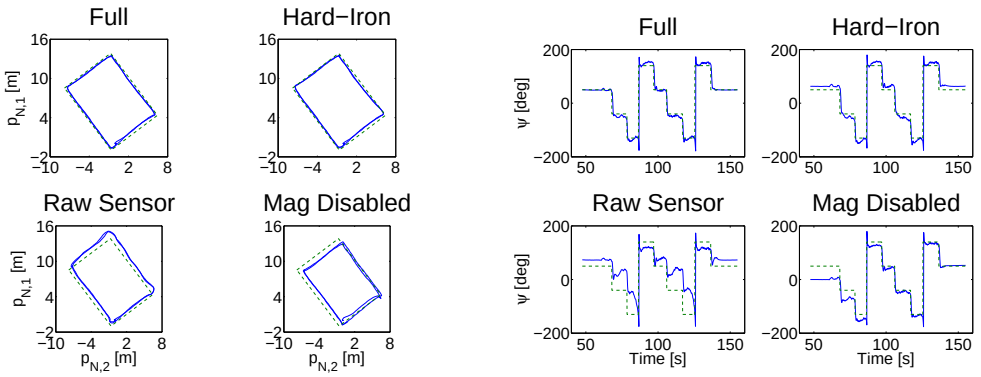

Figure 3.14: Magnetometer Calibration Comparison, Ground Test, Yaw-Only Mag Aiding: Overhead Position; Yaw Angle

sensor data is used throughout, this discrepancy is necessarily an effect of the compensation method. The raw sensor case produces significant error in the yaw estimates, which also affects the position estimates due to the antenna lever arm term in δy_p equation (3.17). This confirms the assertion from Section 2.9 that uncompensated magnetometer readings cannot be trusted. The magnetometer-disabled case demonstrates the observability of $\delta\gamma_3$ under lateral acceleration discussed in Section 3.2.6.2, with the estimated yaw initialized at $\psi_0 = 0$ gradually converging towards its reference value once the helicopter starts moving.

3.4.3 Experimental Flight Results

In the second experimental test, the helicopter takes off from the landing pad, hovers in mid-air with a fixed heading angle and then lands, all under control from an experienced pilot. The ANCL helicopter is equipped with a Futaba GY401 heading-hold gyro [58], standard equipment for R/C helicopters, which regulates the in-flight yaw angle using angular velocity as the sensed output and the tail rotor pitch as the control input c.f. Section 5.3.3.2. The remaining degrees of freedom are much less precise; the helicopter is an underactuated and relatively light vehicle being flown in unsteady wind conditions, making perfectly stationary hover extremely difficult. This fact will be reflected in the plots below. The estimated states were used to generate an animated helicopter model, which was compared against a recorded video of the hover flight, giving a qualitative estimate of the accuracy of the navigation states.

The running engine creates significant vibration in the airframe, in addition to disturbing the sensed magnetic field. The noise covariances of the accelerometer, rate gyro and magnetometer signals were re-computed using IMU sensor data collected while the engine was running, and are listed in Table 3.2. The engine-on parameters in Table 2.1 were used to compensate the magnetometer readings. Due to the fuel limit of the helicopter, we were unable to collect a sufficiently long data set to accurately analyze bias dynamics using Allan Variance (c.f. Section 6.2.1); instead, the engine-off β and σ_b parameters in Table 3.1 are re-used. Due to the uncertainty of the bias dynamics, the entries of the initial covariance matrix P_0^- corresponding to δb_f and δb_ω were experimentally tuned to 1×10^{-3} and 1×10^{-5}, respectively,

Table 3.2: Modified Noise Parameters – Engine On

σ_f $[\mathrm{m/s}^{3/2}]$	σ_ω $[\mathrm{rad}/\sqrt{\mathrm{s}}]$	σ_m $[\mathrm{G}/\sqrt{\mathrm{s}}]$
0.1748	0.0079	0.00414
0.2792	0.0124	0.00875
0.3847	0.0022	0.01042

and the remaining entries of P_0^- were tuned to 1×10^{-3} due to their dependence on bias estimation via dynamics (3.10).

3.4.3.1 Estimation Results in Flight

As in Section 3.4.2.1, we investigate the performance of 3-axis versus yaw-only magnetometer updates while keeping the other filter parameters constant. The plots for the 3-axis case are shown in Figure 3.15. Before take-off, the pilot increases throttle input to the engine, identified as the spool up in the plots, causing a counter-torque on the helicopter body which is in turn compensated by the GY401 unit. The dip in ψ represents a "tail wag" effect of the helicopter prior to take-off, observed in the flight video. This is likely caused by integrator wind-up of the GY401 gyro, which is known to use a PI control law on the sensed yaw angular velocity [58], although the exact details of the algorithm are proprietary. The helicopter takes off, and after a transient period visible in the plots, a stable hover is established with the yaw angle held nearly constant. The remaining states drift around as the pilot actively compensates for the turbulent atmospheric conditions, with roll and pitch motions of the helicopter causing motion in the lateral and longitudinal directions, respectively. After landing, the start of the engine spool down phase and resulting change in ψ is visible before sensor logging was terminated.

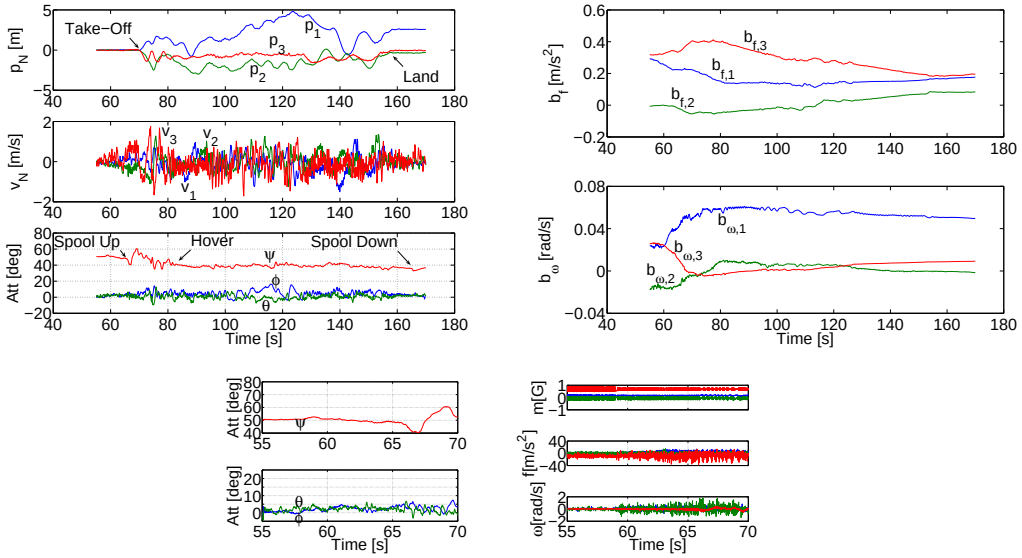

Figure 3.15: State Estimates: Flight Test, 3-Axis Mag Aiding

In addition to the hover phase, where the yaw angle is known to be nearly

constant, we focus on the pre-takeoff phase, with the helicopter's skids on the ground such that $\phi = \theta = 0$. A plot of the estimated attitude angles during this phase is shown at the bottom of Figure 3.15. The tail wag effect discussed above is clearly visible in the plot of ψ. The ϕ and θ estimates oscillate and exhibit a mean value of approximately 2°, indicating the attitude estimates are imperfect but bounded. The errors are caused by a combination of factors, including imperfect $\delta\gamma_1$ and $\delta\gamma_2$ updates from the magnetometer discussed in Section 3.4.2.1, significant noise levels in the rate gyro measurements feeding through into attitude estimate $\hat{R}$ via dynamics (3.10), and the unmodeled effect of engine speed changes on the IMU sensor outputs. This last effect is clearly visible in the sensor data plot in Figure 3.15 which exhibits a pronounced change in the measured signals during engine spool-up. The estimated bias states in Figure 3.15 show the navigation filter compensates, however we can reasonably expect noise and bias model uncertainty to create errors in estimated attitudes. In spite of these factors, using the estimated states to animate a helicopter model and comparing it against the flight video, we find the results are in agreement with reality. Design improvements including better vibration isolation of the avionics unit from the helicopter body, better modeling of the engine-on sensor dynamics, and upgrading to a higher-quality IMU can further improve the performance of the system.

Switching to yaw-only magnetometer updates gives results shown in Figure 3.16. Unlike Section 3.4.2, this method provides significantly worse performance, particularly in attitude estimates. The estimated ψ in hover exhibits drift, while the ϕ and θ estimates are visibly different from those in Figure 3.15. The error is particularly evident in the estimated attitudes prior to take-off, shown at the bottom of Figure 3.16, with estimated ψ incorrectly rising during counter-torque, and ϕ approaching 20° despite the helicopter being level. This issue is discussed below.

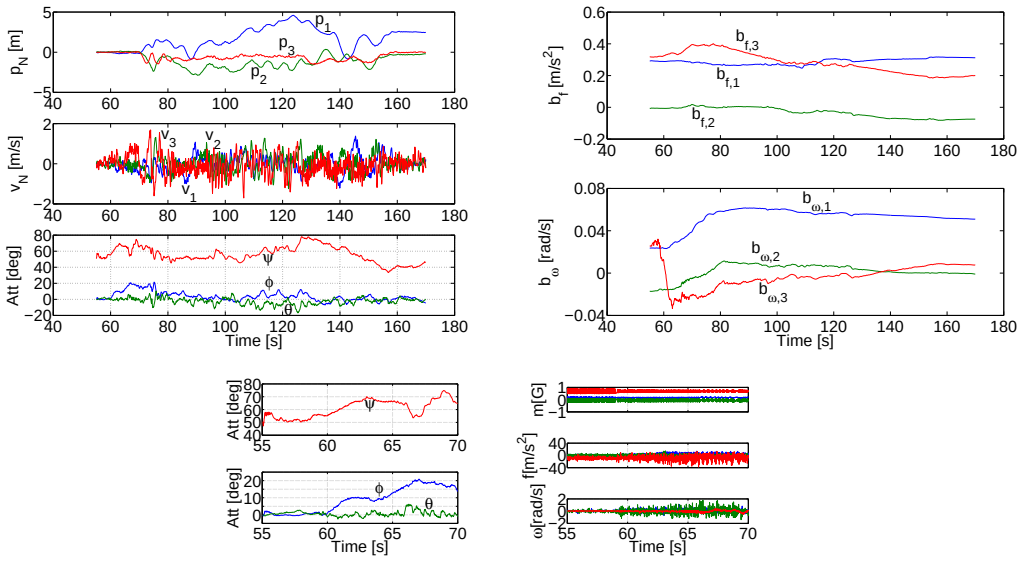

Figure 3.16: State Estimates: Flight Test, Yaw-Only Mag Aiding

For flight testing, the errors created by imperfect $\delta\gamma_1$ and $\delta\gamma_2$ updates from the magnetometer are negligible compared to the errors resulting from discarding

these updates. Of course the error system (3.17) is theoretically fully observable with yaw-only magnetometer updates, c.f. Section 3.2.6.2, however in practice the attitude updates depend on $\tilde{f} - \hat{b}_f$ which enters as a coefficient of $\delta\gamma$ in the dynamics matrix of (3.17), and whose accuracy will in turn be affected by noise and bias dynamics model uncertainty. During spool-up, the combination of increasing engine throttle and angular acceleration of the main rotor leads to a complicated time-varying vibration response of the helicopter, and in Figure 3.16 we can observe a clear correlation between the start of the spool-up period, the increase in $\tilde{f}$ and $\tilde{\omega}$ sensor noise levels and their respective estimated biases, and the growth of error in ϕ. The error in θ is bounded, likely due to the lever-arm effect of the tail-mounted GPS receiver providing aiding for $\delta\gamma_2$, not available for $\delta\gamma_1$ resp. ϕ since the GPS antenna is mounted in the vertical mid-plane of the helicopter. The error in ψ, visible in pre-takeoff as well as in flight, is caused by violating the assumption $\phi = \hat{\phi}$, $\theta = \hat{\theta}$, i.e. perfect roll and pitch estimates from the navigation filter, which was used in Section 3.2.6.2 to derive the yaw-only magnetometer aiding equation. The parameters of the EKF were re-tuned in an effort to reduce the error in θ, ϕ during spool-up. However, no significant improvement in performance was achieved. It is still feasible that these errors could be reduced by a combination of re-tuning the filter parameters, using better models of engine-on bias dynamics, and mechanical vibration isolation of the IMU unit. A practical solution would be to disable the EKF during spool-up given that its performance during flight is comparable to the 3-axis magnetometer update. We propose to simply discard the yaw-only aiding design for flight testing and rely on the 3-axis version with filter parameters from Section 3.4.3 for the final set of flight experiments.

3.4.3.2 Comparison of Calibration Methods

We now provide a flight performance comparison of magnetometer calibration methods using 3-axis updates. As in Section 3.4.2.2, we consider four cases: full compensation, hard-iron compensation, raw sensor readings and magnetometer disabled. The set of engine-on parameters listed at the beginning of Section 3.4.3 is used. The mag-disabled case is manually initialized at the correct ψ_0 initial yaw angle. The estimation results are plotted in Figure 3.17, and we plot only attitude estimates due to their strong dependence on magnetometer aiding.

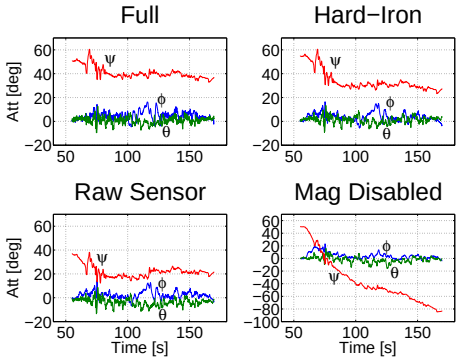

Figure 3.17: Magnetometer Calibration Comparison, Flight Test, 3-Axis Mag Aiding: Estimated Attitude

The full compensation case is the same plot as Figure 3.15, and serves as a reference for the other three. The hard-iron case produces the correct trend in the flight estimates, although the in-flight yaw angle is in error by approximately 10° from the fully compensated case. This may be caused by the significant warping of the magnetometer readings which cannot be compensated for by hard-iron calibration, seen by comparing the engine-on ε, ρ parameters in Table 2.1 with $\varepsilon = 1$, $\rho = 0$ for hard-iron compensation. The raw sensor case has higher errors in yaw angle; in addition, the roll and pitch estimates differ from the reference case, caused by $\delta\gamma_1$ and $\delta\gamma_2$ mag aiding using uncompensated sensor readings. The magnetometer-disabled case shows a complete divergence of ψ, which makes it clear a yaw sensor is critical in hover flights. As expected, the ϕ and θ estimates behave identically to the yaw-only mag aiding case in Figure 3.16.

Chapter 4

Invariant Observer Design for Aided Navigation

4.1 Overview

The Extended Kalman Filter covered in Chapter 3 relies on re-linearization of the system about its latest trajectory, an ad-hoc approach which works well in practice as seen in Sections 3.3 and 3.4, but which makes it impossible to analyze global stability and difficult to quantify the region of attraction of local stability, c.f. [124]. For this reason a direct nonlinear observer design for aided inertial navigation systems is of great interest to us.

This Chapter focuses on the nonlinear design method of invariant (symmetry-preserving) observers [27, 28]. This approach provides a systematic method to obtain a nonlinear observer structure which possesses the same symmetries (formally defined in Section 4.3) as the original model. Using this observer, an invariant version of the (nonlinear) estimation error dynamics exists which simplifies the process of choosing the observer gains. We will demonstrate that both the AHRS and Aided INS treated in Chapter 3 possess the necessary symmetries to make use of the invariant observer design method. An early version of invariant observer theory [25] treating an example of velocity-aided navigation was in fact the initial motivation for studying this method.

After considering a motivating example in Section 4.2, we formally define system symmetries in Section 4.3 and find them for the AHRS (Section 4.4) and Aided INS (Section 4.5). We cover invariant observer theory in Section 4.6 and derive invariant observers for AHRS and Aided INS in Section 4.7 using rotation matrices $R \in SO(3)$ (c.f. Section 2.1), a singularity-free one-to-one parametrization of the $SO(3)$ manifold, making the invariant estimation error dynamics amenable to global stability analysis [88, 38]. With the exception of [28] the invariant observer designs found in the literature are formulated in terms of unit quaternions $q \in \mathbb{H}, \|q\| = 1$ (c.f. Section 2.7) making a global analysis impossible due to their two-to-one covering of $SO(3)$ as noted in [27, Ex. 3].

While choosing the gains of an invariant observer is simplified, the process is non-systematic due to the requirement of stabilizing a nonlinear system using e.g. a Lyapunov analysis. We have found a stabilizing design for the AHRS case which guarantees almost-global stability, c.f. Section 4.8. However for Aided INS a nonlin-

ear stabilizing design has not (yet) been found. A natural approach to systematically achieving stabilization is to apply the EKF to the nonlinear invariant estimation dynamics, an approach originally proposed in [23] and termed the Invariant EKF, later applied to aided navigation examples in [29, 96]. We introduce the Invariant EKF method in Section 4.9 and adapt it to our AHRS and Aided INS examples in a "natural" way, removing the need to formulate the system using invariant noise terms as in [23], c.f. Section 4.9.1. We then provide a comprehensive performance comparison of the invariant observers in both simulation and experiment in Sections 4.10 and 4.11.

4.2 Motivating Example

Consider the AHRS from Section 3.2.3.1. For simplicity we replace the Gauss-Markov process model of the bias dynamics with the Wiener process model $\dot{b}_\omega = \nu_{b_\omega}$. The nominal version of (3.5), (3.6) is then written as

$$\begin{aligned} \dot{R} &= RS(\omega - b_\omega) \\ \dot{b}_\omega &= 0 \\ \begin{bmatrix} y_a \\ y_m \end{bmatrix} &= \begin{bmatrix} R^T a \\ R^T m \end{bmatrix}, \end{aligned} \tag{4.1}$$

where as before $R \in SO(3)$, the rotation matrix from body-fixed to ground-fixed frame, expresses the attitude of the system; S is the skew-symmetric matrix defined in (2.2); ω and b_ω are the measured angular velocity and its bias, respectively, the former available from the on-board rate gyro, the latter an unknown constant; y_a and y_m are readings from the on-board accelerometer and magnetometer; and $a = [0 \quad 0 \quad -9.81]^T$ m/s^2, $m = [B_H \quad 0 \quad B_V]^T$ G represent the ground-frame gravity and magnetic field vectors which are known and constant as discussed in Section 2.8.1. As in Section 3.2.2 we have assumed y_a directly measures gravity i.e. zero translational acceleration and that y_m has been compensated for magnetic field distortions. The task of the AHRS is to estimate attitude R and rate gyro bias b_ω from the signals ω, y_a and y_m — an observer design problem.

Defining $x = (R \quad b_\omega)$ and $u = \omega$, the nonlinear dynamics (4.1) are written

$$\dot{x} = f(x,u) = \begin{pmatrix} RS(\omega - b_\omega) \\ 0 \end{pmatrix}.$$

Consider the change of variables

$$x' = \begin{pmatrix} RR_0 \\ R_0^T(b_\omega + \omega_0) \end{pmatrix}, \qquad u' = R_0^T(\omega + \omega_0) \tag{4.2}$$

where $R_0 \in SO(3)$ and $\omega_0 \in \mathbb{R}^3$ are constants. We directly verify

$$\begin{aligned} f(x',u') &= \begin{pmatrix} RR_0 S\left(R_0^T(\omega + \omega_0) - R_0^T(b_\omega + \omega_0)\right) \\ 0 \end{pmatrix} \\ &= \begin{pmatrix} RR_0 S\left(R_0^T(\omega - b_\omega)\right) \\ 0 \end{pmatrix} = \begin{pmatrix} RS\left(\omega - b_\omega\right) R_0 \\ 0 \end{pmatrix} \end{aligned}$$

and

$$\frac{d}{dt}(x') = \frac{d}{dt}\begin{pmatrix} RR_0 \\ R_0^T(b_\omega + \omega_0)\end{pmatrix} = \begin{pmatrix} \dot{R}R_0 \\ R_0^T(\dot{b}_\omega)\end{pmatrix} = \begin{pmatrix} RS(\omega - b_\omega)R_0 \\ 0\end{pmatrix},$$

i.e. $\dot{x}' = f(x', u')$ under the above change of variables. Similarly, the output in (4.1)

$$y = h(x) = \begin{pmatrix} R^T a \\ R^T m\end{pmatrix}$$

becomes

$$h(x') = \begin{pmatrix} (RR_0)^T a \\ (RR_0)^T m\end{pmatrix} = \begin{pmatrix} R_0^T R^T a \\ R_0^T R^T m\end{pmatrix} = \begin{pmatrix} R_0^T y_a \\ R_0^T y_m\end{pmatrix}$$

which "induces" the change of variables $y' = h(x')$ under the definition

$$y' = \begin{pmatrix} R_0^T y_a \\ R_0^T y_m\end{pmatrix}.$$

System (4.1) can alternatively be written in terms of unit quaternions $q \in \mathbb{H}, \|q\| = 1$ using rotational kinematics (2.21):

$$\begin{aligned} \dot{q} &= \frac{1}{2} q * (\omega - b_\omega) \\ \dot{b}_\omega &= 0 \\ \begin{bmatrix} y_a \\ y_m\end{bmatrix} &= \begin{bmatrix} q^{-1} * a * q \\ q^{-1} * m * q\end{bmatrix}, \end{aligned} \tag{4.3}$$

where $*$ represents quaternion multiplication and q^{-1} is the quaternion inverse; the $\mathbb{R}^3$ vectors $\omega - b_\omega$, a and m are understood to be taken as pure quaternions $v = (0, \vec{v})$ when multiplying q. Denoting the dynamics of (4.3) as $\dot{x} = f(x, u)$ where $x = (q \quad b_\omega)$ and $u = \omega$, consider the change of variables

$$x' = \begin{pmatrix} q * q_0 \\ q_0^{-1} * (b_\omega + \omega_0) * q_0\end{pmatrix}, \qquad u' = q_0^{-1} * (\omega + \omega_0) * q_0$$

where $q_0 \in \mathbb{H}, \|q_0\| = 1$ and $\omega_0 \in \mathbb{R}^3$ are constants, we directly verify

$$\begin{aligned} f(x', u') &= \frac{1}{2} q * q_0 * \left(q_0^{-1} * (\omega + \omega_0) * q_0 - q_0^{-1} * (b_\omega + \omega_0) * q_0\right) \\ &= \frac{1}{2} q * q_0 * \left(q_0^{-1} * (\omega - b_\omega) * q_0\right) \\ &= \frac{1}{2} q * (\omega - b_\omega) * q_0 \end{aligned}$$

and

$$\frac{d}{dt}(x') = \frac{d}{dt}\begin{pmatrix} q * q_0 \\ q_0^{-1} * (b_\omega + \omega_0) * q_0\end{pmatrix} = \begin{pmatrix} \dot{q} * q_0 \\ q_0^{-1} * \dot{b}_\omega * q_0\end{pmatrix} = \frac{1}{2}\begin{pmatrix} q * (\omega - b_\omega) * q_0 \\ 0\end{pmatrix},$$

so once again $\dot{x}' = f(x', u')$ under the proposed change of variables. The output in (4.3)

$$y = h(x) = \begin{bmatrix} q^{-1} * a * q \\ q^{-1} * m * q\end{bmatrix}$$

transforms to

$$h(x') = \begin{bmatrix} (q * q_0)^{-1} * a * q * q_0 \\ (q * q_0)^{-1} * m * q * q_0 \end{bmatrix} = \begin{bmatrix} q_0^{-1} * q^{-1} * a * q * q_0 \\ q_0^{-1} * q^{-1} * m * q * q_0 \end{bmatrix} = \begin{bmatrix} q_0^{-1} * y_a * q_0 \\ q_0^{-1} * y_m * q_0 \end{bmatrix}$$

and induces the change of variables

$$y' = \begin{bmatrix} q_0^{-1} * y_a * q_0 \\ q_0^{-1} * y_m * q_0 \end{bmatrix}$$

such that $y' = h(x')$.

We have directly verified that the AHRS equations (4.1) or (4.3) are *invariant* with respect to certain changes of variables to x, u and y; we refer to these changes as the *symmetries* of the system. The mathematical details of the transformations are quite different for the two cases, however they represent the same symmetries: the transformed state x' corresponds to rotating the body-fixed axes by R_0 or q_0, and adding the constant ω_0 to the sensor bias. Provided that $u = \omega$, the sensed angular velocity in the body-fixed frame, is also transformed by R_0 or q_0 and ω_0, we intuitively expect the governing dynamics to remain the same, which is verified above. The same physical interpretation applies to the output y'. We have seen that invariance is independent of the attitude parametrization used, and the theory will be formulated using the framework of differential geometry to make this independence precise.

For a system with symmetries, there exists a constructive method to be covered in Section 4.6 to build a (nonlinear) observer which possess the same symmetries as the system. The resulting estimation error dynamics possess a reduced-order form which simplifies stability analysis and gain selection, c.f. Section 4.6.3. We work with the same two examples as in Chapter 3 using a Wiener process model for the bias dynamics: the AHRS (4.1), and the Magnetometer-plus-GPS-Aided INS introduced in Section 3.2.3.2 whose symmetries will be provided in Section 4.5.

4.3 System Symmetries

The coordinate-free formulation of the smooth (C^∞) nonlinear control system $\dot{x} = f(x, u)$ is the commutative diagram [107, Sec. 13.5]

$$\begin{array}{ccc} B & \xrightarrow{\quad F \quad} & TM \\ & {\scriptstyle \pi} \searrow \quad \swarrow {\scriptstyle \pi_M} & \\ & M & \end{array} \tag{4.4}$$

where B is the total space of a smooth fiber bundle over M equipped with the surjective map $\pi : B \to M$, TM is the tangent bundle of M with the natural projection map $\pi_M : TM \to M$, and $F : B \to TM$ is a bundle map, also known as a bundle morphism. By definition of a smooth fiber bundle, B, M and TM are smooth manifolds and π, F and π_M are smooth maps. The base manifold M represents the state space of the system, and for each $x \in M$, the fiber $\pi^{-1}(x) \subset B$ represents a state-dependent input space. In this way, diagram (4.4) can describe

the dynamics of systems under state feedback, and is used in e.g. [129, 63] to define system symmetry as the commutativity of

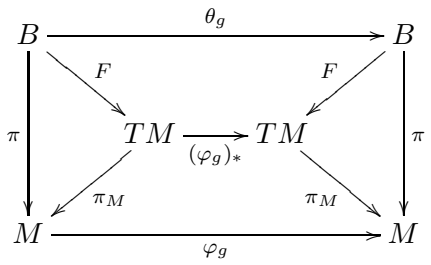

(4.5)

where θ_g, φ_g are group actions of a Lie group $G \ni g$ on the manifolds B and M, respectively, and $(\varphi_g)_*$ denotes the pushforward of the map φ_g.

We briefly elaborate on how (4.4) relates to the usual $\dot{x} = f(x, u)$ coordinate dynamics. A smooth fiber bundle consists of a smooth manifold B together with a surjective smooth map π onto the smooth manifold M. For each $x \in M$, there exists a neighbourhood U of x and a diffeomorphism $\Phi : \pi^{-1}(U) \to U \times V$, where V is a smooth manifold, such that the following diagram commutes:

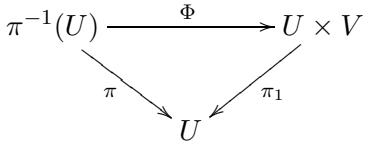

where π_1 is the projection on the first factor. The smooth manifolds B, M and V are known as the total space, base space and standard fiber, respectively, and Φ is the local trivialization of B over U. For any $x_0 \in M$ and $b_0 \in \pi^{-1}(x_0) \subset B$, we have the coordinate functions $(x_1, \ldots, x_n, u_1, \ldots, u_m) = (x, u)$ around $\Phi(b_0)$, such that (x, u) is a local coordinate expression for the total space B. Returning to (4.4), the standard coordinates for TM are written as $(x_1, \ldots, x_n, v_1, \ldots, v_n) = (x, v)$, where x are the same coordinate functions around $x_0 \in M$ as above, and v are the coordinate representations of the component functions of the vector field described by $F : B \to TM$, given by the right-hand side of $\dot{x} = f(x, u)$. In other words, the coordinate representation of $F : B \to TM$ is given by $F(x, u) = (x, f(x, u))$ which recovers the dynamics $\dot{x} = f(x, u)$. As seen in (4.1), (4.3), two coordinate representations of F may look very different from each other.

Because inputs to the observer are not directly functions of its state, we are able to take the total space B in (4.4) as the product manifold $B = M \times V$, making B a trivial fiber bundle over M, where the standard fiber V is the input manifold which is independent of the state manifold M. Remark this simplification does not apply to invariant controller design problems [120, 90, 47].

Using the trivial bundle $B = M \times V$, take $\varphi_g : G \times M \to M$ and $\psi_g : G \times V \to V$ to be smooth Lie group actions (c.f. Section 4.3.1) acting on the system's state and input manifolds, respectively, where G is the Lie group associated to the system known as its symmetry group. We define the system dynamics to be *G-invariant* [90, 27] if

$$(\varphi_g)_* F(x, u) = F(\varphi_g(x), \psi_g(u)) \qquad \forall g \in G,$$

a coordinate-free definition which is consistent with the general symmetry case shown in (4.5). In local coordinates, this is equivalent to

$$\frac{d}{dt}\left(\varphi_g(x)\right) = f(\varphi_g(x), \psi_g(u)) \qquad \forall g \in G,$$

or simply $\dot{x}' = f(x', u')$, the change of variables used in Section 4.2. Similarly, for the output map $H : M \times V \to Y$ where Y is the output manifold, the system output is *G-equivariant* if

$$\rho_g H(x, u) = H(\varphi_g(x), \psi_g(u)) \qquad \forall g \in G,$$

where $\rho_g : G \times Y \to Y$ is a Lie group action on the output manifold Y, which is "induced" by φ_g and ψ_g as seen in Section 4.2. The coordinate version of this is

$$\rho_g y = h(\varphi_g(x), \psi_g(u)) \qquad \forall g \in G,$$

or equivalently $y' = h(x', y')$. The set of Lie group actions $(\varphi_g, \psi_g, \rho_g)$ which verifies a system's G-invariance and G-equivariance are known as its symmetries.

The concept of invariance appears in standard differential geometry references in the following context (e.g. [83, p. 93]): let G be a Lie group, and define left translation $L_g : G \times G \to G$ as the map $L_g(h) = gh$. A vector field $X_g : G \to TG$ is said to be left-invariant if

$$(L_{g'})_* X_g = X_{g'g} \qquad \forall g, g' \in G.$$

The G-invariance of a system defined above can be viewed as a generalization of this definition, and we will see further links between the two in Section 4.6.2. On the other hand, equivariance is a standard concept and applies exactly as above, e.g. [83, p. 212].

4.3.1 Lie Group Actions

A Lie group action $\theta_g : G \times M \to M$ can be either left or right. A left group action θ_g verifies

$$\begin{aligned} \theta_{g_1} \circ \theta_{g_2}(p) &= \theta_{g_1 g_2}(p) \quad \forall g_1, g_2 \in G, \forall p \in M \\ \theta_e(p) &= p \qquad\qquad\quad \forall p \in M \end{aligned}$$

while a right group action θ_g verifies

$$\begin{aligned} \theta_{g_2} \circ \theta_{g_1}(p) &= \theta_{g_1 g_2}(p) \quad \forall g_1, g_2 \in G, \forall p \in M \\ \theta_e(p) &= p \qquad\qquad\quad \forall p \in M \end{aligned}$$

We deal exclusively with smooth Lie group actions, meaning $\theta_g : G \times M \to M$ is a smooth map for all $g \in G$ and $p \in M$. Under this assumption, the inverse $\theta_{g^{-1}}$ for either action type is smooth, making θ_g a diffeomorphism.

For our purposes, we will always work with φ_g, ψ_g, ρ_g as being *left* Lie group actions. We will demonstrate that this is done by correctly defining the group multiplication $g_1 g_2 \in G$. The reason for this is that two steps in the invariant observer design, finding the group invariants (Section 4.6.1) and building an invariant frame (Section 4.6.2) assume a left Lie group action is being used. Although the procedure could be modified to use the right group action case, there is nothing to be gained from doing so. In the sequel, any Lie group action is understood to be left unless explicitly stated otherwise.

4.4 AHRS symmetries

Return to the AHRS in Section 4.2, using version (4.1) written in terms of rotation matrices. Let $G = SO(3) \times \mathbb{R}^3$ be the Lie group acting on $x = (R \quad b_\omega)$, $u = \omega$, $y = (y_a \quad y_m)$, and let $g = (R_0 \quad \omega_0) \in G$. The changes of variables were actually the Lie group actions

$$\varphi_g \begin{pmatrix} R \\ b_\omega \end{pmatrix} = \begin{pmatrix} RR_0 \\ R_0^T(b_\omega + \omega_0) \end{pmatrix}, \quad \psi_g(\omega) = \left(R_0^T(\omega + \omega_0)\right), \quad \rho_g \begin{pmatrix} y_a \\ y_m \end{pmatrix} = \begin{pmatrix} R_0^T y_a \\ R_0^T y_m \end{pmatrix}.$$

Clearly, for $g = e = (I, 0) \in G$, $\varphi_e(x) = x$, $\psi_e(u) = u$ and $\rho_e(y) = y$. In order to meet the left group action assumption in Section 4.3.1, we require $\varphi_{g_1} \circ \varphi_{g_2} = \varphi_{g_1 g_2}$. Consider $g_1 = (R_0', \omega_0') \in G$ and $g_2 = (R_0'', \omega_0'') \in G$. We compute

$$\varphi_{g_1} \circ \varphi_{g_2} \begin{pmatrix} R \\ b_\omega \end{pmatrix} = \varphi_{g_1} \begin{pmatrix} RR_0'' \\ (R_0'')^T(b_\omega + \omega_0'') \end{pmatrix} = \begin{pmatrix} RR_0''R_0' \\ (R_0')^T(R_0'')^T(b_\omega + \omega_0' + \omega_0'') \end{pmatrix}$$

based on which we define group multiplication $g_1 g_2 = (R_0'' R_0', \omega_0' + \omega_0'') \in G$, under which

$$\varphi_{g_1 g_2} \begin{pmatrix} R \\ b_\omega \end{pmatrix} = \begin{pmatrix} RR_0''R_0' \\ (R_0''R_0')^T(b_\omega + \omega_0' + \omega_0'') \end{pmatrix}$$

proving φ_g is a left action. Continuing with the input action ψ_g, we verify

$$\psi_{g_1} \circ \psi_{g_2}(\omega) = \psi_{g_1}\left((R_0'')^T(\omega + \omega_0'')\right) = (R_0')^T(R_0'')^T(\omega + \omega_0' + \omega_0'')$$

and

$$\psi_{g_1 g_2}(\omega) = (R_0''R_0')^T(\omega + \omega_0' + \omega_0'') = (R_0')^T(R_0'')^T(\omega + \omega_0' + \omega_0'')$$

hence ψ_g is also a left action. Finally, for the output action

$$\rho_{g_1} \circ \rho_{g_2} \begin{pmatrix} y_a \\ y_m \end{pmatrix} = \rho_{g_1} \begin{pmatrix} (R_0'')^T y_a \\ (R_0'')^T y_m \end{pmatrix} = \begin{pmatrix} (R_0')^T(R_0'')^T y_a \\ (R_0')^T(R_0'')^T y_m \end{pmatrix}$$

and

$$\rho_{g_1 g_2} \begin{pmatrix} y_a \\ y_m \end{pmatrix} = \begin{pmatrix} (R_0''R_0')^T y_a \\ (R_0''R_0')^T y_m \end{pmatrix} = \begin{pmatrix} (R_0')^T(R_0'')^T y_a \\ (R_0')^T(R_0'')^T y_m \end{pmatrix}$$

hence ρ_g is a left action as well. Using the more "natural" multiplication definition $g_1 g_2 = (R_0' R_0'', \omega_0' + \omega_0'') \in G$ can be directly verified to yield *right* actions φ_g, ψ_g, ρ_g which are not suitable for our use. Note the Lie group actions φ_g, ψ_g, ρ_g can also be taken as acting on (4.3) by writing them in terms of unit quaternions, resulting in different calculation details but the same results as above, c.f. [91].

4.4.1 Ground frame symmetries

The AHRS symmetries considered so far physically represent the rotation of the body-fixed frame. A different set of symmetries can be obtained by considering rotations of the ground-fixed frame. Consider system (4.1) and take $x = (R \quad b_\omega)$, $u = (\omega \quad a \quad m)$, i.e. treat the ground-frame magnetic and gravity fields as additional inputs to the system. Let $G = SO(3) \times \mathbb{R}^3 \ni (Q_0, \omega_0) = g$ be the symmetry group

of the system where Q_0 represents a constant rotation of the ground-fixed frame. Defining the Lie group actions

$$\Phi_g \begin{pmatrix} R \\ b_\omega \end{pmatrix} = \begin{pmatrix} Q_0 R \\ \omega_0 + b_\omega \end{pmatrix}, \qquad \Psi_g \begin{pmatrix} \omega \\ a \\ m \end{pmatrix} = \begin{pmatrix} \omega_0 + \omega \\ Q_0 a \\ Q_0 m \end{pmatrix},$$

we verify

$$f\big(\Phi_g(x), \Psi_g(u)\big) = \begin{pmatrix} Q_0 R S(\omega_0 + \omega - \omega_0 - b_\omega) \\ 0 \end{pmatrix} = \begin{pmatrix} Q_0 R S(\omega - b_\omega) \\ 0 \end{pmatrix}$$
$$\frac{d}{dt}\big(\Phi_g(x)\big) = \frac{d}{dt} \begin{pmatrix} Q_0 R \\ \omega_0 + b_\omega \end{pmatrix} = \begin{pmatrix} Q_0 R S(\omega - b_\omega) \\ 0 \end{pmatrix},$$

and so the dynamics are invariant w.r.t. Φ_g, Ψ_g. These induce the output action Υ_g as

$$\Upsilon_g \begin{pmatrix} y_a \\ y_m \end{pmatrix} = h\big(\Phi_g(x), \Psi_g(u)\big) = \begin{pmatrix} (Q_0 R)^T Q_0 g \\ (Q_0 R)^T Q_0 m \end{pmatrix} = \begin{pmatrix} R^T g \\ R^T m \end{pmatrix} = \begin{pmatrix} y_a \\ y_m \end{pmatrix} \implies \Upsilon_g = \mathrm{Id}$$

Let $g_1 = (Q_0', \omega_0')$, $g_2 = (Q_0'', \omega_0'')$ and compute

$$\Phi_{g_1} \circ \Phi_{g_2} \begin{pmatrix} R \\ b_\omega \end{pmatrix} = \Phi_{g_1} \begin{pmatrix} Q_0'' R \\ \omega_0'' + b_\omega \end{pmatrix} = \begin{pmatrix} Q_0' Q_0'' R \\ \omega_0' + \omega_0'' + b_\omega \end{pmatrix}$$

from which we define $g_1 g_2 = (Q_0' Q_0'', \omega_0' + \omega_0'')$ to make Φ_g a left group action:

$$\Phi_{g_1 g_2} \begin{pmatrix} R \\ b_\omega \end{pmatrix} = \begin{pmatrix} Q_0' Q_0'' R \\ \omega_0' + \omega_0'' + b_\omega \end{pmatrix}$$

Remark that the $g_1 g_2$ definition happens to use a "natural" multiplication order $Q_0' Q_0''$. Considering Ψ_g, we have

$$\Psi_{g_1 g_2} \begin{pmatrix} \omega \\ a \\ m \end{pmatrix} = \begin{pmatrix} \omega_0' + \omega_0'' + \omega \\ Q_0' Q_0'' a \\ Q_0' Q_0'' m \end{pmatrix}$$

and

$$\Psi_{g_1} \circ \Psi_{g_2} \begin{pmatrix} \omega \\ a \\ m \end{pmatrix} = \Psi_{g_1} \begin{pmatrix} \omega_0'' + \omega \\ Q_0'' a \\ Q_0'' m \end{pmatrix} = \begin{pmatrix} \omega_0' + \omega_0'' + \omega \\ Q_0' Q_0'' a \\ Q_0' Q_0'' m \end{pmatrix},$$

verifying Ψ_g is a left action. Finally, $\Upsilon_g = \mathrm{Id}$ is a trivial Lie group action which is left (or right). We have thus shown that the AHRS example (4.1) is G-invariant and G-equivariant w.r.t. the Lie group actions Φ_g, Ψ_g, Υ_g, which physically represent rotations of the ground-fixed reference frame.

4.4.2 Combined symmetries

Since the body and ground-fixed frames can be rotated independently of each other, it's logical to construct a set of combined symmetries containing both Q_0 and R_0 terms. Consider (4.1) with $x = (R \quad b_\omega)$, $u = (\omega \quad a \quad m)$ and $y = (y_a \quad y_m)$ as

the state, input and output spaces, respectively, and define the symmetry group $G = SO(3) \times SO(3) \times \mathbb{R}^3 \ni (Q_0, R_0, \omega_0) = g$, where Q_0 and R_0 represent rotations of the ground and body frames, respectively. The candidate Lie group actions for this case are

$$\xi_g \begin{pmatrix} R \\ b_\omega \end{pmatrix} = \begin{pmatrix} Q_0 R R_0 \\ R_0^T(b_\omega + \omega_0) \end{pmatrix}, \qquad \upsilon_g \begin{pmatrix} \omega \\ a \\ m \end{pmatrix} = \begin{pmatrix} R_0^T(\omega + \omega_0) \\ Q_0 a \\ Q_0 m \end{pmatrix},$$

and we directly verify system invariance:

$$f\big(\xi_g(x), \upsilon_g(u)\big) = \begin{pmatrix} Q_0 R R_0 S\left[R_0^T(\omega + \omega_0) - R_0^T(b_\omega + \omega_0)\right] \\ 0 \end{pmatrix} = \begin{pmatrix} Q_0 R S(\omega - b_\omega) R_0 \\ 0 \end{pmatrix}$$
$$\frac{d}{dt}\big(\xi_g(x)\big) = \frac{d}{dt}\begin{pmatrix} Q_0 R R_0 \\ R_0^T(b_\omega + \omega_0) \end{pmatrix} = \begin{pmatrix} Q_0 R S(\omega - b_\omega) R_0 \\ 0 \end{pmatrix}$$

The induced output action ϱ_g is

$$h\big(\xi_g(x), \upsilon_g(u)\big) = \begin{pmatrix} (Q_0 R R_0)^T Q_0 a \\ (Q_0 R R_0)^T Q_0 m \end{pmatrix} = \begin{pmatrix} R_0^T y_a \\ R_0^T y_m \end{pmatrix} \Longrightarrow \varrho_g \begin{pmatrix} y_a \\ y_m \end{pmatrix} = \begin{pmatrix} R_0^T y_a \\ R_0^T y_m \end{pmatrix}$$

Take $g_1 = (Q_0', R_0', \omega_0') \in G$, $g_2 = (Q_0'', R_0'', \omega_0'') \in G$. We have

$$\xi_{g_1} \circ \xi_{g_2} \begin{pmatrix} R \\ b_\omega \end{pmatrix} = \xi_{g_1} \begin{pmatrix} Q_0'' R R_0'' \\ (R_0'')^T(b_\omega + \omega_0'') \end{pmatrix} = \begin{pmatrix} Q_0' Q_0'' R R_0'' R_0' \\ (R_0')^T (R_0'')^T (b_\omega + \omega_0' + \omega_0'') \end{pmatrix},$$

and thus define $g_1 g_2 = (Q_0' Q_0'', R_0'' R_0', \omega_0' + \omega_0'')$ such that $\xi_{g_1} \circ \xi_{g_2} = \xi_{g_1 g_2}$. The input action υ_g verifies

$$\upsilon_{g_1 g_2} \begin{pmatrix} \omega \\ a \\ m \end{pmatrix} = \begin{pmatrix} (R_0'' R_0')^T(\omega + \omega_0' + \omega_0'') \\ Q_0' Q_0'' a \\ Q_0' Q_0'' m \end{pmatrix}$$

and

$$\upsilon_{g_1} \circ \upsilon_{g_2} \begin{pmatrix} \omega \\ a \\ m \end{pmatrix} = \upsilon_{g_1} \begin{pmatrix} (R_0'')^T(\omega + \omega_0'') \\ Q_0'' a \\ Q_0'' m \end{pmatrix} = \begin{pmatrix} (R_0')^T (R_0'')^T (\omega + \omega_0' + \omega_0'') \\ Q_0' Q_0'' a \\ Q_0' Q_0'' m \end{pmatrix},$$

while the output action ϱ_g verifies

$$\varrho_{g_1 g_2} \begin{pmatrix} y_a \\ y_m \end{pmatrix} = \begin{pmatrix} (R_0'' R_0')^T y_a \\ (R_0'' R_0')^T y_m \end{pmatrix}$$

and

$$\varrho_{g_1} \circ \varrho_{g_2} \begin{pmatrix} y_a \\ y_m \end{pmatrix} = \varrho_{g_1} \begin{pmatrix} (R_0'')^T y_a \\ (R_0'')^T y_m \end{pmatrix} = \begin{pmatrix} (R_0')^T (R_0'')^T y_a \\ (R_0')^T (R_0'')^T y_m \end{pmatrix}$$

so ξ_g, υ_g, ϱ_g are left Lie group actions as required. Remark that by taking $Q_0 = I$ or $R_0 = I$ the actions reduce to $(\varphi_g, \psi_g, \rho_g)$ and $(\Phi_g, \Psi_g, \Upsilon_g)$, respectively.

4.5 Aided INS Symmetries

The second example to be treated is the Magnetometer-plus-GPS-Aided INS introduced in Section 3.2.3.2. As in Section 4.2 we take the b_f and b_ω bias dynamics models as a Wiener process $\dot{b} = \nu$. The nominal version of Aided INS dynamics (3.9) becomes

$$\begin{aligned} \dot{p} &= v \\ \dot{v} &= R(f - b_f) - a \\ \dot{R} &= RS(\omega - b_\omega) \\ \dot{b}_f &= 0 \\ \dot{b}_\omega &= 0 \end{aligned} \tag{4.6}$$

where p, v are the position and velocity of the vehicle relative to the navigation frame origin, $R \in SO(3)$ measures its attitude and b_f, b_ω are the constant, unknown biases of the specific force f and angular velocity ω signals measured by the on-board IMU. The outputs of the system are

$$\begin{aligned} y_p &= p \\ y_m &= R^T m \end{aligned} \tag{4.7}$$

where y_p and y_m are measured by a GPS receiver and magnetometer, respectively; for simplicity, we have taken the vehicle's position p as directly measurable, which assumes the rotation matrix R_E^N and navigation frame location r_E^o have been found (c.f. Section 2.4). The vector $m = [B_x \quad B_y \quad B_z]^T$ is the navigation frame magnetic field which is known and constant (c.f. Section 2.8) and y_m is assumed to have been compensated for magnetic field distortions as in Section 3.2.2.

The state of (4.6), $(p \quad v \quad R \quad b_f \quad b_\omega) \in \mathbb{R}^3 \times \mathbb{R}^3 \times SO(3) \times \mathbb{R}^3 \times \mathbb{R}^3 = M$ is a smooth manifold and we take the symmetry group $G = \mathbb{R}^3 \times SO(3) \times \mathbb{R}^3 \times \mathbb{R}^3 \ni (p_0 \quad R_0 \quad b_{f0} \quad b_{\omega 0})$. We propose the Lie group actions

$$\varphi_{(p_0,R_0,b_{f0},b_{\omega 0})} \begin{pmatrix} p \\ v \\ R \\ b_f \\ b_\omega \end{pmatrix} = \begin{pmatrix} p + p_0 \\ v \\ RR_0 \\ R_0^T(b_f + b_{f0}) \\ R_0^T(b_\omega + b_{\omega 0}) \end{pmatrix}, \quad \psi_{(p_0,R_0,b_{f0},b_{\omega 0})} \begin{pmatrix} f \\ \omega \end{pmatrix} = \begin{pmatrix} R_0^T(f + b_{f0}) \\ R_0^T(\omega + b_{\omega 0}) \end{pmatrix}$$

from which we directly verify

$$f\big(\varphi_g(x), \psi_g(u)\big) = \begin{pmatrix} v \\ RR_0\left[R_0^T(f + b_{f0}) - R_0^T(b_f + b_{f0})\right] - a \\ RR_0 S\left[R_0^T(\omega + b_{\omega 0}) - R_0^T(b_\omega + b_{\omega 0})\right] \\ 0 \\ 0 \end{pmatrix} = \begin{pmatrix} v \\ R(f - b_f) - a \\ RS(\omega - b_\omega)R_0 \\ 0 \\ 0 \end{pmatrix}$$

$$\frac{d}{dt}\varphi_g(x) = \frac{d}{dt}\begin{pmatrix} p + p_0 \\ v \\ RR_0 \\ R_0^T(b_f + b_{f0}) \\ R_0^T(b_\omega + b_{\omega 0}) \end{pmatrix} = \begin{pmatrix} \dot{p} \\ \dot{v} \\ \dot{R}R_0 \\ R_0^T\dot{b}_f \\ R_0^T\dot{b}_\omega \end{pmatrix} = \begin{pmatrix} v \\ R(f - b_f) - a \\ RS(\omega - b_\omega)R_0 \\ 0 \\ 0 \end{pmatrix}$$

and so the system is G-invariant. We then find ρ_g which makes the system G-equivariant:

$$h(\varphi_g(x), \psi_g(u)) = \begin{pmatrix} p + p_0 \\ (RR_0)^T m \end{pmatrix} \Longrightarrow \rho_{(p_0, R_0, b_{f0}, b_{\omega 0})} \begin{pmatrix} y_p \\ y_m \end{pmatrix} = \begin{pmatrix} y_p + p_0 \\ R_0^T y_m \end{pmatrix}$$

Next, we must define the group multiplication on G making φ_g, ψ_g, ρ_g left Lie group actions. Let $g_1 = (p_0' \quad R_0' \quad b_{f0}' \quad b_{\omega 0}')$ and $g_2 = (p_0'' \quad R_0'' \quad b_{f0}'' \quad b_{\omega 0}'')$. We have

$$\varphi_{g_1} \circ \varphi_{g_2} \begin{pmatrix} p \\ v \\ R \\ b_f \\ b_\omega \end{pmatrix} = \varphi_{g_1} \begin{pmatrix} p + p_0'' \\ v \\ RR_0'' \\ (R_0'')^T (b_f + b_{f0}'') \\ (R_0'')^T (b_\omega + b_{\omega 0}'') \end{pmatrix} = \begin{pmatrix} p + p_0' + p_0'' \\ v \\ RR_0'' R_0' \\ (R_0')^T (R_0'')^T (b_f + b_{f0}' + b_{f0}'') \\ (R_0')^T (R_0'')^T (b_\omega + b_{\omega 0}' + b_{\omega 0}'') \end{pmatrix}$$

and so define $g_1 g_2 = (p_0' + p_0'' \quad R_0'' R_0' \quad b_{f0}' + b_{f0}'' \quad b_{\omega 0}' + b_{\omega 0}'')$ such that

$$\varphi_{g_1 g_2} \begin{pmatrix} p \\ v \\ R \\ b_f \\ b_\omega \end{pmatrix} = \begin{pmatrix} p + p_0' + p_0'' \\ v \\ RR_0'' R_0' \\ (R_0'' R_0')^T (b_f + b_{f0}' + b_{f0}'') \\ (R_0'' R_0')^T (b_\omega + b_{\omega 0}' + b_{\omega 0}'') \end{pmatrix} = \varphi_{g_1} \circ \varphi_{g_2} \begin{pmatrix} p \\ v \\ R \\ b_f \\ b_\omega \end{pmatrix}.$$

The input action ψ is left:

$$\psi_{g_1} \circ \psi_{g_2} \begin{pmatrix} f \\ \omega \end{pmatrix} = \psi_{g_1} \begin{pmatrix} (R_0'')^T (f + b_{f0}'') \\ (R_0'')^T (\omega + b_{\omega 0}'') \end{pmatrix} = \begin{pmatrix} (R_0')^T (R_0'')^T (f + b_{f0}' + b_{f0}'') \\ (R_0')^T (R_0'')^T (\omega + b_{\omega 0}' + b_{\omega 0}'') \end{pmatrix}$$

and

$$\psi_{g_1 g_2} \begin{pmatrix} f \\ \omega \end{pmatrix} = \begin{pmatrix} (R_0'' R_0')^T (f + b_{f0}' + b_{f0}'') \\ (R_0'' R_0')^T (\omega + b_{\omega 0}' + b_{\omega 0}'') \end{pmatrix}$$

The output action ρ is also left:

$$\rho_{g_1} \circ \rho_{g_2} \begin{pmatrix} y_p \\ y_m \end{pmatrix} = \rho_{g_1} \begin{pmatrix} y_p + p_0'' \\ (R_0'')^T y_m \end{pmatrix} = \begin{pmatrix} y_p + p_0' + p_0'' \\ (R_0')^T (R_0'')^T y_m \end{pmatrix}$$

and

$$\rho_{g_1 g_2} \begin{pmatrix} y_p \\ y_m \end{pmatrix} = \begin{pmatrix} y_p + p_0' + p_0'' \\ (R_0'' R_0')^T y_m \end{pmatrix}$$

Instead of rotating the body-fixed frame as above, we can rotate the ground-fixed frame by Q_0, such that the symmetry group $G = \mathbb{R}^3 \times SO(3) \times \mathbb{R}^3 \times \mathbb{R}^3$ with $G \ni (p_0, Q_0, b_{f0}, b_{\omega 0}) = g$ acts on the state and input manifolds respectively by Φ_g and Ψ_g:

$$\Phi_{(p_0, Q_0, b_{f0}, b_{\omega 0})} \begin{pmatrix} p \\ v \\ R \\ b_f \\ b_\omega \end{pmatrix} = \begin{pmatrix} Q_0 (p_0 + p) \\ Q_0 v \\ Q_0 R \\ b_{f0} + b_f \\ b_{\omega 0} + b_\omega \end{pmatrix}, \quad \Psi_{(p_0, Q_0, b_{f0}, b_{\omega 0})} \begin{pmatrix} f \\ \omega \\ a \\ m \end{pmatrix} = \begin{pmatrix} b_{f0} + f \\ b_{\omega 0} + \omega \\ Q_0 a \\ Q_0 m \end{pmatrix},$$

We directly verify the G-invariance of (4.6) to Φ_g and Ψ_g:

$$f\big(\Phi_g(x),\Psi_g(u)\big)=\begin{pmatrix} Q_0 v \\ Q_0R\left(f+b_{f0}-b_f-b_{f0}\right)-Q_0a \\ Q_0RS\left(\omega+b_{\omega0}-b_\omega-b_{\omega0}\right) \\ 0 \\ 0 \end{pmatrix}=\begin{pmatrix} Q_0 v \\ Q_0R\left(f-b_f\right)-Q_0a \\ Q_0RS\left(\omega-b_\omega\right) \\ 0 \\ 0 \end{pmatrix}$$

$$\frac{d}{dt}\Phi_g(x)=\frac{d}{dt}\begin{pmatrix} Q_0(p_0+p) \\ Q_0 v \\ Q_0R \\ b_{f0}+b_f \\ b_{\omega0}+b_\omega \end{pmatrix}=\begin{pmatrix} Q_0 v \\ Q_0\left[R(f-b_f)-a\right] \\ Q_0RS(\omega-b_\omega) \\ 0 \\ 0 \end{pmatrix},$$

and find the induced output action Υ_g:

$$h\big(\Phi_g(x),\Psi_g(u)\big)=\begin{pmatrix} Q_0(p_0+p) \\ (Q_0R)^TQ_0m \end{pmatrix}\implies \Upsilon_g\begin{pmatrix} y_p \\ y_m \end{pmatrix}=\begin{pmatrix} Q_0(p_0+y_p) \\ y_m \end{pmatrix}.$$

Take $g_1=(p_0' \quad Q_0' \quad b_{f0}' \quad b_{\omega0}')$ and $g_2=(p_0'' \quad Q_0'' \quad b_{f0}'' \quad b_{\omega0}'')$. We have

$$\Phi_{g_1}\circ\Phi_{g_2}\begin{pmatrix} p \\ v \\ R \\ b_f \\ b_\omega \end{pmatrix}=\Phi_{g_1}\begin{pmatrix} Q_0''(p+p_0'') \\ Q_0'' v \\ Q_0''R \\ b_f+b_{f0}'' \\ b_\omega+b_{\omega0}'' \end{pmatrix}=\begin{pmatrix} Q_0'Q_0''(p+p_0'+p_0'') \\ Q_0'Q_0'' v \\ Q_0'Q_0''R \\ b_f+b_{f0}'+b_{f0}'' \\ b_\omega+b_{\omega0}'+b_{\omega0}'' \end{pmatrix}$$

and defining $g_1g_2=(p_0'+p_0'',Q_0'Q_0'',b_{f0}'+b_{f0}'',b_{\omega0}'+b_{\omega0}'')$ verifies $\Phi_{g_1}\circ\Phi_{g_2}=\Phi_{g_1g_2}$:

$$\Phi_{g_1g_2}\begin{pmatrix} p \\ v \\ R \\ b_f \\ b_\omega \end{pmatrix}=\begin{pmatrix} Q_0'Q_0''(p+p_0'+p_0'') \\ Q_0'Q_0'' v \\ Q_0'Q_0''R \\ b_f+b_{f0}'+b_{f0}'' \\ b_\omega+b_{\omega0}'+b_{\omega0}'' \end{pmatrix}$$

We also verify $\Psi_{g_1}\circ\Psi_{g_2}=\Psi_{g_1g_2}$ for the input action:

$$\Psi_{g_1}\circ\Psi_{g_2}\begin{pmatrix} f \\ \omega \\ a \\ m \end{pmatrix}=\Psi_{g_1}\begin{pmatrix} f+b_{f0}'' \\ \omega+b_{\omega0}'' \\ Q_0''a \\ Q_0''m \end{pmatrix}=\begin{pmatrix} f+b_{f0}'+b_{f0}'' \\ \omega+b_{\omega0}'+b_{\omega0}'' \\ Q_0'Q_0''a \\ Q_0'Q_0''m \end{pmatrix}=\Psi_{g_1g_2}\begin{pmatrix} f \\ \omega \\ a \\ m \end{pmatrix}$$

and $\Upsilon_{g_1}\circ\Upsilon_{g_2}=\Upsilon_{g_1g_2}$ for the output action:

$$\Upsilon_{g_1}\circ\Upsilon_{g_2}\begin{pmatrix} y_p \\ y_m \end{pmatrix}=\Upsilon_{g_1}\begin{pmatrix} Q_0''(y_p+p_0'') \\ y_m \end{pmatrix}=\begin{pmatrix} Q_0'Q_0''(y_p+p_0'+p_0'') \\ y_m \end{pmatrix}=\Upsilon_{g_1g_2}\begin{pmatrix} y_p \\ y_m \end{pmatrix}$$

This confirms Φ_g, Ψ_g and Υ_g are left group actions.

As in Section 4.4.2, we consider the combined case of rotating both the body and the ground frames. The symmetry group is $G=\mathbb{R}^3\times SO(3)\times SO(3)\times\mathbb{R}^3\times\mathbb{R}^3\ni$

$(p_0 \quad Q_0 \quad R_0 \quad b_{f0} \quad b_{\omega 0}) = g$ and the state and input actions are

$$\xi_g \begin{pmatrix} p \\ v \\ R \\ b_f \\ b_\omega \end{pmatrix} = \begin{pmatrix} Q_0(p+p_0) \\ Q_0 v \\ Q_0 R R_0 \\ R_0^T(b_f + b_{f0}) \\ R_0^T(b_\omega + b_{\omega 0}) \end{pmatrix}, \qquad \upsilon_g \begin{pmatrix} f \\ \omega \\ a \\ m \end{pmatrix} = \begin{pmatrix} R_0^T(f + b_{f0}) \\ R_0^T(\omega + b_{\omega 0}) \\ Q_0 a \\ Q_0 m \end{pmatrix}$$

which verify $f\big(\xi_g(x), \upsilon_g(u)\big) = d/dt(\xi_g(x))$,

$$f\big(\xi_g(x), \upsilon_g(u)\big) = \begin{pmatrix} Q_0 v \\ Q_0 R R_0 \left[R_0^T(f + b_{f0}) - R_0^T(b_f + b_{f0})\right] - Q_0 a \\ Q_0 R R_0 S \left[R_0^T(\omega + b_{\omega 0}) - R_0^T(b_\omega + b_{\omega 0})\right] \\ 0 \\ 0 \end{pmatrix}$$

$$\frac{d}{dt}\xi_g(x) = \frac{d}{dt}\begin{pmatrix} Q_0(p+p_0) \\ Q_0 v \\ Q_0 R R_0 \\ R_0^T(b_f + b_{f0}) \\ R_0^T(b_\omega + b_{\omega 0}) \end{pmatrix} = \begin{pmatrix} Q_0 v \\ Q_0\left[R(f - b_f) - a\right] \\ Q_0 R S(\omega - b_\omega) R_0 \\ 0 \\ 0 \end{pmatrix}$$

and induce the output action ϱ_g

$$h\big(\xi_g(x), \upsilon_g(u)\big) = \begin{pmatrix} Q_0(p+p_0) \\ (Q_0 R R_0)^T Q_0 m \end{pmatrix} \implies \varrho_g \begin{pmatrix} y_p \\ y_m \end{pmatrix} = \begin{pmatrix} Q_0(y_p + p_0) \\ R_0^T y_m \end{pmatrix}.$$

Take $g_1 = (p_0' \quad Q_0' \quad R_0' \quad b_{f0}' \quad b_{\omega 0}')$ and $g_2 = (p_0'' \quad Q_0'' \quad R_0'' \quad b_{f0}'' \quad b_{\omega 0}'')$. We have

$$\xi_{g_1} \circ \xi_{g_2} \begin{pmatrix} p \\ v \\ R \\ b_f \\ b_\omega \end{pmatrix} = \xi_{g_1} \begin{pmatrix} Q_0''(p + p_0'') \\ Q_0'' v \\ Q_0'' R R_0'' \\ (R_0'')^T(b_f + b_{f0}'') \\ (R_0'')^T(b_\omega + b_{\omega 0}'') \end{pmatrix} = \begin{pmatrix} Q_0' Q_0''(p + p_0' + p_0'') \\ Q_0' Q_0'' v \\ Q_0' Q_0'' R R_0'' R_0' \\ (R_0')^T(R_0'')^T(b_f + b_{f0}' + b_{f0}'') \\ (R_0')^T(R_0'')^T(b_\omega + b_{\omega 0}' + b_{\omega 0}'') \end{pmatrix}$$

and so we define group multiplication as $g_1 g_2 = (p_0' + p_0'',\, Q_0' Q_0'',\, R_0'' R_0',\, b_{f0}' + b_{f0}'',\, b_{\omega 0}' + b_{\omega 0}'')$ such that $\xi_{g_1} \circ \xi_{g_2} = \xi_{g_1 g_2}$:

$$\xi_{g_1 g_2} \begin{pmatrix} p \\ v \\ R \\ b_f \\ b_\omega \end{pmatrix} = \begin{pmatrix} Q_0' Q_0''(p + p_0' + p_0'') \\ Q_0' Q_0'' v \\ Q_0' Q_0'' R R_0'' R_0' \\ (R_0'' R_0')^T(b_f + b_{f0}' + b_{f0}'') \\ (R_0'' R_0')^T(b_\omega + b_{\omega 0}' + b_{\omega 0}'') \end{pmatrix}$$

We verify $\upsilon_{g_1} \circ \upsilon_{g_2} = \upsilon_{g_1 g_2}$

$$\upsilon_{g_1} \circ \upsilon_{g_2} \begin{pmatrix} f \\ \omega \\ a \\ m \end{pmatrix} = \upsilon_{g_1} \begin{pmatrix} (R_0'')^T(f + b_{f0}'') \\ (R_0'')^T(\omega + b_{\omega 0}'') \\ Q_0'' a \\ Q_0'' m \end{pmatrix} = \begin{pmatrix} (R_0')^T(R_0'')^T(f + b_{f0}' + b_{f0}'') \\ (R_0')^T(R_0'')^T(\omega + b_{\omega 0}' + b_{\omega 0}'') \\ Q_0' Q_0'' a \\ Q_0' Q_0'' m \end{pmatrix}$$

$$\upsilon_{g_1 g_2} \begin{pmatrix} f \\ \omega \\ a \\ m \end{pmatrix} = \begin{pmatrix} (R_0'' R_0')^T(f + b_{f0}' + b_{f0}'') \\ (R_0'' R_0')^T(\omega + b_{\omega 0}' + b_{\omega 0}'') \\ Q_0' Q_0'' a \\ Q_0' Q_0'' m \end{pmatrix}$$

and $\varrho_{g_1} \circ \varrho_{g_2} = \varrho_{g_1 g_2}$

$$\varrho_{g_1} \circ \varrho_{g_2} \begin{pmatrix} y_p \\ y_m \end{pmatrix} = \varrho_{g_1} \begin{pmatrix} Q_0''(y_p + p_0'') \\ (R_0'')^T y_m \end{pmatrix} = \begin{pmatrix} Q_0' Q_0''(y_p + p_0' + p_0'') \\ (R_0')^T (R_0'')^T y_m \end{pmatrix}$$

$$\varrho_{g_1 g_2} \begin{pmatrix} y_p \\ y_m \end{pmatrix} = \begin{pmatrix} Q_0' Q_0''(y_p + p_0' + p_0'') \\ (R_0'' R_0')^T y_m \end{pmatrix}$$

so ξ_g, υ_g, ϱ_g are left actions.

4.6 Invariant Observer Theory

4.6.1 Invariants and Moving Frame

Using notation from Section 4.4 define the Lie group action $\phi_g = \varphi_g \times \psi_g \times \rho_g$ of the symmetry group G acting on the smooth manifold $M = X \times V \times Y$ with $\dim(M) = m$, $\dim(G) = r$ and $r \leq m$. A real-valued function $J : M \to \mathbb{R}$ is defined to be an *invariant of* G [110, p. 77] if

$$J(\phi_g(p)) = J(p) \qquad \forall g \in G, \quad \forall p \in M$$

We will cover an algorithm for obtaining the complete set of invariants of G which are used in Sections 4.6.2 and 4.6.3 below. This procedure uses a *moving frame* which is obtained using the constructive method in [52, 112].

We first review some definitions associated with Lie group actions:

- The *orbit* $\mathcal{O}_p$ of $p \in M$ is the set $\{\phi_g(p) : g \in G\}$
- G acts *semi-regularly* on M if the orbits $\mathcal{O}_p$ all have the same dimension
- G acts *regularly* on M if it acts *semi-regularly* and in addition, each $p \in M$ has arbitrarily small neighborhoods $U \subset M$ whose intersection with each orbit in M is a connected subset of the orbit
- The action ϕ_g is *transitive* if for every $p \in M$, $\mathcal{O}_p = M$
- The *isotropy group* G_p of $p \in M$ is the set $\{g \in G : \phi_g(p) = p\}$
- An action ϕ_g is *free* if for every $p \in M$, $G_p = \{e\}$
- An action ϕ_g is *locally free* if for every $p \in M$, G_p is a discrete subgroup of G

We deal exclusively with regular Lie group actions; the additional conditions over semi-regular actions are easily satisfied except for pathological cases e.g. [112, p. 158], and in exchange much stronger results can be proven specifically the following adapted from [111, Thm. 2.23]:

Theorem 1 *Let G be a Lie group acting regularly on an m-dimensional manifold M with s-dimensional orbits. Then, around every point $p_0 \in M$, there exists a "flat" chart U with local coordinates $(y, z) = (y_1, \ldots, y_s, z_1, \ldots, z_{m-s})$, such that any orbit $\mathcal{O}_p$ intersects U either in the empty set, or in a single s-slice $S \subset U$ defined in coordinates as $S = \{(y, z) | (z_1 = c_1, \ldots, z_{m-s} = c_{m-s}\}$ for some $c = (c_1, \ldots, c_{m-s}) \in \mathbb{R}^{m-s}$.*

Remark: This says that the "flat" coordinate functions $z_i : U \to \mathbb{R}$ are constant along any orbit passing through $U \subset M$. The actual set of values c is different for every orbit, and can be used to (locally) distinguish between them. Because each orbit is the set of points $\{\phi_g(p) : g \in G\}$, the flat coordinate functions define a set of $(m-s)$ invariants of G, $(J_1(x), \ldots, J_{m-s}(x)) = (z_1, \ldots, z_{m-s})$, which exist in a neighborhood U around any point $p_0 \in M$. Any other invariant $J(x)$ can be uniquely expressed as an analytic function of this set [112, Thm. 8.17]: $J(x) = \mathcal{H}(J_1(x), \ldots, J_{m-s}(x))$. Note that although the theorem guarantees existence of the flat charts, it says nothing about how to actually find their local coordinates; this is done using the constructive method of *normalization* discussed below.

Theorem 1 is a consequence of the Frobenius Theorem, used to prove that a Lie group acting smoothly with constant rank forms a *foliation* of the manifold M, where the *leaves* are the individual orbits. Semi-regular actions (i.e. acting with constant rank) are sufficient to prove existence of the foliation and its associated flat charts, however the intersection may occur in a countable union of s-slices, which is why we demand the action to be regular. A proof of the Frobenius Theorem and the existence of foliation is given in [83, Chap. 19].

Theorem 1 can be visualized by considering a simple example. Consider the Lie group of planar rotations $SO(2)$ acting on $\mathbb{R}^2$, a smooth manifold. We know $SO(2)$ acts regularly on $\mathbb{R}^2 \backslash \{0\}$ [112, p. 162]. The orbits of $SO(2)$ on $\mathbb{R}^2$ are circles centered at the origin shown schematically in Figure 4.1, and the dimension of each orbit is 1. Consider the chart of polar coordinates on $\mathbb{R}^2$ with $U = \mathbb{R}^2 \backslash \{0\}$ and coordinate functions

$$\theta(x_1, x_2) = \operatorname{atan2}(x_2, x_1)$$
$$r(x_1, x_2) = \sqrt{x_1^2 + x_2^2}$$

In this particular chart, any orbit of $SO(2)$ intersects U either in the empty set for the circle with radius zero, or in a single 1-slice defined by $\{(\theta, r) | r = R\}$, i.e. a circle centered at the origin where the value of R distinguishes individual orbits. The real-valued coordinate function $r(x_1, x_2) = \sqrt{x_1^2 + x_2^2} = \|x\|$ is an *invariant* of $SO(2)$ because planar rotations do not alter lengths. The existence of this flat chart is guaranteed by Theorem 1, although finding its form is not constructive; remark that a different chart $(U = \mathbb{R}^2 \backslash \{0\}, \mathrm{Id}_{\mathbb{R}^2})$ on $\mathbb{R}^2$ with coordinate functions x_1 and x_2 is clearly *not* flat because x_2 is not an invariant of $SO(2)$.

Each orbit of a regular action forms an s-dimensional embedded submanifold of M [83, p. 174] due to the existence of s-slices guaranteed by Theorem 1. We can thus define a *cross-section* to the orbits as an $(m-s)$-dimensional embedded submanifold K which *intersects transversely* [83, p. 203] with each orbit at most once. Specifically, this means that for $k = \mathcal{O}_p \cap K$, the tangent spaces $T_k\mathcal{O}_p$ and $T_k K$ (with dimensions s and $m-s$, respectively) span $T_k M$, and that $k \in M$ contains at most one element.

For our simple example of $SO(2)$ acting on $\mathbb{R}^2$, the cross-section is a $(2-1) = 1$ dimensional line segment from the origin illustrated in Figure 4.1, which transversely intersects with each orbit at most once because $\mathcal{O}_p \cap K = k$ is a single point and the one-dimensional tangent spaces $T_k\mathcal{O}_p$ and $T_k K$ together span $T_k\mathbb{R}^2$.

We will prove the existence of a cross-section through any point $p \in M$. Let V denote a chart around $p \in M$ with coordinates $(x_1, \ldots, x_m)$ — note V is an *arbitrary* chart, i.e. not necessarily the flat chart of Theorem 1. Fix the first s coordinates,

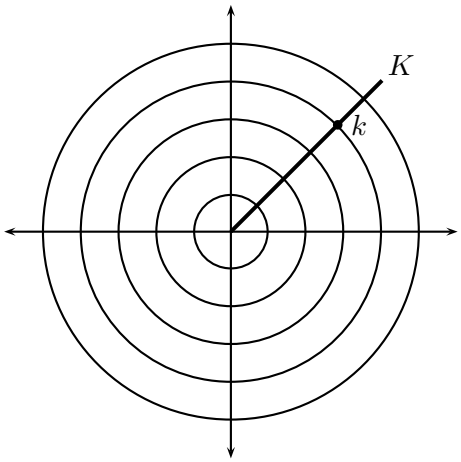

Figure 4.1: Orbits of $SO(2)$ on $\mathbb{R}^2$ and cross-section K

such that $K = \{x_1 = c_1, \ldots, x_s = c_s\}$ is an $(m-s)$ slice in V, which makes K into an $(m-s)$ dimensional embedded submanifold as desired. We now need to prove K intersects each orbit at most once. Assume the set of invariants $(J_1(x), \ldots, J_{m-s}(x))$ is available and has been expressed in the current (not necessarily flat) coordinates $(x_1, \ldots, x_m)$. Recall their existence is guaranteed by Theorem 1, and we will cover their actual construction shortly. The Implicit Function Theorem [83, p. 164] guarantees that if the matrix

$$\frac{\partial(J_1, \ldots, J_{m-s})}{\partial(x_{s+1}, \ldots, x_m)}(x_0)$$

is nonsingular at the point x_0 (which is automatic since the $(m-s)$ invariants J_k are functionally independent), then in a neighbourhood of x_0, the level set $(J_1, \ldots, J_{m-s})(x) = c$ exists if and only if $(x_{s+1}, \ldots, x_m) = \mathcal{F}(x_1, \ldots, x_s)$ for some smooth map $\mathcal{F}$. Since level sets of the fundamental invariants define individual orbits (distinguished by c), and since K was defined by $\{x_1 = c_1, \ldots, x_s = c_s\}$, we conclude *any* orbit intersects K at exactly one point, $(c_1, \ldots, c_s, \mathcal{F}(c_1, \ldots, c_s))$, proving that K is a cross-section as claimed.

Finally, having proven the existence of a cross-section K such that any orbit intersects both transversely and at most once, we introduce the method of *normalization*. Assume the Lie group G acts semi-freely or freely on M. The necessity of this assumption will become clear below, but for now, this only means that for $\dim(G) = r$, the orbits of ϕ_g are r-dimensional [52, Prop. 2.5].

Let $x \in M$ be an arbitrary point, and $\mathcal{O}_x$ its orbit. Define the cross-section K in coordinates as $\{x_1 = c_1, \ldots, x_r = c_r\}$. We have just proved that any orbit intersects this K at exactly one point, and so we can define the map $\xi : M \to M, \xi(x) = \mathcal{O}_x \cap K = k$, which maps an arbitrary point x in M to where its corresponding orbit $\mathcal{O}_x$ intersects K. By construction, $\xi(x) = k = \xi(\phi_g(x))$, i.e. ξ is necessarily invariant with respect to the group action. Writing ξ in the same coordinates as those used to define K, it follows $(\xi_1(x), \ldots, \xi_r(x)) = (c_1, \ldots, c_r)$, the set of constants used to define the cross-section; and that $\{\xi_{m-r}(x), \ldots, \xi_m(x)\}$ are the complete set of $m-r$ invariants of the group action, whose existence has been guaranteed by Theorem 1.

Clearly, if we can construct ξ, we will obtain the set of invariants of the group action. This is done as follows: write the group action ϕ_g in coordinates, and write

the components as $\phi_g = (\phi_g^a, \phi_g^b) \in \mathbb{R}^r \times \mathbb{R}^{m-r}$, choosing K such that $c = (c_1, \ldots, c_r)$ are in the range of ϕ_g^a. Now, we just need to solve $\phi_g^a(x) = c$ for g; since ϕ_g has r-dimensional orbits everywhere, the Jacobian matrix $\partial\phi_g^a/\partial g$ is non-singular, and so by the Implicit Function Theorem, $\phi_g^a(x) = c$ is locally guaranteed to have the solution $g = \gamma(x)$, known as the *moving frame*. Once $\gamma(x)$ is found, we have $\xi(x) = \phi_{\gamma(x)}(x)$, and so $\phi^a_{\gamma(x)}$ recovers the constants defining the cross-section K, and $\phi^b_{\gamma(x)}$ is the complete set of $(m-r)$ invariants.

From the definition of invariance and composition of (left) Lie group actions, we also obtain

$$\phi^b_{\gamma(x)}(x) = \phi^b_{\gamma(\phi_g(x))}(\phi_g(x)) = \phi^b_{\gamma(\phi_g(x))g}(x) \Longrightarrow \gamma(x) = \gamma(\phi_g(x))g,$$

or equivalently $\gamma(\phi_g(x)) = \gamma(x)g^{-1}$, the "right equivariance" property of the moving frame, which implicitly requires ϕ_g to be free as shown next: let $h \in G_x$, the isotropy group of $x \in M$ such that $\phi_h(x) = x$. Then,

$$\gamma(x) = \gamma(\phi_h(x)) = \gamma(x)h^{-1} \Longrightarrow h = e$$

and so $G_x = e$, i.e. ϕ_g is necessarily free. We can relax this requirement by demanding only *local* right equivariance of $\gamma(x)$, i.e. $\gamma(\phi_g(x)) = \gamma(x)g^{-1}$ for all g close to e, for which G_x can be a discrete isotropy group and ϕ_g a semi-free action.

While the concept of cross-sections to orbits is geometric and globally defined due to being based on foliations, the normalization procedure is intrinsically local, since the solution to $\phi_g^a = c$ for $g = \gamma(x)$ is guaranteed only locally by the Implicit Function Theorem. An important exception is the class of problems where ϕ_g^a represents G acting on itself by left or right translation, an action which is regular, free, and transitive [83, p. 209]. This was seen in Section 4.4.1 for an AHRS's symmetry to ground-frame rotations, for which we had

$$\Phi_g \begin{pmatrix} R \\ b_\omega \end{pmatrix} = \begin{pmatrix} Q_0 R \\ \omega_0 + b_\omega \end{pmatrix},$$

where $SO(3) \times \mathbb{R}^3$ acts on itself by left translation. In this case, we can choose $c = e \in G$ and the solution to $\phi_g^a(x) = e$ is $g = x^{-1} = \gamma(x)$, which is clearly defined *globally*. The moving frame is right equivariant due to the freeness, and the invariants are given by $\phi^b_{\gamma(x)} = \phi^b_{x^{-1}}$ as before. This class of symmetries is a subset of the general problem and is the case treated in [28].

4.6.2 Invariant Frame

A vector field $w : M \to TM$ is defined to be G-invariant if

$$(\varphi_g)_* w(x) = w(\varphi_g(x)) \qquad \forall g \in G,$$

essentially identical to the definition of G-invariant dynamics in Section 4.3.

Since TM is by construction a smooth vector bundle of rank m, we can define an *invariant frame* [111, p. 67] as an ordered m-tuple of G-invariant vector fields (w_i) which form a global frame for TM over M, i.e. for each $p \in M$, $\big(w_1(p), \ldots, w_m(p)\big)$ forms a basis for the fiber $\pi^{-1}(p) = T_pM$, an m-dimensional vector space. The following Theorem, adapted from [27, Lem. 1], provides a constructive method to build an invariant frame.

Theorem 2 *The vector fields defined by*

$$w_i(x) = \left(\varphi_{\gamma(x)^{-1}}\right)_* v_i \qquad i = 1, \ldots, m \tag{4.8}$$

where $\gamma(x) : M \to G$ is the moving frame constructed previously, and $v_i \in T_pM$ are basis vectors of the tangent space at some $p \in M$, form an invariant frame.

Proof: We use the following two properties of pushforwards [83, Lem. 3.5]: If $F : M \to N$ is a diffeomorphism, $F_* : T_pM \to T_{F(p)}N$ is an isomorphism; and $(G \circ F)_* = G_* \circ F_*$.

Since T_pM is an m-dimensional vector space [83, Lem. 3.9], a set of basis vectors $(v_1, \ldots, v_m)$ can be chosen. Since φ_g is a diffeomorphism, $(\varphi_{\gamma(x)^{-1}})_* : T_pM \to T_xM$ is an isomorphism, proving $(w_i(x))$ is a frame.

We prove invariance of w_i by direct verification. Applying φ_g to $w_i(x)$ above, we have

$$w_i(\varphi_g(x)) = \left(\varphi_{\gamma(\varphi_g(x))^{-1}}\right)_* v_i$$

and because $\gamma(x)$ is the moving frame, $\gamma(\varphi_g(x))^{-1} = \left(\gamma(x)g^{-1}\right)^{-1} = g\gamma(x)^{-1}$. We thus have

$$w_i(\varphi_g(x)) = \left(\varphi_{g\gamma(x)^{-1}}\right)_* v_i = \left(\varphi_g \circ \varphi_{\gamma(x)^{-1}}\right)_* v_i = \left(\varphi_g\right)_* \circ \left(\varphi_{\gamma(x)^{-1}}\right)_* v_i = \left(\varphi_g\right)_* w_i(x),$$

i.e. $w_i(x)$ is G-invariant. QED.

The particular case of $M = G$ and $\varphi_g = L_g$ above is well-known in differential geometry, where vector fields verifying $(L_g)_* w(h) = w(gh)$ with $g, h \in G$ are said to be left-invariant (c.f. Section 4.3). The set of all left-invariant vector fields on G can be shown to form a finite-dimensional Lie algebra denoted as $\mathrm{Lie}(G)$, with dimension equal to $\dim(G)$ [83, Thm. 4.20]. For this case, the moving frame is computed to be $\gamma(g) = g^{-1}$ (as discussed earlier for G acting on itself by left translation), and the corresponding invariant vector field $w(x) = (L_g)_* v_i$ with $v_i \in T_eG$ is in fact the isomorphism between T_eG and $\mathrm{Lie}(G)$ used to prove the latter is finite-dimensional.

The isomorphism between $\mathrm{Lie}(G)$ and T_eG is used extensively in differential geometry: for a given Lie group G, we define the Lie algebra $\mathfrak{g}$ as the vector space T_eG equipped with a Lie bracket chosen such that $\mathrm{Lie}(G)$ and $\mathfrak{g}$ are isomorphic as Lie algebras. Since the state manifolds of the AHRS (Section 4.2) and Aided INS (Section 4.5) are products of the Lie groups $\mathbb{R}^n$, $SO(3)$ and $\mathbb{H}_1 \subset \mathbb{H}$, we can use their Lie algebras and $p = e$ to immediately obtain expressions for the $v_i \in T_eG$ basis vectors used in (4.8):

- Euclidian space $\mathbb{R}^n$: The Lie algebra is $\mathbb{R}^n$ with the trivial bracket $[v_1, v_2] = 0$ [83, p. 96]. The basis vectors of $T_0\mathbb{R}^n$ can thus be chosen as $v_i = e_i$, i.e.

$$v_1 = \begin{pmatrix} 1 \\ 0 \\ 0 \end{pmatrix}, \quad v_2 = \begin{pmatrix} 0 \\ 1 \\ 0 \end{pmatrix}, \quad v_3 = \begin{pmatrix} 0 \\ 0 \\ 1 \end{pmatrix}$$

- Rotation matrices $SO(3)$: The Lie algebra $so(3)$ consists of skew-symmetric matrices $S(v), v \in \mathbb{R}^3$ under the commutator bracket [83, p. 205]

$$[S(v_1), S(v_2)] = S(v_1)S(v_2) - S(v_2)S(v_1)$$

The basis vectors for $T_I SO(3)$ are taken as $v_i = S(e_i)$, specifically

$$v_1 = \begin{bmatrix} 0 & 0 & 0 \\ 0 & 0 & -1 \\ 0 & 1 & 0 \end{bmatrix}, \quad v_2 = \begin{bmatrix} 0 & 0 & 1 \\ 0 & 0 & 0 \\ -1 & 0 & 0 \end{bmatrix}, \quad v_3 = \begin{bmatrix} 0 & -1 & 0 \\ 1 & 0 & 0 \\ 0 & 0 & 0 \end{bmatrix}$$

- Unit quaternions $\mathbb{H}_1$: The Lie algebra consists of pure quaternions (real entry equal to zero), with quaternion multiplication used as the Lie bracket [83, p. 204]. The basis vectors are the quaternions $\boldsymbol{i}$, $\boldsymbol{j}$ and $\boldsymbol{k}$, i.e.

$$v_1 = \begin{pmatrix} 0 \\ 1 \\ 0 \\ 0 \end{pmatrix}, \quad v_2 = \begin{pmatrix} 0 \\ 0 \\ 1 \\ 0 \end{pmatrix}, \quad v_3 = \begin{pmatrix} 0 \\ 0 \\ 0 \\ 1 \end{pmatrix}$$

In order to compute the pushforward in (4.8), we use the following method from [83, pp. 76-77]: for any $X \in T_pM$, define the smooth curve $\Gamma : \mathbb{R} \to M$ whose tangent vector for $\mathbb{R} \ni \tau = 0$ is X; then, $F_*X = (F \circ \gamma)'(0)$. In our case, we have $F = \varphi_{\gamma(x)^{-1}}$ and $X = v_i$, define $\Gamma(\tau) = v_i\tau$, and obtain

$$\left(\varphi_{\gamma(x)^{-1}}\right)_* v_i = \frac{d}{d\tau}\left(\varphi_{\gamma(x)^{-1}}(v_i\tau)\right)\Big|_{\tau=0} = w_i(x) \tag{4.9}$$

4.6.3 Invariant Observer, Invariant Output Error

For the system dynamics $\dot{x} = f(x,u)$, $y = h(x,u)$, an *invariant observer* is the system

$$\dot{\hat{x}} = F(\hat{x}, u, y)$$

with the following three properties:

- $(\varphi_g)_* F(\hat{x}, u, y) = F(\varphi_g(\hat{x}), \psi_g(u), \rho_g(y))$ (F is G-invariant)
- $F(x, u, h(x,u)) = f(x,u)$ (F is a pre-observer)
- $(\hat{x} - x) \to 0$ as $t \to \infty$ for all $\hat{x}(0)$, or for all $\hat{x}(0)$ close to $x(0)$ (the observer error dynamics are globally or locally asymptotically stable)

A constructive method to build the invariant observer will be given below. One ingredient of this construction is an *invariant output error*, the smooth vector-valued map $E(\hat{x}, u, y)$ with the following two properties:

- $E(\hat{x}, u, y) = 0 \iff y = h(\hat{x}, u)$ (E is an output error)
- $E(\varphi_g(\hat{x}), \psi_g(u), \rho_g(y)) = E(\hat{x}, u, y)$ (E is an invariant)

We recall Section 4.6.1, where the group action $\phi_g = \varphi_g \times \psi_g \times \rho_g$ acting (regularly) on the product manifold $M = X \times V \times Y$ with $\dim(M) = m$ and $\dim(G) = r$, $r \leq m$ gave the complete set of invariants of G as $\phi^b_{\gamma(x)}(x) : M \to \mathbb{R}^{m-r}$. Let $\dim(X) = n$, $\dim(V) = o$, $\dim(Y) = p$ denote the number of states, inputs and outputs of our system, respectively. Since Y clearly depends on X and V through the output map,

we further assume $r \leq n+o$ and define $I(x,u)$ as the set of functionally independent invariants

$$I(x,u) = \left(\varphi^b_{\gamma(x)}(x), \psi_{\gamma(x)}(u)\right) \in \mathbb{R}^{n+o-r} \tag{4.10}$$

and $J_h(x,y)$ as the remaining invariants

$$J_h(x,y) = \rho_{\gamma(x)}(y) \in \mathbb{R}^p.$$

We now prove that the construction

$$E(\hat{x},u,y) = J_h(\hat{x}, h(\hat{x},u)) - J_h(\hat{x},y) \tag{4.11}$$

is an invariant output error. Assume $y = h(\hat{x},u)$; clearly $E(\hat{x},u,h(\hat{x},u)) = 0$. Conversely, assume $E(\hat{x},u,y) = 0$. From (4.11) where $J_h(\hat{x},y) = \rho_{\gamma(\hat{x})}(y)$, we see $y \mapsto E(\hat{x},u,y)$ is invertible for any $\hat{x},u$ because $\rho_g(y)$ is a diffeomorphism for any $g \in G$, as discussed in Section 4.3.1. This guarantees $E(\hat{x},u,y) = 0$ for a single y value, meaning $E(\hat{x},u,y) = 0 \implies y = h(\hat{x},u)$. This proves E is an output error, i.e. $E(\hat{x},u,y) = 0 \iff y = h(\hat{x},u)$. The invariance of (4.11) is verified directly: $J_h(\varphi_g(\hat{x}), \rho_g(y)) = J_h(\hat{x},y)$ because J_h is an invariant, and $J_h(\varphi_g(\hat{x}), h(\varphi_g(\hat{x}), \psi_g(u))) = J_h(\varphi_g(\hat{x}), \rho_g h(\hat{x},u)) = J_h(\varphi_g(\hat{x}), \rho_g(\hat{y}))$ since the system output is G-equivariant. QED.

Equation (4.11) is obviously not the only possible invariant output error; however, we can prove that any other invariant output error is written as $\widetilde{E}(\hat{x},u,y) = \mathcal{L}(I(\hat{x},u), E(\hat{x},u,y))$, where $\mathcal{L}$ is a smooth function such that $\mathcal{L}(I,E) = 0 \iff E = 0$: since $\widetilde{E}$ is an invariant, $\widetilde{E}(\hat{x},u,y) = \mathcal{F}(I(\hat{x},u), J_h(\hat{x},y))$ where $\mathcal{F}$ is an analytic function as discussed in Section 4.6.1. We have $J_h(\hat{x},y) = J_h(\hat{x}, h(\hat{x},u)) - E(\hat{x},u,y)$ and since $J_h(\hat{x}, h(\hat{x},u))$ is an invariant, it must be a function of the fundamental invariants $I(\hat{x},u)$. It follows that $\widetilde{E}(\hat{x},u,y) = \mathcal{L}(I(\hat{x},u), E(\hat{x},u,y))$. Since both E and $\widetilde{E}$ are invariant output errors, $E = 0 \iff y = h(\hat{x},u) \iff 0 = \widetilde{E} = \mathcal{L}(I,E)$. QED.

Using the constructions above, we now state the main theorem regarding invariant *pre*-observers [27, Thm. 1]. Convergence will be addressed afterwards.

Theorem 3 *$\dot{\hat{x}} = F(\hat{x},u,y)$ is an invariant pre-observer for the G-invariant and G-equivariant system $\dot{x} = f(x,u)$, $y = h(x,u)$ if and only if*

$$F(\hat{x},u,y) = f(\hat{x},u) + \sum_{i=1}^{n} \mathcal{L}_i\left(I(\hat{x},u), E(\hat{x},u,y)\right) w_i(\hat{x}), \tag{4.12}$$

where $I(\hat{x},u)$ is the set of invariants (4.10)*, $E(\hat{x},u,y)$ is the invariant output error* (4.11)*, $\mathcal{L}_i$ are smooth functions such that $\mathcal{L}_i(I,0) = 0$, and $w_i(\hat{x})$ are the invariant frame vector fields* (4.8)*.*

Proof: ($\Longleftarrow$) We first verify that (4.12) is a pre-observer: for $\hat{x} = x$ and $y = h(x,u)$, we have

$$\begin{aligned} F(x,u,y) &= f(x,u) + \sum_{i=1}^{n} \mathcal{L}_i\left(I(x,u), E(x,u,h(x,u))\right) w_i(x) \\ &= f(x,u) + \sum_{i=1}^{n} \mathcal{L}_i\left(I,0\right) w_i = f(x,u). \end{aligned}$$

We also verify G-invariance of (4.12) directly: $I(\hat{x},u)$ and $E(\hat{x},u,y)$ are invariants thus so is $\mathcal{L}_i\left(I(\hat{x},u),E(\hat{x},u,y)\right)$. By G-invariance of $f(\hat{x},u)$ and $w_i(\hat{x})$, we have

$$\begin{aligned}F(\varphi_g(\hat{x}),\psi_g(u),\rho_g(y)) &= (\varphi_g)_* f(\hat{x},u) + \sum_{i=1}^{n} \mathcal{L}_i\left(I(\hat{x},u),E(\hat{x},u,y)\right)(\varphi_g)_* w_i(\hat{x}) \\ &= (\varphi_g)_* F(\hat{x},u,y),\end{aligned}$$

the last equality due to the linearity of the pushforward.

($\Longrightarrow$) Let $\dot{\hat{x}} = F(\hat{x},u,y)$ be an invariant pre-observer. By the discussion in Section 4.3, the dynamics $F(\hat{x},u,y)$ map to the tangent bundle TM, so they can be expressed as

$$F(\hat{x},u,y) = \sum_{i=1}^{n} F_i(\hat{x},u,y) w_i(\hat{x}),$$

where $F_i(\hat{x},u,y)$ are smooth real-valued functions and $(w_i(\hat{x}))$ is the invariant frame (4.8), which was proven to be a global frame for TM in Section 4.6.2. Since F is G-invariant,

$$\begin{aligned}F(\varphi_g(\hat{x}),\psi_g(u),\rho_g(y)) &= \sum_{i=1}^{n} F_i\left(\varphi_g(\hat{x}),\psi_g(u),\rho_g(y)\right) w_i(\varphi_g(\hat{x})) \\ &= (\varphi_g)_* F(\hat{x},u,y) = (\varphi_g)_* \sum_{i=1}^{n} F_i(\hat{x},u,y) w_i(\hat{x}).\end{aligned}$$

Since $(\varphi_g)_* w_i(\hat{x}) = w_i(\varphi_g(\hat{x}))$ and the pushforward is linear, it follows that

$$F_i\left(\varphi_g(\hat{x}),\psi_g(u),\rho_g(y)\right) = F_i(\hat{x},u,y),$$

i.e. $F_i(\hat{x},u,y)$ are invariants of G. Since F is a pre-observer,

$$f(x,u) = F(x,u,h(x,u)) = \sum_{i=1}^{n} F_i(x,u,h(x,u)) w_i(x),$$

and we can then write

$$\begin{aligned}F(\hat{x},u,y) &= f(\hat{x},u) + F(\hat{x},u,y) - f(\hat{x},u) \\ &= f(\hat{x},u) + \sum_{i=1}^{n} \left[F_i(\hat{x},u,y) - F_i(\hat{x},u,h(\hat{x},u))\right] w_i(\hat{x}),\end{aligned}$$

and since F_i are invariants, we conclude

$$F_i(\hat{x},u,y) - F_i(\hat{x},u,h(\hat{x},u)) = \mathcal{L}_i\left(I(\hat{x},u),E(\hat{x},u,y)\right)$$

with $\mathcal{L}_i(I,0) = 0$ because E is an output error and F is a pre-observer. QED.

Equation (4.12) has an equivalent form obtained by re-writing the real-valued gains $\mathcal{L}_i(I,E)$ as $\overline{\mathcal{L}}_i E$, where each $\overline{\mathcal{L}}_i$ is a $1\times p$ gain vector whose entries are arbitrary functions of I and E. The invariant pre-observer (4.12) is rewritten as

$$F(\hat{x},u,y) = f(\hat{x},u) + \sum_{i=1}^{n} \left[\overline{\mathcal{L}}_i\, E(\hat{x},u,y)\right] w_i(\hat{x}), \tag{4.13}$$

which clearly satisfies $\mathcal{L}_i(I,0)=0$ for *any* $\overline{\mathcal{L}}_i$, including constant entries. Concatenating the vector fields as $W(\hat{x})=(w_1(\hat{x}),\cdots,w_n(\hat{x}))$ and the gain vectors as $\overline{\mathcal{L}}=\left(\overline{\mathcal{L}}_1^T,\cdots,\overline{\mathcal{L}}_n^T\right)^T$, (4.13) can be written as $F(\hat{x},u,y)=f(\hat{x},u)+W(\hat{x})\,\overline{\mathcal{L}}\,E(\hat{x},u,y)$.

We now address convergence of the invariant pre-observer (4.12) resp. (4.13). Not surprisingly, there is no general constructive procedure for choosing gains $\mathcal{L}$ or $\overline{\mathcal{L}}$ to guarantee convergence. However, the stability analysis of the invariant pre-observer can be greatly simplified by considering the *invariant estimation error*

$$\eta(x,\hat{x})=\varphi_{\gamma(x)}(\hat{x})-\varphi_{\gamma(x)}(x) \tag{4.14}$$

Clearly, $x=\hat{x}\implies\eta=0$, and since φ_g is a diffeomorphism $\forall g\in G$, $\hat{x}=\varphi_{\gamma(x)^{-1}}\eta(x,\hat{x})+x$, hence $\eta=0\iff x=\hat{x}$. We also verify $\eta(x,\hat{x})$ is an invariant:

$$\eta\left(\varphi_g(x),\varphi_g(\hat{x})\right)=\varphi_{\gamma(\varphi_g(x))}(\varphi_g(\hat{x}))-\varphi_{\gamma(\varphi_g(x))}(\varphi_g(x))=\varphi_{\gamma(\varphi_g(x))g}(\hat{x})-\varphi_{\gamma(\varphi_g(x))g}(x)$$

and since $\gamma(\varphi_g(x))g=\gamma(x)$ by the right equivariance of $\gamma(x)$ established in Section 4.6.1, (4.14) is an invariant: $\eta\left(\varphi_g(x),\varphi_g(\hat{x})\right)=\eta(x,\hat{x})$. The convergence of x to $\hat{x}$ is equivalent to the stability of η dynamics, whose analysis is (potentially greatly) simplified due to the following result [27, Thm. 3]:

Theorem 4 *The dynamics of the invariant estimation error $\eta(x,\hat{x})$ depend on the system trajectory only through the set of fundamental invariants $I(x,u)$, i.e.*

$$\frac{d}{dt}\eta=\Upsilon\left(\eta,I(x,u)\right).$$

Proof: As shown above, η is an invariant: $\eta(x,\hat{x})=\eta\left(\varphi_g(x),\varphi_g(\hat{x})\right)$, from which it follows

$$\frac{d}{dt}\eta(x,\hat{x})=\frac{d}{dt}\eta\left(\varphi_g(x),\varphi_g(\hat{x})\right).$$

Using the chain rule, we have

$$\begin{aligned}
\frac{d}{dt}\eta(x,\hat{x}) &= \frac{\partial\eta}{\partial x}(x,\hat{x})\frac{d}{dt}x+\frac{\partial\eta}{\partial\hat{x}}(x,\hat{x})\frac{d}{dt}\hat{x}\\
&= \frac{\partial\eta}{\partial x}(x,\hat{x})f(x,u)+\frac{\partial\eta}{\partial\hat{x}}(x,\hat{x})F(\hat{x},u,h(x,u))\\
&:= \sigma(x,\hat{x},u),\\
\frac{d}{dt}\eta(\varphi_g(x),\varphi_g(\hat{x})) &= \frac{\partial\eta}{\partial x}(\varphi_g(x),\varphi_g(\hat{x}))\frac{d}{dt}\varphi_g(x)+\frac{\partial\eta}{\partial\hat{x}}(\varphi_g(x),\varphi_g(\hat{x}))\frac{d}{dt}\varphi_g(\hat{x})\\
&= \frac{\partial\eta}{\partial x}(\varphi_g(x),\varphi_g(\hat{x}))f(\varphi_g(x),\psi_g(u))\\
&\quad+\frac{\partial\eta}{\partial\hat{x}}(\varphi_g(x),\varphi_g(\hat{x}))F(\varphi_g(\hat{x}),\psi_g(u),h(\varphi_g(x),\psi_g(u))\\
&= \sigma(\varphi_g(x),\varphi_g(\hat{x}),\psi_g(u)),
\end{aligned}$$

i.e. the function $\sigma(x,\hat{x},u)$ is an invariant. We have $\hat{x}=\varphi_{\gamma(x)^{-1}}\eta+x=\mathcal{F}(x,\eta)$ as before. Since $\sigma(x,\hat{x},u)=\sigma(x,\mathcal{F}(x,\eta),u)$ is an invariant it must be a function of the fundamental set of invariants $I(x,u)$ as well as η: $\sigma(x,\mathcal{F}(x,\eta),u)=\Upsilon(\eta,I(x,u))=\sigma(x,\hat{x},u)=(d/dt)\eta$. QED.

The key point of Theorem 4 is that the convergence properties of the invariant observer (4.12) or (4.13) depend on the system trajectory through the invariants $I(x,u)$ rather than (x,u) as in the general case. This guarantees a simplified stability analysis and gain selection because by (4.10) $I(x,u) \in \mathbb{R}^{n+o-r}$ where n, o are the dimensions of the state and input manifolds and r is the dimension of the symmetry group G.

It can be shown that for a subclass of G-invariant systems, namely those with $X = G$, dynamics of the form

$$\frac{d}{dt}x = F(x,u) = (L_x)_* u$$

and which are G-invariant to $\varphi_g(x) = R_g x$ and $\psi_g(u) = \left(L_{g^{-1}} R_g\right)_* u$ possess invariant error dynamics which are *autonomous* from the system trajectory (x,u) [26, 28]; a concrete example is the AHRS (4.1) without bias estimation,

$$\begin{aligned} \dot{R} &= RS(\omega) \\ \begin{bmatrix} y_a \\ y_m \end{bmatrix} &= \begin{bmatrix} R^T a \\ R^T m \end{bmatrix}. \end{aligned}$$

Autonomy of the η dynamics greatly simplifies convergence analysis, however it can only be guaranteed for a small subset of symmetry-possessing systems. In particular the AHRS (4.1) and Aided INS (4.6) do not possess the required form, and the η dynamics computed in Section 4.7 are dependent on the system trajectory through $I(x,u)$ exactly as stated by Theorem 4.

We will employ Theorem 4 using the estimated version of invariants (4.10),

$$\frac{d}{dt}\eta = \hat{\Upsilon}(\eta, I(\hat{x},u)).$$

This holds because $(d/dt)\eta = \sigma(x,\hat{x},u)$ is an invariant and thus a function of $I(x)$ and $I(\hat{x},u)$; but $\eta = \varphi_{\gamma(x)}(\hat{x}) - \varphi_{\gamma(x)}(x)$ always contains $I(x) = \varphi^b_{\gamma(x)}(x)$ as a subset, and the remaining part is necessarily a function of $I(\hat{x},u)$ since $\eta(x,\hat{x})$ is an invariant. It follows that $\sigma(x,\hat{x},u) = \hat{\Upsilon}(\eta, I(\hat{x},u)) = (d/dt)\eta$ as claimed.

4.7 Invariant Observer Design

We now apply the invariant observer construction method in Section 4.6 to the AHRS (4.1) and Aided INS (4.6), (4.7). The symmetries of both systems are known from Sections 4.4 and 4.5 and all the steps are systematic.

4.7.1 Invariant AHRS Design

The AHRS system dynamics written in terms of rotation matrices $R \in SO(3)$ are (4.1)

$$\begin{aligned} \dot{R} &= RS(\omega - b_\omega) \\ \dot{b}_\omega &= 0 \\ \begin{bmatrix} y_a \\ y_m \end{bmatrix} &= \begin{bmatrix} R^T a \\ R^T m \end{bmatrix}, \end{aligned}$$

4.7.1.1 Body frame symmetries

The first set of symmetries physically represents rotating the body-fixed reference frame. The Lie group actions of $G = SO(3) \times \mathbb{R}^3 \ni (R_0, \omega_0) = g$ are

$$\varphi_g \begin{pmatrix} R \\ b_\omega \end{pmatrix} = \begin{pmatrix} RR_0 \\ R_0^T(b_\omega + \omega_0) \end{pmatrix}, \quad \psi_g(\omega) = \left(R_0^T(\omega + \omega_0)\right), \quad \rho_g \begin{pmatrix} y_a \\ y_m \end{pmatrix} = \begin{pmatrix} R_0^T y_a \\ R_0^T y_m \end{pmatrix}$$

We first find the moving frame and complete set of invariants as in Section 4.6.1. The composite Lie group action $\phi_g = \varphi_g \times \psi_g \times \rho_g$ acts regularly and freely on the product manifold $M = X \times V \times Y$. Since $\dim(G) = 6$ and $\dim(X) = 6$ we partition ϕ_g as $\phi_g^a = \varphi_g$ and $\phi_g^b = (\psi_g \times \rho_g)$ and solve $\phi_g^a(x) = c$ for g, the image of the moving frame $\gamma(x)$:

$$\varphi_g \begin{pmatrix} R \\ b_\omega \end{pmatrix} = \begin{pmatrix} RR_0 \\ R_0^T(b_\omega + \omega_0) \end{pmatrix} = \begin{pmatrix} I \\ 0 \end{pmatrix} \Longrightarrow g = (R^T, -b_\omega) = \gamma(x)$$

The complete set of invariants is then $\phi^b_{\gamma(x)}(x) = \psi_{\gamma(x)} \times \rho_{\gamma(x)}$ which we partition as

$$I(x,u) = \psi_{\gamma(x)}(u) = \psi_{(R^T,-b_\omega)}(\omega) = R(\omega - b_\omega)$$
$$J_h(x,y) = \rho_{\gamma(x)}(y) = \rho_{(R^T,-b_\omega)} \begin{pmatrix} y_a \\ y_m \end{pmatrix} = \begin{pmatrix} Ry_a \\ Ry_m \end{pmatrix}$$

The invariant output error is computed by (4.11)

$$E(\hat{x}, u, y) = J_h(\hat{x}, h(\hat{x}, u)) - J_h(\hat{x}, y) = \begin{pmatrix} \hat{R}\hat{R}^T a \\ \hat{R}\hat{R}^T m \end{pmatrix} - \begin{pmatrix} \hat{R}y_a \\ \hat{R}y_m \end{pmatrix} = \begin{pmatrix} a - \hat{R}y_a \\ m - \hat{R}y_m \end{pmatrix}$$

From Section 4.6.2, the invariant frame for the state manifold $X = SO(3) \times \mathbb{R}^3$ is defined by the set of vectors (4.8) where $v_i^R = (S(e_i) \quad 0)^T$ and $v_i^\omega = (0 \quad e_i)^T$, $i = 1, 2, 3$ span the tangent space T_eX. We have $\gamma(x) = (R^T, -b_\omega) \Longrightarrow \gamma(x)^{-1} = (R, b_\omega)$ and we compute the invariant frame vectors using (4.9)

$$w_i^R(x) = \frac{d}{d\tau}\left(\varphi_{(R,b_\omega)} \begin{pmatrix} S(e_i)\tau \\ 0 \end{pmatrix}\right)\Big|_{\tau=0} = \frac{d}{d\tau}\begin{pmatrix} S(e_i)R\tau \\ 0 \end{pmatrix}\Big|_{\tau=0} = \begin{pmatrix} S(e_i)R \\ 0 \end{pmatrix}$$
$$w_i^\omega(x) = \frac{d}{d\tau}\left(\varphi_{(R,b_\omega)} \begin{pmatrix} 0 \\ e_i\tau \end{pmatrix}\right)\Big|_{\tau=0} = \frac{d}{d\tau}\begin{pmatrix} 0 \\ R^T(e_i\tau + b_\omega) \end{pmatrix}\Big|_{\tau=0} = \begin{pmatrix} 0 \\ R^T e_i \end{pmatrix}$$

The invariant observer is written as (4.13)

$$\dot{\hat{R}} = \hat{R}S(\omega - \hat{b}_\omega) + \sum_{i=1}^{3} \left[\overline{\mathcal{L}}_i^R E\right] S(e_i)\hat{R}$$
$$\dot{\hat{b}}_\omega = \sum_{i=1}^{3} \left[\overline{\mathcal{L}}_i^\omega E\right] \hat{R}^T e_i$$

We re-arrange the observer to obtain a more compact expression. The invariant output error column vector is partitioned as $E = [E_a^T \quad E_m^T]^T$ and the row gains $\overline{\mathcal{L}}_i^R$,

$\overline{\mathcal{L}}_i^\omega$ are each partitioned as $\overline{\mathcal{L}}_i = [\overline{\mathcal{L}}_{i,a} \quad \overline{\mathcal{L}}_{i,m}]$ giving

$$\dot{\hat{R}} = \hat{R}S(\omega - \hat{b}_\omega) + \sum_{i=1}^{3} \left\{ \overline{\mathcal{L}}_{i,a}^R E_a + \overline{\mathcal{L}}_{i,m}^R E_m \right\} S(e_i)\hat{R}$$

$$\dot{\hat{b}}_\omega = \sum_{i=1}^{3} \left\{ \overline{\mathcal{L}}_{i,a}^\omega E_a + \overline{\mathcal{L}}_{i,m}^\omega E_m \right\} \hat{R}^T e_i$$

Remark $\{\cdot\cdot\} \in \mathbb{R}$ so the $\hat{R}$ terms can be factored out:

$$\dot{\hat{R}} = \hat{R}S(\omega - \hat{b}_\omega) + \left[\sum_{i=1}^{3} \left\{ \overline{\mathcal{L}}_{i,a}^R E_a + \overline{\mathcal{L}}_{i,m}^R E_m \right\} S(e_i) \right] \hat{R}$$

$$\dot{\hat{b}}_\omega = \hat{R}^T \left[\sum_{i=1}^{3} \left\{ \overline{\mathcal{L}}_{i,a}^\omega E_a + \overline{\mathcal{L}}_{i,m}^\omega E_m \right\} e_i \right]$$

The $[\cdot\cdot]$ terms are now written using matrix-vector multiplication:

$$\begin{aligned} \dot{\hat{R}} &= \hat{R}S(\omega - \hat{b}_\omega) + S\big(L_a^R E_a + L_m^R E_m\big)\hat{R} \\ \dot{\hat{b}}_\omega &= \hat{R}^T\big(L_a^\omega E_a + L_m^\omega E_m\big), \end{aligned} \tag{4.15}$$

where each L is a 3×3 matrix of gains such that $L = L(I, E)$. The invariant estimation error associated with (4.15) is computed using (4.14):

$$\varphi_{\gamma(x)}(\hat{x}) - \varphi_{\gamma(x)}(x) = \varphi_{(R^T, -b_\omega)} \begin{pmatrix} \hat{R} \\ \hat{b}_\omega \end{pmatrix} - \varphi_{(R^T, -b_\omega)} \begin{pmatrix} R \\ b_\omega \end{pmatrix} = \begin{pmatrix} \hat{R}R^T - I \\ R(\hat{b}_\omega - b_\omega) \end{pmatrix} = \begin{pmatrix} \eta_R \\ \eta_\omega \end{pmatrix}$$

For convenience we re-define $\eta_R = \hat{R}R^T$, such that $R = \hat{R} \iff \eta_R = I$ (instead of 0). We now compute the dynamics of η, which by Theorem 4 are known to depend on η and I only. Remark

$$\begin{pmatrix} E_a \\ E_m \end{pmatrix} = \begin{pmatrix} a - \hat{R}y_a \\ m - \hat{R}y_m \end{pmatrix} = \begin{pmatrix} a - \hat{R}R^T a \\ m - \hat{R}R^T m \end{pmatrix} = \begin{pmatrix} a - \eta_R a \\ m - \eta_R m \end{pmatrix}$$

i.e. both terms are functions of η_R and the known constants a and m. Time differentiating the identity $RR^T = I$ we have

$$\dot{R}R^T + R\frac{d}{dt}(R^T) = 0 \Longrightarrow \frac{d}{dt}(R^T) = -R^T\dot{R}R^T$$

By direct computation, we now find

$$\begin{aligned} \frac{d}{dt}\eta_R &= \dot{\hat{R}}R^T + \hat{R}\frac{d}{dt}(R^T) \\ &= \hat{R}S(\omega - \hat{b}_\omega)R^T + S\big(L_a^R E_a + L_m^R E_m\big)\hat{R}R^T + \hat{R}\left(-R^T RS(\omega - b_\omega)R^T\right) \\ &= \hat{R}S(b_\omega - \hat{b}_\omega)R^T + S\big(L_a^R E_a + L_m^R E_m\big)\hat{R}R^T \\ &= \hat{R}R^T RS(b_\omega - \hat{b}_\omega)R^T + S\big(L_a^R E_a + L_m^R E_m\big)\hat{R}R^T \\ &= \hat{R}R^T S\left[R(b_\omega - \hat{b}_\omega)\right] + S\big(L_a^R E_a + L_m^R E_m\big)\hat{R}R^T \\ \frac{d}{dt}\eta_R &= \eta_R S(-\eta_\omega) + S\big(L_a^R E_a + L_m^R E_m\big)\eta_R, \end{aligned}$$

which together with $E = E(\eta_R)$ confirms Theorem 4. Remark the dynamics of η_R are nonlinear, coupled with η_ω, and autonomous. Moving to η_ω we have

$$\begin{aligned}
\frac{d}{dt}\eta_\omega &= \dot{R}(\hat{b}_\omega - b_\omega) + R(\dot{\hat{b}}_\omega - \dot{b}_\omega) \\
&= RS(\omega - b_\omega)(\hat{b}_\omega - b_\omega) + R\hat{R}^T\left(L_a^\omega E_a + L_m^\omega E_m\right) \\
&= RS(\omega - \hat{b}_\omega + \hat{b}_\omega - b_\omega)R^T R(\hat{b}_\omega - b_\omega) + R\hat{R}^T\left(L_a^\omega E_a + L_m^\omega E_m\right) \\
&= \left\{R\hat{R}^T\hat{R}S(\omega - \hat{b}_\omega)\hat{R}^T\hat{R}R^T + RS(\hat{b}_\omega - b_\omega)R^T\right\}R(\hat{b}_\omega - b_\omega) \\
&\quad + (\hat{R}R^T)^T\left(L_a^\omega E_a + L_m^\omega E_m\right) \\
&= \left\{(\hat{R}R^T)^T S\left[\hat{R}(\omega - \hat{b}_\omega)\right]\hat{R}R^T + S\left[R(\hat{b}_\omega - b_\omega)\right]\right\}R(\hat{b}_\omega - b_\omega) \\
&\quad + (\hat{R}R^T)^T\left(L_a^\omega E_a + L_m^\omega E_m\right) \\
&= \left\{(\eta_R)^T S\left[I(\hat{x}, u)\right]\eta_R + S\left[\eta_\omega\right]\right\}\eta_\omega + (\eta_R)^T\left(L_a^\omega E_a + L_m^\omega E_m\right) \\
\frac{d}{dt}\eta_\omega &= S\left[(\eta_R)^T I(\hat{x}, u)\right]\eta_\omega + (\eta_R)^T\left(L_a^\omega E_a + L_m^\omega E_m\right),
\end{aligned}$$

where the last line follows from $S[\eta_\omega]\eta_\omega = \eta_\omega \times \eta_\omega = 0$. Theorem 4 is confirmed once again; remark that $\dot{\eta}_\omega$ is not autonomous, but depends on the system trajectory through the (known) estimated invariant $I(\hat{x}, u) = \hat{R}(\omega - \hat{b}_\omega)$.

4.7.1.2 Ground frame symmetries

We now consider the AHRS symmetries representing rotations of the ground-fixed frame covered in Section 4.4.1. The symmetry group $G = SO(3) \times \mathbb{R}^3 \ni (Q_0, \omega_0) = g$, where Q_0 represents the rotation of the ground frame, acts on the system through the Lie group actions

$$\Phi_g\begin{pmatrix} R \\ b_\omega \end{pmatrix} = \begin{pmatrix} Q_0 R \\ \omega_0 + b_\omega \end{pmatrix}, \qquad \Psi_g\begin{pmatrix} \omega \\ a \\ m \end{pmatrix} = \begin{pmatrix} \omega_0 + \omega \\ Q_0 a \\ Q_0 m \end{pmatrix}, \qquad \Upsilon_g\begin{pmatrix} y_a \\ y_m \end{pmatrix} = \begin{pmatrix} y_a \\ y_m \end{pmatrix}$$

We have $\phi_g = \Phi_g \times \Psi_g \times \Upsilon_g$ acting on $M = X \times V \times Y$. With $\dim(G) = 6$ and $\dim(X) = 6$, we partition ϕ_g as $\phi_g^a = \Phi_g$ and $\phi_g^b = (\Psi_g \times \Upsilon_g)$ and solve $\phi_g^a(x) = c$ for $g = \gamma(x)$. Remark that in the present case Φ_g is the Lie group G acting on itself by left multiplication, which guarantees the global existence of $\gamma(x)$ as discussed at the end of Section 4.6.1. The calculation procedure is identical to Section 4.7.1.1:

$$\Phi_g\begin{pmatrix} R \\ b_\omega \end{pmatrix} = \begin{pmatrix} Q_0 R \\ \omega_0 + b_\omega \end{pmatrix} = \begin{pmatrix} I \\ 0 \end{pmatrix} \Longrightarrow g = (R^T, -b_\omega) = \gamma(x)$$

The complete set of invariants $\phi^b_{\gamma(x)}(x)$ is partitioned as

$$\begin{aligned}
I(x, u) = \Psi_{\gamma(x)}(u) &= \Psi_{(R^T, -b_\omega)}\begin{pmatrix} \omega \\ a \\ m \end{pmatrix} = \begin{pmatrix} -b_\omega + \omega \\ R^T a \\ R^T m \end{pmatrix} = \begin{pmatrix} I_\omega \\ I_a \\ I_m \end{pmatrix} \\
J_h(x, y) = \Upsilon_{\gamma(x)}(y) &= \Upsilon_{(R^T, -b_\omega)}\begin{pmatrix} y_a \\ y_m \end{pmatrix} = \begin{pmatrix} y_a \\ y_m \end{pmatrix}
\end{aligned}$$

The invariant output error is given by (4.11)

$$E(\hat{x},u,y) = J_h(\hat{x},h(\hat{x},u)) - J_h(\hat{x},y) = \begin{pmatrix}\hat{R}^T a \\ \hat{R}^T m\end{pmatrix} - \begin{pmatrix} y_a \\ y_m\end{pmatrix} = \begin{pmatrix}\hat{R}^T a - y_a \\ \hat{R}^T m - y_m\end{pmatrix}$$

The invariant frame for the state manifold $X = SO(3)\times\mathbb{R}^3$ is defined by the set of vectors (4.8) where $v_i^R = (S(e_i) \quad 0)^T$ and $v_i^\omega = (0 \quad e_i)^T$, $i = 1,2,3$ span the tangent space T_eX. We have $\gamma(x) = (R^T, -b_\omega) \Longrightarrow \gamma(x)^{-1} = (R, b_\omega)$ and by (4.9)

$$w_i^R(x) = \frac{d}{d\tau}\left(\Phi_{(R,b_\omega)}\begin{pmatrix}S(e_i)\tau \\ 0\end{pmatrix}\right)\Big|_{\tau=0} = \frac{d}{d\tau}\begin{pmatrix}RS(e_i)\tau \\ 0\end{pmatrix}\Big|_{\tau=0} = \begin{pmatrix}RS(e_i) \\ 0\end{pmatrix}$$
$$w_i^\omega(x) = \frac{d}{d\tau}\left(\Phi_{(R,b_\omega)}\begin{pmatrix}0 \\ e_i\tau\end{pmatrix}\right)\Big|_{\tau=0} = \frac{d}{d\tau}\begin{pmatrix}0 \\ b_\omega + e_i\tau\end{pmatrix}\Big|_{\tau=0} = \begin{pmatrix}0 \\ e_i\end{pmatrix}$$

The invariant observer is given by (4.13)

$$\dot{\hat{R}} = \hat{R}S(\omega - \hat{b}_\omega) + \sum_{i=1}^{3}\left[\overline{\mathcal{L}}_i^R E\right]\hat{R}S(e_i)$$
$$\dot{\hat{b}}_\omega = \sum_{i=1}^{3}\left[\overline{\mathcal{L}}_i^\omega E\right]e_i$$

As in Section 4.7.1.1, we partition $\overline{\mathcal{L}}_i^R$ and $\overline{\mathcal{L}}_i^\omega$ as $\overline{\mathcal{L}}_i = [\overline{\mathcal{L}}_{i,a} \quad \overline{\mathcal{L}}_{i,m}]$ and $E = [E_a^T \quad E_m^T]^T$, using the invariant output error E computed above. We get

$$\dot{\hat{R}} = \hat{R}S(\omega - \hat{b}_\omega) + \sum_{i=1}^{3}\left\{\overline{\mathcal{L}}_{i,a}^R E_a + \overline{\mathcal{L}}_{i,m}^R E_m\right\}\hat{R}S(e_i)$$
$$\dot{\hat{b}}_\omega = \sum_{i=1}^{3}\left\{\overline{\mathcal{L}}_{i,a}^\omega E_a + \overline{\mathcal{L}}_{i,m}^\omega E_m\right\}e_i$$

This can be equivalently written using matrix-vector multiplication as

$$\begin{aligned}\dot{\hat{R}} &= \hat{R}S(\omega - \hat{b}_\omega) + \hat{R}S\Big(L_a^R E_a + L_m^R E_m\Big) \\ \dot{\hat{b}}_\omega &= L_a^\omega E_a + L_m^\omega E_m\end{aligned} \tag{4.16}$$

where L are 3×3 gain matrices such that $L = L(I,E)$.

The invariant estimation error associated with this observer is obtained from (4.14):

$$\eta = \Phi_{\gamma(x)}(\hat{x}) - \Phi_{\gamma(x)}(x) = \Phi_{(R^T,-b_\omega)}\begin{pmatrix}\hat{R} \\ \hat{b}_\omega\end{pmatrix} - \Phi_{(R^T,-b_\omega)}\begin{pmatrix}R \\ b_\omega\end{pmatrix} = \begin{pmatrix}R^T\hat{R} - I \\ \hat{b}_\omega - b_\omega\end{pmatrix} = \begin{pmatrix}\eta_R \\ \eta_\omega\end{pmatrix}$$

As before, we re-define $\eta_R = R^T\hat{R}$, such that $R = \hat{R} \Longleftrightarrow \eta_R = I$ instead of 0. Finally, we compute the dynamics of η. Remark

$$\begin{pmatrix}E_a \\ E_m\end{pmatrix} = \begin{pmatrix}\hat{R}^T a - y_a \\ \hat{R}^T m - y_m\end{pmatrix} = \begin{pmatrix}\hat{R}^T a - R^T\hat{R}\hat{R}^T a \\ \hat{R}^T m - R^T\hat{R}\hat{R}^T m\end{pmatrix} = \begin{pmatrix}I_a - \eta_R I_a \\ I_m - \eta_R I_m\end{pmatrix}$$

where $I_a = \hat{R}^T a$, $I_m = \hat{R}^T m$ are (known) invariants, and so E is a function of η_R and $I(\hat{x}, u)$. The dynamics of η are found by direct computation:

$$\begin{aligned}
\frac{d}{dt}\eta_R &= \frac{d}{dt}(R^T)\hat{R} + R^T\dot{\hat{R}} \\
&= -R^T\dot{R}R^T\hat{R} + R^T\dot{\hat{R}} \\
&= -R^T RS(\omega - b_\omega)R^T\hat{R} + R^T\hat{R}S(\omega - \hat{b}_\omega) + R^T\hat{R}S\Big(L_a^R E_a + L_m^R E_m\Big) \\
&= -S(\omega - \hat{b}_\omega + \hat{b}_\omega - b_\omega)R^T\hat{R} + R^T\hat{R}S(\omega - \hat{b}_\omega) + R^T\hat{R}S\Big(L_a^R E_a + L_m^R E_m\Big) \\
&= -S(I_\omega + \eta_\omega)\eta_R + \eta_R S(I_\omega) + \eta_R S\Big(L_a^R E_a + L_m^R E_m\Big) \\
\frac{d}{dt}\eta_R &= \eta_R S(I_\omega) - S(I_\omega)\eta_R - S(\eta_\omega)\eta_R + \eta_R S\Big(L_a^R E_a + L_m^R E_m\Big),
\end{aligned}$$

which together with $E = E(\eta_R, I_a, I_m)$ confirms Theorem 4. The dynamics of η_ω are very easy to compute,

$$\frac{d}{dt}\eta_\omega = \dot{\hat{b}}_\omega - \dot{b}_\omega = L_a^\omega E_a + L_m^\omega E_m$$

and also confirm Theorem 4.

4.7.1.3 Combined symmetries

The final AHRS design considers the case of combined symmetries in Section 4.4.2, where the body and ground frame are independently rotated. It turns out this case isn't interesting as shown below.

The symmetry group in the combined case is $G = SO(3) \times SO(3) \times \mathbb{R}^3 \ni (Q_0, R_0, \omega_0) = g$ so $\dim(G) = 9$ and we require $\phi_g^a \in \mathbb{R}^9$. Since $\xi_g \in \mathbb{R}^6$, we need to use a component from the input action υ to construct ϕ_g^a; we choose $\upsilon_g^a = \upsilon_g(a) = Q_0 a$. Remark this extra step was not required in Sections 4.7.1.1 and 4.7.1.2, however the method of normalization in Section 4.6.1 is unaffected and manually picking components of ϕ_g^a is normal when solving for the moving frame [112, p. 163]. Using $\phi_g^a = \xi_g \times \upsilon_g^a$ we find $\gamma(x)$,

$$\phi_g^a \begin{pmatrix} R \\ b_\omega \\ a \end{pmatrix} = \begin{pmatrix} Q_0 R R_0 \\ R_0^T(b_\omega + \omega_0) \\ Q_0 a \end{pmatrix} = \begin{pmatrix} I \\ 0 \\ a \end{pmatrix} \Longrightarrow Q_0 = I \Longrightarrow \gamma(x) = (I, R^T, -b_\omega),$$

and the complete set of invariants is

$$\phi^b_{\gamma(x)} \begin{pmatrix} \omega \\ m \\ y_a \\ y_m \end{pmatrix} = \begin{pmatrix} R(\omega - \hat{b}_\omega) \\ m \\ R y_a \\ R y_m \end{pmatrix} = \begin{pmatrix} I(x,u) \\ J_h(x,y) \end{pmatrix}.$$

We see that the $I(x,u)$ and $J_h(x,y)$ terms are *identical* to Section 4.7.1.1, the body-symmetry case, and so the invariant observer for the combined symmetries case has already been worked out as (4.15). Further, since $Q_0 = I$ in $\gamma(x)$, the invariant estimation error $\eta(x, \hat{x})$ and its dynamics will be identical to those of Section 4.7.1.1 as well. In this sense, we have not gained anything from using the more complicated symmetry group actions, although they still lead to a valid invariant observer design.

4.7.2 Invariant Aided INS Design

We now consider the Mag-plus-GPS-Aided INS in Section 4.5. The system equations (4.6), (4.7) are

$$\begin{aligned}
\dot{p} &= v \\
\dot{v} &= R(f - b_f) - a \\
\dot{R} &= RS(\omega - b_\omega) \\
\dot{b}_f &= 0 \\
\dot{b}_\omega &= 0 \\
\begin{bmatrix} y_p \\ y_m \end{bmatrix} &= \begin{bmatrix} p \\ R^T m \end{bmatrix}
\end{aligned}$$

4.7.2.1 Body frame symmetries

We verified in Section 4.5 that the Aided INS admits the symmetry group $G = \mathbb{R}^3 \times SO(3) \times \mathbb{R}^3 \times \mathbb{R}^3 \ni (p_0, R_0, b_{f0}, b_{\omega 0}) = g$, where R_0 physically represents a constant rotation of the body-fixed frame, through the set of Lie group actions

$$\begin{aligned}
\varphi_{(p_0,R_0,b_{f0},b_{\omega 0})} \begin{pmatrix} p \\ v \\ R \\ b_f \\ b_\omega \end{pmatrix} &= \begin{pmatrix} p + p_0 \\ v \\ RR_0 \\ R_0^T(b_f + b_{f0}) \\ R_0^T(b_\omega + b_{\omega 0}) \end{pmatrix} \\
\psi_{(p_0,R_0,b_{f0},b_{\omega 0})} \begin{pmatrix} f \\ \omega \end{pmatrix} &= \begin{pmatrix} R_0^T(f + b_{f0}) \\ R_0^T(\omega + b_{\omega 0}) \end{pmatrix} \\
\rho_{(p_0,R_0,b_{f0},b_{\omega 0})} \begin{pmatrix} y_p \\ y_m \end{pmatrix} &= \begin{pmatrix} y_p + p_0 \\ R_0^T y_m \end{pmatrix}
\end{aligned}$$

Following Section 4.6.1 we take $\phi_g^a = \varphi_g^a = \varphi_g^a(p, R, b_f, b_\omega)$ and $\phi_g^b = \varphi_g^b \times \psi_g \times \rho_g$ such that $\dim(\phi_g^a) = \dim(G)$. We then solve for the moving frame:

$$\begin{aligned}
\phi_g^a(x) = c \Longrightarrow \varphi_{(p_0,R_0,b_{f0},b_{\omega 0})} \begin{pmatrix} p \\ R \\ b_f \\ b_\omega \end{pmatrix} &= \begin{pmatrix} p + p_0 \\ RR_0 \\ R_0^T(b_f + b_{f0}) \\ R_0^T(b_\omega + b_{\omega 0}) \end{pmatrix} = \begin{pmatrix} 0 \\ I \\ 0 \\ 0 \end{pmatrix} \\
\Longrightarrow g = (-p, R^T, -b_f, -b_\omega) &= \gamma(x)
\end{aligned}$$

Using $\gamma(x) = (-p, R^T, -b_f, -b_\omega)$, we obtain the complete set of invariants as in Section 4.6.3,

$$\begin{aligned}
I(x,u) = \left(\varphi_{\gamma(x)}^b(x), \psi_{\gamma(x)}(u)\right) &= \begin{pmatrix} \varphi_{\gamma(x)}^b(v) \\ \psi_{\gamma(x)} \begin{pmatrix} f \\ \omega \end{pmatrix} \end{pmatrix} = \begin{pmatrix} v \\ R(f - b_f) \\ R(\omega - b_\omega) \end{pmatrix} = \begin{pmatrix} I_v \\ I_f \\ I_\omega \end{pmatrix} \\
J_h(x,y) = \rho_{\gamma(x)}(y) = \rho_{\gamma(x)} \begin{pmatrix} y_p \\ y_m \end{pmatrix} &= \begin{pmatrix} y_p - p \\ Ry_m \end{pmatrix}
\end{aligned}$$

and the invariant output error $E(\hat{x}, u, y)$ is

$$J_h(\hat{x}, h(\hat{x}, u)) - J_h(\hat{x}, y) = \begin{pmatrix} \hat{p} - \hat{p} \\ \hat{R}\hat{R}^T m \end{pmatrix} - \begin{pmatrix} y_p - \hat{p} \\ \hat{R}y_m \end{pmatrix} = \begin{pmatrix} \hat{p} - y_p \\ m - \hat{R}y_m \end{pmatrix} = \begin{pmatrix} E_p \\ E_m \end{pmatrix}$$

The invariant frame is computed as in Section 4.6.2. We have $\gamma(x)^{-1} = (p, R, b_f, b_\omega)$, and for each $\{p, v, b_f, b_\omega\} \in \mathbb{R}^3$, $T_e\mathbb{R}^3 \ni v_i = e_i$ while $R \in SO(3) \Longrightarrow T_eSO(3) \ni v_i = S(e_i)$, $i = 1, 2, 3$. Denoting $\underline{w}_i(x)$ and $\underline{v}_i$ as the concatenated invariant frames and basis vectors, respectively, we find

$$\begin{aligned}
\underline{w}_i(x) &= \left(\varphi_{\gamma(x)^{-1}}\right)_* \underline{v}_i \\
&= \frac{d}{d\tau}\left(\varphi_{\gamma(x)^{-1}}(\underline{v}_i\tau)\right)\Big|_{\tau=0} \\
&= \frac{d}{d\tau}\,\varphi_{\gamma(x)^{-1}}\begin{pmatrix} e_i\tau \\ e_i\tau \\ S(e_i)\tau \\ e_i\tau \\ e_i\tau \end{pmatrix}\Bigg|_{\tau=0} \\
&= \frac{d}{d\tau}\begin{pmatrix} e_i\tau + p \\ e_i\tau \\ S(e_i)\tau R \\ R^T(e_i\tau + b_f) \\ R^T(e_i\tau + b_\omega) \end{pmatrix}\Bigg|_{\tau=0} = \begin{pmatrix} e_i \\ e_i \\ S(e_i)R \\ R^Te_i \\ R^Te_i \end{pmatrix} = \begin{pmatrix} w_i^p \\ w_i^v \\ w_i^R(x) \\ w_i^{bf}(x) \\ w_i^{b\omega}(x) \end{pmatrix}
\end{aligned}$$

The invariant observer is then given as (4.13) in Section 4.6.3 where we partition the row gains $\overline{\mathcal{L}}_i$ as $[\overline{\mathcal{L}}_{i,p} \quad \overline{\mathcal{L}}_{i,m}]$ and the invariant output error vector as $E = [E_p^T \quad E_m^T]^T$:

$$\begin{aligned}
\dot{\hat{p}} &= \hat{v} + \sum_{i=1}^{3}\{\overline{\mathcal{L}}_{i,p}^p E_p + \overline{\mathcal{L}}_{i,m}^p E_m\}e_i = \hat{v} + L_p^p E_p + L_m^p E_m \\
\dot{\hat{v}} &= \hat{R}(f - \hat{b}_f) - a + \sum_{i=1}^{3}\{\overline{\mathcal{L}}_{i,p}^v E_p + \overline{\mathcal{L}}_{i,m}^v E_m\}e_i = \hat{R}(f - \hat{b}_f) - a + L_p^v E_p + L_m^v E_m \\
\dot{\hat{R}} &= \hat{R}S(\omega - \hat{b}_\omega) + \sum_{i=1}^{3}\{\overline{\mathcal{L}}_{i,p}^R E_p + \overline{\mathcal{L}}_{i,m}^R E_m\}S(e_i)\hat{R} \\
&= \hat{R}S(\omega - \hat{b}_\omega) + S\big[L_p^R E_p + L_m^R E_m\big]\hat{R} \\
\dot{\hat{b}}_f &= \sum_{i=1}^{3}\{\overline{\mathcal{L}}_{i,p}^{bf} E_p + \overline{\mathcal{L}}_{i,m}^{bf} E_m\}\hat{R}^T e_i = \hat{R}^T\big(L_p^{bf} E_p + L_m^{bf} E_m\big) \\
\dot{\hat{b}}_\omega &= \sum_{i=1}^{3}\{\overline{\mathcal{L}}_{i,p}^{b\omega} E_p + \overline{\mathcal{L}}_{i,m}^{b\omega} E_m\}\hat{R}^T e_i = \hat{R}^T\big(L_p^{b\omega} E_p + L_m^{b\omega} E_m\big)
\end{aligned} \tag{4.17}$$

where the L terms are 3×3 matrix gains whose entries are in general functions of $I(\hat{x}, u)$ and $E(\hat{x}, u, y)$ by Theorem 3. The invariant estimation error η associated to

the above observer is calculated from (4.14)

$$\begin{aligned}\eta &= \varphi_{\gamma(x)}(\hat{x}) - \varphi_{\gamma(x)}(x) \\ &= \begin{pmatrix} \hat{p} - p \\ \hat{v} \\ \hat{R}R^T \\ R(\hat{b}_f - b_f) \\ R(\hat{b}_\omega - b_\omega) \end{pmatrix} - \begin{pmatrix} p - p \\ v \\ RR^T \\ R(b_f - b_f) \\ R(b_\omega - b_\omega) \end{pmatrix} = \begin{pmatrix} \hat{p} - p \\ \hat{v} - v \\ \hat{R}R^T - I \\ R(\hat{b}_f - b_f) \\ R(\hat{b}_\omega - b_\omega) \end{pmatrix} = \begin{pmatrix} \eta_p \\ \eta_v \\ \eta_R - I \\ \eta_{bf} \\ \eta_{b\omega} \end{pmatrix}\end{aligned}$$

where as before we have taken $\eta_R = \hat{R}R^T$ instead of $\hat{R}R^T - I$ for convenience. We will work out the dynamics $\dot{\eta}$ below, which by Theorem 4 are guaranteed to depend on the system's trajectories only through the invariants I_v, I_f and I_ω found above. The invariant output error components can be expressed as

$$\begin{aligned} E_p &= \hat{p} - y_p = \hat{p} - p = \eta_p \\ E_m &= m - \hat{R}y_m = m - \hat{R}R^T m = m - \eta_R m \end{aligned}$$

and we proceed to compute the individual η dynamics:

$$\begin{aligned}\dot{\eta}_p &= \dot{\hat{p}} - \dot{p} \\ &= \hat{v} + L_p^p E_p + L_m^p E_m - v \\ &= \eta_v + L_p^p E_p + L_m^p E_m\end{aligned}$$

$$\begin{aligned}\dot{\eta}_v &= \dot{\hat{v}} - \dot{v} \\ &= \hat{R}(f - \hat{b}_f) - a + L_p^v E_p + L_m^v E_m - R(f - b_f) + a \\ &= I_f + L_p^v E_p + L_m^v E_m - R(f - \hat{b}_f + \hat{b}_f - b_f) \\ &= I_f + L_p^v E_p + L_m^v E_m - R\hat{R}^T\hat{R}(f - \hat{b}_f) - R(\hat{b}_f - b_f) \\ &= I_f + L_p^v E_p + L_m^v E_m - (\eta_R)^T I_f - \eta_{bf}\end{aligned}$$

$$\begin{aligned}\dot{\eta}_R &= \dot{\hat{R}}R^T - \hat{R}R^T\dot{R}R^T \\ &= \hat{R}S(\omega - \hat{b}_\omega)R^T + S\big[L_p^R E_p + L_m^R E_m\big]\hat{R}R^T - \hat{R}R^T RS(\omega - b_\omega)R^T \\ &= \hat{R}S(b_\omega - \hat{b}_\omega)R^T + S\big[L_p^R E_p + L_m^R E_m\big]\eta_R \\ &= -\hat{R}R^T RS(\hat{b}_\omega - b_\omega)R^T + S\big[L_p^R E_p + L_m^R E_m\big]\eta_R \\ &= -\eta_R S(\eta_{b\omega}) + S\big[L_p^R E_p + L_m^R E_m\big]\eta_R\end{aligned}$$

$$
\begin{aligned}
\dot{\eta}_{bf} &= \dot{R}(\hat{b}_f - b_f) + R(\dot{\hat{b}}_f - \dot{b}_f) \\
&= RS(\omega - b_\omega)(\hat{b}_f - b_f) + R\hat{R}^T\big(L_p^{bf}E_p + L_m^{bf}E_m\big) \\
&= RS(\omega - \hat{b}_\omega + \hat{b}_\omega - b_\omega)(\hat{b}_f - b_f) + (\eta_R)^T\big(L_p^{bf}E_p + L_m^{bf}E_m\big) \\
&= R\hat{R}^T\hat{R}S(\omega - \hat{b}_\omega)\hat{R}^T\hat{R}R^TR(\hat{b}_f - b_f) + RS(\hat{b}_\omega - b_\omega)R^TR(\hat{b}_f - b_f) \\
&\quad + (\eta_R)^T\big(L_p^{bf}E_p + L_m^{bf}E_m\big) \\
&= (\eta_R)^TS(I_\omega)\eta_R\eta_{bf} + S(\eta_{b\omega})\eta_{bf} + (\eta_R)^T\big(L_p^{bf}E_p + L_m^{bf}E_m\big) \\
&= S\big[(\eta_R)^TI_\omega + \eta_{b\omega}\big]\eta_{bf} + (\eta_R)^T\big(L_p^{bf}E_p + L_m^{bf}E_m\big)
\end{aligned}
$$

$$
\begin{aligned}
\dot{\eta}_{b\omega} &= \dot{R}(\hat{b}_\omega - b_\omega) + R(\dot{\hat{b}}_\omega - \dot{b}_\omega) \\
&= RS(\omega - b_\omega)(\hat{b}_\omega - b_\omega) + R\hat{R}^T\big(L_p^{b\omega}E_p + L_m^{b\omega}E_m\big) \\
&= RS(\omega - \hat{b}_\omega + \hat{b}_\omega - b_\omega)(\hat{b}_\omega - b_\omega) + (\eta_R)^T\big(L_p^{b\omega}E_p + L_m^{b\omega}E_m\big) \\
&= R\hat{R}^T\hat{R}S(\omega - \hat{b}_\omega)\hat{R}^T\hat{R}R^TR(\hat{b}_\omega - b_\omega) + RS(\hat{b}_\omega - b_\omega)R^TR(\hat{b}_\omega - b_\omega) \\
&\quad + (\eta_R)^T\big(L_p^{b\omega}E_p + L_m^{b\omega}E_m\big) \\
&= (\eta_R)^TS(I_\omega)\eta_R\eta_{b\omega} + S(\eta_{b\omega})\eta_{b\omega} + (\eta_R)^T\big(L_p^{b\omega}E_p + L_m^{b\omega}E_m\big) \\
&= S\big[(\eta_R)^TI_\omega\big]\eta_{b\omega} + (\eta_R)^T\big(L_p^{b\omega}E_p + L_m^{b\omega}E_m\big)
\end{aligned}
$$

The above error dynamics clearly verify Theorem 4. The error system is non-autonomous and depends on the estimated states $\hat{R}$, $\hat{b}_f$ and $\hat{b}_\omega$ as well as input signals f and ω through the I_f and I_ω terms. Remark the η dynamics are independent of both position and velocity $\hat{p}$ and $\hat{v}$ which simplifies stability analysis and gain selection over the general case.

4.7.2.2 Ground frame symmetries

We now consider the ground-frame symmetries of the Aided INS for which the symmetry group is $G = \mathbb{R}^3 \times SO(3) \times \mathbb{R}^3 \times \mathbb{R}^3 \ni (p_0, Q_0, b_{f0}, b_{\omega 0}) = g$ where Q_0 represents a constant rotation of the ground frame. From Section 4.5 the corresponding Lie group actions on the state, input and output manifolds are

$$
\begin{aligned}
\Phi_{(p_0,Q_0,b_{f0},b_{\omega 0})}\begin{pmatrix} p \\ v \\ R \\ b_f \\ b_\omega \end{pmatrix} &= \begin{pmatrix} Q_0(p + p_0) \\ Q_0 v \\ Q_0 R \\ b_f + b_{f0} \\ b_\omega + b_{\omega 0} \end{pmatrix} \\
\Psi_{(p_0,Q_0,b_{f0},b_{\omega 0})}\begin{pmatrix} f \\ \omega \\ a \\ m \end{pmatrix} &= \begin{pmatrix} f + b_{f0} \\ \omega + b_{\omega 0} \\ Q_0 a \\ Q_0 m \end{pmatrix} \\
\Upsilon_{(p_0,Q_0,b_{f0},b_{\omega 0})}\begin{pmatrix} y_p \\ y_m \end{pmatrix} &= \begin{pmatrix} Q_0(y_p + p_0) \\ y_m \end{pmatrix}
\end{aligned}
$$

We partition the Lie group action $\phi_g = \Phi_g \times \Psi_g \times \Upsilon_g$ as $\phi_g^a = \Phi_g^a = \Phi_g^a(p, R, b_f, b_\omega)$ and $\phi_g^b = \Phi_g^b \times \Psi_g \times \Upsilon_g$ and solve $\phi_g^a(x) = c$ for the moving frame:

$$\Phi_g^a \begin{pmatrix} p \\ R \\ b_f \\ b_\omega \end{pmatrix} = \begin{pmatrix} Q_0(p + p_0) \\ Q_0 R \\ b_f + b_{f0} \\ b_\omega + b_{\omega 0} \end{pmatrix} = \begin{pmatrix} 0 \\ I \\ 0 \\ 0 \end{pmatrix} \Longrightarrow g = (-p, R^T, -b_f, -b_\omega) = \gamma(x)$$

The complete set of invariants is then

$$I(x,u) = \begin{pmatrix} \Phi^b_{\gamma(x)}(x) \\ \Psi_{\gamma(x)}(u) \end{pmatrix} = \begin{pmatrix} \Phi^b_{(-p,R^T,-b_f,-b_\omega)}(v) \\ \Psi_{(-p,R^T,-b_f,-b_\omega)} \begin{pmatrix} f \\ \omega \\ a \\ m \end{pmatrix} \end{pmatrix} = \begin{pmatrix} R^T v \\ f - b_f \\ \omega - b_\omega \\ R^T a \\ R^T m \end{pmatrix} = \begin{pmatrix} I_v \\ I_f \\ I_\omega \\ I_a \\ I_m \end{pmatrix}$$

$$J_h(x,y) = \Upsilon_{\gamma(x)}(y) = \Upsilon_{(-p,R^T,-b_f,-b_\omega)} \begin{pmatrix} y_p \\ y_m \end{pmatrix} = \begin{pmatrix} R^T(y_p - p) \\ y_m \end{pmatrix}$$

The invariant output error is

$$\begin{aligned} E(\hat{x}, u, y) &= J_h(\hat{x}, h(\hat{x}, u)) - J_h(\hat{x}, y) \\ &= \begin{pmatrix} \hat{R}^T(\hat{p} - \hat{p}) \\ \hat{R}^T m \end{pmatrix} - \begin{pmatrix} \hat{R}^T(y_p - \hat{p}) \\ y_m \end{pmatrix} = \begin{pmatrix} \hat{R}^T(\hat{p} - y_p) \\ \hat{R}^T m - y_m \end{pmatrix} = \begin{pmatrix} E_p \\ E_m \end{pmatrix} \end{aligned}$$

For the invariant frame computation, we have $\gamma(x)^{-1} = (p, R, b_f, b_\omega)$ and the same $\underline{v}_i$ as in Section 4.7.2.1. We find

$$\begin{aligned} \underline{w}_i(x) &= \left(\Phi_{\gamma(x)^{-1}}\right)_* \underline{v}_i \\ &= \frac{d}{d\tau} \left(\Phi_{\gamma(x)^{-1}}(\underline{v}_i \tau) \right) \Big|_{\tau=0} \\ &= \frac{d}{d\tau} \, \Phi_{\gamma(x)^{-1}} \begin{pmatrix} e_i \tau \\ e_i \tau \\ S(e_i)\tau \\ e_i \tau \\ e_i \tau \end{pmatrix} \Bigg|_{\tau=0} \\ &= \frac{d}{d\tau} \begin{pmatrix} R(e_i\tau + p) \\ Re_i\tau \\ RS(e_i)\tau \\ e_i\tau + b_f \\ e_i\tau + b_\omega \end{pmatrix} \Bigg|_{\tau=0} = \begin{pmatrix} Re_i \\ Re_i \\ RS(e_i) \\ e_i \\ e_i \end{pmatrix} = \begin{pmatrix} w_i^p(x) \\ w_i^v(x) \\ w_i^R(x) \\ w_i^{bf} \\ w_i^{b\omega} \end{pmatrix} \end{aligned}$$

The invariant observer is then

$$
\begin{aligned}
\dot{\hat{p}} &= \hat{v} + \sum_{i=1}^{3} \{\overline{\mathcal{L}}_{i,p}^{p} E_p + \overline{\mathcal{L}}_{i,m}^{p} E_m\} \hat{R} e_i = \hat{v} + \hat{R}\big(L_p^p E_p + L_m^p E_m\big) \\
\dot{\hat{v}} &= \hat{R}(f - \hat{b}_f) - a + \sum_{i=1}^{3} \{\overline{\mathcal{L}}_{i,p}^{v} E_p + \overline{\mathcal{L}}_{i,m}^{v} E_m\} \hat{R} e_i \\
&= \hat{R}(f - \hat{b}_f) - a + \hat{R}\big(L_p^v E_p + L_m^v E_m\big) \\
\dot{\hat{R}} &= \hat{R} S(\omega - \hat{b}_\omega) + \sum_{i=1}^{3} \{\overline{\mathcal{L}}_{i,p}^{R} E_p + \overline{\mathcal{L}}_{i,m}^{R} E_m\} \hat{R} S(e_i) \\
&= \hat{R} S(\omega - \hat{b}_\omega) + \hat{R} S\big[L_p^R E_p + L_m^R E_m\big] \\
\dot{\hat{b}}_f &= \sum_{i=1}^{3} \{\overline{\mathcal{L}}_{i,p}^{bf} E_p + \overline{\mathcal{L}}_{i,m}^{bf} E_m\} e_i = L_p^{bf} E_p + L_m^{bf} E_m \\
\dot{\hat{b}}_\omega &= \sum_{i=1}^{3} \{\overline{\mathcal{L}}_{i,p}^{b\omega} E_p + \overline{\mathcal{L}}_{i,m}^{b\omega} E_m\} e_i = L_p^{b\omega} E_p + L_m^{b\omega} E_m
\end{aligned}
\tag{4.18}
$$

where as in Section 4.7.2.1 the L terms are 3×3 matrix gains whose entries are in general functions of $I(\hat{x}, u)$ and $E(\hat{x}, u, y)$. The invariant estimation error η for this observer is

$$
\begin{aligned}
\eta &= \Phi_{\gamma(x)}(\hat{x}) - \Phi_{\gamma(x)}(x) \\
&= \begin{pmatrix} R^T(\hat{p} - p) \\ R^T \hat{v} \\ R^T \hat{R} \\ \hat{b}_f - b_f \\ \hat{b}_\omega - b_\omega \end{pmatrix} - \begin{pmatrix} R^T(p - p) \\ R^T v \\ R^T R \\ b_f - b_f \\ b_\omega - b_\omega \end{pmatrix} = \begin{pmatrix} R^T(\hat{p} - p) \\ R^T(\hat{v} - v) \\ R^T \hat{R} - I \\ \hat{b}_f - b_f \\ \hat{b}_\omega - b_\omega \end{pmatrix} = \begin{pmatrix} \eta_p \\ \eta_v \\ \eta_R - I \\ \eta_{bf} \\ \eta_{b\omega} \end{pmatrix}
\end{aligned}
$$

The invariant output error E components are written as

$$
\begin{aligned}
E_p &= \hat{R}^T(\hat{p} - y_p) = \hat{R}^T R R^T(\hat{p} - p) = (\eta_R)^T \eta_p \\
E_m &= \hat{R}^T m - y_m = \hat{R}^T m - R^T m = I_m - R^T \hat{R} \hat{R}^T m = I_m - \eta_R I_m
\end{aligned}
$$

We now work out the $\dot{\eta}$ dynamics:

$$\begin{aligned}
\dot{\eta}_p &= -R^T\dot{R}R^T(\hat{p}-p) + R^T(\dot{\hat{p}}-\dot{p}) \\
&= -R^TRS(\omega-b_\omega)R^T(\hat{p}-p) + R^T\Big(\hat{v}+\hat{R}\big(L^p_pE_p+L^p_mE_m\big)-v\Big) \\
&= -S(\omega-\hat{b}_\omega+\hat{b}_\omega-b_\omega)\eta_p+\eta_v+R^T\hat{R}\big(L^p_pE_p+L^p_mE_m\big) \\
&= -S\big[I_\omega+\eta_{b\omega}\big]\eta_p+\eta_v+\eta_R\big(L^p_pE_p+L^p_mE_m\big)
\end{aligned}$$

$$\begin{aligned}
\dot{\eta}_v &= -R^T\dot{R}R^T(\hat{v}-v) + R^T(\dot{\hat{v}}-\dot{v}) \\
&= -R^TRS(\omega-b_\omega)R^T(\hat{v}-v) \\
&\quad + R^T\big\{\hat{R}(f-\hat{b}_f)-a+\hat{R}\big(L^v_pE_p+L^v_mE_m\big)-R(f-b_f)+a\big\} \\
&= -S(\omega-\hat{b}_\omega+\hat{b}_\omega-b_\omega)\eta_v+\eta_RI_f+\eta_R\big(L^v_pE_p+L^v_mE_m\big)-(f-\hat{b}_f+\hat{b}_f-b_f) \\
&= -S\big[I_\omega+\eta_{b\omega}\big]\eta_v+\eta_RI_f+\eta_R\big(L^v_pE_p+L^v_mE_m\big)-I_f-\eta_{bf}
\end{aligned}$$

$$\begin{aligned}
\dot{\eta}_R &= -R^T\dot{R}R^T\hat{R}+R^T\dot{\hat{R}} \\
&= -R^TRS(\omega-b_\omega)R^T\hat{R}+R^T\hat{R}S(\omega-\hat{b}_\omega)+R^T\hat{R}S\big[L^R_pE_p+L^R_mE_m\big] \\
&= -S(\omega-\hat{b}_\omega+\hat{b}_\omega-b_\omega)\eta_R+\eta_RS(I_\omega)+\eta_RS\big[L^R_pE_p+L^R_mE_m\big] \\
&= -S\big[I_\omega+\eta_{b\omega}\big]\eta_R+\eta_RS(I_\omega)+\eta_RS\big[L^R_pE_p+L^R_mE_m\big]
\end{aligned}$$

$$\begin{aligned}
\dot{\eta}_{bf} &= \dot{\hat{b}}_f-\dot{b}_f \\
&= L^{bf}_pE_p+L^{bf}_mE_m
\end{aligned}$$

$$\begin{aligned}
\dot{\eta}_{b\omega} &= \dot{\hat{b}}_\omega-\dot{b}_\omega \\
&= L^{b\omega}_pE_p+L^{b\omega}_mE_m
\end{aligned}$$

The ground-frame symmetry version of the invariant observer has properties similar to the body-frame symmetry version in Section 4.7.2.1: the estimation error dynamics $\dot{\eta}$ are a function of the system estimates via $\hat{R}$, $\hat{b}_f$ and $\hat{b}_\omega$ as well as inputs f, ω but independent of position and velocity $\hat{p}$ and $\hat{v}$.

4.7.2.3 Combined symmetries

In Section 4.5 we also considered the combined symmetry case of rotating both the body and ground frames. The corresponding Lie group actions were denoted by ξ_g, υ_g and ϱ_g. Based on Section 4.7.1.3, we may expect this case to reduce to one of the previous results.

Take the Lie group action $\phi_g = \xi_g \times \upsilon_g \times \varrho_g$; with the symmetry group $G = \mathbb{R}^3 \times SO(3) \times SO(3) \times \mathbb{R}^3 \times \mathbb{R}^3 \ni (p_0, Q_0, R_0, b_{f0}, b_{\omega 0}) = g$ and state manifold $X = \mathbb{R}^3 \times \mathbb{R}^3 \times SO(3) \times \mathbb{R}^3 \times \mathbb{R}^3 \ni (p, v, R, b_f, b_\omega) = g$ both of dimension 15, we logically partition $\phi^a_g = \xi_g$, $\phi^b_g = \upsilon_g \times \varrho_g$ and (attempt to) solve for the moving

frame:

$$\xi_g \begin{pmatrix} p \\ v \\ R \\ b_f \\ b_\omega \end{pmatrix} = \begin{pmatrix} Q_0(p+p_0) \\ Q_0 v \\ Q_0 R R_0 \\ R_0^T(b_f + b_{f0}) \\ R_0^T(b_\omega + b_{\omega 0}) \end{pmatrix} = \begin{pmatrix} 0 \\ 0 \\ I \\ 0 \\ 0 \end{pmatrix}$$

We immediately see two problems:

- $Q_0 v = 0$ has no solution for $Q_0 \in SO(3)$ except in the trivial case of $v = 0$. In the more general case of $Q_0 v = c$, $c \in \mathbb{R}^3$, a solution will exist only if $\|v\| = \|c\|$.
- $Q_0 R R_0 = I$ has a non-unique solution: $Q_0 = (R R_0)^T$ or alternatively $R_0 = (Q_0 R)^T$.

We deal with this problem by a different choice of ϕ_g^a components, c.f. Section 4.7.1.3. We remove the $\xi_g(v)$ component and replace it with $\upsilon_g(a)$ which provides a system which can be solved for the moving frame:

$$\phi_g^a \begin{pmatrix} p \\ a \\ R \\ b_f \\ b_\omega \end{pmatrix} = \begin{pmatrix} Q_0(p+p_0) \\ Q_0 a \\ Q_0 R R_0 \\ R_0^T(b_f + b_{f0}) \\ R_0^T(b_\omega + b_{\omega 0}) \end{pmatrix} = \begin{pmatrix} 0 \\ a \\ I \\ 0 \\ 0 \end{pmatrix} \Longrightarrow g = (-p, I, R^T, -b_f, -b_\omega) = \gamma(x)$$

and the complete set of invariants is

$$\phi^b_{\gamma(x)} \begin{pmatrix} v \\ f \\ \omega \\ m \\ y_p \\ y_m \end{pmatrix} = \begin{pmatrix} v \\ R(f - b_f) \\ R(\omega - b_\omega) \\ m \\ y_p - p \\ R y_m \end{pmatrix} = \begin{pmatrix} I(x,u) \\ J_h(x,y) \end{pmatrix}$$

which are precisely the invariants in Section 4.7.2.1, such that the invariant observer for the combined symmetries case will be identical to the earlier design. The invariant estimation error and its dynamics will also be identical to Section 4.7.2.1 due to the $Q_0 = I$ term. While using the combined symmetries case is valid, it results in greater complexity and provides the same design as a simpler case. A combined symmetries version of invariant observer design was used in [92] for an Aided INS example with different dynamics and outputs than (4.6) and (4.7).

4.8 Nonlinear Observer Gain Design

So far, we have not said anything about gain selection for stabilizing the observer. As mentioned in Section 4.6.3, there is no general systematic approach for choosing the nonlinear observer gains L. Using the invariant AHRS observer (4.15) with body-frame symmetries in Section 4.7.1.1, we now show how a particular choice of gains reduces it to the "explicit complementary filter with bias correction" in [88,

Thm. 5.1], for which *almost* global asymptotic stability [78][1] has been proven using a Lyapunov analysis; this is the strongest result achievable since any system whose state manifold includes $SO(3)$ cannot be globally asymptotically stable [20]. Observer (4.15) is repeated here for convenience:

$$\begin{aligned}\dot{\hat{R}} &= \hat{R}S(\omega - \hat{b}_\omega) + S\big(L_a^R E_a + L_m^R E_m\big)\hat{R} \\ \dot{\hat{b}}_\omega &= \hat{R}^T\big(L_a^\omega E_a + L_m^\omega E_m\big)\end{aligned}$$

We make the following gain choices:

$$\begin{aligned} L_a^R &= k_P l_a S(a) \quad & L_m^R &= k_P l_m S(m) \\ L_a^\omega &= -k_I l_a S(a) \quad & L_m^\omega &= -k_I l_m S(m) \end{aligned} \tag{4.19}$$

where $k_P, k_I, l_a, l_m \in \mathbb{R}$ are user-selected constants and $a, m \in \mathbb{R}^3$ are the ground-frame gravity and magnetic field vectors used previously. This set of constant gains obviously satisfies $L = L(I, E)$ and so the observer is invariant. Remark that we have reduced the tuning degrees of freedom from $4 \times 9 = 36$ to 4.

Using the above gains and the invariant error definitions $E_a = a - \hat{R}y_a$, $E_m = m - \hat{R}y_m$ in (4.15) gives

$$\begin{aligned}\dot{\hat{R}} &= \hat{R}S(\omega - \hat{b}_\omega) + S\big(k_P l_a S(a)(a - \hat{R}y_a) + k_P l_m S(m)(m - \hat{R}y_m)\big)\hat{R} \\ \dot{\hat{b}}_\omega &= \hat{R}^T\big(- k_I l_a S(a)(a - \hat{R}y_a) - k_I l_m S(m)(m - \hat{R}y_m)\big)\end{aligned}$$

since $S(a)a = a \times a = 0$ and $S(m)m = m \times m = 0$, we have

$$\begin{aligned}\dot{\hat{R}} &= \hat{R}S(\omega - \hat{b}_\omega) - k_P S\big(l_a S(a)\hat{R}y_a + l_m S(m)\hat{R}y_m\big)\hat{R} \\ \dot{\hat{b}}_\omega &= k_I \hat{R}^T\big(l_a S(a)\hat{R}y_a + l_m S(m)\hat{R}y_m\big)\end{aligned}$$

Using $R^T S(v)R = S(R^T v) \Longrightarrow S(v)R = RS(R^T v)$ from Section 2.2, we have

$$\begin{aligned}\dot{\hat{R}} &= \hat{R}S(\omega - \hat{b}_\omega) - k_P \hat{R}S\big(l_a \hat{R}^T S(a)\hat{R}y_a + l_m \hat{R}^T S(m)\hat{R}y_m\big) \\ \dot{\hat{b}}_\omega &= k_I\big(l_a \hat{R}^T S(a)\hat{R}y_a + l_m \hat{R}^T S(m)\hat{R}y_m\big)\end{aligned}$$

We also have $\hat{R}^T S(v)\hat{R} = S(\hat{R}^T v) = S(\hat{y}_v)$ where $v = a, m$:

$$\begin{aligned}\dot{\hat{R}} &= \hat{R}S(\omega - \hat{b}_\omega) - k_P \hat{R}S\big(l_a S(\hat{y}_a)y_a + l_m S(\hat{y}_m)y_m\big) \\ \dot{\hat{b}}_\omega &= k_I\big(l_a S(\hat{y}_a)y_a + l_m S(\hat{y}_m)y_m\big)\end{aligned}$$

And since $S(\hat{y}_v)y_v = \hat{y}_v \times y_v = -y_v \times \hat{y}_v$ we obtain

$$\begin{aligned}\dot{\hat{R}} &= \hat{R}\Big(S(\omega - \hat{b}_\omega) + k_P S\big(l_a y_a \times \hat{y}_a + l_m y_m \times \hat{y}_m\big)\Big) \\ \dot{\hat{b}}_\omega &= -k_I\big(l_a y_a \times \hat{y}_a + l_m y_m \times \hat{y}_m\big),\end{aligned}$$

[1] A system is almost globally asymptotically stable if all trajectories starting in an open dense subset of the state space asymptotically converge to a stable equilibrium; or equivalently, the set of initial conditions for which the trajectories do not converge form a set of zero Lebesgue measure [103].

which is identical to [88, Eqn. (32)] modulo choice of notation.

It is also possible to reduce the ground-frame symmetries invariant observer (4.16),

$$\begin{aligned}\dot{\hat{R}} &= \hat{R}S(\omega - \hat{b}_\omega) + \hat{R}S\Big(L^R_a E_a + L^R_m E_m\Big)\\ \dot{\hat{b}}_\omega &= L^\omega_a E_a + L^\omega_m E_m,\end{aligned}$$

to [88, Eqn. (32)] using the (different) set of gains

$$\begin{aligned} L^R_a &= k_P l_a S(\hat{R}^T a) \quad & L^R_m &= k_P l_m S(\hat{R}^T m)\\ L^\omega_a &= -k_I l_a S(\hat{R}^T a) \quad & L^\omega_m &= -k_I l_m S(\hat{R}^T m)\end{aligned} \tag{4.20}$$

where as before k_P, k_I, l_a, l_m are constant scalars. Note that in Section 4.7.1.2, we computed $I_a = \hat{R}^T a$, $I_m = \hat{R}^T m$ and so the above gains respect the invariant observer condition $L = L(I, E)$. Using these gains and $E_a = \hat{R}^T a - y_a$, $E_m = \hat{R}^T m - y_m$ in (4.16) gives

$$\begin{aligned}\dot{\hat{R}} &= \hat{R}S(\omega - \hat{b}_\omega) + \hat{R}S\big[k_P l_a S(\hat{R}^T a)(\hat{R}^T a - y_a) + k_P l_m S(\hat{R}^T m)(\hat{R}^T m - y_m)\big]\\ \dot{\hat{b}}_\omega &= -k_I l_a S(\hat{R}^T a)(\hat{R}^T a - y_a) - k_I l_m S(\hat{R}^T m)(\hat{R}^T m - y_m)\end{aligned}$$

using $\hat{R}^T a = \hat{y}_a$, $\hat{R}^T m = \hat{y}_m$, $S(x)y = x \times y$ and $y \times y = 0$ we obtain

$$\begin{aligned}\dot{\hat{R}} &= \hat{R}S(\omega - \hat{b}_\omega) - k_P \hat{R}S\big(l_a \hat{y}_a \times y_a + l_m \hat{y}_m \times y_m\big)\\ \dot{\hat{b}}_\omega &= k_I\big(l_a \hat{y}_a \times y_a + l_m \hat{y}_m \times y_m\big)\end{aligned}$$

and then from $x \times y = -y \times x$ we have

$$\begin{aligned}\dot{\hat{R}} &= \hat{R}\Big(S(\omega - \hat{b}_\omega) + k_P S\big(l_a y_a \times \hat{y}_a + l_m y_m \times \hat{y}_m\big)\Big)\\ \dot{\hat{b}}_\omega &= -k_I\big(l_a y_a \times \hat{y}_a + l_m y_m \times \hat{y}_m\big),\end{aligned}$$

the observer [88, Eqn. (32)]. Remark the gain choices for L are different for the body-frame symmetries observer (4.15) and the ground-frame symmetries observer (4.16), but in both cases the observer in [88] is (a particular choice of) an invariant observer.

A nonlinear design for the gains of Aided INS observers (4.17), (4.18) remains an open problem. Recent work in [31, 24] provides direct nonlinear gain designs for a GPS-aided dead-reckoning system (c.f. [51, Ch. 9]) guaranteeing local, almost global or global stability depending on the level of assumptions made about the system's state and inputs. Dead reckoning is a 2-dimensional aided navigation problem and so it is reasonable to expect the analysis method can be extended to Aided INS (4.6), (4.7) in Section 4.5, however no results have been obtained at the time of writing. Another source of ideas are the direct nonlinear observer designs in [69, 118] for the velocity-aided inertial navigation example considered in [27].

4.9 Invariant Extended Kalman Filter

Although a direct nonlinear design for the observer gains L is the most elegant approach, it is also difficult and non-systematic. In this Section we propose a method

of gain assignment based on the Extended Kalman Filter covered in Section 3.2. The Invariant EKF re-linearizes the invariant estimation error η dynamics (instead of the system dynamics $f(x,u)$ as in the conventional EKF) about the latest estimated state and computes optimal observer gains L for the resulting system. This provides a fully systematic approach to obtaining the observer gains, which are also automatically updated in the case of changing noise conditions due to the optimality of the Kalman Filter. The obvious disadvantage is that the Invariant EKF guarantees only local stability whose region of attraction is difficult to analyze as discussed in Section 4.1.

Using an EKF to find the gains of an invariant observer was first proposed in [23] and applied to different examples in [29, 96]. The method in [23] was formulated for the class of systems where the Lie group G acts on itself by left or right translation (c.f. Section 4.6.1) and required defining invariant noise terms which preserve the symmetry of the system. We adapt the method to apply to the general class of G-invariant systems defined in Section 4.3 and such that the noise terms can enter the dynamics naturally as part of the sensor models, c.f. Section 3.2.2. The modified Invariant EKF can thus be applied to AHRS with body-frame symmetries (Section 4.4) and Aided INS (Section 4.5).

4.9.1 Invariant EKF Overview

We first review the continuous-time Kalman filter, e.g. [34, Chap. 7]. The filter applies to LTV systems

$$\begin{aligned} \dot{x} &= A(t)x + B(t)w \\ y &= C(t)x + D(t)v \end{aligned} \tag{4.21}$$

where w and v are the process and measurement Gaussian white noise vectors with covariances $Q = E\langle ww^T\rangle$, $R = E\langle vv^T\rangle$, respectively, and zero cross-correlation: $E\langle wv^T\rangle = 0$. The Kalman filter for (4.21) is

$$\begin{aligned} \dot{\hat{x}} &= A\hat{x} + K(y - C\hat{x}) \\ K &= PC^T(DRD^T)^{-1} \\ \dot{P} &= AP + PA^T - PC^T(DRD^T)^{-1}CP + BQB^T, \end{aligned} \tag{4.22}$$

a linear optimal observer designed to minimize the covariance of the estimation error $e = \hat{x} - x$, specifically $\min\big(\text{trace}(E\langle e\, e^T\rangle)\big)$. From (4.22) and (4.21), the estimation error dynamics are

$$\begin{aligned} \dot{e} &= \dot{\hat{x}} - \dot{x} \\ &= A\hat{x} + K\left(Cx + Dv - C\hat{x}\right) - Ax - Bw \\ &= (A - KC)(\hat{x} - x) - Bw + KDv \\ \dot{e} &= (A - KC)e - Bw + KDv \end{aligned} \tag{4.23}$$

The method of the Invariant EKF is as follows: introduce the sensor noise models $\tilde{u} = u + w$, $\tilde{y} = y + v$ from Section 3.2.2 into the nominal system dynamics and corresponding invariant observer as

$$\dot{x} = f(x,u) = f(x, \tilde{u} - w) \tag{4.24a}$$

$$\dot{\hat{x}} = F(\hat{x}, \tilde{u}, \tilde{y}) = F(\hat{x}, \tilde{u}, y + v) \tag{4.24b}$$

Using the existing invariant estimation error η (4.14) for this system, compute $(d/dt)\eta$ using terms (4.24) which yields the nonlinear dynamics

$$\frac{d}{dt}\eta = \Xi(\eta, \hat{x}, \tilde{u}, w, v), \tag{4.25}$$

a more complicated system than in Theorem 4 due to the use of (4.24); note Ξ necessarily reduces to $\hat{\Upsilon}(\eta, I(\hat{x}, u))$ when $w = v = 0$. Let $\overline{\eta}$ denote zero estimation error, e.g. $\overline{\eta}_R = I$ and $\overline{\eta}_\omega = 0$ for the Invariant AHRS observer in Section 4.7.1, and define $\delta\eta := \eta - \overline{\eta}$. Due to the form of the invariant estimation error (4.14)

$$\eta = \varphi_{\gamma(x)}(\hat{x}) - \varphi_{\gamma(x)}(x)$$

when computing Ξ, the terms $\dot{x}$ (4.24a) and $\dot{\hat{x}}$ (4.24b) which respectively contain w and v, K (K denotes the matrix of observer gains L) do not appear together in product terms. Thus linearizing (4.25) about $\eta = \overline{\eta}$, $w = 0$ and $v = 0$ leads to the same form as (4.23),

$$\delta\dot{\eta} = (A - KC)\delta\eta - Bw + KDv \tag{4.26}$$

from which we can read off the (A, B, C, D) and K matrices and use (4.22) to compute the observer gains L which make up the matrix K. Remark that the entries of the A, B, C, D matrices will in general be functions of $(\hat{x}, \tilde{u})$, so as stated in Section 4.9 we are re-linearizing the invariant estimation error dynamics about the latest state estimate.

4.9.2 Invariant AHRS EKF design

As mentioned in Section 4.2, we model the AHRS bias dynamics using the Wiener process model $\dot{b} = \nu$. We also employ the rate gyro sensor model $\tilde{\omega} = \omega + b_\omega + \nu_\omega$ and accelerometer and magnetometer output models $\tilde{y} = y + \nu$ from Section 3.2.2. Under these noise models the dynamics of (4.1) become (4.24a)

$$\begin{aligned} \dot{R} &= RS(\tilde{\omega} - b_\omega - \nu_\omega) \\ \dot{b}_\omega &= \nu_{b_\omega} \end{aligned} \tag{4.27}$$

where $w = [\nu_\omega \quad \nu_{b_\omega}]^T$ is the process noise vector. The system outputs with noise are

$$\begin{bmatrix} \tilde{y}_a \\ \tilde{y}_m \end{bmatrix} = \begin{bmatrix} R^T a + \nu_a \\ R^T m + \nu_m \end{bmatrix} \tag{4.28}$$

with $v = [\nu_a \quad \nu_m]^T$ the measurement noise vector; as discussed in Section 4.2 we assume the accelerometer measures the gravity vector and the magnetometer reading has been compensated.

4.9.2.1 Body frame symmetries

The nominal invariant observer is available from Section 4.7.1.1 as (4.15). Using the noise models in Section 4.9.2 we obtain (4.24b)

$$\begin{aligned} \dot{\hat{R}} &= \hat{R}S(\tilde{\omega} - \hat{b}_\omega) + S\big(L_a^R \tilde{E}_a + L_m^R \tilde{E}_m\big)\hat{R} \\ \dot{\hat{b}}_\omega &= \hat{R}^T\big(L_a^\omega \tilde{E}_a + L_m^\omega \tilde{E}_m\big) \end{aligned} \tag{4.29}$$

where $\tilde{\omega}$ is the measured rate gyro signal. The $\tilde{E}_a$, $\tilde{E}_m$ invariant output errors in (4.29) and $I(\hat{x},\tilde{u})$ invariants used below are also available from Section 4.7.1.1:

$$\begin{pmatrix}\tilde{E}_a\\ \tilde{E}_m\end{pmatrix}=\begin{pmatrix}a-\hat{R}\tilde{y}_a\\ m-\hat{R}\tilde{y}_m\end{pmatrix},\qquad I(\hat{x},\tilde{u})=\hat{R}(\tilde{\omega}-\hat{b}_\omega), \tag{4.30}$$

where $\tilde{y}_a$, $\tilde{y}_m$ are the output measurements and $I(\hat{x},\tilde{u})$ is known and will appear below. The invariant error η (4.14) is a function of x and $\hat{x}$ only and remains unchanged from Section 4.7.1.1, i.e. $\eta_R=\hat{R}R^T$, $\eta_\omega=R(\hat{b}_\omega-b_\omega)$. As explained in Section 4.9.1, computing $(d/dt)\eta$ using (4.27) and (4.29) will cause the process noise vector $w=[\nu_\omega \quad \nu_{b_\omega}]^T$ to appear along with the measurement noise vector $v=[\nu_a \quad \nu_m]^T$ embedded in $\tilde{E}$. Starting with η_R we directly compute

$$\begin{aligned}
\dot{\eta}_R &= \dot{\hat{R}}R^T+\hat{R}\frac{d}{dt}(R^T)\\
&= \hat{R}S(\tilde{\omega}-\hat{b}_\omega)R^T+S\big(L_a^R\tilde{E}_a+L_m^R\tilde{E}_m\big)\hat{R}R^T+\hat{R}\left(-R^TRS(\tilde{\omega}-b_\omega-\nu_\omega)R^T\right)\\
&= \hat{R}S(b_\omega-\hat{b}_\omega)R^T+S\big(L_a^R\tilde{E}_a+L_m^R\tilde{E}_m\big)\hat{R}R^T+\hat{R}S(\nu_\omega)R^T\\
&= \hat{R}R^TRS(b_\omega-\hat{b}_\omega)R^T+S\big(L_a^R\tilde{E}_a+L_m^R\tilde{E}_m\big)\hat{R}R^T+\hat{R}S(\nu_\omega)\hat{R}^T\hat{R}R^T\\
&= \hat{R}R^TS\left[R(b_\omega-\hat{b}_\omega)\right]+S\big(L_a^R\tilde{E}_a+L_m^R\tilde{E}_m\big)\hat{R}R^T+S(\hat{R}\nu_\omega)\hat{R}R^T\\
\dot{\eta}_R &= \eta_RS(-\eta_\omega)+S\big(L_a^R\tilde{E}_a+L_m^R\tilde{E}_m\big)\eta_R+S(\hat{R}\nu_\omega)\eta_R
\end{aligned}$$

and for η_ω we have

$$\begin{aligned}
\dot{\eta}_\omega &= \dot{R}(\hat{b}_\omega-b_\omega)+R(\dot{\hat{b}}_\omega-\dot{b}_\omega)\\
&= RS(\tilde{\omega}-b_\omega-\nu_\omega)(\hat{b}_\omega-b_\omega)+R\left\{\hat{R}^T\big(L_a^\omega\tilde{E}_a+L_m^\omega\tilde{E}_m\big)-\nu_{b_\omega}\right\}\\
&= RS(\tilde{\omega}-\hat{b}_\omega+\hat{b}_\omega-b_\omega)(\hat{b}_\omega-b_\omega)+R\hat{R}^T\big(L_a^\omega\tilde{E}_a+L_m^\omega\tilde{E}_m\big)\\
&\quad -R\nu_{b_\omega}-RS(\nu_\omega)(\hat{b}_\omega-b_\omega)\\
&= RS(\tilde{\omega}-\hat{b}_\omega+\hat{b}_\omega-b_\omega)R^TR(\hat{b}_\omega-b_\omega)+R\hat{R}^T\big(L_a^\omega\tilde{E}_a+L_m^\omega\tilde{E}_m\big)\\
&\quad -R\nu_{b_\omega}+RS(\hat{b}_\omega-b_\omega)\nu_\omega\\
&= \left\{RS(\tilde{\omega}-\hat{b}_\omega)R^T+RS(\hat{b}_\omega-b_\omega)R^T\right\}R(\hat{b}_\omega-b_\omega)+(\hat{R}R^T)^T\big(L_a^\omega\tilde{E}_a+L_m^\omega\tilde{E}_m\big)\\
&\quad -R\hat{R}^T\hat{R}\nu_{b_\omega}+RS(\hat{b}_\omega-b_\omega)R^TR\hat{R}^T\hat{R}\nu_\omega\\
&= \left\{R\hat{R}^T\hat{R}S(\tilde{\omega}-\hat{b}_\omega)\hat{R}^T\hat{R}R^T+S\left[R(\hat{b}_\omega-b_\omega)\right]\right\}R(\hat{b}_\omega-b_\omega)\\
&\quad +(\hat{R}R^T)^T\big(L_a^\omega\tilde{E}_a+L_m^\omega\tilde{E}_m\big)-(\hat{R}R^T)^T\hat{R}\nu_{b_\omega}+S\left[R(\hat{b}_\omega-b_\omega)\right](\hat{R}R^T)^T\hat{R}\nu_\omega\\
&= (\hat{R}R^T)^TS\left[\hat{R}(\tilde{\omega}-\hat{b}_\omega)\right]\hat{R}R^T\eta_\omega+(\eta_R)^T\big(L_a^\omega\tilde{E}_a+L_m^\omega\tilde{E}_m\big)\\
&\quad -(\eta_R)^T\hat{R}\nu_{b_\omega}+S\left[\eta_\omega\right](\eta_R)^T\hat{R}\nu_\omega\\
\dot{\eta}_\omega &= S\left[(\eta_R)^TI(\hat{x},\tilde{u})\right]\eta_\omega+(\eta_R)^T\big(L_a^\omega\tilde{E}_a+L_m^\omega\tilde{E}_m\big)-(\eta_R)^T\hat{R}\nu_{b_\omega}+S\left[\eta_\omega\right](\eta_R)^T\hat{R}\nu_\omega
\end{aligned}$$

where the $\tilde{E}$ terms are written as

$$\begin{pmatrix}\tilde{E}_a\\ \tilde{E}_m\end{pmatrix}=\begin{pmatrix}a-\hat{R}\tilde{y}_a\\ m-\hat{R}\tilde{y}_m\end{pmatrix}=\begin{pmatrix}a-\hat{R}(R^Ta+\nu_a)\\ m-\hat{R}(R^Tm+\nu_m)\end{pmatrix}=\begin{pmatrix}a-\eta_Ra-\hat{R}\nu_a\\ m-\eta_Rm-\hat{R}\nu_m\end{pmatrix}$$

which contains the measurement noise vector $v = [\nu_a \quad \nu_m]^T$. Remark $I(\hat{x}, \tilde{u})$ appears in the $\dot{\eta}_\omega$ term above, and as expected setting $w = v = 0$ reduces both dynamics to the form $(d/dt)\eta = \Upsilon(\eta, I(\hat{x}, u))$ guaranteed by Theorem 4.

We now linearize the above η_R and η_ω dynamics about $\bar{\eta}_R = I$, $\bar{\eta}_\omega = 0$ and $\bar{\nu} = 0$ to obtain system (4.26) with states $\delta\eta = \eta - \bar{\eta}$. The $\tilde{E}_v, v \in \{a, m\}$ terms become

$$\begin{aligned}
\delta\tilde{E}_v &= \tilde{E}_v - \overline{\tilde{E}}_v = v - \eta_R v - \hat{R}\nu_v - v + \bar{\eta}_R v + \hat{R}\bar{\nu}_v = -\delta\eta_R v - \hat{R}\nu_v \\
\overline{\tilde{E}}_v &= v - \bar{\eta}_R v - \hat{R}\bar{\nu}_v = v - v = 0.
\end{aligned}$$

Linearizing $\dot{\eta}_R$ we obtain

$$\begin{aligned}
\delta\dot{\eta}_R &= \dot{\eta}_R - \dot{\bar{\eta}}_R \\
&= \eta_R S(-\eta_\omega) + S\big(L_a^R\tilde{E}_a + L_m^R\tilde{E}_m\big)\eta_R + S(\hat{R}\nu_\omega)\eta_R \\
&\quad - \bar{\eta}_R S(-\bar{\eta}_\omega) - S\big(\bar{\mathcal{L}}_a^R\overline{\tilde{E}}_a - \bar{\mathcal{L}}_m^R\overline{\tilde{E}}_m\big)\overline{\eta}_R - S(\hat{R}\bar{\nu}_\omega)\bar{\eta}_R \\
&= (\delta\eta_R + \bar{\eta}_R)S(-\delta\eta_\omega - \bar{\eta}_\omega) + S\big[L_a^R(\delta\tilde{E}_a + \overline{\tilde{E}}_a) + L_m^R(\delta\tilde{E}_m + \overline{\tilde{E}}_m)\big](\delta\eta_R + \bar{\eta}_R) \\
&\quad + S\big[\hat{R}(\delta\nu_\omega + \bar{\nu}_\omega)\big](\delta\eta_R + \bar{\eta}_R) - \bar{\eta}_R S(-\bar{\eta}_\omega) - S\big(\bar{\mathcal{L}}_a^R\overline{\tilde{E}}_a - \bar{\mathcal{L}}_m^R\overline{\tilde{E}}_m\big)\overline{\eta}_R \\
&\quad - S(\hat{R}\bar{\nu}_\omega)\bar{\eta}_R \\
&= (\delta\eta_R + \bar{\eta}_R)S(-\delta\eta_\omega) + S\big[L_a^R\delta\tilde{E}_a + L_m^R\delta\tilde{E}_m\big](\delta\eta_R + \bar{\eta}_R) \\
&\quad + S\big[\hat{R}(\delta\nu_\omega)\big](\delta\eta_R + \bar{\eta}_R) \\
&= \bar{\eta}_R S(-\delta\eta_\omega) + S\big[L_a^R\delta\tilde{E}_a + L_m^R\delta\tilde{E}_m\big]\bar{\eta}_R + S\big[\hat{R}(\delta\nu_\omega)\big]\bar{\eta}_R \\
&= S(-\delta\eta_\omega) + S\big[L_a^R(-\delta\eta_R a - \hat{R}\nu_a) + L_m^R(-\delta\eta_R m - \hat{R}\nu_m)\big] + S[\hat{R}\nu_\omega]
\end{aligned}$$

where we have dropped quadratic terms in δ on the second-last line in order to obtain a linear equation. For $\dot{\eta}_\omega$ we obtain the linearization

$$\begin{aligned}
\delta\dot{\eta}_\omega &= \dot{\eta}_\omega - \dot{\bar{\eta}}_\omega \\
&= S\big[(\eta_R)^T I(\hat{x}, \tilde{u})\big]\eta_\omega + (\eta_R)^T\big(L_a^\omega\tilde{E}_a + L_m^\omega\tilde{E}_m\big) - (\eta_R)^T\hat{R}\nu_{b_\omega} + S[\eta_\omega](\eta_R)^T\hat{R}\nu_\omega \\
&\quad - S\big[(\bar{\eta}_R)^T I(\hat{x}, \tilde{u})\big]\bar{\eta}_\omega - (\bar{\eta}_R)^T\big(L_a^\omega\overline{\tilde{E}}_a - L_m^\omega\overline{\tilde{E}}_m\big) + (\bar{\eta}_R)^T\hat{R}\bar{\nu}_{b_\omega} \\
&\quad - S[\bar{\eta}_\omega](\bar{\eta}_R)^T\hat{R}\bar{\nu}_\omega \\
&= S\big[(\delta\eta_R + \bar{\eta}_R)^T I(\hat{x}, \tilde{u})\big](\delta\eta_\omega + \bar{\eta}_\omega) + (\delta\eta_R + \bar{\eta}_R)^T\big(L_a^\omega(\delta\tilde{E}_a + \overline{\tilde{E}}_a) \\
&\quad + L_m^\omega(\delta\tilde{E}_m + \overline{\tilde{E}}_m)\big) - (\delta\eta_R + \bar{\eta}_R)^T\hat{R}(\delta\nu_{b_\omega} + \bar{\nu}_{b_\omega}) \\
&\quad + S[\delta\eta_\omega + \bar{\eta}_\omega](\delta\eta_R + \bar{\eta}_R)^T\hat{R}(\delta\nu_\omega + \bar{\nu}_\omega) \\
&= S\big[(\bar{\eta}_R)^T I(\hat{x}, \tilde{u})\big]\delta\eta_\omega + (\bar{\eta}_R)^T\big(L_a^\omega\delta\tilde{E}_a + L_m^\omega\delta\tilde{E}_m\big) - (\bar{\eta}_R)^T\hat{R}\delta\nu_{b_\omega} \\
&= S[I(\hat{x}, \tilde{u})]\delta\eta_\omega + L_a^\omega(-\delta\eta_R a - \hat{R}\nu_a) + L_m^\omega(-\delta\eta_R m - \hat{R}\nu_m) - \hat{R}\nu_{b_\omega}
\end{aligned}$$

where we have again dropped all quadratics in δ on the second-last line above. We further simplify the above expressions by re-expressing $\delta\eta_R = \eta_R - \bar{\eta}_R = \hat{R}R^T - I$ using the same technique as in Section 3.2.5: take the ground-frame rotational kinematics (2.3) $(d/dt)R = S(\omega)R$ and define $\omega = d\gamma/dt$. The kinematics get written as $dR/dt = S(d\gamma/dt)R \implies dR = S(d\gamma)R$. For the linearization point $\bar{\eta}_R = I$, we can write $dR \approx \hat{R} - R$ and $d\gamma = \hat{\gamma} - \gamma$, and so $\hat{R} - R \approx S(\hat{\gamma} - \gamma)R \implies \hat{R}R^T - I = S(\hat{\gamma} - \gamma) \implies \delta\eta_R = S(\delta\gamma)$, where $\delta\gamma$ gets used to represent attitude error in the linearized system in place of $\delta\eta_R$.

Using $\delta\eta_R = S(\delta\gamma)$ in the $\dot{\eta}_R$ and $\dot{\eta}_\omega$ expressions above, we obtain

$$\begin{aligned}
S(\delta\dot{\gamma}) &= S(-\delta\eta_\omega) + S\big[L_a^R(-S(\delta\gamma)a - \hat{R}\nu_a) + L_m^R(-S(\delta\gamma)m - \hat{R}\nu_m)\big] + S[\hat{R}\nu_\omega] \\
S(\delta\dot{\gamma}) &= S\big[-\delta\eta_\omega + L_a^R(S(a)\delta\gamma - \hat{R}\nu_a) + L_m^R(S(m)\delta\gamma - \hat{R}\nu_m) + \hat{R}\nu_\omega\big] \\
\delta\dot{\gamma} &= -\delta\eta_\omega + \big[L_a^R S(a) + L_m^R S(m)\big]\delta\gamma - L_a^R\hat{R}\nu_a - L_m^R\hat{R}\nu_m + \hat{R}\nu_\omega
\end{aligned}$$

for $\delta\dot{\eta}_R$, and for $\delta\dot{\eta}_\omega$ we have

$$\begin{aligned}
\delta\dot{\eta}_\omega &= S[I(\hat{x},\tilde{u})]\delta\eta_\omega + L_a^\omega(-S(\delta\gamma)a - \hat{R}\nu_a) + L_m^\omega(-S(\delta\gamma)m - \hat{R}\nu_m) - \hat{R}\nu_{b_\omega} \\
&= S[I(\hat{x},\tilde{u})]\delta\eta_\omega + L_a^\omega(S(a)\delta\gamma - \hat{R}\nu_a) + L_m^\omega(S(m)\delta\gamma - \hat{R}\nu_m) - \hat{R}\nu_{b_\omega} \\
\delta\dot{\eta}_\omega &= S[I(\hat{x},\tilde{u})]\delta\eta_\omega + \big[L_a^\omega S(a) + L_m^\omega S(m)\big]\delta\gamma - L_a^\omega\hat{R}\nu_a - L_m^\omega\hat{R}\nu_m - \hat{R}\nu_{b_\omega}
\end{aligned}$$

The $\delta\dot{\gamma}$ and $\delta\dot{\eta}_\omega$ expressions are rewritten as (4.26)

$$\begin{aligned}
\begin{bmatrix}\delta\dot{\gamma}\\ \delta\dot{\eta}_\omega\end{bmatrix} &= \underbrace{\begin{bmatrix}0 & -I\\ 0 & S[I(\hat{x},\tilde{u})]\end{bmatrix}}_{A}\begin{bmatrix}\delta\gamma\\ \delta\eta_\omega\end{bmatrix} - \underbrace{\begin{bmatrix}L_a^R & L_m^R\\ L_a^\omega & L_m^\omega\end{bmatrix}}_{K}\underbrace{\begin{bmatrix}-S(a) & 0\\ -S(m) & 0\end{bmatrix}}_{C}\begin{bmatrix}\delta\gamma\\ \delta\eta_\omega\end{bmatrix} \\
&\quad - \underbrace{\begin{bmatrix}-\hat{R} & 0\\ 0 & \hat{R}\end{bmatrix}}_{B}\underbrace{\begin{bmatrix}\nu_\omega\\ \nu_{b_\omega}\end{bmatrix}}_{w} + \underbrace{\begin{bmatrix}L_a^R & L_m^R\\ L_a^\omega & L_m^\omega\end{bmatrix}}_{K}\underbrace{\begin{bmatrix}-\hat{R} & 0\\ 0 & -\hat{R}\end{bmatrix}}_{D}\underbrace{\begin{bmatrix}\nu_a\\ \nu_m\end{bmatrix}}_{v}
\end{aligned} \tag{4.31}$$

Using the set of matrices (A, B, C, D) along with the (identified) noise covariances $Q = E\langle ww^T\rangle$, $R = E\langle vv^T\rangle$ we use (4.22) to calculate K and use the resulting gains L in the invariant observer (4.29) resp. (4.15).

4.9.2.2 Ground frame symmetries

We also design an Invariant EKF for the AHRS ground-frame symmetry case covered in Section 4.7.1.2. Under additive noise, the system dynamics and outputs are still given by (4.27), (4.28)

$$\begin{aligned}
\dot{R} &= RS(\tilde{\omega} - b_\omega - \nu_\omega) \\
\dot{b}_\omega &= \nu_{b_\omega} \\
\begin{bmatrix}\tilde{y}_a\\ \tilde{y}_m\end{bmatrix} &= \begin{bmatrix}R^T a + \nu_a\\ R^T m + \nu_m\end{bmatrix}
\end{aligned}$$

while the observer (4.16) becomes

$$\begin{aligned}
\dot{\hat{R}} &= \hat{R}S(\tilde{\omega} - \hat{b}_\omega) + \hat{R}S\Big(L_a^R\tilde{E}_a + L_m^R\tilde{E}_m\Big) \\
\dot{\hat{b}}_\omega &= L_a^\omega\tilde{E}_a + L_m^\omega\tilde{E}_m
\end{aligned}$$

where $\tilde{E}_a = \hat{R}^T a - \tilde{y}_a$, $\tilde{E}_m = \hat{R}^T m - \tilde{y}_m$. The invariant estimation errors $\eta_R = R^T\hat{R}$, $\eta_\omega = \hat{b}_\omega - b_\omega$ are unchanged from Section 4.7.1.2, and we compute their dynamics

below:

$$\begin{aligned}
\dot{\eta}_R &= -R^T\dot{R}R^T\hat{R} + R^T\dot{\hat{R}} \\
&= -R^TRS(\tilde{\omega} - b_\omega - \nu_\omega)R^T\hat{R} + R^T\hat{R}S(\tilde{\omega} - \hat{b}_\omega) + R^T\hat{R}S\Big(L_a^R\tilde{E}_a + L_m^R\tilde{E}_m\Big) \\
&= \eta_R S(\tilde{I}_\omega) - S(\tilde{I}_\omega)\eta_R - S(\eta_\omega)\eta_R + \eta_R S\Big(L_a^R\tilde{E}_a + L_m^R\tilde{E}_m\Big) + S(\nu_\omega)\eta_R
\end{aligned}$$

$$\begin{aligned}
\dot{\eta}_\omega &= \dot{\hat{b}}_\omega - \dot{b}_\omega \\
&= L_a^\omega\tilde{E}_a + L_m^\omega\tilde{E}_m - \nu_{b_\omega}
\end{aligned}$$

where $\tilde{I}_\omega = \tilde{\omega} - \hat{b}_\omega$ as well as $I_a = \hat{R}^T a$, $I_m = \hat{R}^T m$ are the invariants of the system, the latter two appearing in the invariant output errors:

$$\begin{aligned}
\tilde{E}_a &= \hat{R}^T a - \tilde{y}_a = \hat{R}^T a - R^T a - \nu_a = I_a - R^T\hat{R}\hat{R}^T a - \nu_a = I_a - \eta_R I_a - \nu_a \\
\tilde{E}_m &= \hat{R}^T m - \tilde{y}_m = \hat{R}^T m - R^T m - \nu_m = I_m - R^T\hat{R}\hat{R}^T m - \nu_m = I_m - \eta_R I_m - \nu_m
\end{aligned}$$

Next, we linearize the above η dynamics about $\bar{\eta}_R = I$, $\bar{\eta}_\omega = 0$ and $\bar{\nu} = 0$. The $\tilde{E}$ terms will become

$$\begin{aligned}
\delta\tilde{E}_a &= \tilde{E}_a - \overline{\tilde{E}}_a = I_a - \eta_R I_a - \nu_a - I_a + \bar{\eta}_R I_a + \bar{\nu}_a = -\delta\eta_R I_a - \nu_a \\
\delta\tilde{E}_m &= \tilde{E}_m - \overline{\tilde{E}}_m = I_m - \eta_R I_m - \nu_m - I_m + \bar{\eta}_R I_m + \bar{\nu}_m = -\delta\eta_R I_m - \nu_m
\end{aligned}$$

where $\overline{\tilde{E}}_a = \overline{\tilde{E}}_m = 0$. Using $\delta\eta_R = S(\delta\gamma)$ as in Section 4.9.2.1, we have

$$\begin{aligned}
\delta\tilde{E}_a &= -S(\delta\gamma)I_a - \nu_a = S(I_a)\delta\gamma - \nu_a \\
\delta\tilde{E}_m &= -S(\delta\gamma)I_m - \nu_m = S(I_m)\delta\gamma - \nu_m
\end{aligned}$$

Finally, we calculate the linearized $\delta\eta$ dynamics as

$$\begin{aligned}
\delta\dot{\eta}_R &= \dot{\eta}_R - \dot{\bar{\eta}}_R \\
&= \eta_R S(\tilde{I}_\omega) - S(\tilde{I}_\omega)\eta_R - S(\eta_\omega)\eta_R + \eta_R S\Big(L_a^R\tilde{E}_a + L_m^R\tilde{E}_m\Big) + S(\nu_\omega)\eta_R - 0 \\
&= (\delta\eta_R + \bar{\eta}_R)S(\tilde{I}_\omega) - S(\tilde{I}_\omega)(\delta\eta_R + \bar{\eta}_R) - S[\delta\eta_\omega + \bar{\eta}_\omega](\delta\eta_R + \bar{\eta}_R) \\
&\quad + (\delta\eta_R + \bar{\eta}_R)S\Big(L_a^R(\delta\tilde{E}_a + \overline{\tilde{E}}_a) + L_m^R(\delta\tilde{E}_m + \overline{\tilde{E}}_m)\Big) \\
&\quad + S[\delta\nu_\omega + \bar{\nu}_\omega](\delta\eta_R + \bar{\eta}_R) \\
&= \delta\eta_R S(\tilde{I}_\omega) - S(\tilde{I}_\omega)\delta\eta_R - S(\delta\eta_\omega)\bar{\eta}_R + \bar{\eta}_R S\Big(L_a^R\delta\tilde{E}_a + L_m^R\delta\tilde{E}_m\Big) + S(\delta\nu_\omega)\bar{\eta}_R
\end{aligned}$$

$$S(\delta\dot{\gamma}) = S(\delta\gamma)S(\tilde{I}_\omega) - S(\tilde{I}_\omega)S(\delta\gamma) - S(\delta\eta_\omega) + S\Big(L_a^R\delta\tilde{E}_a + L_m^R\delta\tilde{E}_m\Big) + S(\nu_\omega)$$

$$\begin{aligned}
\delta\dot{\gamma} &= \delta\gamma \times \tilde{I}_\omega - \delta\eta_\omega + L_a^R\delta\tilde{E}_a + L_m^R\delta\tilde{E}_m + \nu_\omega \\
&= -S(\tilde{I}_\omega)\delta\gamma - \delta\eta_\omega + L_a^R\big(S(I_a)\delta\gamma - \nu_a\big) + L_m^R\big(S(I_m)\delta\gamma - \nu_m\big) + \nu_\omega
\end{aligned}$$

and

$$\begin{aligned}
\delta\dot{\eta}_\omega &= \dot{\eta}_\omega - \dot{\bar{\eta}}_\omega \\
&= L_a^\omega\tilde{E}_a + L_m^\omega\tilde{E}_m - \nu_{b_\omega} - L_a^\omega\overline{\tilde{E}}_a - L_m^\omega\overline{\tilde{E}}_m + \bar{\nu}_{b_\omega} \\
&= L_a^\omega\delta\tilde{E}_a + L_m^\omega\delta\tilde{E}_m - \nu_{b_\omega} \\
&= L_a^\omega\big(S(I_a)\delta\gamma - \nu_a\big) + L_m^\omega\big(S(I_m)\delta\gamma - \nu_m\big) - \nu_{b_\omega}
\end{aligned}$$

which is rewritten in form (4.26) as

$$\begin{bmatrix}\delta\dot{\gamma}\\ \delta\dot{\eta}_\omega\end{bmatrix} = \underbrace{\begin{bmatrix}-S[\tilde{\omega}-\hat{b}_\omega] & -I\\ 0 & 0\end{bmatrix}}_{A}\begin{bmatrix}\delta\gamma\\ \delta\eta_\omega\end{bmatrix} - \underbrace{\begin{bmatrix}L_a^R & L_m^R\\ L_a^\omega & L_m^\omega\end{bmatrix}}_{K}\underbrace{\begin{bmatrix}-S[\hat{R}^T a] & 0\\ -S[\hat{R}^T m] & 0\end{bmatrix}}_{C}\begin{bmatrix}\delta\gamma\\ \delta\eta_\omega\end{bmatrix} - \underbrace{\begin{bmatrix}-I & 0\\ 0 & I\end{bmatrix}}_{B}\underbrace{\begin{bmatrix}\nu_\omega\\ \nu_{b_\omega}\end{bmatrix}}_{w} + \underbrace{\begin{bmatrix}L_a^R & L_m^R\\ L_a^\omega & L_m^\omega\end{bmatrix}}_{K}\underbrace{\begin{bmatrix}-I & 0\\ 0 & -I\end{bmatrix}}_{D}\underbrace{\begin{bmatrix}\nu_a\\ \nu_m\end{bmatrix}}_{v} \tag{4.32}$$

Which provides the set (A, B, C, D) used in (4.22) to calculate the gains L of the invariant observer (4.16).

4.9.3 Invariant Aided INS EKF design

In order to assign the gains L to the Aided INS observers designed in Sections 4.7.2.1 and 4.7.2.2, we use the Invariant EKF methodology of Section 4.9.1. We consider both the body-frame and ground-frame symmetries versions below. Using the accelerometer and rate gyro sensor models (3.4) $\tilde{f} = f + b_f + \nu_f$, $\tilde{\omega} = \omega + b_\omega + \nu_\omega$ from Section 3.2.2 along with a Wiener process model for the bias dynamics $\dot{b} = \nu$ as mentioned in Section 4.5, the Aided INS dynamics (4.6) become (4.24a)

$$\begin{aligned}\dot{p} &= v\\ \dot{v} &= R(\tilde{f} - b_f - \nu_f) - a\\ \dot{R} &= RS(\tilde{\omega} - b_\omega - \nu_\omega)\\ \dot{b}_f &= \nu_{bf}\\ \dot{b}_\omega &= \nu_{b\omega}\end{aligned} \tag{4.33}$$

with process noise vector $w = [\nu_f \quad \nu_\omega \quad \nu_{bf} \quad \nu_{b\omega}]^T$. The nominal output equations (4.7) become

$$\begin{bmatrix}\tilde{y}_p\\ \tilde{y}_m\end{bmatrix} = \begin{bmatrix}p + \nu_p\\ R^T m + \nu_m\end{bmatrix} \tag{4.34}$$

where $v = [\nu_p \quad \nu_m]^T$ is the measurement noise vector. As discussed in Section (4.5) we assume the Navigation to ECEF rotation matrix R_E^N and location of navigation frame r_E^o have been found such that the vehicle's navigation frame position p is directly measurable. The vector m is the navigation frame magnetic field vector, c.f. Section 2.8, and $\tilde{y}_m$ is assumed compensated such that $\nu_m := \nu_m^c$, c.f. Section 3.2.2.

4.9.3.1 Body frame symmetries

From Section 4.7.2.1, the invariant observer (4.17) with noise models from Section 4.9.3 takes the form (4.24b)

$$\begin{aligned}
\dot{\hat{p}} &= \hat{v} + L_p^p \tilde{E}_p + L_m^p \tilde{E}_m \\
\dot{\hat{v}} &= \hat{R}(\tilde{f} - \hat{b}_f) - a + L_p^v \tilde{E}_p + L_m^v \tilde{E}_m \\
\dot{\hat{R}} &= \hat{R} S(\tilde{\omega} - \hat{b}_\omega) + S\big[L_p^R \tilde{E}_p + L_m^R \tilde{E}_m\big]\hat{R} \\
\dot{\hat{b}}_f &= \hat{R}^T \big(L_p^{bf} \tilde{E}_p + L_m^{bf} \tilde{E}_m\big) \\
\dot{\hat{b}}_\omega &= \hat{R}^T \big(L_p^{b\omega} \tilde{E}_p + L_m^{b\omega} \tilde{E}_m\big)
\end{aligned}$$

where $\tilde{E}_p = \hat{p} - \tilde{y}_p$ and $\tilde{E}_m = m - \hat{R}\tilde{y}_m$. The invariant estimation errors η remain unchanged, and the dynamics $\dot{\eta}$ are expected to contain the invariants $I_v = \hat{v}$, $\tilde{I}_f = \hat{R}(\tilde{f} - \hat{b}_f)$ and $\tilde{I}_\omega = \hat{R}(\tilde{\omega} - \hat{b}_\omega)$. By direct computation:

$$\begin{aligned}
\dot{\eta}_p &= \dot{\hat{p}} - \dot{p} \\
&= \hat{v} + L_p^p \tilde{E}_p + L_m^p \tilde{E}_m - v \\
&= \eta_v + L_p^p \tilde{E}_p + L_m^p \tilde{E}_m
\end{aligned}$$

$$\begin{aligned}
\dot{\eta}_v &= \dot{\hat{v}} - \dot{v} \\
&= \hat{R}(\tilde{f} - \hat{b}_f) - a + L_p^v \tilde{E}_p + L_m^v \tilde{E}_m - R(\tilde{f} - b_f - \nu_f) + a \\
&= \tilde{I}_f + L_p^v \tilde{E}_p + L_m^v \tilde{E}_m - (\eta_R)^T \tilde{I}_f - \eta_{bf} + R\nu_f \\
&= \tilde{I}_f + L_p^v \tilde{E}_p + L_m^v \tilde{E}_m - (\eta_R)^T \tilde{I}_f - \eta_{bf} + (\eta_R)^T \hat{R}\nu_f
\end{aligned}$$

$$\begin{aligned}
\dot{\eta}_R &= \dot{\hat{R}} R^T - \hat{R} R^T \dot{R} R^T \\
&= \hat{R} S(\tilde{\omega} - \hat{b}_\omega) R^T + S\big[L_p^R \tilde{E}_p + L_m^R \tilde{E}_m\big]\hat{R} R^T - \hat{R} R^T R S(\tilde{\omega} - b_\omega - \nu_\omega) R^T \\
&= -\eta_R S(\eta_{b\omega}) + S\big[L_p^R \tilde{E}_p + L_m^R \tilde{E}_m\big]\eta_R + \hat{R} S(\nu_\omega) R^T \\
&= -\eta_R S(\eta_{b\omega}) + S\big[L_p^R \tilde{E}_p + L_m^R \tilde{E}_m\big]\eta_R + \hat{R} S(\nu_\omega) \hat{R}^T \hat{R} R^T \\
&= -\eta_R S(\eta_{b\omega}) + S\big[L_p^R \tilde{E}_p + L_m^R \tilde{E}_m\big]\eta_R + S\big[\hat{R}\nu_\omega\big]\eta_R
\end{aligned}$$

$$
\begin{aligned}
\dot{\eta}_{bf} &= \dot{R}(\hat{b}_f - b_f) + R(\dot{\hat{b}}_f - \dot{b}_f) \\
&= RS(\tilde{\omega} - b_\omega - \nu_\omega)(\hat{b}_f - b_f) + R\hat{R}^T\big(L_p^{bf}\tilde{E}_p + L_m^{bf}\tilde{E}_m\big) - R\nu_{bf} \\
&= S\big[(\eta_R)^T\tilde{I}_\omega + \eta_{b\omega}\big]\eta_{bf} + (\eta_R)^T\big(L_p^{bf}\tilde{E}_p + L_m^{bf}\tilde{E}_m\big) - RS(\nu_\omega)(\hat{b}_f - b_f) - R\nu_{bf} \\
&= S\big[(\eta_R)^T\tilde{I}_\omega + \eta_{b\omega}\big]\eta_{bf} + (\eta_R)^T\big(L_p^{bf}\tilde{E}_p + L_m^{bf}\tilde{E}_m\big) + RS[\hat{b}_f - b_f]\nu_\omega - R\nu_{bf} \\
&= S\big[(\eta_R)^T\tilde{I}_\omega + \eta_{b\omega}\big]\eta_{bf} + (\eta_R)^T\big(L_p^{bf}\tilde{E}_p + L_m^{bf}\tilde{E}_m\big) + RS[\hat{b}_f - b_f]R^TR\hat{R}^T\hat{R}\nu_\omega \\
&\quad - R\hat{R}^T\hat{R}\nu_{bf} \\
&= S\big[(\eta_R)^T\tilde{I}_\omega + \eta_{b\omega}\big]\eta_{bf} + (\eta_R)^T\big(L_p^{bf}\tilde{E}_p + L_m^{bf}\tilde{E}_m\big) + S[\eta_{bf}](\eta_R)^T\hat{R}\nu_\omega \\
&\quad - (\eta_R)^T\hat{R}\nu_{bf}
\end{aligned}
$$

$$
\begin{aligned}
\dot{\eta}_{b\omega} &= \dot{R}(\hat{b}_\omega - b_\omega) + R(\dot{\hat{b}}_\omega - \dot{b}_\omega) \\
&= RS(\tilde{\omega} - b_\omega - \nu_\omega)(\hat{b}_\omega - b_\omega) + R\hat{R}^T\big(L_p^{b\omega}\tilde{E}_p + L_m^{b\omega}\tilde{E}_m\big) - R\nu_{b\omega} \\
&= S\big[(\eta_R)^T\tilde{I}_\omega\big]\eta_{b\omega} + (\eta_R)^T\big(L_p^{b\omega}\tilde{E}_p + L_m^{b\omega}\tilde{E}_m\big) - RS(\nu_\omega)(\hat{b}_\omega - b_\omega) - R\nu_{b\omega} \\
&= S\big[(\eta_R)^T\tilde{I}_\omega\big]\eta_{b\omega} + (\eta_R)^T\big(L_p^{b\omega}\tilde{E}_p + L_m^{b\omega}\tilde{E}_m\big) + RS[\hat{b}_\omega - b_\omega]\nu_\omega - R\nu_{b\omega} \\
&= S\big[(\eta_R)^T\tilde{I}_\omega\big]\eta_{b\omega} + (\eta_R)^T\big(L_p^{b\omega}\tilde{E}_p + L_m^{b\omega}\tilde{E}_m\big) + RS[\hat{b}_\omega - b_\omega]R^TR\hat{R}^T\hat{R}\nu_\omega \\
&\quad - R\hat{R}^T\hat{R}\nu_{b\omega} \\
&= S\big[(\eta_R)^T\tilde{I}_\omega\big]\eta_{b\omega} + (\eta_R)^T\big(L_p^{b\omega}\tilde{E}_p + L_m^{b\omega}\tilde{E}_m\big) + S[\eta_{b\omega}](\eta_R)^T\hat{R}\nu_\omega - (\eta_R)^T\hat{R}\nu_{b\omega}
\end{aligned}
$$

where we have

$$
\begin{aligned}
\tilde{E}_p &= \hat{p} - \tilde{y}_p = \hat{p} - p - \nu_p = \eta_p - \nu_p \\
\tilde{E}_m &= m - \hat{R}\tilde{y}_m = m - \hat{R}R^Tm - \hat{R}\nu_m = m - \eta_R m - \hat{R}\nu_m
\end{aligned}
$$

We now linearize the error dynamics above about $\bar{\eta} = 0$ ($\bar{\eta}_R = I$) and $\bar{\nu} = 0$. The invariant output error terms become

$$
\begin{aligned}
\delta\tilde{E}_p &= \tilde{E}_p - \overline{\tilde{E}}_p = \eta_p - \nu_p - \bar{\eta}_p + \bar{\nu}_p = \delta\eta_p - \nu_p \\
\delta\tilde{E}_m &= \tilde{E}_m - \overline{\tilde{E}}_m \\
&= m - \eta_R m - \hat{R}\nu_m - m + \bar{\eta}_R m + \hat{R}\bar{\nu}_m = -\delta\eta_R m - \hat{R}\nu_m = S(m)\delta\gamma - \hat{R}\nu_m
\end{aligned}
$$

where we have used $\delta\eta_R = S(\delta\gamma)$ with $\delta\gamma = \hat{\gamma} - \gamma$ as explained in Section 4.9.2.1. Remark that $\overline{\tilde{E}}_p = \overline{\tilde{E}}_m = 0$. We now proceed to calculate the linearizations:

$$\begin{aligned}
\delta\dot{\eta}_p &= \dot{\eta}_p - \dot{\bar{\eta}}_p \\
&= \eta_v + L_p^p \tilde{E}_p + L_m^p \tilde{E}_m - \bar{\eta}_v - L_p^p \overline{\tilde{E}}_p - L_m^p \overline{\tilde{E}}_m \\
&= \delta\eta_v + L_p^p \delta\tilde{E}_p + L_m^p \delta\tilde{E}_m \\
&= \delta\eta_v + L_p^p\big(\delta\eta_p - \nu_p\big) + L_m^p\big(S(m)\delta\gamma - \hat{R}\nu_m\big)
\end{aligned}$$

$$\begin{aligned}
\delta\dot{\eta}_v &= \dot{\eta}_v - \dot{\bar{\eta}}_v \\
&= \tilde{I}_f + L_p^v \tilde{E}_p + L_m^v \tilde{E}_m - (\eta_R)^T \tilde{I}_f - \eta_{bf} + (\eta_R)^T \hat{R}\nu_f \\
&\quad - \tilde{I}_f - L_p^v \overline{\tilde{E}}_p - L_m^v \overline{\tilde{E}}_m + (\bar{\eta}_R)^T \tilde{I}_f + \bar{\eta}_{bf} - (\bar{\eta}_R)^T \hat{R}\bar{\nu}_f \\
&= L_p^v \delta\tilde{E}_p + L_m^v \delta\tilde{E}_m - (\delta\eta_R)^T \tilde{I}_f - \delta\eta_{bf} + (\delta\eta_R + \bar{\eta}_R)^T \hat{R}(\delta\nu_f + \bar{\nu}_f) \\
&= L_p^v \delta\tilde{E}_p + L_m^v \delta\tilde{E}_m - \big(S(\delta\gamma)\big)^T \tilde{I}_f - \delta\eta_{bf} + (\bar{\eta}_R)^T \hat{R}\delta\nu_f \\
&= L_p^v\big(\delta\eta_p - \nu_p\big) + L_m^v\big(S(m)\delta\gamma - \hat{R}\nu_m\big) - S(\tilde{I}_f)\delta\gamma - \delta\eta_{bf} + \hat{R}\nu_f
\end{aligned}$$

$$\begin{aligned}
\delta\dot{\eta}_R &= \dot{\eta}_R - \dot{\bar{\eta}}_R \\
&= -\eta_R S(\eta_{b\omega}) + S\big[L_p^R \tilde{E}_p + L_m^R \tilde{E}_m\big]\eta_R + S(\hat{R}\nu_\omega)\eta_R - 0 \\
&= -\big(\delta\eta_R + \bar{\eta}_R\big)S\big[\delta\eta_{b\omega} + \bar{\eta}_{b\omega}\big] + S\big[L_p^R\big(\delta\tilde{E}_p + \overline{\tilde{E}}_p\big) \\
&\quad + L_m^R\big(\delta\tilde{E}_m + \overline{\tilde{E}}_m\big)\big]\big(\delta\eta_R + \bar{\eta}_R\big) + S\big[\hat{R}\big(\delta\nu_\omega + \bar{\nu}_\omega\big)\big]\big(\delta\eta_R + \bar{\eta}_R\big) \\
\delta\dot{\eta}_R &= -\bar{\eta}_R S(\delta\eta_{b\omega}) + S\big[L_p^R \delta\tilde{E}_p + L_m^R \delta\tilde{E}_m\big]\bar{\eta}_R + S\big[\hat{R}\delta\nu_\omega\big]\bar{\eta}_R \\
S(\delta\dot{\gamma}) &= S(-\delta\eta_{b\omega}) + S\Big[L_p^R\big(\delta\eta_p - \nu_p\big) + L_m^R\big(S(m)\delta\gamma - \hat{R}\nu_m\big)\Big] + S\big[\hat{R}\nu_\omega\big] \\
\delta\dot{\gamma} &= -\delta\eta_{b\omega} + L_p^R\big(\delta\eta_p - \nu_p\big) + L_m^R\big(S(m)\delta\gamma - \hat{R}\nu_m\big) + \hat{R}\nu_\omega
\end{aligned}$$

$$
\begin{aligned}
\delta\dot{\eta}_{bf} &= \dot{\eta}_{bf} - \dot{\bar{\eta}}_{bf} \\
&= S\big[(\eta_R)^T \tilde{I}_\omega + \eta_{b\omega}\big]\eta_{bf} + (\eta_R)^T\big(L_p^{bf}\tilde{E}_p + L_m^{bf}\tilde{E}_m\big) \\
&\quad + S[\eta_{bf}](\eta_R)^T\hat{R}\nu_\omega - (\eta_R)^T\hat{R}\nu_{bf} - 0 \\
&= S\big[\big(\delta\eta_R + \bar{\eta}_R\big)^T\tilde{I}_\omega + \big(\delta\eta_{b\omega} + \bar{\eta}_{b\omega}\big)\big]\big(\delta\eta_{bf} + \bar{\eta}_{bf}\big) \\
&\quad + \big(\delta\eta_R + \bar{\eta}_R\big)^T\Big(L_p^{bf}\big(\delta\tilde{E}_p + \overline{\tilde{E}}_p\big) + L_m^{bf}\big(\delta\tilde{E}_m + \overline{\tilde{E}}_m\big)\Big) \\
&\quad + S\big[\delta\eta_{bf} + \bar{\eta}_{bf}\big]\big(\delta\eta_R + \bar{\eta}_R\big)^T\hat{R}\big(\delta\nu_\omega + \bar{\nu}_\omega\big) - \big(\delta\eta_R + \bar{\eta}_R\big)^T\hat{R}\big(\delta\nu_{bf} + \bar{\nu}_{bf}\big) \\
&= S\big[\big(\bar{\eta}_R\big)^T\tilde{I}_\omega\big]\delta\eta_{bf} + \big(\bar{\eta}_R\big)^T\Big(L_p^{bf}\delta\tilde{E}_p + L_m^{bf}\delta\tilde{E}_m\Big) \\
&\quad + S\big[\delta\eta_{bf}\big]\big(\bar{\eta}_R\big)^T\hat{R}\delta\nu_\omega - \big(\bar{\eta}_R\big)^T\hat{R}\delta\nu_{bf} \\
&= S\big[\tilde{I}_\omega\big]\delta\eta_{bf} + L_p^{bf}\big(\delta\eta_p - \nu_p\big) + L_m^{bf}\big(S(m)\delta\gamma - \hat{R}\nu_m\big) - \hat{R}\nu_{bf}
\end{aligned}
$$

$$
\begin{aligned}
\delta\dot{\eta}_{b\omega} &= \dot{\eta}_{b\omega} - \dot{\bar{\eta}}_{b\omega} \\
&= S\big[(\eta_R)^T\tilde{I}_\omega\big]\eta_{b\omega} + (\eta_R)^T\big(L_p^{b\omega}\tilde{E}_p + L_m^{b\omega}\tilde{E}_m\big) \\
&\quad + S[\eta_{b\omega}](\eta_R)^T\hat{R}\nu_\omega - (\eta_R)^T\hat{R}\nu_{b\omega} - 0 \\
&= S\big[\big(\delta\eta_R + \bar{\eta}_R\big)^T\tilde{I}_\omega\big]\big(\delta\eta_{b\omega} + \bar{\eta}_{b\omega}\big) \\
&\quad + \big(\delta\eta_R + \bar{\eta}_R\big)^T\Big(L_p^{b\omega}\big(\delta\tilde{E}_p + \overline{\tilde{E}}_p\big) + L_m^{b\omega}\big(\delta\tilde{E}_m + \overline{\tilde{E}}_m\big)\Big) \\
&\quad + S\big[\delta\eta_{b\omega} + \bar{\eta}_{b\omega}\big]\big(\delta\eta_R + \bar{\eta}_R\big)^T\hat{R}\big(\delta\nu_\omega + \bar{\nu}_\omega\big) - \big(\delta\eta_R + \bar{\eta}_R\big)^T\hat{R}\big(\delta\nu_{b\omega} + \bar{\nu}_{b\omega}\big) \\
&= S\big[\big(\bar{\eta}_R\big)^T\tilde{I}_\omega\big]\delta\eta_{b\omega} + \big(\bar{\eta}_R\big)^T\Big(L_p^{b\omega}\delta\tilde{E}_p + L_m^{b\omega}\delta\tilde{E}_m\Big) \\
&\quad + S\big[\delta\eta_{b\omega}\big]\big(\bar{\eta}_R\big)^T\hat{R}\delta\nu_\omega - \big(\bar{\eta}_R\big)^T\hat{R}\delta\nu_{b\omega} \\
&= S\big[\tilde{I}_\omega\big]\delta\eta_{b\omega} + L_p^{b\omega}\big(\delta\eta_p - \nu_p\big) + L_m^{b\omega}\big(S(m)\delta\gamma - \hat{R}\nu_m\big) - \hat{R}\nu_{b\omega}
\end{aligned}
$$

The preceding are rewritten in the form (4.26):

$$\begin{bmatrix} \delta\dot{\eta}_p \\ \delta\dot{\eta}_v \\ \delta\dot{\gamma} \\ \delta\dot{\eta}_{bf} \\ \delta\dot{\eta}_{b\omega} \end{bmatrix} = \underbrace{\begin{bmatrix} 0 & I & 0 & 0 & 0 \\ 0 & 0 & -S[\tilde{I}_f] & -I & 0 \\ 0 & 0 & 0 & 0 & -I \\ 0 & 0 & 0 & S[\tilde{I}_\omega] & 0 \\ 0 & 0 & 0 & 0 & S[\tilde{I}_\omega] \end{bmatrix}}_{A} \begin{bmatrix} \delta\eta_p \\ \delta\eta_v \\ \delta\gamma \\ \delta\eta_{bf} \\ \delta\eta_{b\omega} \end{bmatrix}$$

$$- \underbrace{\begin{bmatrix} L_p^p & L_m^p \\ L_p^v & L_m^v \\ L_p^R & L_m^R \\ L_p^{bf} & L_m^{bf} \\ L_p^{b\omega} & L_m^{b\omega} \end{bmatrix}}_{K} \underbrace{\begin{bmatrix} -I & 0 & 0 & 0 & 0 \\ 0 & 0 & -S(m) & 0 & 0 \end{bmatrix}}_{C} \begin{bmatrix} \delta\eta_p \\ \delta\eta_v \\ \delta\gamma \\ \delta\eta_{bf} \\ \delta\eta_{b\omega} \end{bmatrix}$$

$$- \underbrace{\begin{bmatrix} 0 & 0 & 0 & 0 \\ -\hat{R} & 0 & 0 & 0 \\ 0 & -\hat{R} & 0 & 0 \\ 0 & 0 & \hat{R} & 0 \\ 0 & 0 & 0 & \hat{R} \end{bmatrix}}_{B} \underbrace{\begin{bmatrix} \nu_f \\ \nu_\omega \\ \nu_{bf} \\ \nu_{b\omega} \end{bmatrix}}_{w} + \underbrace{\begin{bmatrix} L_p^p & L_m^p \\ L_p^v & L_m^v \\ L_p^R & L_m^R \\ L_p^{bf} & L_m^{bf} \\ L_p^{b\omega} & L_m^{b\omega} \end{bmatrix}}_{K} \underbrace{\begin{bmatrix} -I & 0 \\ 0 & -\hat{R} \end{bmatrix}}_{D} \underbrace{\begin{bmatrix} \nu_p \\ \nu_m \end{bmatrix}}_{v}$$

which provides the required (A, B, C, D) matrices to compute K via (4.22) giving the gains L of observer (4.17).

4.9.3.2 Ground frame symmetries

From Section 4.7.2.2, the invariant observer (4.18) with noise models from Section 4.9.3 takes the form (4.24b)

$$\begin{aligned}
\dot{\hat{p}} &= \hat{v} + \hat{R}\big(L_p^p \tilde{E}_p + L_m^p \tilde{E}_m\big) \\
\dot{\hat{v}} &= \hat{R}(\tilde{f} - \hat{b}_f) - a + \hat{R}\big(L_p^v \tilde{E}_p + L_m^v \tilde{E}_m\big) \\
\dot{\hat{R}} &= \hat{R}S(\tilde{\omega} - \hat{b}_\omega) + \hat{R}S\big[L_p^R \tilde{E}_p + L_m^R \tilde{E}_m\big] \\
\dot{\hat{b}}_f &= L_p^{bf} \tilde{E}_p + L_m^{bf} \tilde{E}_m \\
\dot{\hat{b}}_\omega &= L_p^{b\omega} \tilde{E}_p + L_m^{b\omega} \tilde{E}_m
\end{aligned}$$

As before the η expressions are unchanged by the addition of noise. We directly work out their dynamics below:

$$\begin{aligned}
\dot{\eta}_p &= -R^T\dot{R}R^T(\hat{p}-p) + R^T(\dot{\hat{p}}-\dot{p}) \\
&= -R^TRS(\tilde{\omega}-b_\omega-\nu_\omega)R^T(\hat{p}-p) + R^T\left(\hat{v}+\hat{R}\big(L_p^p\tilde{E}_p+L_m^p\tilde{E}_m\big)-v\right) \\
&= -S\big[\tilde{I}_\omega+\eta_{b\omega}\big]\eta_p+\eta_v+\eta_R\big(L_p^p\tilde{E}_p+L_m^p\tilde{E}_m\big)+S(\nu_\omega)R^T(\hat{p}-p) \\
&= -S\big[\tilde{I}_\omega+\eta_{b\omega}\big]\eta_p+\eta_v+\eta_R\big(L_p^p\tilde{E}_p+L_m^p\tilde{E}_m\big)-S(\eta_p)\nu_\omega
\end{aligned}$$

$$\begin{aligned}
\dot{\eta}_v &= -R^T\dot{R}R^T(\hat{v}-v) + R^T(\dot{\hat{v}}-\dot{v}) \\
&= -R^TRS(\tilde{\omega}-b_\omega-\nu_\omega)R^T(\hat{v}-v) \\
&\quad + R^T\big\{\hat{R}(\tilde{f}-\hat{b}_f)-a+\hat{R}\big(L_p^v\tilde{E}_p+L_m^v\tilde{E}_m\big)-R(\tilde{f}-b_f-\nu_f)+a\big\} \\
&= -S\big[\tilde{I}_\omega+\eta_{b\omega}\big]\eta_v+\eta_R\tilde{I}_f+\eta_R\big(L_p^v\tilde{E}_p+L_m^v\tilde{E}_m\big) \\
&\quad -\tilde{I}_f-\eta_{bf}+S(\nu_\omega)R^T(\hat{v}-v)+\nu_f \\
&= -S\big[\tilde{I}_\omega+\eta_{b\omega}\big]\eta_v+\eta_R\tilde{I}_f+\eta_R\big(L_p^v\tilde{E}_p+L_m^v\tilde{E}_m\big)-\tilde{I}_f-\eta_{bf}-S(\eta_v)\nu_\omega+\nu_f
\end{aligned}$$

$$\begin{aligned}
\dot{\eta}_R &= -R^T\dot{R}R^T\hat{R}+R^T\dot{\hat{R}} \\
&= -R^TRS(\tilde{\omega}-b_\omega-\nu_\omega)R^T\hat{R}+R^T\hat{R}S(\tilde{\omega}-\hat{b}_\omega)+R^T\hat{R}S\big[L_p^R\tilde{E}_p+L_m^R\tilde{E}_m\big] \\
&= -S\big[\tilde{I}_\omega+\eta_{b\omega}\big]\eta_R+\eta_RS(\tilde{I}_\omega)+\eta_RS\big[L_p^R\tilde{E}_p+L_m^R\tilde{E}_m\big]+S(\nu_\omega)\eta_R
\end{aligned}$$

$$\begin{aligned}
\dot{\eta}_{bf} &= \dot{\hat{b}}_f-\dot{b}_f \\
&= L_p^{bf}\tilde{E}_p+L_m^{bf}\tilde{E}_m-\nu_{bf}
\end{aligned}$$

$$\begin{aligned}
\dot{\eta}_{b\omega} &= \dot{\hat{b}}_\omega-\dot{b}_\omega \\
&= L_p^{b\omega}\tilde{E}_p+L_m^{b\omega}\tilde{E}_m-\nu_{b\omega}
\end{aligned}$$

where $\tilde{I}_\omega=\tilde{\omega}-\hat{b}_\omega$, $\tilde{I}_f=\tilde{f}-\hat{b}_f$ as well as $I_m=\hat{R}^Tm$ which appears in the invariant output errors:

$$\tilde{E}_p=\hat{R}^T(\hat{p}-\tilde{y}_p)=\hat{R}^T(\hat{p}-p-\nu_p)=\hat{R}^TRR^T(\hat{p}-p)-\hat{R}^T\nu_p=(\eta_R)^T\eta_p-\hat{R}^T\nu_p$$
$$E_m=\hat{R}^Tm-\tilde{y}_m=\hat{R}^Tm-R^Tm-\nu_m=I_m-R^T\hat{R}\hat{R}^Tm-\nu_m=I_m-\eta_RI_m-\nu_m$$

We linearize the system about $\bar{\eta}=0$ ($\bar{\eta}_R=I$), $\bar{\nu}=0$. We have

$$\begin{aligned}
\delta\tilde{E}_p &= \tilde{E}_p-\overline{\tilde{E}}_p \\
&= (\eta_R)^T\eta_p-\hat{R}^T\nu_p-(\bar{\eta}_R)^T\bar{\eta}_p+\hat{R}^T\bar{\nu}_p \\
&= (\delta\eta_R+\bar{\eta}_R)^T(\delta\eta_p+\bar{\eta}_p)-\hat{R}^T\nu_p \\
&= (\bar{\eta}_R)^T\delta\eta_p-\hat{R}^T\nu_p=\delta\eta_p-\hat{R}^T\nu_p \\
\delta\tilde{E}_m &= \tilde{E}_m-\overline{\tilde{E}}_m \\
&= I_m-\eta_RI_m-\nu_m-I_m+\bar{\eta}_RI_m+\bar{\nu}_m \\
&= -(\delta\eta_R)I_m-\nu_m=-S(\delta\gamma)I_m-\nu_m=S(I_m)\delta\gamma-\nu_m
\end{aligned}$$

and for the invariant estimation dynamics

$$
\begin{aligned}
\delta\dot{\eta}_p &= \dot{\eta}_p - \dot{\bar{\eta}}_p \\
&= -S\big[\tilde{I}_\omega + \eta_{b\omega}\big]\eta_p + \eta_v + \eta_R\big(L_p^p\tilde{E}_p + L_m^p\tilde{E}_m\big) - S(\eta_p)\nu_\omega - 0 \\
&= -S\big[\tilde{I}_\omega + \delta\eta_{b\omega} + \bar{\eta}_{b\omega}\big]\big(\delta\eta_p + \bar{\eta}_p\big) + \delta\eta_v + \bar{\eta}_v \\
&\quad + \big(\delta\eta_R + \bar{\eta}_R\big)\Big(L_p^p\big(\delta\tilde{E}_p + \overline{\tilde{E}}_p\big) + L_m^p\big(\delta\tilde{E}_m + \overline{\tilde{E}}_m\big)\Big) \\
&\quad - S\big[\delta\eta_p + \bar{\eta}_p\big]\big(\delta\nu_\omega + \bar{\nu}_\omega\big) \\
&= -S(\tilde{I}_\omega)\delta\eta_p + \delta\eta_v + \bar{\eta}_R\Big(L_p^p\delta\tilde{E}_p + L_m^p\delta\tilde{E}_m\Big) \\
&= -S(\tilde{I}_\omega)\delta\eta_p + \delta\eta_v + L_p^p\big(\delta\eta_p - \hat{R}^T\nu_p\big) + L_m^p\big(S(I_m)\delta\gamma - \nu_m\big)
\end{aligned}
$$

$$
\begin{aligned}
\delta\dot{\eta}_v &= \dot{\eta}_v - \dot{\bar{\eta}}_v \\
&= -S\big[\tilde{I}_\omega + \eta_{b\omega}\big]\eta_v + \eta_R\tilde{I}_f + \eta_R\big(L_p^v\tilde{E}_p + L_m^v\tilde{E}_m\big) - \tilde{I}_f - \eta_{bf} - S(\eta_v)\nu_\omega + \nu_f \\
&\quad + S\big[\tilde{I}_\omega + \bar{\eta}_{b\omega}\big]\bar{\eta}_v - \bar{\eta}_R\tilde{I}_f - \bar{\eta}_R\big(L_p^v\overline{\tilde{E}}_p + L_m^v\overline{\tilde{E}}_m\big) + \tilde{I}_f + \bar{\eta}_{bf} + S(\bar{\eta}_v)\bar{\nu}_\omega - \bar{\nu}_f \\
&= -S(\tilde{I}_\omega)\delta\eta_v - S\big[\delta\eta_{b\omega} + \bar{\eta}_{b\omega}\big]\big(\delta\eta_v + \bar{\eta}_v\big) + \delta\eta_R\tilde{I}_f \\
&\quad + \big(\delta\eta_R + \bar{\eta}_R\big)\Big(L_p^v\big(\delta\tilde{E}_p + \overline{\tilde{E}}_p\big) + L_m^v\big(\delta\tilde{E}_m + \overline{\tilde{E}}_m\big)\Big) \\
&\quad - \delta\eta_{bf} - S\big[\delta\eta_v + \bar{\eta}_v\big]\big(\delta\nu_\omega + \bar{\nu}_\omega\big) + \nu_f \\
&= -S(\tilde{I}_\omega)\delta\eta_v + S(\delta\gamma)\tilde{I}_f + \bar{\eta}_R\big(L_p^v\delta\tilde{E}_p + L_m^v\delta\tilde{E}_m\big) - \delta\eta_{bf} + \nu_f \\
&= -S(\tilde{I}_\omega)\delta\eta_v - S(\tilde{I}_f)\delta\gamma + L_p^v\big(\delta\eta_p - \hat{R}^T\nu_p\big) + L_m^v\big(S(I_m)\delta\gamma - \nu_m\big) - \delta\eta_{bf} + \nu_f
\end{aligned}
$$

$$
\begin{aligned}
\delta\dot{\eta}_R &= \dot{\eta}_R - \dot{\bar{\eta}}_R \\
&= -S\big[\tilde{I}_\omega + \eta_{b\omega}\big]\eta_R + \eta_R S(\tilde{I}_\omega) + \eta_R S\big[L_p^R\tilde{E}_p + L_m^R\tilde{E}_m\big] + S(\nu_\omega)\eta_R \\
&\quad + S\big[\tilde{I}_\omega + \bar{\eta}_{b\omega}\big]\bar{\eta}_R - \bar{\eta}_R S(\tilde{I}_\omega) - \bar{\eta}_R S\big[L_p^R\overline{\tilde{E}}_p + L_m^R\overline{\tilde{E}}_m\big] - S(\bar{\nu}_\omega)\bar{\eta}_R \\
&= -S(\tilde{I}_\omega)\delta\eta_R - S\big[\delta\eta_{b\omega} + \bar{\eta}_{b\omega}\big]\big(\delta\eta_R + \bar{\eta}_R\big) + \delta\eta_R S(\tilde{I}_\omega) \\
&\quad + \big(\delta\eta_R + \bar{\eta}_R\big)S\Big[L_p^R\big(\delta\tilde{E}_p + \overline{\tilde{E}}_p\big) + L_m^R\big(\delta\tilde{E}_m + \overline{\tilde{E}}_m\big)\Big] \\
&\quad + S\big[\delta\nu_\omega + \bar{\nu}_\omega\big]\big(\delta\eta_R + \bar{\eta}_R\big) \\
\delta\dot{\eta}_R &= \delta\eta_R S(\tilde{I}_\omega) - S(\tilde{I}_\omega)\delta\eta_R - S\big[\delta\eta_{b\omega}\big]\bar{\eta}_R + \bar{\eta}_R S\big[L_p^R\delta\tilde{E}_p + L_m^R\delta\tilde{E}_m\big] + S\big[\delta\nu_\omega\big]\bar{\eta}_R \\
S(\delta\dot{\gamma}) &= S(\delta\gamma)S(\tilde{I}_\omega) - S(\tilde{I}_\omega)S(\delta\gamma) - S\big[\delta\eta_{b\omega}\big] + S\big[L_p^R\delta\tilde{E}_p + L_m^R\delta\tilde{E}_m\big] + S\big[\nu_\omega\big] \\
\delta\dot{\gamma} &= \delta\gamma \times \tilde{I}_\omega - \delta\eta_{b\omega} + L_p^R\delta\tilde{E}_p + L_m^R\delta\tilde{E}_m + \nu_\omega \\
&= -S(\tilde{I}_\omega)\delta\gamma - \delta\eta_{b\omega} + L_p^R\big(\delta\eta_p - \hat{R}^T\nu_p\big) + L_m^R\big(S(I_m)\delta\gamma - \nu_m\big) + \nu_\omega
\end{aligned}
$$

$$
\begin{aligned}
\delta\dot{\eta}_{bf} &= \dot{\eta}_{bf} - \dot{\bar{\eta}}_{bf} \\
&= L_p^{bf}\tilde{E}_p + L_m^{bf}\tilde{E}_m - \nu_{bf} - L_p^{bf}\overline{\tilde{E}}_p - L_m^{bf}\overline{\tilde{E}}_m + \bar{\nu}_{bf} \\
&= L_p^{bf}\big(\delta\eta_p - \hat{R}^T\nu_p\big) + L_m^{bf}\big(S(I_m)\delta\gamma - \nu_m\big) - \nu_{bf}
\end{aligned}
$$

$$
\begin{aligned}
\delta\dot{\eta}_{b\omega} &= \dot{\eta}_{b\omega} - \dot{\bar{\eta}}_{b\omega} \\
&= L_p^{b\omega}\tilde{E}_p + L_m^{b\omega}\tilde{E}_m - \nu_{b\omega} - L_p^{b\omega}\overline{\tilde{E}}_p - L_m^{b\omega}\overline{\tilde{E}}_m + \bar{\nu}_{b\omega} \\
&= L_p^{b\omega}\big(\delta\eta_p - \hat{R}^T\nu_p\big) + L_m^{b\omega}\big(S(I_m)\delta\gamma - \nu_m\big) - \nu_{b\omega}
\end{aligned}
$$

We then rearrange the above expressions into form (4.26):

$$
\begin{bmatrix} \delta\dot{\eta}_p \\ \delta\dot{\eta}_v \\ \delta\dot{\gamma} \\ \delta\dot{\eta}_{bf} \\ \delta\dot{\eta}_{b\omega} \end{bmatrix} = \underbrace{\begin{bmatrix} -S(\tilde{I}_\omega) & I & 0 & 0 & 0 \\ 0 & -S(\tilde{I}_\omega) & -S(\tilde{I}_f) & -I & 0 \\ 0 & 0 & -S(\tilde{I}_\omega) & 0 & -I \\ 0 & 0 & 0 & 0 & 0 \\ 0 & 0 & 0 & 0 & 0 \end{bmatrix}}_{A} \begin{bmatrix} \delta\eta_p \\ \delta\eta_v \\ \delta\gamma \\ \delta\eta_{bf} \\ \delta\eta_{b\omega} \end{bmatrix}
$$

$$
- \underbrace{\begin{bmatrix} L_p^p & L_m^p \\ L_p^v & L_m^v \\ L_p^R & L_m^R \\ L_p^{bf} & L_m^{bf} \\ L_p^{b\omega} & L_m^{b\omega} \end{bmatrix}}_{K} \underbrace{\begin{bmatrix} -I & 0 & 0 & 0 & 0 \\ 0 & 0 & -S(I_m) & 0 & 0 \end{bmatrix}}_{C} \begin{bmatrix} \delta\eta_p \\ \delta\eta_v \\ \delta\gamma \\ \delta\eta_{bf} \\ \delta\eta_{b\omega} \end{bmatrix}
$$

$$
- \underbrace{\begin{bmatrix} 0 & 0 & 0 & 0 \\ -I & 0 & 0 & 0 \\ 0 & -I & 0 & 0 \\ 0 & 0 & I & 0 \\ 0 & 0 & 0 & I \end{bmatrix}}_{B} \underbrace{\begin{bmatrix} \nu_f \\ \nu_\omega \\ \nu_{bf} \\ \nu_{b\omega} \end{bmatrix}}_{w} + \underbrace{\begin{bmatrix} L_p^p & L_m^p \\ L_p^v & L_m^v \\ L_p^R & L_m^R \\ L_p^{bf} & L_m^{bf} \\ L_p^{b\omega} & L_m^{b\omega} \end{bmatrix}}_{K} \underbrace{\begin{bmatrix} -\hat{R}^T & 0 \\ 0 & -I \end{bmatrix}}_{D} \underbrace{\begin{bmatrix} \nu_p \\ \nu_m \end{bmatrix}}_{v}
$$

giving the set of (A, B, C, D) matrices used with (4.22) to compute K resp. the gains L of observer (4.18).

4.10 Invariant AHRS testing

4.10.1 Implementation Details

The invariant AHRS observers were designed in Section 4.7.1 and will be summarized below. We numerically implement the equations using the modified Euler method, e.g. [35, p. 280]: for $\dot{x} = F(x,t)$, $x(t_0) = x_0$, the approximated states $w_i = x(t_i)$, $t_i = t_0 + iT$ with T representing the step size are calculated by

$$
\begin{aligned}
w_0 &= x_0 \\
w_{i+1} &= w_i + \frac{T}{2}\Big(F(t_i, w_i) + F(t_{i+1}, w_i + TF(t_i, w_i))\Big) \qquad i = 0, 1, 2, \ldots
\end{aligned}
$$

As in Section 3.2.1, we employ a complementary filter topology: the system dynamics part of the observer $f(\hat{x}, u)$ is integrated at the IMU sampling period T_{IMU} to

produce rough state estimates $\hat{x}$, which are periodically updated using aiding measurements y_a, y_m resp. E_a, E_m and observer gains L at the user-selectable period $T_{\text{Aid}} \geq T_{\text{IMU}}$. The terms L are available either from the direct nonlinear design in Section 4.8, or from the Invariant EKF in Section 4.9. In the latter case we numerically integrate (4.22)

$$\dot{P} = AP + PA^T - PC^T(DRD^T)^{-1}CP + BQB^T$$

at the period of T_{Aid} and from $K = PC^T(DRD^T)^{-1}$ obtain the matrix of AHRS observer gains

$$K = \begin{bmatrix} L_a^R & L_m^R \\ L_a^\omega & L_m^\omega \end{bmatrix}.$$

The Q and R process and measurement noise covariance matrix entries are taken from Table 3.1 in Section 3.2.2 and the initial covariance matrix is assigned as $P_0 = 0_{6\times 6}$, c.f. Section 3.2.9. In both methods, the initial observer state $\hat{x}_0$ is computed during an initialization period described in Section 3.2.11.1 and we choose $T_{\text{Aid}} = 0.04$ s, i.e. an aiding rate of 25 Hz.

4.10.1.1 Body frame symmetries

From Section 4.7.1.1 the invariant AHRS observer is (4.15)

$$\begin{aligned} \dot{\hat{R}} &= \hat{R}S(\omega - \hat{b}_\omega) + S\big(L_a^R E_a + L_m^R E_m\big)\hat{R} \\ \dot{\hat{b}}_\omega &= \hat{R}^T\big(L_a^\omega E_a + L_m^\omega E_m\big), \end{aligned}$$

with invariant output errors

$$\begin{bmatrix} E_a \\ E_m \end{bmatrix} = \begin{bmatrix} a - \hat{R}y_a \\ m - \hat{R}y_m \end{bmatrix}$$

The observer gains L are available from a direct nonlinear design in Section 4.8 as (4.19)

$$\begin{aligned} L_a^R &= k_P l_a S(a) \quad & L_m^R &= k_P l_m S(m) \\ L_a^\omega &= -k_I l_a S(a) \quad & L_m^\omega &= -k_I l_m S(m) \end{aligned}$$

whose parameter values are chosen as $k_P = 2.5$, $k_I = 0.4$ and $l_a = l_m = 0.01$ to obtain good performance. Alternatively, the gains can be computed using the Invariant EKF method of Section 4.9 with the set of matrices (4.31)

$$A = \begin{bmatrix} 0 & -I \\ 0 & S[\hat{R}(\tilde{\omega} - \hat{b}_\omega)] \end{bmatrix},\ B = \begin{bmatrix} -\hat{R} & 0 \\ 0 & \hat{R} \end{bmatrix},\ C = \begin{bmatrix} -S(a) & 0 \\ -S(m) & 0 \end{bmatrix},\ D = \begin{bmatrix} -\hat{R} & 0 \\ 0 & -\hat{R} \end{bmatrix}$$

4.10.1.2 Ground frame symmetries

From Section 4.7.1.2, the invariant AHRS observer is (4.16)

$$\begin{aligned} \dot{\hat{R}} &= \hat{R}S(\omega - \hat{b}_\omega) + \hat{R}S\Big(L_a^R E_a + L_m^R E_m\Big) \\ \dot{\hat{b}}_\omega &= L_a^\omega E_a + L_m^\omega E_m \end{aligned}$$

where the invariant output errors are

$$\begin{bmatrix} E_a \\ E_m \end{bmatrix} = \begin{bmatrix} \hat{R}^T a - y_a \\ \hat{R}^T m - y_m \end{bmatrix}$$

By direct nonlinear design in Section 4.8 the observer gains L are (4.20)

$$\begin{aligned} L_a^R &= k_P l_a S(\hat{R}^T a) \quad & L_m^R &= k_P l_m S(\hat{R}^T m) \\ L_a^\omega &= -k_I l_a S(\hat{R}^T a) \quad & L_m^\omega &= -k_I l_m S(\hat{R}^T m) \end{aligned}$$

with the same parameter choices as before: $k_P = 2.5$, $k_I = 0.4$, $l_a = l_m = 0.01$. The gains L can alternatively be computed using the Invariant EKF method using the matrices (4.32)

$$A = \begin{bmatrix} -S[\tilde{\omega} - \hat{b}_\omega] & -I \\ 0 & 0 \end{bmatrix}, B = \begin{bmatrix} -I & 0 \\ 0 & I \end{bmatrix}, C = \begin{bmatrix} -S[\hat{R}^T a] & 0 \\ -S[\hat{R}^T m] & 0 \end{bmatrix}, D = \begin{bmatrix} -I & 0 \\ 0 & -I \end{bmatrix}$$

4.10.2 Simulation Results

We use the following reference trajectory for simulation: the system is stationary for 5 s with attitude $(\phi, \theta, \psi) = (0, 0, 0)$, the initialization period. Next, the system moves to $(60°, -60°, 60°)$, $(-60°, 60°, -60°)$ and back to $(60°, -60°, 60°)$ at times $t_1 = 10$, $t_2 = 15$, $t_3 = 20$ s, respectively. This last attitude is then held constant while the system undergoes linear vibration $\ddot{p} = A\sin(\omega t)$ during $20 < t < 25$ s where $A = 8$ m/s^2 and $\omega = 2.5$ Hz are representative values for the hardware unit being violently shaken by hand; the sensor model y_a is in error during this period as discussed in Section 3.2.2. The system is then stationary for $25 \leq t \leq 30$ s to allow the observer estimates to re-converge. This reference trajectory is converted to rate gyro, accelerometer and magnetometer signals, which are then corrupted using additive bias and white noise terms whose parameters are taken from Table 3.1[2]. The resulting IMU sensor log is used as the input to the observer designs.

4.10.2.1 Body frame symmetries

The body-frame symmetries observer simulation results are shown in Figure 4.2 where we plot the estimated attitude $\hat{R}$ (using Euler angles) and rate gyro bias $\hat{\omega}_b$ versus the reference trajectory. The body-frame symmetry observer (4.15) is validated to work under both the nonlinear design and the Invariant EKF gain selection methods. During the manoeuvering phase $5 \leq t \leq 20$ s the two cases provide perfect tracking performance and are essentially identical to each other. The shaking interval $20 \leq t \leq 25$ s exhibits (bounded) tracking errors caused by inertial acceleration violating the output model y_a as discussed in Section 3.2.2. Here the estimation performance is different between the two gain selection methods, for instance b_ω^x and b_ω^y which are strongly dependent on y_a are seen to drift in the Invariant EKF design, caused by the internal adjustment of gain matrix K due to changes in the estimation error covariance matrix P. The attitude estimates are in error during this phase; the ψ^m for the nonlinear gain design can be seen to have

[2]The simulated time-varying bias employs a Gauss-Markov process model whereas the invariant observer assumes a (simpler) Wiener process model.

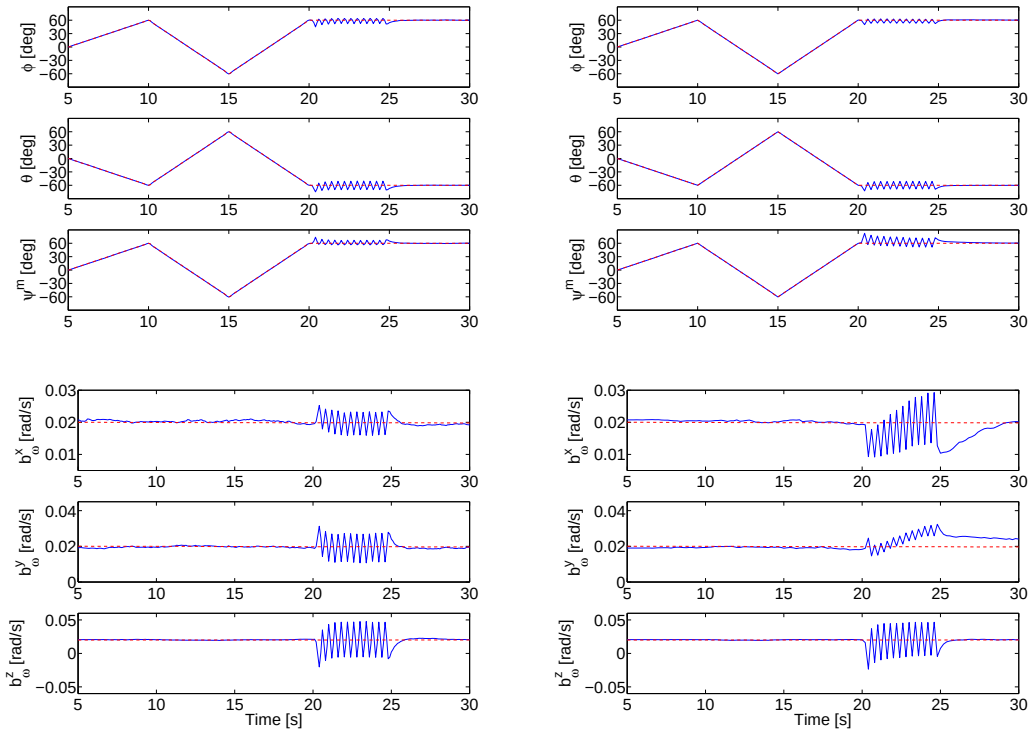

Figure 4.2: Invariant AHRS Simulation: Body-Frame Symmetry Observer (4.15) using gains from nonlinear design (left); Invariant EKF (right)

a slightly smaller error bound than the Invariant EKF version. Once shaking is terminated, the attitude estimates quickly re-converge to their reference values and the estimated biases do so at a slower rate.

4.10.2.2 Ground frame symmetries

The ground-frame symmetries observer estimates are plotted in Figure 4.3. The observer (4.16) for the ground-frame symmetries case is validated to work for both the nonlinear design and Invariant EKF gain selection methods: the estimated states track the reference trajectory on $5 \leq t \leq 20$ s, provide a bounded tracking error during the shaking interval $20 \leq t \leq 25$ s with y_a in error due to the inertial acceleration, and restore accurate estimates on $25 \leq t \leq 30$ s where the shaking has been stopped.

The performance obtained is very similar to the body-frame symmetries case in Section 4.10.2.1 and the estimation errors for the two versions will be explicitly compared in Section 4.10.2.3. In particular, the two symmetry versions of the nonlinear gain design are theoretically equivalent because the gains (4.19) and (4.20) reduce (4.15) and (4.16) to the same observer, c.f. Section 4.8. As discussed in Section 4.6.1 the ground-frame symmetries observer (4.16) has the advantage of the moving frame $\gamma(x)$ being guaranteed global existence.

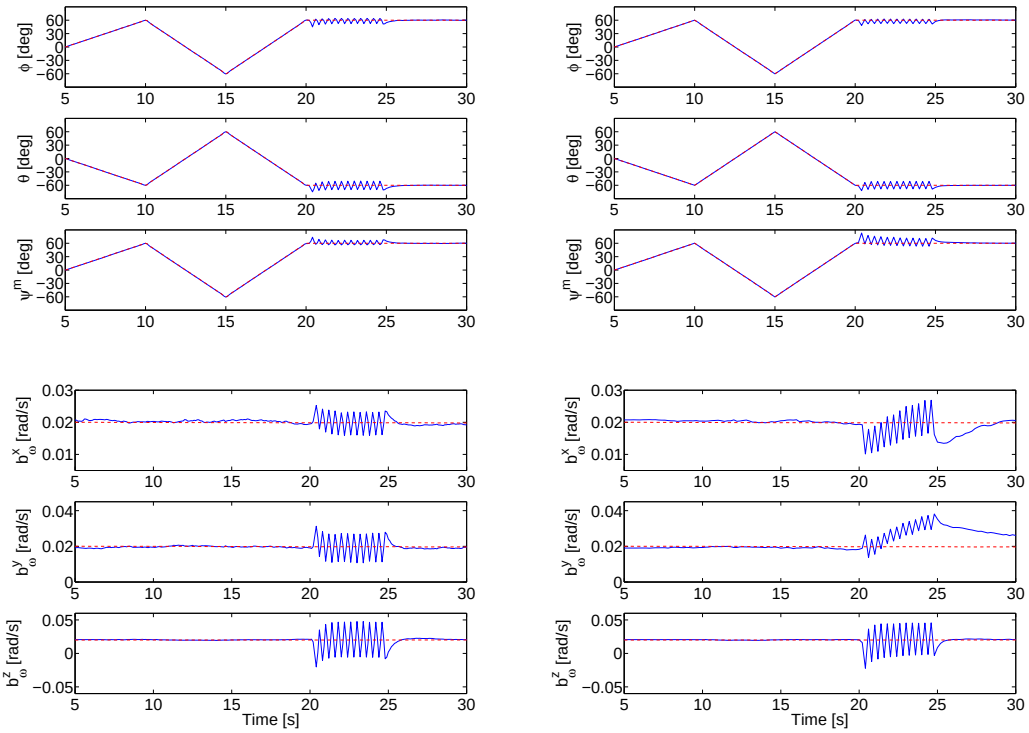

Figure 4.3: Invariant AHRS Simulation: Ground-Frame Symmetry Observer (4.16) using gains from nonlinear design (left); Invariant EKF (right)

4.10.2.3 Estimation performance comparison

We now compare the estimation errors for the body-frame nonlinear gain design, the body-frame Invariant EKF, the ground-frame nonlinear design and the ground-frame Invariant EKF. The resulting errors are plotted in Figure 4.4.

During the maneuvering interval $5 \leq t < 20$ s, all four designs provide essentially perfect attitude tracking performance, with peak errors $< 0.5°$ and typical errors on the order of $0.1°$. All designs exhibit large estimation errors during the shaking phase $20 \leq t < 25$ s which converge back to zero once shaking is terminated on $25 \leq t < 30$ s; the attitude errors re-converge to zero faster than the bias errors however. The ground-frame IEKF performs slightly better than the body-frame IEKF design, with peak attitude errors during the shaking phase approximately $0.5°$ smaller in the former visible when zooming in. Both Invariant EKF designs exhibit a drift in the mean value of the estimates $20 \leq t < 25$ s which is characteristic of the observer gains being re-adjusted by the Kalman filter, and indeed this effect is not present in the nonlinear designs.

As discussed in Section 4.10.2.2, the two versions of the nonlinear design are theoretically equivalent, and their corresponding plots are essentially indistinguishable from each other. The nonlinear designs provide slightly lower error bounds on $20 \leq t < 25$ s and faster re-converge on $25 \leq t < 30$ s compared to the Invariant EKF versions. However, the true advantage of the nonlinear design approach is the big savings in processor load realized by not employing the computationally expensive EKF algorithm. As mentioned in Section 3.2.10.1 our existing avionics system

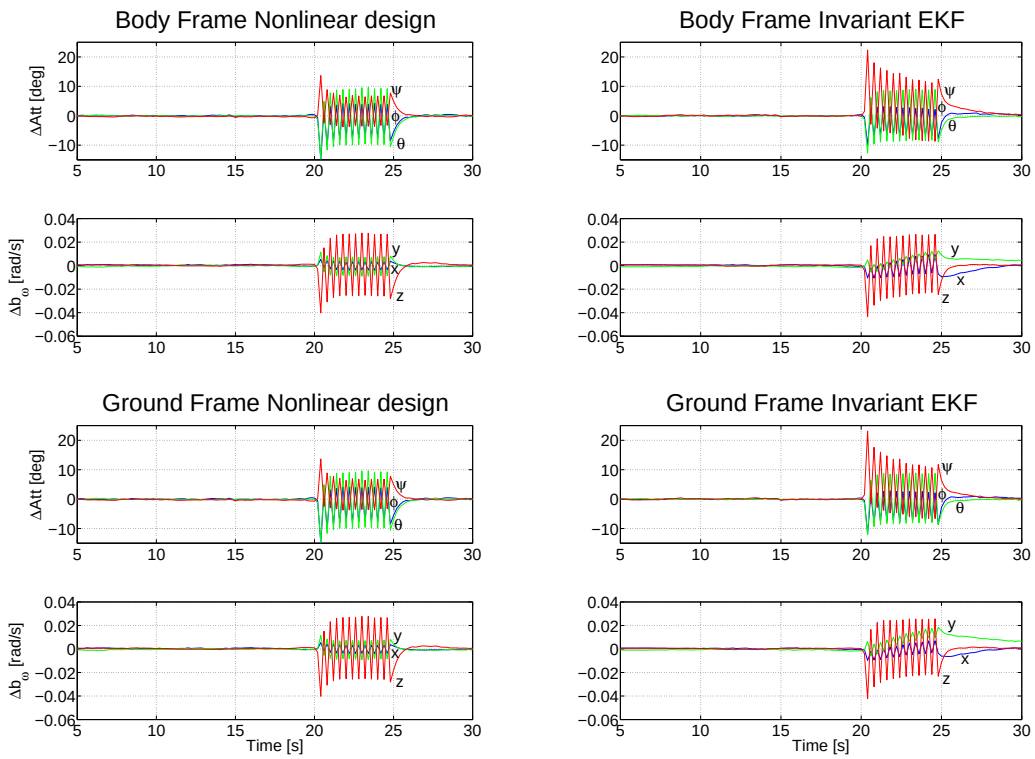

Figure 4.4: Invariant AHRS Simulation: Comparison of estimation errors

provides tremendous computing power and can easily run an EKF algorithm, however these saving would be of great importance on a low-power embedded system platform such as those used on small indoor autonomous UAV's.

4.10.3 Experimental Results

We now implement and test the invariant observers summarized in Section 4.10.1 in experiment, using the dataset from Section 3.3.2 which includes reference attitudes from the Vicon motion-capture system. The experiment consists of an initialization period where the unit is level; it is then picked up by hand and executes a sequence of positive and negative roll, positive and negative pitch and negative and positive yaw motions, returning to level configuration in-between. The unit is then shaken along its three axes with attitude held level, then set down allowing the estimates to re-converge. The yaw is reported as $\psi = \psi^m - \psi_0^m$ where ψ_0^m is found in initialization (c.f. Section 3.2.11.1) because the Vicon system uses the AHRS unit's initial orientation as its zero datum for reported attitude.

The observer parameters are the same as in simulation, namely a 25 Hz aiding rate, $k_P = 2.5$, $k_I = 0.4$, $l_a = l_m = 0.01$ for the nonlinear design gains, and Q, R from Table 3.1 and $P_0 = 0_{6\times 6}$ for the Invariant EKF. The y_m measurements are compensated using terms K_m, b_m resp. A_c, b_c obtained from an a priori magnetometer calibration, c.f. Sections 2.9 and 3.2.2. We have also found it necessary to implement verification of accelerometer data in experiment: as in Section 3.2.10.1,

each y_a aiding measurement is used for aiding only if

$$\frac{|\|y_a\| - g|}{g} \leq \text{tol} = 0.5,$$

otherwise aiding is omitted at that instant of time.

4.10.3.1 Body frame symmetries

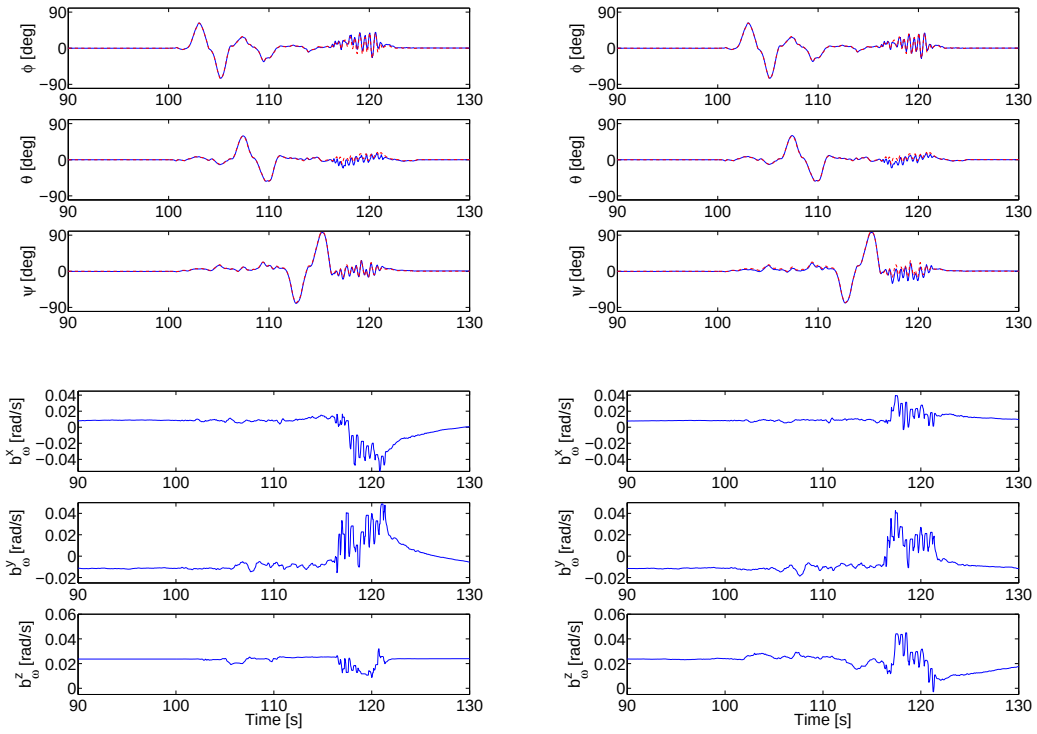

Figure 4.5: Invariant AHRS Experiment: Body-Frame Symmetry Observer (4.15) using gains from nonlinear design (left); Invariant EKF (right)

The experimental results for the body-frame symmetries observer (4.15) using the nonlinear design and Invariant EKF approaches to gain selection are plotted in Figure 4.5. We see the observer works in experiment for both approaches, tracking the reference attitude trajectory, providing a bounded error during the shaking period and re-converging to the correct values once shaking is terminated; from Figure 3.6 in Section 3.3.2, the shaking time interval is known to be $116 \leq t \leq 122$ s. Remark that the estimates of b^x_ω and b^y_ω are more perturbed in the nonlinear design than in the Invariant EKF case, but vice-versa for b^z_ω. This is due to the way the accelerometer output error is defined, namely $y_a \times \hat{y}_a = y_a \times \hat{R}^T a$ in the nonlinear design (c.f. Section 4.8) and $E_a = a - \hat{R} y_a$ in the body-frame Invariant EKF where $a = [0, 0, -g]^T$ (c.f. Section 4.2). For the level attitude during shaking, using the Euler angle parametrization of $\hat{R}$ (2.15) we have

$$\hat{\phi} = \hat{\theta} = 0 \Longrightarrow \hat{R} = \begin{bmatrix} * & * & 0 \\ * & * & 0 \\ 0 & 0 & 1 \end{bmatrix}$$

and so $\hat{R}^T a = [0, 0, *]^T \implies y_a \times \hat{R}^T a = [*, *, 0]^T$, i.e. the perturbed accelerometer measurements y_a do not enter b_ω^z in the nonlinear design case. By contrast $\hat{R} y_a = [*, *, *]^T$ such that $a - \hat{R} y_a = [*, *, *]^T$ in the Invariant EKF, so errors in y_a affect all three components of b_ω. This effect applies only if the shaking attitude is level, e.g. the simulated trajectory in Section 4.10.2 with final attitude $(\phi, \theta, \psi) = (60°, -60°, 60°)$ does not exhibit this behaviour, while changing this to $(0, 0, 0)$ would make it appear. The effect of the perturbed b_ω estimates on attitude error will be analyzed in Section 4.10.3.3.

4.10.3.2 Ground frame symmetries

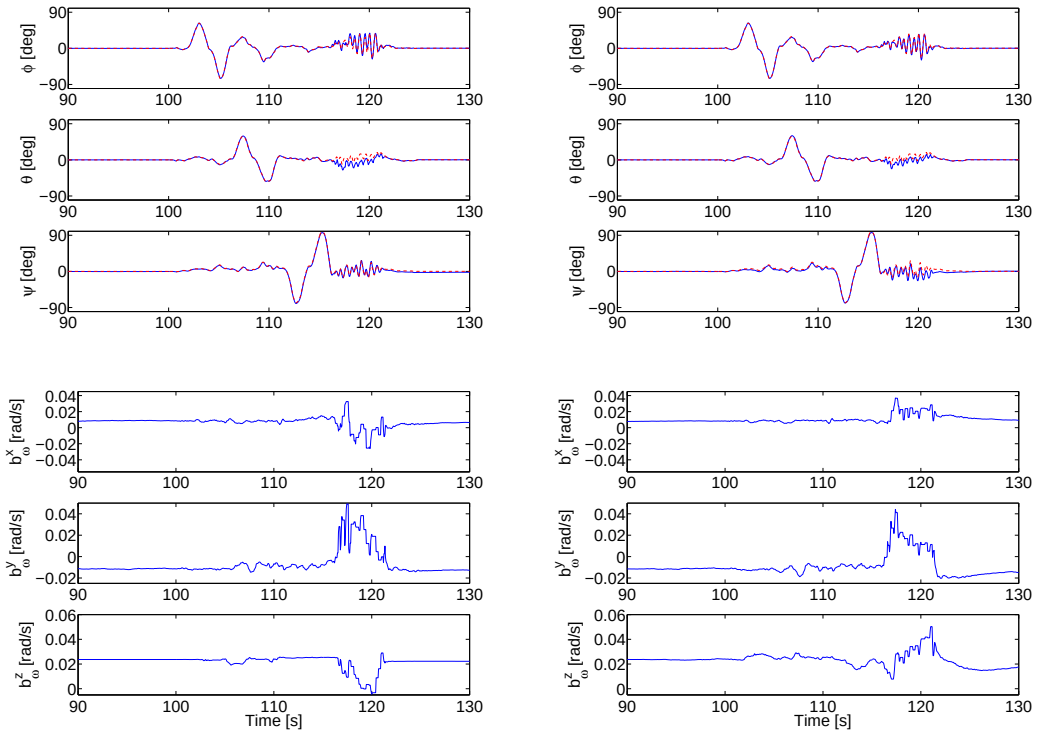

Figure 4.6: Invariant AHRS Experiment: Ground-Frame Symmetry Observer (4.16) using gains from nonlinear design (left); Invariant EKF (right)

The experimental estimates from the ground-frame symmetries observer (4.16) are shown in Figure 4.6 where the gains are obtained either by nonlinear design or by the Invariant EKF method. The observer and its associated gain selection methods are validated to work in experiment. During the shaking phase, the biases estimates b_ω are visibly different than the previous body-symmetry version plotted in Figure 4.5 in Section 4.10.3.1. For the present observer the invariant accelerometer output error is $E_a = \hat{R}^T a - y_a$ whereas the previous one uses $E_a = a - \hat{R} y_a$; this means errors in the attitude state R and measurement y_a are added in the present (ground-frame symmetries) observer but multiplied in the previous (body-frame symmetries) one. This leads to a difference in estimated states during the shaking phase where the system is in error due to violating the y_a output model as discussed

in Section 3.2.2. The effect of these differences on attitude estimation errors will be analyzed below in Section 4.10.3.3.

4.10.3.3 Performance comparison

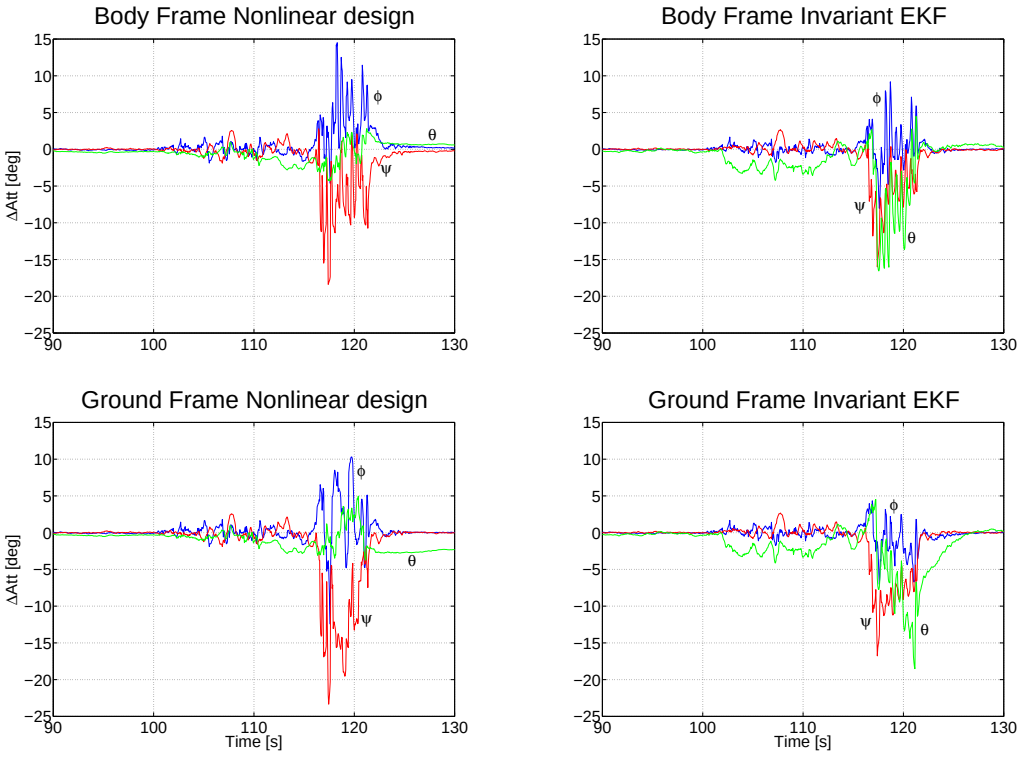

Figure 4.7: Invariant AHRS Experiment: Comparison of attitude estimation errors

We now compare the experimental performance of the body-frame symmetries observer (4.15) and the ground-frame symmetries observer (4.16) under the nonlinear design and Invariant EKF gain selection methods, for a total of four permutations. The error between estimated attitude (expressed as Euler angles) and the attitude reported by the Vicon motion-capture system is shown in Figure 4.7.

Based on the plots in Figure 4.7 we make the following comments: on the pre-shaking interval $90 \leq t \leq 116$ s the two nonlinear gain designs provide smaller estimation errors than the Invariant EKF versions. As discussed in Section 4.10.2.3 the nonlinear gain design method is preferable due to its lower computational requirements. For the shaking period $116 \leq t \leq 122$ s, the Invariant EKF designs provide smaller estimation error bounds than the nonlinear designs. This is likely due to the EKF's ability to adjust the observer gains when the estimation error covariance matrix P changes, and cannot be achieved by the nonlinear design which does not adapt its gains during runtime. On the other hand, the shaking interval is introduced as a test for system robustness, and so estimation performance during typical manoeuvering can be considered as a better metric of observer quality. Finally, the body-frame symmetry versions of both gain selection methods provide smaller error bounds during the shaking interval and faster re-convergence once shaking is terminated on $122 \leq t \leq 130$ s. This is probably due to the difference in form of

invariant output errors E_a and E_m in the two designs discussed in Section 4.10.3.2: for the body-frame version, errors in attitude R and measurements y_a, y_m multiply which provides an attenuating effect assuming the errors are smaller than unity. By contrast the ground-frame invariant output errors E_a, E_m superimpose attitude and measurement errors, which does not provide this attenuation effect. In this sense the body-frame version is superior for experiment even though the ground-frame version has the theoretical advantage of guaranteeing global existence of the moving frame $\gamma(x)$, c.f. Section 4.10.2.2.

4.11 Invariant Aided INS testing

4.11.1 Implementation details

We now implement the Aided INS invariant observers designed in Section 4.7.2 and summarized below. As mentioned at the end of Section 4.8 a nonlinear observer gain design for this case is not available, hence we use the Invariant EKF method of gain assignment (c.f. Section 4.9) whose (A, B, C, D) matrices were designed in Section 4.9.3 and will be summarized below.

As discussed in Section 4.5 the Aided INS outputs (4.7) assume the rotation matrix R_E^N and navigation frame location r_E^o are found during an initialization period, such that the vehicle's CM position measurement $y_p = p_N$ in navigation frame coordinates is converted from the GPS measurement r_E^a of the tail-mounted antenna position in ECEF frame coordinates by

$$y_p = p_N = R_N^E(r_E^a - r_E^o) - Rl_B$$

where l_B is the antenna lever-arm vector, c.f. Section 3.2.3.2. The GPS receiver reports the discrete-time covariance $\sigma_{p,d}^2$ and solution status of every measurement. The former is converted to continuous-time covariance $\sigma_p^2 = E\langle \nu_p \nu_p^T \rangle$ in the navigation frame by (c.f. Section 3.2.7)

$$\sigma_p^2 = T_{\text{GPS}} \left(R_N^E \sigma_{p,d}^2 R_E^N \right)$$

where $T_{\text{GPS}} = 0.01$ s is the nominal period between GPS measurements. The solution status is used to determine whether or not the current y_p is used for aiding; we employ the same criterion as in Section 3.2.10.2 i.e. only measurements with floating narrow-lane ambiguity or better are used for aiding. The second Aided INS output is the magnetometer measurement $y_m = R^T m$ where m is the local magnetic field vector in the navigation frame, available from a reference model as discussed in Section 2.8. Magnetometer measurements are corrected using the full compensation method in Section 2.9, such that as in Section 3.2.2, $y_m = A_c \tilde{m} + b_c$ and $(\sigma_m^c)^2 = A_c \sigma_m^2 (A_c)^T$ are the compensated aiding measurement and its covariance matrix, where $\tilde{m}$ is provided by the on-board triaxial magnetometer and σ_m^2 is the identified covariance of its measurements. The measurement noise covariance matrix $R_\nu = \text{diag}(\sigma_p^2, (\sigma_m^c)^2)$ is used together with the process noise covariance matrix $Q_\nu = \text{diag}(\sigma_f^2, \sigma_\omega^2, \sigma_{bf}^2, \sigma_{b\omega}^2)$ and the linearized system's (A, B, C, D) matrices in the

Invariant EKF computation (4.26) to obtain the matrix of observer gains

$$K = \begin{bmatrix} L_p^p & L_m^p \\ L_p^v & L_m^v \\ L_p^R & L_m^R \\ L_p^{bf} & L_m^{bf} \\ L_p^{b\omega} & L_m^{b\omega} \end{bmatrix}$$

The identified values of sensor covariances σ^2 are available from Table 3.1 in Section 3.2.2. The Invariant Aided INS observers are numerically implemented using the modified Euler method discussed in Section 4.10.1. Similarly to Section 4.10.3, if a position aiding measurement y_p is rejected due to insufficient precision of the GPS solution, the observer correction is skipped for this instant of time, increasing the time step h used by the observer at the next aiding measurement.

4.11.1.1 Body frame symmetries

From Section 4.7.2.1, the Aided INS body-frame symmetries observer is (4.17)

$$\begin{aligned} \dot{\hat{p}} &= \hat{v} + L_p^p E_p + L_m^p E_m \\ \dot{\hat{v}} &= \hat{R}(f - \hat{b}_f) - a + L_p^v E_p + L_m^v E_m \\ \dot{\hat{R}} &= \hat{R} S(\omega - \hat{b}_\omega) + S\big[L_p^R E_p + L_m^R E_m\big]\hat{R} \\ \dot{\hat{b}}_f &= \hat{R}^T \big(L_p^{bf} E_p + L_m^{bf} E_m\big) \\ \dot{\hat{b}}_\omega &= \hat{R}^T \big(L_p^{b\omega} E_p + L_m^{b\omega} E_m\big) \end{aligned}$$

with invariant output errors

$$\begin{bmatrix} E_p \\ E_m \end{bmatrix} = \begin{bmatrix} \hat{p} - y_p \\ m - \hat{R} y_m \end{bmatrix}$$

The gains L are then computed using the Invariant EKF method with the set of matrices from Section 4.9.3.1

$$A = \begin{bmatrix} 0 & I & 0 & 0 & 0 \\ 0 & 0 & -S[\hat{R}(f - \hat{b}_f)] & -I & 0 \\ 0 & 0 & 0 & 0 & -I \\ 0 & 0 & 0 & S[\hat{R}(\omega - \hat{b}_\omega)] & 0 \\ 0 & 0 & 0 & 0 & S[\hat{R}(\omega - \hat{b}_\omega)] \end{bmatrix}$$

$$B = \begin{bmatrix} 0 & 0 & 0 & 0 \\ -\hat{R} & 0 & 0 & 0 \\ 0 & -\hat{R} & 0 & 0 \\ 0 & 0 & \hat{R} & 0 \\ 0 & 0 & 0 & \hat{R} \end{bmatrix} \quad C = \begin{bmatrix} -I & 0 & 0 & 0 & 0 \\ 0 & 0 & -S(m) & 0 & 0 \end{bmatrix} \quad D = \begin{bmatrix} -I & 0 \\ 0 & -\hat{R} \end{bmatrix}$$

4.11.1.2 Ground frame symmetries

From Section 4.7.2.2, the Aided INS ground-frame symmetries observer is (4.18)

$$\begin{aligned}
\dot{\hat{p}} &= \hat{v} + \hat{R}\big(L_p^p E_p + L_m^p E_m\big) \\
\dot{\hat{v}} &= \hat{R}(f - \hat{b}_f) - a + \hat{R}\big(L_p^v E_p + L_m^v E_m\big) \\
\dot{\hat{R}} &= \hat{R}S(\omega - \hat{b}_\omega) + \hat{R}S\big[L_p^R E_p + L_m^R E_m\big] \\
\dot{\hat{b}}_f &= L_p^{bf} E_p + L_m^{bf} E_m \\
\dot{\hat{b}}_\omega &= L_p^{b\omega} E_p + L_m^{b\omega} E_m
\end{aligned}$$

with invariant output errors

$$\begin{bmatrix} E_p \\ E_m \end{bmatrix} = \begin{bmatrix} \hat{R}^T(\hat{p} - y_p) \\ \hat{R}^T m - y_m \end{bmatrix}.$$

The gains L are computed using the Invariant EKF method employing the matrices in Section 4.9.3.2

$$A = \begin{bmatrix} -S(\omega - \hat{b}_\omega) & I & 0 & 0 & 0 \\ 0 & -S(\omega - \hat{b}_\omega) & -S(f - \hat{b}_f) & -I & 0 \\ 0 & 0 & -S(\omega - \hat{b}_\omega) & 0 & -I \\ 0 & 0 & 0 & 0 & 0 \\ 0 & 0 & 0 & 0 & 0 \end{bmatrix} \quad B = \begin{bmatrix} 0 & 0 & 0 & 0 \\ -I & 0 & 0 & 0 \\ 0 & -I & 0 & 0 \\ 0 & 0 & I & 0 \\ 0 & 0 & 0 & I \end{bmatrix}$$

$$C = \begin{bmatrix} -I & 0 & 0 & 0 & 0 \\ 0 & 0 & -S(\hat{R}^T m) & 0 & 0 \end{bmatrix} \qquad D = \begin{bmatrix} -\hat{R}^T & 0 \\ 0 & -I \end{bmatrix}$$

4.11.2 Simulation results

4.11.2.1 Hover Simulation

The first simulation test is a hover manoeuver identical to that in Section 3.4.1.1: the vehicle starts off on the ground with $\phi_0 = \theta_0 = 0$ i.e. level and $\psi_0 = \pi/2$ i.e. facing geographic East and remains stationary for 45 s to simulate an initialization period. It then flies vertically up by 5 m in 5 s followed by a counter-clockwise turn of 180° over 5 s to end up facing West. These position and attitude configurations are connected using quintic and cubic splines, respectively. The resulting reference trajectory is converted to magnetometer m, accelerometer f, rate gyro ω and GPS r_E^a signals which are corrupted with simulated bias and noise using parameters from Table 3.1 in Section 3.2.2 and employing a Gauss-Markov process model for the time-varying bias terms. The noisy sensor log is used as an input to the body-frame invariant Aided INS observer (4.17) and ground-frame observer (4.18) using the Invariant EKF method of gain selection with Q and R covariance matrix entries taken from Table 3.1 and initial error covariance $P_0 = 0_{15\times 15}$, c.f. Section 4.10.1. The resulting state estimates are plotted in Figures 4.8 and 4.9 for the body-frame symmetry and ground-frame symmetry observers, respectively.

Both versions of the observer are shown to work and provide correct estimates of the position, velocity and attitude states of the hover manoeuver, which are essentially identical between the two designs. The estimated biases b_f and b_ω vary slightly

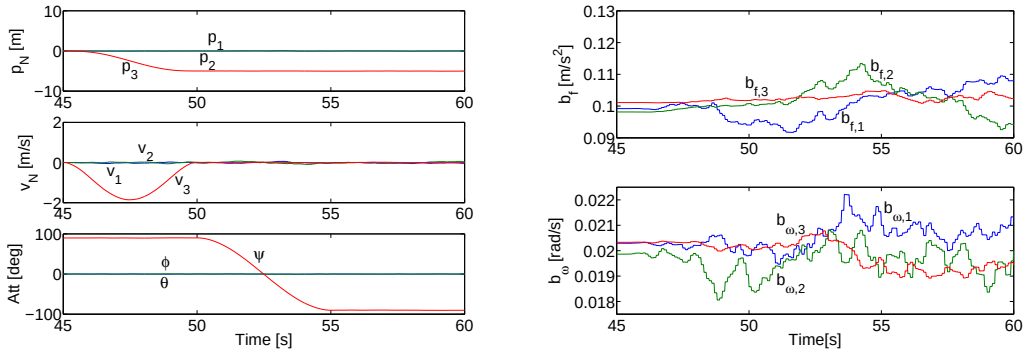

Figure 4.8: Body-Frame Invariant Aided INS: Simulated Hover

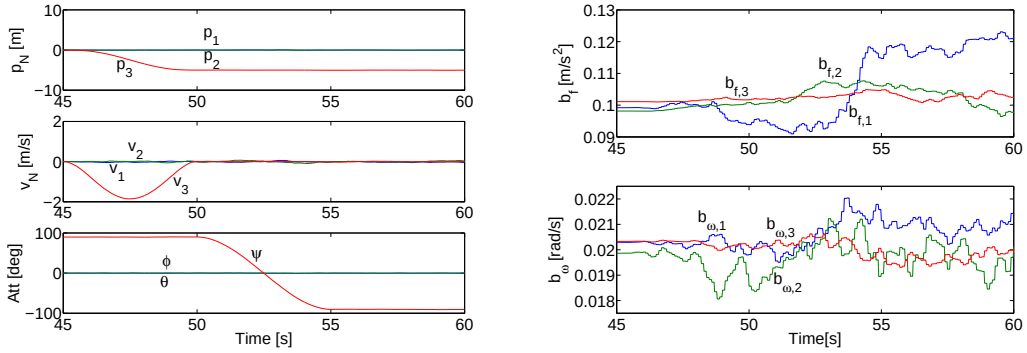

Figure 4.9: Ground-Frame Invariant Aided INS: Simulated Hover

between the two observer versions, likely caused by differences in the symbolic forms of the two observers and associated IEKF matrices affecting the numerical integration, for instance the estimated attitude R enters the b_f and b_ω dynamics in the body-frame symmetries observer (4.17) but not in the ground-frame symmetries observer (4.18). These differences are small, however, and the main point of this simulation is to establish that both versions of the invariant observer work correctly.

4.11.2.2 Trajectory Simulation

The next simulation involves the figure-8 trajectory from Section 3.4.1.2 with position and attitude described by the parametric curves (3.27) and (3.28) using the same parameter values as before: major and minor diameters of $M = 50$ m, $m = 25$ m for each lobe, a vertical delta of $H = 10$ m and the geometric center of the figure-8 placed at $p_N = (0, 0, -15)$ m with a full circuit flight period of $T = 50$ s. The simulated vehicle starts out level and stationary on the ground with $\psi_0 = 90°$ for 45 s, then the trajectory splines into the full-speed figure-8 flight over 10 s. The same Invariant EKF parameters as in Section 4.11.2.1 are used here. The state estimates for the body-frame and ground-frame symmetries observers are shown in Figures 4.10 and 4.11, respectively.

As in Section 4.11.2.1, both versions of the invariant observer are confirmed to work for the simulated trajectory. The flight states are estimated correctly and only

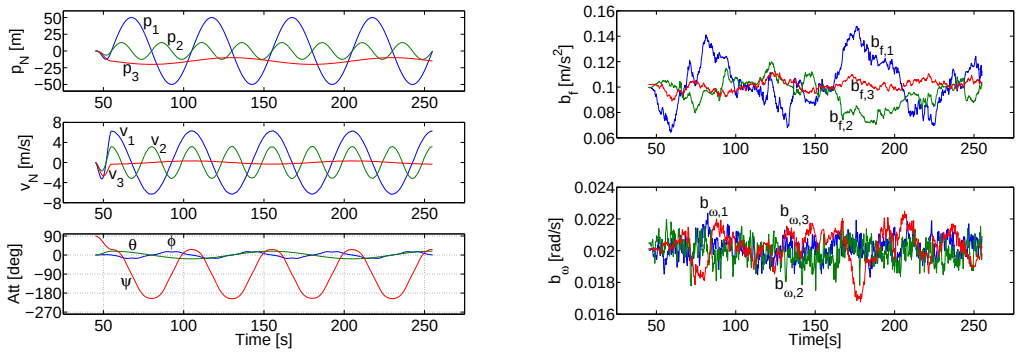

Figure 4.10: Body-Frame Invariant Aided INS: Simulated Figure-8 flight

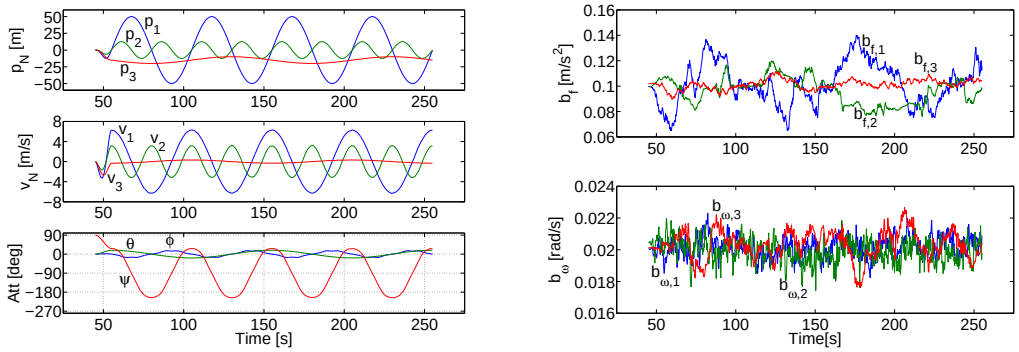

Figure 4.11: Ground-Frame Invariant Aided INS: Simulated Figure-8 flight

small discrepancies are visible between the two designs. This is more clearly seen in Figure 4.12, where we plot the error between the estimated states and the generated reference trajectory for each observer.

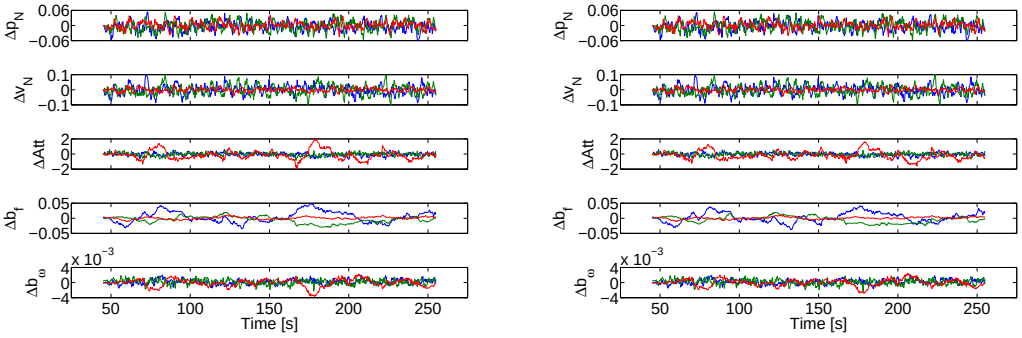

Figure 4.12: Invariant Aided INS: Simulated Figure-8 flight estimation errors: Body-frame symmetry; Ground-frame symmetry

4.11.3 Experimental results

4.11.3.1 Ground Test

This test uses sensor logs from the experiment described in Section 3.4.2: the engine-off helicopter is manually carried around the periphery of a rectangular landing pad at the flight field, held level with its heading aligned with the direction of travel and executing a 90° counter-clockwise turn at every corner for two complete circuits. The experiment includes an initialization period where the helicopter is left stationary and level at the southern-most corner of the pad aligned with the initial direction of travel; the helicopter is also set down at this spot once its circuit is complete. We employ the magnetometer compensation technique described in Section 2.9 using parameters from Table 2.1 to construct the terms A_c and b_c. We use the same observer parameters as for the simulations in Sections 4.11.2.1 and 4.11.2.2, namely Invariant EKF process and measurement covariance matrices Q and R from Table 3.1 and initial estimation error covariance matrix $P_0 = 0_{15\times15}$. The resulting state estimates are plotted in Figure 4.13 for the body-frame symmetries invariant observer and Figure 4.14 for the ground-frame version.

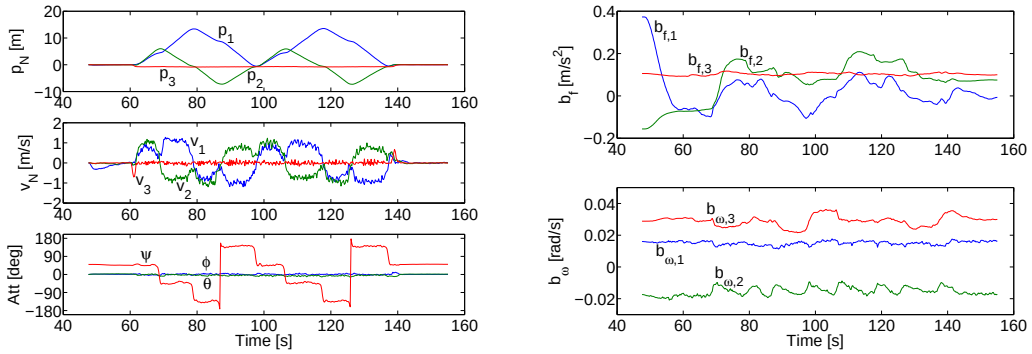

Figure 4.13: Body-Frame Invariant Aided INS: Experimental engine-off walk

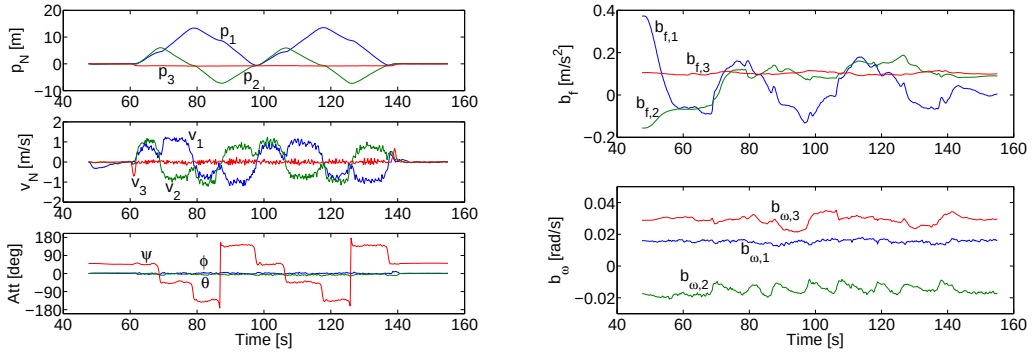

Figure 4.14: Ground-Frame Invariant Aided INS: Experimental engine-off walk

Similarly to the simulation case, the two invariant observer versions perform very similarly to each other. Remark the non-zero component of v_N during the pre-pickup $t \leq 60$ s due to the use of 3-axis magnetometer updates as discussed in

Section 3.4.2.1; unlike Figure 3.12, however, the error is eliminated by the invariant observer adjusting estimates of $b_{f,1}$ and $b_{f,2}$, such that the end velocity is correctly estimated as zero. The position and attitude estimates are qualitatively correct: p_1 and p_2 show the circuit trajectory is repeated exactly twice, p_3 identifies the pick-up and set-down times of the helicopter, ϕ and θ and kept near zero due to the helicopter being level while ψ increases by 90° at each (counter-clockwise) corner turn. Although an exact reference is not available (unlike the AHRS experiment in Section 4.10.3), we can use the measured dimensions of the landing pad and its yaw angle w.r.t. geographic North to create an approximated reference trajectory for the overhead position and yaw angle. This is done in Figure 4.15 for the body-frame and ground-frame symmetries observers. The two versions are seen to provide good performance relative to the available reference.

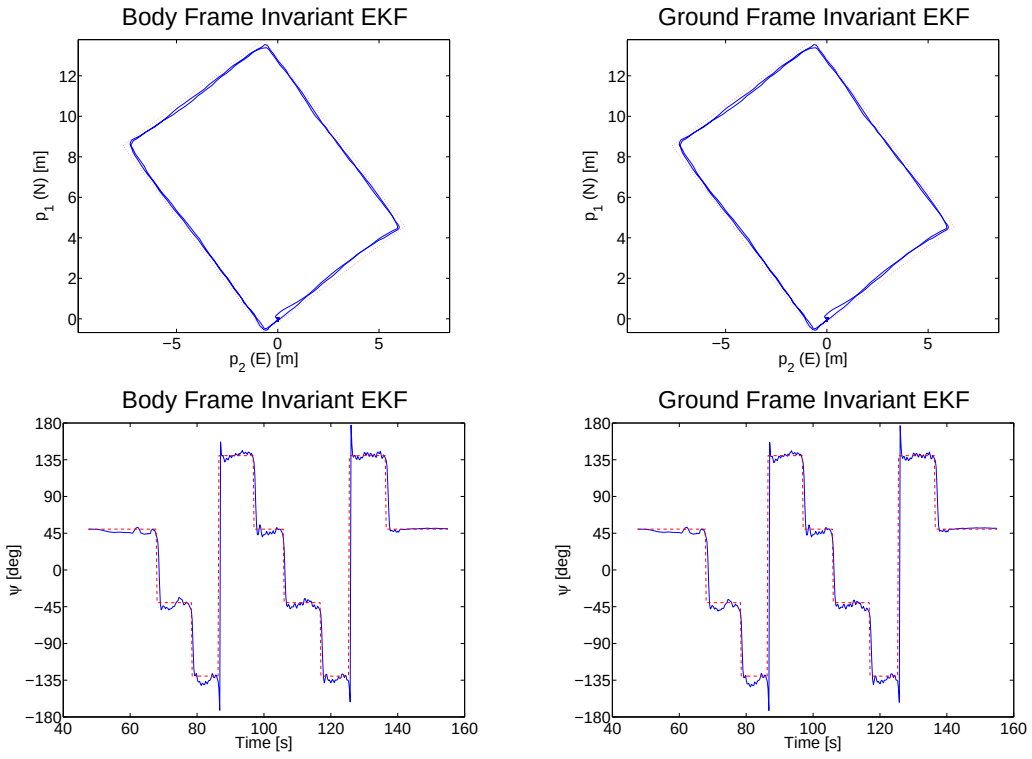

Figure 4.15: Invariant Aided INS: Experimental engine-off walk comparison: Body-frame symmetry; Ground-frame symmetry

4.11.3.2 Flight Test

The final experimental test is the engine-on hover flight previously seen in Section 3.4.3. The helicopter starts out stationary on the landing pad running the engine in idle setting. The throttle input is then increased, causing the main rotor to spool up until lift-off is achieved. After a transient take-off phase a stable hover is achieved characterized by a near-constant yaw angle provided by the tail gyro's heading-hold mode; the helicopter still drifts around due to strong cross-winds and constant stick input from the pilot required to maintain stable hover. The helicopter then lands.

Table 4.1: Engine-on Invariant Aided INS observer parameters

Body Frame Invariant EKF				
$\text{diag}(Q_f)$ $[\text{m}^2/\text{s}^3]$	$\text{diag}(Q_\omega)$ $[\text{rad}^2/\text{s}]$	$\text{diag}(Q_{bf})$ $[\text{m}^2/\text{s}^4]$	$\text{diag}(Q_{b\omega})$ $[\text{rad}^2/\text{s}^2]$	$\text{diag}(R_m)$ $[\text{G}^2\,\text{s}]$
$100 \cdot 0.0079^2$	$10 \cdot 0.0017^2$	$1 \cdot 0.0042^2$	$1 \cdot 0.00029^2$	$50 \cdot 0.00058^2$
$100 \cdot 0.0074^2$	$10 \cdot 0.0017^2$	$1 \cdot 0.0020^2$	$1 \cdot 0.00038^2$	$50 \cdot 0.00051^2$
$100 \cdot 0.0090^2$	$10 \cdot 0.0021^2$	$1 \cdot 0.0016^2$	$1 \cdot 0.00032^2$	$50 \cdot 0.00051^2$
Ground Frame Invariant EKF				
$\text{diag}(Q_f)$ $[\text{m}^2/\text{s}^3]$	$\text{diag}(Q_\omega)$ $[\text{rad}^2/\text{s}]$	$\text{diag}(Q_{bf})$ $[\text{m}^2/\text{s}^4]$	$\text{diag}(Q_{b\omega})$ $[\text{rad}^2/\text{s}^2]$	$\text{diag}(R_m)$ $[\text{G}^2\,\text{s}]$
$100 \cdot 0.0079^2$	$10 \cdot 0.0017^2$	$0.01 \cdot 0.0042^2$	$0.01 \cdot 0.00029^2$	$50 \cdot 0.00058^2$
$100 \cdot 0.0074^2$	$10 \cdot 0.0017^2$	$0.01 \cdot 0.0020^2$	$0.01 \cdot 0.00038^2$	$50 \cdot 0.00051^2$
$100 \cdot 0.0090^2$	$1 \cdot 0.0021^2$	$0.01 \cdot 0.0016^2$	$0.01 \cdot 0.00032^2$	$50 \cdot 0.00051^2$

The key challenge is the uncertainty in noise and bias modeling for the engine-on case. As noted in Section 3.4.3, the identified noise characteristics from the engine-off case as well as initial error covariance matrix P_0 entries must be tuned to make the filter work in the engine-on case. In addition the noise characteristics vary with time, e.g. the spool-up resonant frequency effect discussed in Section 3.4.3.1. As explained below we found it necessary to adjust the Invariant EKF Q and R matrices differently for the body-frame and ground-frame symmetries cases as summarized in Table 4.1. In addition, we set the initial bias estimation error covariances of b_f, b_ω in P_0 as follows: for the body-frame case, $P_{f,1} = P_{f,2} = 1 \times 10^{-3}$; $P_{f,3} = 1 \times 10^{-7}$; $P_{\omega,1} = P_{\omega,2} = 1 \times 10^{-5}$; $P_{\omega,3} = 1 \times 10^{-7}$; for the ground-frame case, $P_{f,1} = P_{f,2} = P_{f,3} = 1 \times 10^{-4}$ and $P_{\omega,1} = P_{\omega,2} = P_{\omega,3} = 1 \times 10^{-5}$. The resulting estimates are plotted in Figure 4.16 for the body-frame version and Figure 4.17 for the ground-frame version.

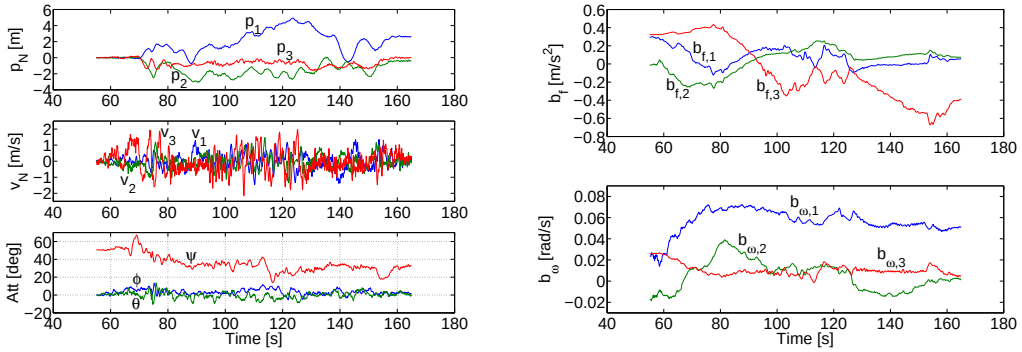

Figure 4.16: Body-Frame Invariant Aided INS: Experimental engine-on hover

Unlike the results in Section 4.11.2 and Section 4.11.3.1, there is a noticeable difference in performance between the body-frame and ground-frame version of the observer, with the latter performing much closer to the conventional EKF version plotted in Figure 3.15 in Section 3.4.3.1; the nearly constant ψ provided by the heading-hold tail gyro is clearly visible in Figure 4.17 but not in Figure 4.16. The ground-frame version is also the case reported in [18].

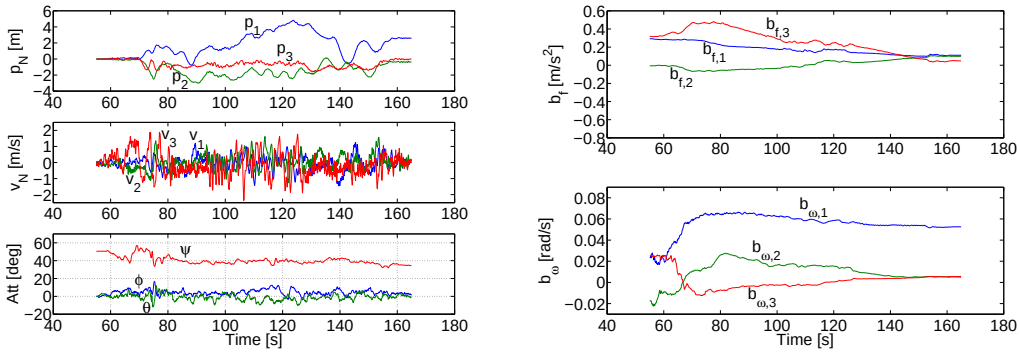

Figure 4.17: Ground-Frame Invariant Aided INS: Experimental engine-on hover

The reason for the discrepancy and need for different observer parameters can be explained by looking at the form of the body-frame invariant observer (4.17) summarized in Section 4.11.1.1 versus the ground-frame observer (4.18) in Section 4.11.1.2: the estimated attitude R enters the bias b_f, b_ω dynamics in the former but not in the latter. This means that any errors in estimated attitude immediately affect the bias estimates in the body-frame version, which further aggravates the problem due to b_ω used for the high-rate integration of R dynamics. Remark that in the ground-frame observer (4.18) the estimated attitude R enters the p and v dynamics whereas it does not in the body-frame observer (4.17). Indeed zooming in on the estimated position p_N for the pre-takeoff period of $55 \leq t \leq 70$ s as shown in Figure 4.18, we see the body-frame version provides better position estimates (p closer to zero) than the ground-frame version. However, given that position is directly aided by the GPS modulo the lever-arm term, the ground-frame invariant observer is more robust to poor bias and sensor noise modeling than the body-frame version as seen in Figures 4.16 and 4.17. Of course a better model of the engine-on noise characteristics would reduce this discrepancy, as seen in the engine-off experimental tests in Section 4.11.3.1 where the noise parameters are well-identified [75, Chap. 4].

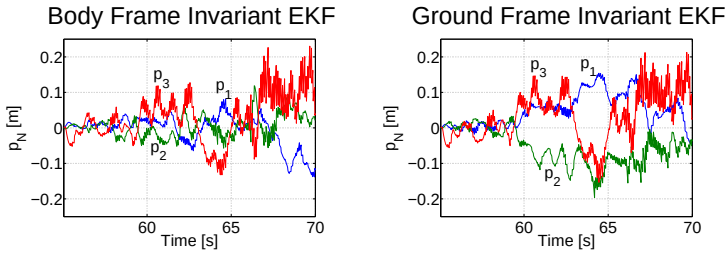

Figure 4.18: Invariant Aided INS: Pre-takeoff estimated position zoom-in view

Chapter 5

Nonlinear Model of a Helicopter UAV

5.1 Overview

The dynamics of the helicopter are governed by the 6 DoF nonlinear equations of motion of a rigid body [105, p. 167] whose forcing terms are gravity as well as force and moment vectors created by aerodynamic effects, both controlled (e.g. rotor thrust) and uncontrolled (e.g. drag forces), which must be modeled as functions of the vehicle state and pilot inputs.

In contrast to rigid-body dynamics, aerodynamics are much more complicated to model due to the large number of physical processes involved, including unsteady flow through the rotating helicopter blades, wake-body interactions, vortex formation and turbulence at the rotor tips, blade stall, flow compressibility effects and aeroelasticity of the blades. High-fidelity helicopter models use a finite-element approach to accurately model the physics of the flow. For control design, the better approach is to use lumped-parameter models of the individual helicopter subsystems — main rotor, main rotor blade flapping, fuselage body, tail horizontal stabilizer, tail vertical stabilizer and tail rotor — using simplified aerodynamics equations, whose parameters are experimentally identified and can be further adjusted to tune the model output to match experimental flight data. This "minimum-complexity" approach [65], originally applied to full-sized helicopter modeling and control studies carried out by NASA [43] has been used for helicopter UAVs in [101, 59, 21] with excellent results.

A visual representation of the proposed model structure is shown in Figure 5.1. The rigid-body equations of motion are derived in Section 5.2. We develop expressions for the individual subsystems' forces and moments as functions of the helicopter state and pilot inputs throughout Section 5.3. The resulting model is summarized in Section 5.4 and its identified parameter values are listed in Section 5.5.

5.2 Rigid-Body Model

In this Section, we derive the 6 DoF rigid-body dynamics governing the motion of the helicopter, shown schematically in Figure 5.2. The ground-fixed (inertial) navigation frame has orthonormal basis vectors (n_1, n_2, n_3) and the body-fixed (non-inertial)

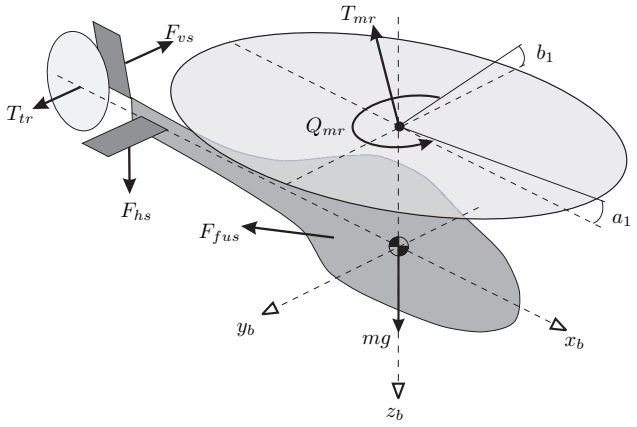

Figure 5.1: Helicopter Model: Overall View [59]

body frame has orthonormal basis vectors (b_1, b_2, b_3). The origin of the B frame is placed at the centre of mass of the helicopter.

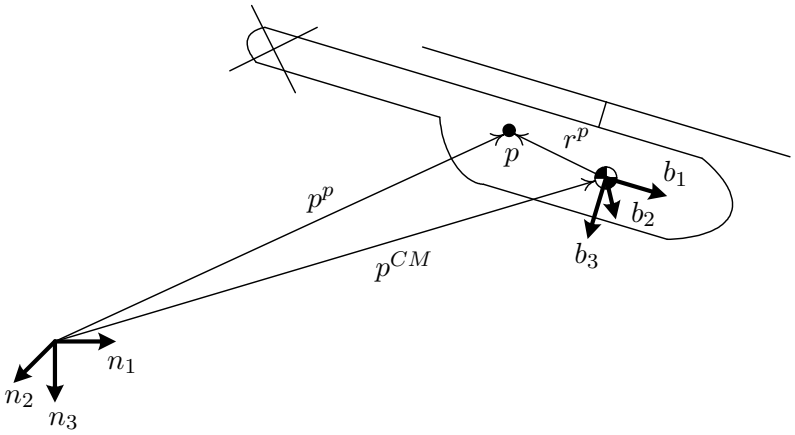

Figure 5.2: Navigation and Body Frames on Helicopter

By inspection of Figure 5.2, the position of any point p on the helicopter body is described by the vector $p^p = p^{CM} + r^p$ where by construction p^p and p^{CM} start at the N frame origin while r^p starts at the B frame origin. Using frame coordinates this is written as

$$p_N^p(t) = p_N^{CM}(t) + R(t) r_B^p,$$

where the rotation matrix $R(t) \in SO(3)$ is the coordinate transformation matrix from B to N. Physically, R measures the attitude of the helicopter, e.g. $R = I$ means the B and N frames are aligned and so the helicopter is level with zero yaw. Differentiating with respect to time gives

$$v_N^p(t) = v_N^{CM}(t) + \dot{R}(t) r_B^p, \tag{5.1}$$

where $v_N^p(t)$ and $v_N^{CM}(t) := \bar{v}_N(t)$ are the velocities of p and the centre of mass w.r.t. the navigation frame origin.

The linear momentum vector of a point mass m is $G = mv$ and its angular momentum vector about a point P is $H^P = d^P \times mv$ where d^P denotes the vector

from P to the mass. The linear momentum vector of a rigid body is defined as the integral of infinitesimal linear momentums, i.e.

$$G = \int_V v^p \, dm, \tag{5.2}$$

where v^p is the velocity vector of the infinitesimal mass element $dm = \rho \, dV$, where v^p and mass density ρ vary over the volume. Similarly, the angular momentum vector of the rigid body about a point P is defined by

$$H^P = \int_V d^P \times v^p \, dm, \tag{5.3}$$

with d^P the position vector from P to dm. The G and H^P vectors are expressed in the same frame as their integrands, i.e. using (5.1) in (5.2) gives

$$G_N(t) = \int_V \left(\bar{v}_N(t) + \dot{R}(t) r_B^p \right) dm = \bar{v}_N(t) \int_V dm + \dot{R}(t) \int_V r_B^p \, dm = m \bar{v}_N(t) \tag{5.4}$$

where m is the total mass of the body. The second integral in (5.4) is zero by construction: the CM position vector $\bar{p}$ of a rigid body is defined by

$$\bar{p} := \frac{1}{m} \int_V p^p \, dm,$$

but due to placing the B frame origin at the centre of mass, we have $p^p = r^p$, $\bar{p} = \bar{r} = 0$ and $\bar{r}_B = 0 \implies \int_V r_B^p \, dm = 0$. Next, using (5.1) in (5.3) and taking $P = CM$ we have

$$H_N^{CM}(t) = \int_V d_N^{CM}(t) \times \bar{v}_N(t) \, dm + \int_V d_N^{CM}(t) \times \dot{R}(t) r_B^p \, dm \tag{5.5}$$

Using $d_N^{CM}(t) = R(t) d_B^{CM}$ and $d_B^{CM} = r_B^p$ the first integral in (5.5) becomes

$$\int_V R(t) r_B^p \times \bar{v}_N(t) \, dm = -\bar{v}_N(t) \times R(t) \int_V r_B^p \, dm = 0$$

due to $\int_V r_B^p \, dm = 0$ as above. Using the rotational kinematics $\dot{R}(t) = R(t) S\big(\omega_B(t)\big)$ where $\omega(t)$ is the angular velocity vector and S is the skew-symmetric matrix such that $x \times y = S(x)y$, $x, y \in \mathbb{R}^3$ along with the identity $S(Rx) = RS(x)R^T$, $R \in SO(3)$, the second integral in (5.5) becomes

$$\int_V R(t) r_B^p \times R(t) S\big(\omega_B(t)\big) r_B^p \, dm = R(t) \int_V S(r_B^p) S\big(\omega_B(t)\big) r_B^p dm.$$

Denoting $r_B^p = [x \quad y \quad z]^T$ and $\omega_B(t) = [p \quad q \quad r]^T$ the integrand becomes

$$\begin{aligned} S(r_B^p) S(\omega_B(t)) r_B^p &= \begin{bmatrix} 0 & -z & y \\ z & 0 & -x \\ -y & x & 0 \end{bmatrix} \begin{bmatrix} 0 & -r & q \\ r & 0 & -p \\ -q & p & 0 \end{bmatrix} \begin{bmatrix} x \\ y \\ z \end{bmatrix} \\ &= \begin{bmatrix} -rxz + pz^2 - qxy + py^2 \\ -ryz + qz^2 + qx^2 - pxy \\ ry^2 - qyz + rx^2 - pxz \end{bmatrix} \\ &= \underbrace{\begin{bmatrix} y^2 + z^2 & -xy & -xz \\ -xy & x^2 + z^2 & -yz \\ -xz & -yz & x^2 + y^2 \end{bmatrix}}_{\mathcal{I}} \underbrace{\begin{bmatrix} p \\ q \\ r \end{bmatrix}}_{\omega_B(t)}. \end{aligned}$$

Returning to (5.5) we have

$$H_N^{CM}(t) = R(t)\int_V \mathcal{I}\omega_B(t)dm = R(t)J\omega_B(t) \tag{5.6}$$

where $J = \int_V \mathcal{I}\,dm$ is the *inertia matrix*, a function of the geometry and mass distribution of the body. Remark $\mathcal{I}$ hence J is symmetric and so it is always diagonalizable. Physically this corresponds to correctly orienting the body-fixed frame B, whose origin is still required to be taken at the centre of mass. In this case $J = \text{diag}(J_{xx}, J_{yy}, J_{zz})$ and (b_1, b_2, b_3) define the *principal axes* of the body. For now we leave J as a general (non-diagonalized) inertia matrix.

The dynamics of a rigid body are governed by Euler's laws of motion

$$F = \frac{d}{dt}G(t) \qquad \text{and} \qquad M^{CM} = \frac{d}{dt}H^{CM}(t), \tag{5.7}$$

where F, M^{CM} are the net external force and moment vectors acting on the body. Equations (5.7) hold under the following conditions:

- The mass of the body must remain constant,
- The moment and angular momentum vectors must be taken about the centre of mass of the body,
- The linear and angular momentum vectors must be expressed in an inertial frame.

Note it is possible to treat systems which do not meet one or more of these conditions by generalizing the laws of motion. The case of time-varying mass, important in e.g. rocketry where the fuel burn rate creates a significant loss in mass is treated in [99, Art. 53]. Taking the angular momentum about a general, possibly accelerating point will be developed in Section 5.2.2 and involves defining an angular momentum *relative* to the moving point. Finally, it is possible to formulate the problem in a non-inertial frame by using the principles of relative motion [99, Art. 38], which transforms the velocity and acceleration observed in a non-inertial frame to their absolute values by employing the acceleration and rotation of the non-inertial frame. The present system avoids these complications, however, and so (5.7) holds.

Using the linear momentum vector (5.4) (expressed in inertial frame N) in (5.7) gives

$$F_N(t) = \frac{d}{dt}\big(m\bar{v}_N(t)\big) \Longrightarrow F_N(t) = m\dot{\bar{v}}_N(t), \tag{5.8}$$

i.e. the familiar $F = ma$. It is possible to express (5.8) in the body frame, for reasons which will be explained shortly. We have

$$\begin{aligned} R(t)F_B(t) &= \frac{d}{dt}\big(mR(t)\bar{v}_B(t)\big) \\ &= m\dot{R}(t)\bar{v}_B(t) + mR(t)\dot{\bar{v}}_B(t) \\ &= mR(t)S(\omega_B(t))\bar{v}_B(t) + mR(t)\dot{\bar{v}}_B(t) \\ R(t)F_B(t) &= mR(t)\omega_B(t) \times \bar{v}_B(t) + mR(t)\dot{\bar{v}}_B(t), \end{aligned}$$

and left-multiplying by $R^T(t)$ yields

$$F_B(t) = m\Big(\omega_B(t) \times \bar{v}_B(t) + \dot{\bar{v}}_B(t)\Big), \tag{5.9}$$

the body-frame version of $F = ma$ where $\bar{v} = [u \quad v \quad w]^T$ denotes the velocity vector of the helicopter's CM expressed in body frame components. Although (5.9) is more complicated than (5.8), the reason for using it is that the aerodynamic forces, e.g. the main rotor thrust, are naturally formulated in the body-fixed B frame. The one exception is gravity which always acts downwards and must be transformed into B frame coordinates as $R^T(t)g_N$ where $g_N = [0 \quad 0 \quad g]^T$.

Using (5.6) (taken about CM and expressed in the inertial frame N as required) in (5.7) gives

$$\begin{aligned} M_N^{CM}(t) &= \frac{d}{dt}\big(R(t)J\omega_B(t)\big) \\ &= \dot{R}(t)J\omega_B(t) + R(t)J\dot{\omega}_B(t) \\ M_N^{CM}(t) &= R(t)S(\omega_B(t))J\omega_B(t) + R(t)J\dot{\omega}_B(t) \\ R(t)M_B^{CM}(t) &= R(t)\omega_B(t) \times J\omega_B(t) + R(t)J\dot{\omega}_B(t). \end{aligned}$$

Left-multiplying by $R^T(t)$ then gives

$$M_B^{CM}(t) = \omega_B(t) \times J\omega_B(t) + J\dot{\omega}_B(t). \tag{5.10}$$

Together (5.9) and (5.10) are known as the Newton-Euler equations, e.g. [105, p. 167], which govern the translational and rotational dynamics of the helicopter.

As discussed above, the J matrix can be diagonalized by properly orienting the B frame axes. We assume the helicopter's roll-pitch-yaw axes are sufficiently aligned with the principal axes such that $J \approx \text{diag}(J_{xx}, J_{yy}, J_{zz})$. Although this assumption is not required, it greatly simplifies the form of (5.10) and has been used in other experimentally-validated helicopter models [59, 101, 122]. Expanding out (5.9) and (5.10) with gravity force $mg_B = mR^T g_N$ we obtain

$$\begin{aligned} \dot{u} &= rv - qw + R_{31}g + X/m \\ \dot{v} &= pw - ru + R_{32}g + Y/m \\ \dot{w} &= qu - pv + R_{33}g + Z/m \\ \dot{p} &= qr(J_{yy} - J_{zz})/J_{xx} + L/J_{xx} \\ \dot{q} &= pr(J_{zz} - J_{xx})/J_{yy} + M/J_{yy} \\ \dot{r} &= pq(J_{xx} - J_{yy})/J_{zz} + N/J_{zz} \end{aligned} \tag{5.11}$$

where (X, Y, Z), (L, M, N) are the components of the aerodynamic force and moment vectors expressed in the roll-pitch-yaw body frame, respectively. The dynamics (5.11) are integrated to obtain $v_B = [u \quad v \quad w]^T$, $\omega_B = [p \quad q \quad r]^T$ which in turn are integrated through the kinematics

$$\begin{aligned} \dot{R} &= RS(\omega_B) \\ \dot{p}_N &= Rv_B \end{aligned} \tag{5.12}$$

to obtain attitude and position of the helicopter with respect to the ground-fixed navigation frame.

The mass m in (5.11) is measured directly using a digital scale. The location of the CM was identified by balancing the side of the helicopter on a knife-edge and is shown in Figure 5.3, where the CM is located on the vertical centerline plane of the vehicle. The mass moment of inertias J_{xx}, J_{yy} and J_{zz} were first attempted to be measured using a trifilar pendulum apparatus [114, p. 3.18] as suggested by [36, Sec. 6.3.2.2], however this method proved unusable due to lateral swinging motions of the helicopter during experimental testing [53]. We then successfully obtained the values using a torsional pendulum apparatus described in Section 5.2.1.

Figure 5.3: Helicopter UAV with identified CM location

5.2.1 Torsional Pendulum

The torsional pendulum system is sketched in Figure 5.4. A circular disk with mass m_0, radius r_0 and mass moment of inertia J_0 (around the vertical axis) rotates by angle θ as shown. The disk is supported by three long, thin wires of uniform length l, fixed above the disk and attached at the outer rim.

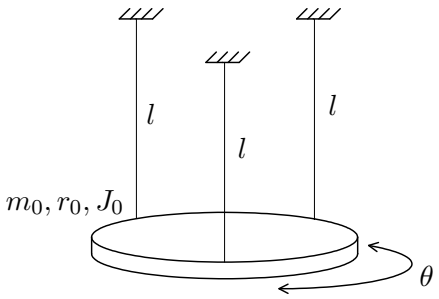

Figure 5.4: Torsional pendulum schematic

We derive the pendulum's equation of motion using Lagrange's equation. Since the top supports are fixed and the cables have constant lengths, the disk must move upwards when it rotates away from its neutral configuration. Consider the side view of a single cable subject to a disk rotation of θ, shown in Figure 5.5. The cable bottom advances by $r_0\theta$ units horizontally, while the whole disk rises vertically by h.

From Figure 5.5, we immediately see $h = l - \sqrt{l^2 - r_0^2\theta^2}$. The Lagrangian

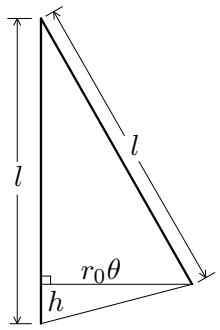

Figure 5.5: Geometry of support cable; disk rotated by θ

$L = T - V$, the difference between kinetic and potential energy, is

$$L = \frac{1}{2} J_0 (\dot{\theta})^2 - m_0 g \left(l - \sqrt{l^2 - r_0^2 \theta^2} \right),$$

from which the equation of motion is obtained by

$$\frac{d}{dt}\left(\frac{dL}{d\dot{\theta}}\right) - \frac{dL}{d\theta} = 0 \Longrightarrow J_0 \ddot{\theta} + \frac{m_0 g r_0^2 \theta}{\sqrt{l^2 - r_0^2 \theta^2}} = 0,$$

a nonlinear ODE. Consider the denominator of the second term,

$$\frac{l}{l}\sqrt{l^2 - r_0^2 \theta^2} = l\sqrt{1 - \left(\frac{r_0}{l}\right)^2 \theta^2}.$$

If the support cables are made much longer than the disk radius, $r_0/l << 1$ and hence $(r_0/l)^2 \approx 0$. The equation of motion then becomes

$$J_0 \ddot{\theta} + \frac{m_0 g r_0^2}{l} \theta = 0,$$

an undamped linear oscillator with natural frequency

$$\omega_n^2 = \frac{m_0 g r_0^2}{J_0 l}. \tag{5.13}$$

Equation (5.13) is used to find J_0 by giving the disk an initial rotation then allowing it to oscillate back-and-forth about its vertical centerline. The period of oscillation $T = 2\pi/\omega_n$ is directly measured and substituted into the above to solve for J_0.

Consider a body with (known) mass m and (unknown) mass moment of inertia J. The body is rigidly attached to the disk in Figure 5.4, such that the vertical disk axis passes through the center of mass of the measured object. The derivation above now uses mass $m_0 + m$ and inertia $J_0 + J$, giving the natural frequency

$$\omega_n^2 = \frac{(m_0 + m) g r_0^2}{(J_0 + J) l} = \left(\frac{2\pi}{T}\right)^2,$$

where T is the period of oscillation of the composite system. Solving for the unknown inertia,

$$J = \frac{(m_0 + m) g r_0^2 T^2}{4\pi^2 l} - J_0 \tag{5.14}$$

the measured body's mass moment of inertia *about the vertical axis*, so the measurement is performed for the yaw, pitch and roll axes of the helicopter, the last requiring using a stand attached to the disk in order to hold the helicopter in position. The stand must be accounted for by measuring its mass m_s and identifying J_0 of the disk-stand assembly using Equation (5.13) with mass term $(m_0 + m_s)$. We also reiterate the need for the support cables to be as long as possible such that the linearizing approximation holds. Pictures of the experimental setup for the pitch and roll axes are shown in Figure 5.6; remark the stand used for the roll axis as well as the hanging weight used to align the helicopter's CM with the center of the disk below it. The computed J_{xx}, J_{yy}, J_{zz} values are provided in Section 5.5.

Figure 5.6: Experimental measurement of J using a torsional pendulum [53]: pitch axis, roll axis.

5.2.2 Extended Moment Equation

As mentioned in Section 5.2, it is possible to generalize the second Euler equation (5.7) to take moments about a general (non-CM) point. This will be used in Section 5.3.1.3 to derive the flapping dynamics of the main rotor.

A general rigid body is shown schematically in Figure 5.7 where N is the ground-fixed inertial frame, B is the body-fixed frame with point o on its origin, p is an arbitrary point on the body, p^p and p^o are the position vectors from the origin of N to points p and o, respectively, while r^p is the position vector from the origin of B to p. The rigid body and its attached frame B are free to accelerate. By definition the rigid body possesses a center of mass, but its coordinates are not important at the moment.

By inspection of Figure 5.7 we have the vector expression $p^p_N(t) = p^o_N(t) + r^p_N(t)$ whose components are functions of time due to the motion of the rigid body.

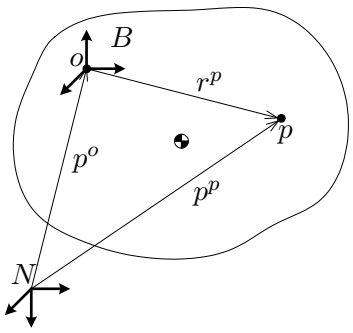

Figure 5.7: Rigid body with body frame fixed at arbitrary point o

Differentiating with respect to time we obtain

$$v_N^p(t) = v_N^o(t) + \underline{v}_N^p(t) \tag{5.15}$$

where $\underline{v}_N^p(t) := (d/dt)r_N^p(t)$ physically represents the *relative velocity* of point p with respect to point o; remark $\underline{v}_N^p$ is a *non-inertial* measurement if o is accelerating. Following (5.3) we define the relative angular momentum of the body as

$$\underline{H}_N^o(t) = \int_V r_N^p(t) \times \underline{v}_N^p(t) dm \tag{5.16}$$

Since $\underline{H}_N^o(t)$ is not taken about the centre of mass or a fixed point, Euler's equations (5.7) do not apply directly. Instead we take the time derivative of (5.16) and obtain

$$\frac{d}{dt}\underline{H}_N^o(t) = \int_V \underline{v}_N^p(t) \times \underline{v}_N^p(t) dm + \int_V r_N^p(t) \times \underline{a}_N^p(t) dm,$$

where $\underline{a}_N^p(t) := (d/dt)\underline{v}_N^p(t)$ is the relative acceleration of point p w.r.t. point o, a non-inertial measurement if the body is accelerating. The first integrand above is zero. Differentiating (5.15) we obtain $\underline{a}_N^p(t) = a_N^p(t) - a_N^o(t)$, a difference of *inertial* accelerations. We have

$$\frac{d}{dt}\underline{H}_N^o(t) = \int_V r_N^p(t) \times a_N^p(t) dm - \int_V r_N^p(t) \times a_N^o(t) dm.$$

The first integrand contains $a_N^p(t)dm = dF_N^p$, the external force acting on the infinitesimal point p with mass dm. We thus have $\int_V r_N^p(t) \times dF_N^p = M_N^o$, the net external moment about point o acting on the rigid body. The second integral becomes

$$-\int_V r_N^p(t) \times a_N^o(t) dm = a_N^o(t) \times \int_V r_N^p(t) dm = a_N^o(t) \times m r_N^{CM}(t)$$

by definition of center of mass location $r^{CM} = \frac{1}{m}\int_V r dm$; physically $r_N^{CM}(t)$ represents the position vector from o to the CM expressed in N frame coordinates. We have obtained

$$\frac{d}{dt}\underline{H}_N^o(t) = M_N^o - m r_N^{CM}(t) \times a_N^o(t). \tag{5.17}$$

We now return to (5.16). Using $r_N^p(t) = R(t)r_B^p$ and $\underline{v}_N^p(t) = (d/dt)r_N^p(t) = \dot{R}(t)r_B^p = R(t)S\big(\omega_B(t)\big)r_B^p$ we have

$$\underline{H}_N^o(t) = \int_V R(t)r_B^p \times R(t)S\big(\omega_B(t)\big)r_B^p dm$$

Just as in Section 5.2 we use the identity $S(Rx) = RS(x)R^T$, $R \in SO(3)$ and obtain

$$\underline{H}_N^o(t) = R(t)\int_V S(r_B^p)S\big(\omega_B(t)\big)r_B^p dm := R(t)\int_V \mathcal{I}^o\omega_B(t)dm = R(t)J^o\omega_B(t)$$

where we wrote $r_B^p = [x^o \quad y^o \quad z^o]^T$ and defined

$$\mathcal{I}^o = \begin{bmatrix} (y^o)^2+(z^o)^2 & -x^oy^o & -x^oz^o \\ -x^oy^o & (x^o)^2+(z^o)^2 & -y^oz^o \\ -x^oz^o & -y^oz^o & (x^o)^2+(y^o)^2 \end{bmatrix} \text{ and } J^o = \int_V \mathcal{I}^o dm.$$

Remark $\mathcal{I}^o$ resp. J^o are taken about o whereas $\mathcal{I}$ and J in Section 5.2 were taken about the CM; the mass moments of inertia can be related using the parallel-axis theorem $J^o = J + m\|r^{CM}\|^2$. Taking the time derivative of the last $\underline{H}_N^o(t)$ above gives

$$\frac{d}{dt}\underline{H}_N^o(t) = \dot{R}(t)J^o\omega_B(t) + R(t)J^o\dot{\omega}_B(t) = R(t)S\big(\omega_B(t)\big)J^o\omega_B(t) + R(t)J^o\dot{\omega}_B(t),$$

and substituting this into (5.17) gives

$$R(t)S\big(\omega_B(t)\big)J^o\omega_B(t) + R(t)J^o\dot{\omega}_B(t) = M_N^o - mr_N^{CM}(t) \times a_N^o(t)$$

which is pre-multiplied by $R^T(t)$ to give

$$M_B^o = \omega_B(t) \times J^o\omega_B(t) + J^o\dot{\omega}_B(t) + mr_B^{CM} \times a_B^o(t), \tag{5.18}$$

the "extended" [33, p. 363] version of the Euler equation (5.10) from Section 5.2. As expected setting $r_B^{CM} = 0$ in (5.18) recovers (5.10) since in this case the moment is taken about the CM. Alternatively, setting $a_B^o(t) = 0$ gives $M_B^o = \omega_B(t) \times J^o\omega_B(t) + J^o\dot{\omega}_B(t)$, the dynamics of a rigid body rotating about a fixed (or more generally non-accelerating) point o [99, Art. 25].

5.3 Aerodynamics and Subsystem Modeling

5.3.1 Main Rotor

The following suite of assumptions is used for modeling the main rotor [61, 42]:

- Rotor blades are rigid in bending and torsion
- Both the flapping angle β and inflow angle Φ are assumed small
- The effects of helicopter body motion on flapping are limited to the helicopter's angular velocities p, q, angular accelerations $\dot{p}, \dot{q}$ and normal acceleration $(a_B \cdot b_3)$

- The reversed flow region is ignored and compressibility and stall effects disregarded
- The inflow is assumed uniform across the rotor disc and no inflow dynamics are used
- Tip loss is neglected

The above assumptions are considered valid for advance ratios $\mu = V/(\Omega R) < 0.3$ where V is the helicopter's forward velocity. For the Bergen Industrial Twin with $\Omega = 1650$ RPM and $R = 0.810$ m, this works out to $V < 42$ m/s, well above the maximum speeds achievable in forward flight.

5.3.1.1 Induced Velocity

The main rotor consists of two airfoil blades rotating clockwise at a rate of Ω. As the blades rotate, a mass flow of air is sucked through the rotor disc traced out by the spinning blades (illustrated in Figure 5.1) which generates a reaction force perpendicular to the rotor disc known as the thrust T. The average velocity of the airstream passing through the rotor disc is known as the induced velocity v_i, which is understood to be parallel to the thrust vector.

We first consider the hover case, where the relationship between v_i and resulting thrust T is worked out using control volume analysis [104, Ch. 5], assuming the flow is steady, inviscid and incompressible and using the stream tube shown in Figure 5.8 as the control volume.

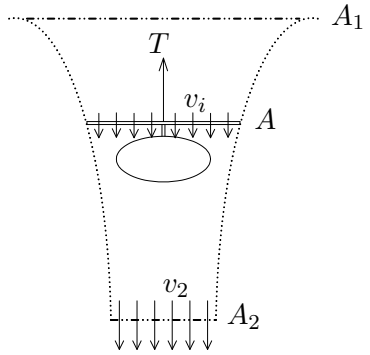

Figure 5.8: Rotor inflow in hover

In Figure 5.8, the fully developed wake region has stream tube area A_2 and average flow velocity v_2. The top of the stream tube A_1 represents an area far upstream of the flow where the velocity is zero; A is the area of the rotor disc and is known from the helicopter blade length. The continuity equation gives $\rho A v_i = \rho A_2 v_2 = \dot{m}$, the mass flow rate. The momentum equation gives $F_{cv} = \int_{cs} v\rho v \cdot n dA$, and since $v_0 = 0$ the force on the flow $F_{cv} = 0 - v_2 \rho v_2 A_2 \Longrightarrow T = v_2^2 \rho A_2$, the reaction force on the helicopter body. Finally the energy equation gives $\dot{W}_{cv} = \int_{cs} \varepsilon \rho v \cdot n dA$ where $\dot{W}$ is the rate of work done on the flow and ε is the total specific energy of the flow, taken as the kinetic energy $\varepsilon = v^2/2$ since we neglect changes in internal and potential energy. We know $\dot{W}_{cv} = T v_i$, the power imparted to the flow by the helicopter rotor, so $T v_i = (v_2^2/2)\rho v_2 A_2 \Longrightarrow v_i = v_2/2$ using the momentum equation.

Using the continuity equation we also have $A/2 = A_2$, the wake contraction shown in Figure 5.8. Using the last two results we obtain $T = 2v_i^2\rho A$.

The same control volume analysis applies in vertical flight where the helicopter in Figure 5.8 is climbing with velocity V. In this case, the flow velocity at A_1 is V, the velocity through the rotor disc A is $V+v_i$, and the wake velocity at A_2 is $V+v_2$. The continuity equation gives $\dot{m} = \rho A_1 V = \rho A(V + v_i) = \rho A_2(V + v_2)$, the momentum equation gives $F_{cv} = V\rho V A_1 - (V+v_2)\rho(V+v_2)A_2 = V\dot{m} - (V+v_2)\dot{m} \Longrightarrow T = v_2\dot{m}$ and the energy equation gives $\dot{W}_{cv} = -\frac{1}{2}V^2\rho V A_1 + \frac{1}{2}(V + v_2)^2\rho(V + v_2)A_2 \Longrightarrow T(V + v_i) = Vv_2\dot{m} + \frac{1}{2}v_2^2\dot{m}$. Combining the last two results gives $v_2\dot{m}(V + v_i) = Vv_2\dot{m} + v_2^2/2\dot{m} \Longrightarrow v_i = v_2/2$, just as in the hover case, and so $T = 2v_i(V + v_i)\rho A$ which correctly reduces to the hover thrust expression above when $V = 0$.

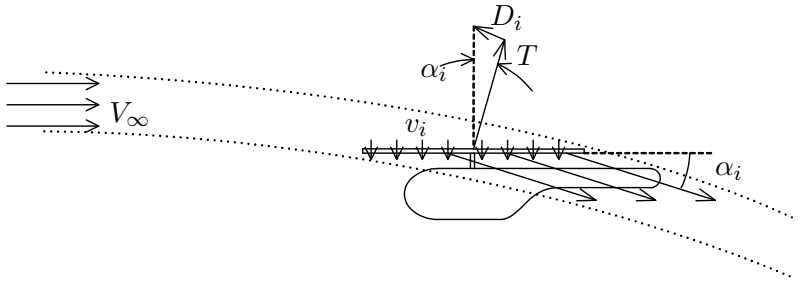

Figure 5.9: Rotor inflow in fast forward flight

Fast forward flight is shown schematically in Figure 5.9. As before, we assume uniform inflow v_i across the rotor disc; based on experimental testing results [115, p. 124] this assumption is not as accurate as in the hover case, however this is mitigated by the fact that $V \gg v_i$ [72, p. 126]. In order to obtain a relationship between v_i and T, we view the rotor disc as a fixed, finite-width wing and employ lifting-line theory [13, Sec. 5.3], where v_i is the *downwash* which reduces the effective angle of attack of the wing and creates the induced drag D_i parallel to the local inflow. This is illustrated in Figure 5.9, where the rotor must generate the induced drag force D_i in addition to the usual thrust force T to maintain unaccelerated flight. We assume an elliptical distribution of circulation across the wing, which is known to yield uniform downwash over the span of the wing [13, p. 411] as desired. For the elliptical distribution, the relationship between lift and drag is analytically calculated to be [13, Eq. (5.43)]

$$C_{D,i} = \frac{C_L^2}{\pi AR},$$

where $C_{D,i} = D_i/(q_\infty S)$ is the coefficient of induced drag with $q_\infty = (1/2)\rho_\infty V_\infty$ the free-stream dynamic pressure and S the wing planform area; $C_L = L/(q_\infty S)$ is the coefficient of lift with $L = T$ perpendicular to the local inflow; and $AR = b^2/S$ is the wing aspect ratio with b the span of the wing. For the helicopter rotor disc $b = 2R$ and $S = \pi R^2 = A$ where R is measured from the blade geometry (A was previously used in Figure 5.8). From Figure 5.9 we have

$$\tan\alpha_i = \frac{v_i}{V_\infty} = \frac{C_{D,i}}{C_L} = \frac{C_L^2}{\pi AR C_L} = \frac{T}{\frac{1}{2}\rho_\infty V_\infty^2 S\pi(2R)^2/S} \Longrightarrow v_i = \frac{T}{2\rho_\infty V_\infty A}$$

We now seek a universal expression for v_i which applies to any flight condition of the helicopter. The control volume used for this analysis is shown in Figure 5.10. The stream velocity V shown corresponds to the helicopter flying up and forwards. The velocities perpendicular to the horizontal cross-sections with areas A_1, A and A_2 are thus $V\sin\alpha$, $V\sin\alpha+v_i$ and $V\sin\alpha+v_2$, respectively, where v_i is the induced velocity at the rotor and v_2 is the downstream induced velocity as in the vertical climb case.

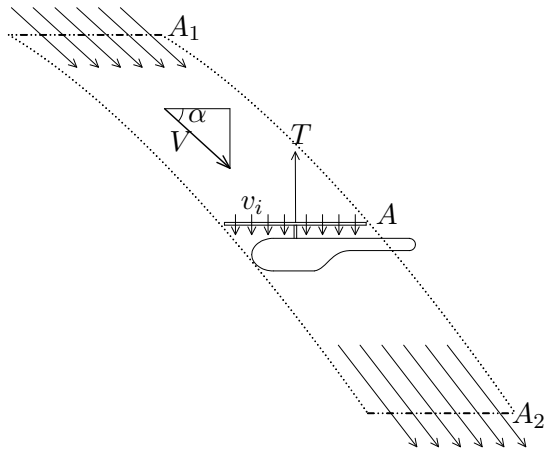

Figure 5.10: Rotor inflow in general flight

The continuity equation $\int_{cs}\rho v\cdot ndA=0$ gives $\rho V\sin\alpha A_1=\rho(V\sin\alpha+v_i)A=\rho(V\sin\alpha+v_2)A_2\equiv\dot{m}$, the mass flow rate perpendicular to the horizontal cross-sections. The momentum equation $F_{cv}=\int_{cs}v\rho v\cdot ndA$ along the vertical direction gives $F_{cv}^v=V\sin\alpha\rho V\sin\alpha A_1-(V\sin\alpha+v_2)\rho(V\sin\alpha+v_2)A_2\implies T=-V\sin\alpha\dot{m}+(V\sin\alpha+v_2)\dot{m}=v_2\dot{m}$. Finally, the energy equation $\dot{W}_{cv}=\int_{cs}\varepsilon\rho v\cdot ndA$ where ε represents the specific kinetic energy of the flow $(1/2)v^2$ gives $T(V\sin\alpha+v_i)=-(1/2)V^2\rho V\sin\alpha A_1+(1/2)[(V\cos\alpha)^2+(V\sin\alpha+v_2)^2]\rho(V\sin\alpha+v_2)A_2=-(1/2)V^2\dot{m}+(1/2)[V^2+2Vv_2\sin\alpha+v_2^2]\dot{m}\Rightarrow Vv_2\sin\alpha\dot{m}+(1/2)v_2^2\dot{m}=v_2\dot{m}(V\sin\alpha+v_i)\Rightarrow v_2=2v_i$ just as in the hover and vertical climb cases. The momentum equation thus becomes $T=2v_i\dot{m}$. Although $\dot{m}$ represents the vertical mass flow rate, following [62] we redefine $\dot{m}=\rho AU$ where $U=\sqrt{(V\cos\alpha)^2+(V\sin\alpha+v_i)^2}$ is the *total* velocity of the stream at the rotor disc. Using this definition the induced velocity is

$$v_i=\frac{T}{2\rho A\sqrt{(V\cos\alpha)^2+(V\sin\alpha+v_i)^2}}. \tag{5.19}$$

For vertical climb $\alpha=\pi/2$ and (5.19) becomes $v_i=T/(2\rho A(V+v_i))$ which agrees with the earlier analysis. For fast forward flight $\alpha=0$, $V\gg v_i$ and (5.19) becomes $v_i=T/(2\rho A\sqrt{V^2+v_i^2})\approx T/(2\rho AV)$ which also agrees with the previous analysis. This is precisely the reason for redefining $\dot{m}$ as above; although this step is not mathematically rigorous, [72, Sec. 4-1.1] points out that v_i predicted by (5.19) agrees with experimental data as well as more complicated theories. The result has been accepted in newer helicopter books [115, 113] and used in experimentally-validated helicopter models [59, 21]. Remark (5.19) is an implicit equation for v_i which can be solved using numerical root-finding [72, p. 129].

5.3.1.2 Blade lift and drag

A cross-section of the main rotor blade airfoil with infinitesimal width dl and chord length c is shown in Figure 5.11 where Θ is the blade pitch angle, (U_T, U_P) are the tangential and perpendicular components of the approaching airstream vector with inflow angle Φ, α is the angle of attack of the airfoil and dL, dD are the resulting lift and drag forces, respectively, which by definition are perpendicular and parallel to the incoming airstream vector.

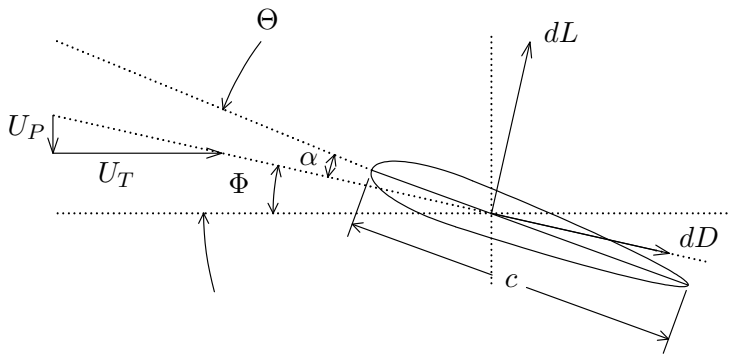

Figure 5.11: Blade cross-section

In the absence of stall, the lift force dL acting on the airfoil section is

$$dL = \frac{1}{2}\rho U^2 C_L c dl,$$

where ρ is air density as before, $U = (U_T^2 + U_P^2)^{1/2}$ is the airstream vector magnitude, c is the chord length of the airfoil and C_L is the coefficient of lift. The drag force on the airfoil is

$$dD = \frac{1}{2}\rho U^2 C_D c dl,$$

where C_D is the coefficient of drag. The values of C_L and C_D versus angle of attack α can be obtained from wind tunnel experiments and are tabulated based on airfoil geometry, discussed below, and Reynolds number

$$\mathrm{Re} := \frac{\rho V c}{\mu} \tag{5.20}$$

where $\mu = 1.789 \times 10^{-5}$ N s/m^2 is the dynamic viscosity of air at ground altitude by the International Standard Atmosphere (ISA).

The main rotor blade is a symmetric airfoil with chord length $c = 66.3$ mm and maximum thickness $t = 9.3$ mm at $x = 19$ mm from the leading edge; these values were directly measured using a digital caliper. Based on the ratios $t/c = 0.14$, $x/c = 0.29$ the blade is classified as a NACA 0014 airfoil [8, p. 114], where the first two integers indicate percent camber and fractional location from the leading edge (00 for a symmetric airfoil), and the last two integers indicate the maximum thickness in percent of the chord, which by definition occurs at $x/c = 0.3$ in all 4-digit NACA series airfoils. Experimental data plots for C_L vs α as well as C_D vs α for a variety of airfoils and Reynolds numbers — see e.g. [8, pp. 462-463] for a NACA 0012 airfoil at $\mathrm{Re} = 3 \times 10^6, 6 \times 10^6, 9 \times 10^6$ — show that C_L is a linear

function of α and C_D is nearly constant with α for roughly $|\alpha| \leq 10°$. For symmetric airfoils we denote

$$C_L = a\alpha$$

where a is the slope of the lift curve in its linear range.

Experimental data is not always available for all airfoil shapes, e.g. [8] does not include NACA 0014 data. In this case the alternative approach is a numerical calculation of the lift and drag forces, which can be done analytically for "thin" airfoils ($t/c \leq 0.12$) by modeling them as a vortex sheet [13, Sec. 4.7], or for more general airfoil shapes by using the vortex panel numerical method [13, Sec. 4.10]. The latter method is implemented by the online applet JavaFoil[1] which lets the user specify the airfoil geometry according to NACA series and computes the lift and drag coefficients as a function of Reynolds number and range of angles of attack. The Reynolds number for the main blades is obtained from (5.20) using $V = \Omega R$ with $\Omega = 55\pi$ rad/s and $R = 0.810$ m giving $\mathrm{Re} \approx 6 \times 10^5$. The resulting plots are shown in Figure 5.12 and the lift curve slope a and drag coefficient C_D are obtained using a least-squares fit in the linear range; remark α is reported in degrees and the slope value is converted to C_L/rad to obtain a.

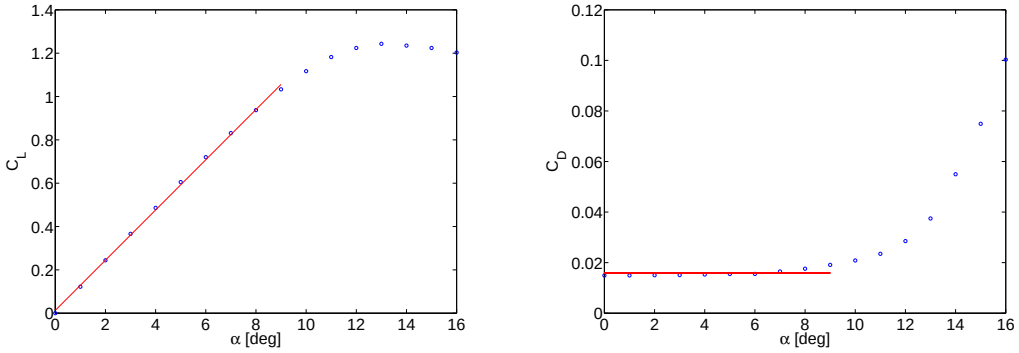

Figure 5.12: NACA 0014 data from JavaFoil: Coefficients of lift and drag vs angle of attack

We now obtain expressions for the aerodynamic force components $dF^{\perp}$ and $dF^{\parallel}$ perpendicular and parallel to the tangential airstream U_T which will be used in Sections 5.3.1.3 and 5.3.1.5 below. From Figure 5.11 we have $\alpha = \Theta - \Phi$ where the inflow angle Φ is assumed small (c.f. Section 5.3.1) and so $\Phi = \arctan(U_P/U_T) \approx U_P/U_T$. Due to the high rotational speed of the main rotor $U_T^2 \gg U_P^2$ and so $U^2 = U_T^2 + U_P^2 \approx U_T^2$. Since C_L is typically an order of magnitude larger than C_D as seen in Figure 5.12 we can neglect the contribution of dD to $dF^{\perp}$, although we cannot make this assumption for $dF^{\parallel}$. The resulting expressions are

$$\begin{aligned} dF^{\perp} &= dL\cos\Phi - dD\sin\Phi \approx dL = \frac{1}{2}\rho ac\left(\Theta U_T^2 - U_T U_P\right) dl \\ dF^{\parallel} &= dL\sin\Phi + dD\cos\Phi \approx \Phi dL + dD = \frac{1}{2}\rho ac\left(\Theta U_T U_P - U_P^2\right) dl + \frac{1}{2}\rho c C_D U_T^2 dl \end{aligned} \tag{5.21}$$

[1] `http://www.mh-aerotools.de/airfoils/javafoil.htm`

5.3.1.3 Main rotor flapping dynamics

Each rotor blade is an airfoil rotating at the rate Ω whose azimuth ψ denotes the clockwise angle from the tail boom. The blade is allowed to move up and down relative to the helicopter's horizontal plane either via a hinge mounted near the rotor hub, as done in full-sized helicopters, or by a combination of blade bending and an elastomeric flapping restraint, the latter design known as a "hingeless" rotor which is typically used on RC helicopters including our Bergen Industrial Twin. The helicopter head design, to be discussed in Section 5.3.2, generates the periodic blade pitch

$$\Theta = A_0 + A_1 \cos\psi + B_1 \sin\psi \tag{5.22}$$

where A_0, A_1 and B_1 are directly controlled through a series of mechanical linkages. Since the lift force on an airfoil is proportional to its pitch angle, the A_1, B_1 coefficients in (5.22) cause periodic up/down motion of each blade known as flapping, causing the rotor disc and thrust vector to tilt about the longitudinal and lateral axes, respectively, providing underactuated control over 4 of the 6 DoF's of the helicopter.

The flapping dynamics are obtained by performing a moment balance on an individual blade, modeled as a rigid body hinged at the main rotor shaft and shown schematically in Figure 5.13. The blade is modeled as a uniform thin plate with linear mass density ρ_b and length R. The blade's flapping angle β is measured from the helicopter's horizontal plane. The torsional spring k_β is a lumped model of the elastomeric flapping restraint and the blade's elasticity, producing the restoring moment $-k_\beta\beta$ about the flapping axis. The flapping motion is also forced by the infinitesimal aerodynamic force $dF^\perp$ which must be integrated along the length, and the blade weight mR acting at the CM located at $l = R/2$ since the blade was assumed uniform. The blade's angular velocity is a combination of $\dot\beta$ plus main rotor speed Ω and the body's roll and pitch rates p and q, respectively. In addition, the hinge point undergoes linear acceleration a^z along the helicopter's normal direction (b_3 axis) as assumed in Section 5.3.1, i.e. we neglect the a^x and a^y components. The actual expression for this term is obtained from (5.11) resp. (5.9) as $a^z = \dot w + pv - qu$, specifically the third component of the inertial acceleration vector of the helicopter's CM expressed along the body-fixed frame.

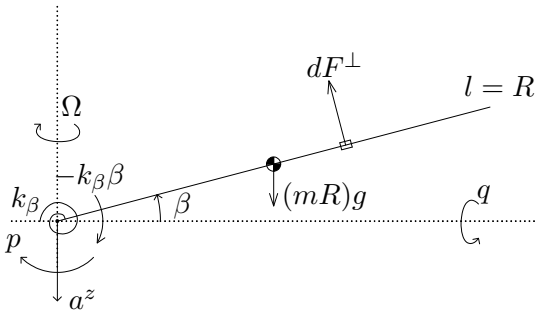

Figure 5.13: Main Rotor: Blade free-body diagram

The moment balance on the blade in Figure 5.13 will be performed about the flapping hinge such that reaction forces can be neglected. We place the blade-fixed frame at the flapping hinge as shown in Figure 5.14 where the frame's $\boldsymbol{i}$, $\boldsymbol{j}$ and $\boldsymbol{k}$

axes are aligned with the blade's feathering, flapping and lagging axes, respectively. We will employ the generalized moment equation (5.18) developed in Section 5.2.2.

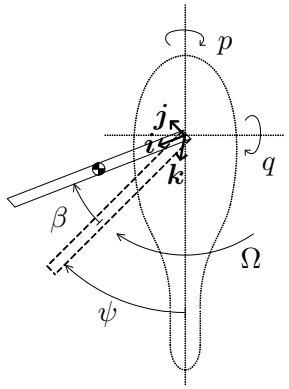

Figure 5.14: Blade flapping kinematics

The blade-fixed frame in Figure 5.14 is aligned with the symmetry axes of the blade and so $J^o = \text{diag}(J^o_{xx}, J^o_{yy}, J^o_{zz})$. The blade is modeled as a thin plate of width w, thickness t, length R and total mass $M = mR$. The components of J^o are obtained from standard mass moment of inertia expressions, e.g. [100, p. 713], then approximated using $t \ll w$. We get

$$\begin{aligned} J^o_{xx} &= \frac{1}{12}M(w^2+t^2) \approx \frac{1}{12}Mw^2 \\ J^o_{yy} &= \frac{1}{12}Mt^2 + \frac{1}{3}MR^2 \approx \frac{1}{3}MR^2 \\ J^o_{zz} &= \frac{1}{12}Mw^2 + \frac{1}{3}MR^2 = J^o_{xx} + J^o_{yy} \end{aligned} \tag{5.23}$$

We write $M^o_B = [L^o \quad M^o \quad N^o]^T$, $\omega_B = [p^b \quad q^b \quad r^b]^T$ and $a^o_B = [a^o_x \quad a^o_y \quad a^o_z]^T$ which represent the body-frame vector components of the total external moment about the hinge axis, inertial angular velocity of the blade and inertial linear acceleration of the hinge point, respectively. We have $r^{CM}_B = [R/2 \quad 0 \quad 0]^T$ since the blade is uniform. Using these in (5.18) along with $J^o = \text{diag}(J^o_{xx}, J^o_{yy}, J^o_{zz})$ and total blade mass mR, we obtain

$$\begin{pmatrix} L^o \\ M^o \\ N^o \end{pmatrix} = \begin{pmatrix} q^b r^b (J^o_{zz} - J^o_{yy}) \\ p^b r^b (J^o_{xx} - J^o_{zz}) \\ p^b q^b (J^o_{yy} - J^o_{xx}) \end{pmatrix} + \begin{pmatrix} J^o_{xx}\dot{p}^b \\ J^o_{yy}\dot{q}^b \\ J^o_{zz}\dot{r}^b \end{pmatrix} + mR \begin{pmatrix} 0 \\ -(R/2)a^o_z \\ (R/2)a^o_y \end{pmatrix}$$

Flapping takes place around the $\boldsymbol{j}$ axis so we employ only the second component of the above equations. Using $J^o_{xx} - J^o_{zz} = -J^o_{yy}$ from (5.23) and defining $J_\beta := J^o_{yy}$, $M_\beta := \rho_b R^2/2$ as in [42] we obtain

$$M^o = J_\beta \dot{q}^b - J_\beta p^b r^b - M_\beta a^o_z \tag{5.24}$$

In Figure 5.13 we had $a^z = \dot{w} + pv - qu$, the hinge's inertial acceleration[2] parallel to the helicopter's b_3 axis. For the blade-fixed frame shown in Figure 5.14 we have

$$a^o_z = (\dot{w} + pv - qu)\cos\beta \tag{5.25}$$

[2]Recall we neglect the helicopter's lateral accelerations a^x and a^y for analyzing the flapping dynamics, i.e. employ only the normal component a^z, by assumption from Section 5.3.1.

We also need expressions for p^b, r^b and $\dot{q}^b = (d/dt)q^b$, the inertial angular accelerations of the blade expressed along the blade-fixed frame axes. These can be obtained by inspection of Figure 5.14:

$$\begin{aligned} p^b &= -p\cos\psi\cos\beta - q\sin\psi\cos\beta - \Omega\sin\beta \\ q^b &= p\sin\psi - q\cos\psi + \dot{\beta} \\ r^b &= -p\cos\psi\sin\beta - q\sin\psi\sin\beta + \Omega\cos\beta \end{aligned}$$

Computing $(d/dt)q^b$ using $\dot{\psi} = \Omega$ we get

$$\dot{q}^b = \dot{p}\sin\psi + p\Omega\cos\psi - \dot{q}\cos\psi + q\Omega\sin\psi + \ddot{\beta}$$

The above are used to expand $J_\beta(\dot{q}^b - p^b r^b)$ in (5.24) and higher-order terms are simplified as [42] $\cos^2\beta \approx 1$, $\sin^2\beta \approx 0$, $p^2 \approx 0$, $q^2 \approx 0$ and $pq \approx 0$; the simplifications are justified by small flapping angles β and $p, q \ll \Omega$. The result is

$$J_\beta(\dot{q}^b - p^b r^b) = J_\beta\big(\ddot{\beta} + \dot{p}\sin\psi - \dot{q}\cos\psi + 2p\Omega\cos\psi + 2q\Omega\sin\psi + \Omega^2\cos\beta\sin\beta\big) \quad (5.26)$$

The net moment about the flapping hinge M^o consists of the three external forces shown in Figure 5.13: the blade weight moment $M^w = -(mR)g(R/2)\cos\beta = -M_\beta g\cos\beta$; the torsional spring restoring moment $M^{k_\beta} = -k_\beta\beta$; and the aerodynamic moment $M^A = \int_0^R l dF^\perp$ where $dF^\perp$ is given by (5.21) in Section 5.3.1.2. Based on Figure 5.14 the blade cross-section at azimuth ψ and distance l from the flapping axis experiences the airstream velocity components

$$\begin{aligned} U_T &= \Omega l\cos\beta + u\sin\psi - v\cos\psi \\ U_P &= (v_i - w)\cos\beta + u\sin\beta\cos\psi + v\sin\beta\sin\psi + \dot{\beta}l + pl\sin\psi - ql\cos\psi \end{aligned} \quad (5.27)$$

where $[u \quad v \quad w]^T$ is the body-frame component velocity of the helicopter, v_i is the induced velocity covered in Section 5.14, and p, q are the helicopter roll and pitch rates as before. The aerodynamic moment integral is

$$M^A = \int_{l=0}^{R} l dF^\perp = \frac{1}{2}\rho a c\int_{l=0}^{R} l\Big(\Theta U_T^2 - U_T U_P\Big)dl$$

Substituting Θ from (5.22) and U_P, U_T from (5.27) into the integrand and assuming small flapping angles such that $\cos\beta \approx 1$, $\sin\beta \approx \beta$ gives

$$\begin{aligned} M^A = \frac{1}{24}\rho a c R^2\Bigg\{ & -2R\Big[pu + qv + 2\Omega(v_i - w)\Big] \\ & + \Big[6v_i v - 6vw + R\Omega(3Rq - 4u\beta)\Big]\cos\psi \\ & + 2\Big[R(pu - qv) + 3uv\beta\Big]\cos 2\psi - \Big[6v_i u - 6uw + R\Omega(3Rp + 4v\beta)\Big]\sin\psi \\ & + \Big[2R(qu + pv) + 3\beta(-u^2 + v^2)\Big]\sin 2\psi + (A_0 + A_1\cos\psi + B_1\sin\psi) \\ & \Big[3(u^2 + v^2 + (R\Omega)^2) - 8R\Omega v\cos\psi - 3(u^2 - v^2)\cos 2\psi \\ & + 8R\Omega u\sin\psi - 6uv\sin 2\psi\Big] - R\dot{\beta}\Big[3R\Omega - 4v\cos\psi + 4u\sin\psi\Big]\Bigg\} \end{aligned} \quad (5.28)$$

Returning to (5.24), using (5.25), (5.26) assuming a small β angle and employing $M^o = M^w + M^{k_\beta} + M^A$ gives the governing equation for the flapping angle β of an individual blade:

$$\ddot{\beta}+\dot{p}\sin\psi-\dot{q}\cos\psi+2p\Omega\cos\psi+2q\Omega\sin\psi+\Omega^2\beta = \frac{M_\beta}{J_\beta}(\dot{w}+pv-qu-g)-\frac{k_\beta}{J_\beta}\beta+\frac{1}{J_\beta}M^A$$

Substituting (5.28) into the above gives a linear, second-order, non-homogenous differential equation for $\beta(t)$:

$$\begin{aligned}
&\ddot{\beta} + \frac{\rho acR^3}{24J_\beta}\Big\{3R\Omega - 4v\cos\psi + 4u\sin\psi\Big\}\dot{\beta} + \Big\{\Big(\frac{k_\beta}{J_\beta}+\Omega^2\Big)\\
&+ \frac{\rho acR^2}{24J_\beta}\Big(4R\Omega u\cos\psi - 6uv\cos 2\psi + 4R\Omega v\sin\psi + 3(u^2-v^2)\sin 2\psi\Big)\Big\}\beta\\
&= \frac{M_\beta}{J_\beta}\Big(\dot{w}+pv-qu-g\Big) - \dot{p}\sin\psi + \dot{q}\cos\psi - 2p\Omega\cos\psi - 2q\Omega\sin\psi\\
&+ \frac{\rho acR^2}{24J_\beta}\Big\{-2R\Big[pu+qv+2\Omega(v_i-w)\Big] + 3\Big[2v_iv - 2vw + R^2\Omega q\Big]\cos\psi\\
&+ 2R(pu-qv)\cos 2\psi - 3\Big[2v_iu - 2uw + R^2\Omega p\Big]\sin\psi + 2R(qu+pv)\sin 2\psi\\
&+ (A_0 + A_1\cos\psi + B_1\sin\psi)\Big[3(u^2+v^2+(R\Omega)^2) - 8R\Omega v\cos\psi\\
&- 3(u^2-v^2)\cos 2\psi + 8R\Omega u\sin\psi - 6uv\sin 2\psi\Big]\Big\}
\end{aligned} \tag{5.29}$$

In order to get an expression for the flapping dynamics in the helicopter-fixed (non-rotating) frame, we use the classical method [61, p. 153] of writing the 2π-periodic $\beta(t)$ as a Fourier series then neglecting all second and higher harmonics:

$$\beta(t,\psi) \approx a_0(t) - a_1(t)\cos\psi + b_1(t)\sin\psi \tag{5.30}$$

where a_0, a_1 and b_1 physically represent the coning, longitudinal tilt and lateral tilt angles of the rotor disc traced out by the tips of the spinning blades, and the a_1, b_1 signs have been assigned for consistency with Figure 5.1 on p. 140. This approach is justified by experiment, where the amplitude of in-plane weaving (second harmonic) is an order of magnitude smaller than the coning and tilting motion. Differentiating (5.30) twice with respect to time, we obtain

$$\begin{aligned}
\dot{\beta} &= \dot{a}_0 - \dot{a}_1\cos\psi + a_1\Omega\sin\psi + \dot{b}_1\sin\psi + b_1\Omega\cos\psi\\
&= \dot{a}_0 + (-\dot{a}_1 + b_1\Omega)\cos\psi + (a_1\Omega + \dot{b}_1)\sin\psi
\end{aligned} \tag{5.31}$$

$$\begin{aligned}
\ddot{\beta} &= \ddot{a}_0 - \ddot{a}_1\cos\psi + 2\dot{a}_1\Omega\sin\psi + a_1\Omega^2\cos\psi + \ddot{b}_1\sin\psi + 2\dot{b}_1\Omega\cos\psi - b_1\Omega^2\sin\psi\\
&= \ddot{a}_0 + (-\ddot{a}_1 + a_1\Omega^2 + 2\dot{b}_1\Omega)\cos\psi + (2\dot{a}_1\Omega + \ddot{b}_1 - b_1\Omega^2)\sin\psi
\end{aligned} \tag{5.32}$$

Expressions (5.32), (5.31) and (5.30) are then substituted into the LHS of (5.29) and the coefficients of the constant, $\cos\psi$ and $\sin\psi$ terms are matched in order to obtain the dynamics of $x = [a_0 \quad a_1 \quad b_1]^T$, the tip path plane angles resulting in the system $\ddot{x} + D\dot{x} + K = F$.

Based on the results in [42], we are able to pre-simplify our expressions. A key parameter in flapping dynamics is the Lock number

$$\gamma := \frac{\rho a c R^4}{J_\beta}$$

For the Bergen Industrial Twin, using the identified parameters given in Section 5.5 we compute $\gamma = 4.03$ and by [42, Fig. 8], we see that the advance ratio μ has negligible effect on the flapping modes for this "low" ($\gamma < 8$) Lock number. This means we can disregard the translational velocity terms u, v in (5.29), whose LHS becomes

$$\ddot{\beta} + \frac{\rho a c R^3}{24 J_\beta}\Big\{3R\Omega\Big\}\dot{\beta} + \left\{\frac{k_\beta}{J_\beta} + \Omega^2\right\}\beta = \ddot{\beta} + \frac{\gamma\Omega}{8}\dot{\beta} + \left(\frac{k_\beta}{J_\beta} + \Omega^2\right)\beta$$

Substituting (5.32), (5.31) and (5.30) into the above and grouping terms yields

$$\begin{aligned}
&\ddot{a}_0 + \frac{\gamma\Omega}{8}\dot{a}_0 + \left(\frac{k_\beta}{J_\beta} + \Omega^2\right) a_0 + \Big\{ - \ddot{a}_1 + a_1\Omega^2 + 2\dot{b}_1\Omega + \frac{\gamma\Omega}{8}(-\dot{a}_1 + b_1\Omega) \\
&- \left(\frac{k_\beta}{J_\beta} + \Omega^2\right) a_1 \Big\}\cos\psi + \Big\{ 2\dot{a}_1\Omega + \ddot{b}_1 - b_1\Omega^2 + \frac{\gamma\Omega}{8}(a_1\Omega + \dot{b}_1) + \left(\frac{k_\beta}{J_\beta} + \Omega^2\right) b_1 \Big\}\sin\psi
\end{aligned}$$

while the RHS of (5.29) with $u = v = 0$ is

$$\begin{aligned}
&\frac{M_\beta}{J_\beta}\Big(\dot{w} - g\Big) - \dot{p}\sin\psi + \dot{q}\cos\psi - 2p\Omega\cos\psi - 2q\Omega\sin\psi + \frac{\gamma}{24R^2}\Big\{ - 4R\Omega(v_i - w) \\
&\qquad + 3R^2\Omega q\cos\psi - 3R^2\Omega p\sin\psi + (A_0 + A_1\cos\psi + B_1\sin\psi)\Big[3(R\Omega)^2\Big]\Big\}
\end{aligned}$$

Matching the constant, $\cos\psi$ and $\sin\psi$ coefficients gives

$$\begin{aligned}
\ddot{a}_0 + \frac{\gamma\Omega}{8}\dot{a}_0 + \left(\frac{k_\beta}{J_\beta} + \Omega^2\right) a_0 &= \frac{M_\beta}{J_\beta}\Big(\dot{w} - g\Big) - \frac{\gamma\Omega}{6R}(v_i - w) + \frac{\gamma\Omega^2}{8}A_0 \\
-\ddot{a}_1 + 2\dot{b}_1\Omega + \frac{\gamma\Omega}{8}(-\dot{a}_1 + b_1\Omega) - \frac{k_\beta}{J_\beta}a_1 &= \dot{q} - 2p\Omega + \frac{\gamma\Omega}{8}q + \frac{\gamma\Omega^2}{8}A_1 \\
2\dot{a}_1\Omega + \ddot{b}_1 + \frac{\gamma\Omega}{8}(a_1\Omega + \dot{b}_1) + \frac{k_\beta}{J_\beta}b_1 &= -\dot{p} - 2q\Omega - \frac{\gamma\Omega}{8}p + \frac{\gamma\Omega^2}{8}B_1
\end{aligned} \tag{5.33}$$

The first equation describes the dynamics of the coning mode a_0, with natural frequency $\omega_0 = \sqrt{k_\beta/J_\beta + \Omega^2}$ and forcing terms consisting of normal motion w and $\dot{w}$, gravity g and collective pitch A_0; it can be verified $\zeta_0 = (\gamma\Omega)/(16\omega_0)$ although this term is not required in the sequel. The remaining two equations are a coupled dynamics system for flapping angles a_1, b_1, which can be rewritten in the form $\ddot{x} + D\dot{x} + Kx = F$ as

$$\begin{bmatrix}\ddot{a}_1 \\ \ddot{b}_1\end{bmatrix} + \begin{bmatrix}\frac{\gamma\Omega}{8} & -2\Omega \\ 2\Omega & \frac{\gamma\Omega}{8}\end{bmatrix}\begin{bmatrix}\dot{a}_1 \\ \dot{b}_1\end{bmatrix} + \begin{bmatrix}\frac{k_\beta}{J_\beta} & -\frac{\gamma\Omega^2}{8} \\ \frac{\gamma\Omega^2}{8} & \frac{k_\beta}{J_\beta}\end{bmatrix}\begin{bmatrix}a_1 \\ b_1\end{bmatrix} = \begin{bmatrix}-\dot{q} + 2p\Omega - \frac{\gamma\Omega}{8}q - \frac{\gamma\Omega^2}{8}A_1 \\ -\dot{p} - 2q\Omega - \frac{\gamma\Omega}{8}p + \frac{\gamma\Omega^2}{8}B_1\end{bmatrix} \tag{5.34}$$

The natural frequencies and damping ratios of (5.34) can be calculated using the method of complex modal analysis [70, pp. 332–334]. The homogenous version of (5.34) $\ddot{x} + D\dot{x} + Kx = 0$ is written in state-space form by defining $x_1 = x$, $x_2 = \dot{x}$:

$$\begin{bmatrix} \dot{x}_1 \\ \dot{x}_2 \end{bmatrix} = \begin{bmatrix} 0 & I \\ -K & -D \end{bmatrix} \begin{bmatrix} x_1 \\ x_2 \end{bmatrix}$$

The eigenvalues of the above matrix are two complex-conjugate pairs λ_1 and λ_2, corresponding to the system's two vibration modes, whose natural frequencies and damping ratios are respectively calculated by

$$\omega_i = \sqrt{\mathrm{Re}\{\lambda_i\}^2 + \mathrm{Im}\{\lambda_i\}^2} \qquad \text{and} \qquad \zeta_i = \frac{-\mathrm{Re}\{\lambda_i\}}{\sqrt{\mathrm{Re}\{\lambda_i\}^2 + \mathrm{Im}\{\lambda_i\}^2}}$$

By direct computation we find

$$\begin{aligned}
\lambda_1 &= -\frac{\gamma\Omega}{16} \pm \frac{j}{4J_\beta}\sqrt{32(J_\beta\Omega)^2 + 16J_\beta k_\beta - \frac{1}{16}(\gamma J_\beta\Omega)^2 + 2J_\beta\Omega\,\xi} \\
\lambda_2 &= -\frac{\gamma\Omega}{16} \pm \frac{j}{4J_\beta}\sqrt{32(J_\beta\Omega)^2 + 16J_\beta k_\beta - \frac{1}{16}(\gamma J_\beta\Omega)^2 - 2J_\beta\Omega\,\xi} \\
\xi &:= \sqrt{256(J_\beta\Omega)^2 + 256J_\beta k_\beta - (\gamma J_\beta\Omega)^2}
\end{aligned}$$

Remark the only difference between the two eigenvalue pairs is the sign in front of the ξ term. We then have

$$\begin{aligned}
\omega_1 &= \left(\Omega^2 + \omega_0^2 + \frac{\Omega}{8}\sqrt{(16\omega_0)^2 - (\gamma\Omega)^2}\right)^{1/2} \qquad \zeta_1 = \frac{\gamma\Omega}{16\omega_1} \\
\omega_2 &= \left(\Omega^2 + \omega_0^2 - \frac{\Omega}{8}\sqrt{(16\omega_0)^2 - (\gamma\Omega)^2}\right)^{1/2} \qquad \zeta_2 = \frac{\gamma\Omega}{16\omega_2}
\end{aligned}$$

where

$$\omega_0 = \left(\Omega^2 + \frac{k_\beta}{J_\beta}\right)^{1/2}$$

is the frequency of the coning mode as before. The vibration modes characterized by (ω_1, ζ_1) and (ω_2, ζ_2) are known as the advancing and regressing flapping modes, respectively. As discussed in [42] we retain only the regressive flapping mode, whose frequency is sufficiently low to couple into the rigid-body motions of the helicopter. A good approximation of this mode can be obtained by setting $\ddot{a}_1 = \ddot{b}_1 = 0$ in (5.34). Further, for this low-frequency effect we can omit the effect of angular accelerations by setting $\dot{p} = \dot{q} = 0$. The flapping dynamics become simplified to

$$\begin{aligned}
2\dot{b}_1\Omega + \frac{\gamma\Omega}{8}(-\dot{a}_1 + b_1\Omega) - \frac{k_\beta}{J_\beta}a_1 &= -2p\Omega + \frac{\gamma\Omega}{8}q + \frac{\gamma\Omega^2}{8}A_1 \\
2\dot{a}_1\Omega + \frac{\gamma\Omega}{8}(a_1\Omega + \dot{b}_1) + \frac{k_\beta}{J_\beta}b_1 &= -2q\Omega - \frac{\gamma\Omega}{8}p + \frac{\gamma\Omega^2}{8}B_1
\end{aligned}$$

Remark each of the cyclic inputs A_1 and B_1 affects both $\dot{a}_1$ and $\dot{b}_1$ in the simplified equations above. In reality, the control linkages are designed to achieve perfect 90°

phase lag between cyclic input and maximum flapping angle in order to decouple the flapping response. Mathematically, this means that in steady-state, the A_1 cyclic pitch component should affect only the lateral flapping angle b_1 and the B_1 only the longitudinal a_1; this is done by dropping the $\dot{a}_1$ term from the first equation and the $\dot{b}_1$ term from the second one in the simplified model above, as seen in [101, p. 73] who uses this approach without comment. The regressing mode dynamics become

$$
\begin{aligned}
2\dot{b}_1\Omega + \frac{\gamma\Omega}{8}(b_1\Omega) - \frac{k_\beta}{J_\beta}a_1 &= -2p\Omega + \frac{\gamma\Omega}{8}q + \frac{\gamma\Omega^2}{8}A_1 \\
2\dot{a}_1\Omega + \frac{\gamma\Omega}{8}(a_1\Omega) + \frac{k_\beta}{J_\beta}b_1 &= -2q\Omega - \frac{\gamma\Omega}{8}p + \frac{\gamma\Omega^2}{8}B_1
\end{aligned}
$$

and interchanging their order and normalizing the coefficients of A_1, B_1 gives

$$
\begin{aligned}
\frac{16}{\gamma\Omega}\dot{a}_1 + a_1 &= \frac{-8k_\beta}{\gamma\Omega^2 J_\beta}b_1 - \frac{16}{\gamma\Omega}q - \frac{1}{\Omega}p + B_1 \\
\frac{16}{\gamma\Omega}\dot{b}_1 + b_1 &= \frac{8k_\beta}{\gamma\Omega^2 J_\beta}a_1 - \frac{16}{\gamma\Omega}p + \frac{1}{\Omega}q + A_1
\end{aligned}
\tag{5.35}
$$

The dynamics (5.35) are a highly simplified form of the flapping dynamics of the main rotor. They offer insight into the physics of flapping and can be used for a simulation model with some parameter identification, c.f. [65, p. 16]. A more complete model of the flapping dynamics can be obtained by returning to (5.29) and substituting the tip-path plane expression (5.30) but without neglecting translational velocity terms as done in [42, 21], at the expense of a dramatic increase in symbolic complexity. The regressing mode approximation could also be avoided by using (5.34) resp. (5.33) when integrating for the flapping dynamics. We will not pursue these avenues further.

5.3.1.4 Flapping Dynamics Simplifications

In Section 5.3.1.3 we have used identified parameters values for the Bergen Industrial Twin to compute the Lock number $\gamma = 4.03$ and simplify the flapping dynamics. Using the same numerical approach we can obtain further simplifications of our model.

The ANCL helicopter uses an approximate head speed of $\Omega = 1650$ RPM $= 55\pi$ rad/s. We also use the following identified values from Section 5.5: $k_\beta = 122\ \mathrm{N\,m/rad}$; $J_\beta = 0.057\ \mathrm{kg\,m^2}$. We numerically compute the natural frequency and damping ratio pairs for the coning (ω_0, ζ_0), advancing (ω_1, ζ_1) and regressing (ω_2, ζ_2) modes as

$$
\begin{aligned}
\omega_0 &= 178.87 \text{ rad/s} = 28.47 \text{ Hz} & \zeta_0 &= 0.2433 \\
\omega_1 &= 349.01 \text{ rad/s} = 55.55 \text{ Hz} & \zeta_1 &= 0.1247 \\
\omega_2 &= 43.53 \text{ rad/s} = 6.93 \text{ Hz} & \zeta_2 &= 0.9999
\end{aligned}
$$

As predicted only the regressing mode has a frequency low enough (6.93 Hz) to possibly couple into the motion of the helicopter body, although the other flapping frequencies will show up in the frequency content of the IMU sensor signal. Remark the regressing mode is nearly critically damped and hence the approach of approximating it as a first-order system (5.35) is justified.

Using a 5% criterion the settling time for a unit step input into the regressing mode is given by [109, p. 233] $t_s = 3/(\zeta\omega_n) = 0.069$ s, or for the approximate system (5.35) with time constant $\tau = 16/(\gamma\Omega)$ this value is $3\tau = 0.069$ s, identical to before. Based on these numbers we are justified in taking the flapping response of the main rotor as instantaneous. Physically this is due to the high angular speed of the main rotor ($\Omega = 1650$ RPM $= 27.5$ Hz) which makes the transient period of the flapping dynamics negligibly short. This is the reason why a Bell-Hiller stabilizer system, to be discussed in Section 5.3.2, is used on the Bergen Industrial Twin and other RC helicopters — to slow down the effective flapping response of the main rotor and make the helicopter flyable for a human pilot. A new generation of flybarless RC helicopters fly under closed-loop control and allow the pilot to tune the main rotor response in real-time to suit their preferences.

Neglecting the flapping dynamics of the main rotor is done by dropping the $\dot{a}_1$, $\dot{b}_1$ terms in (5.35). We can simplify further as follows: since the coning frequency $\omega_0 = \sqrt{k_\beta/J_\beta + \Omega^2} = 178.87$ rad/s is less than 4% from the natural rotor frequency $\sqrt{\Omega^2} = 172.79$ rad/s, we can drop the k_β/J_β term from (5.35). Evaluating the coefficients $16/(\gamma\Omega) = 0.023$ and $1/\Omega = 0.0058$ we also see that the effect of on-axis and off-axis angular rates on disc tilt is respectively two and three orders of magnitude lower than the cyclic amplitude terms A_1 and B_1. Under all these simplifications equation (5.35) reduces to the steady-state expression

$$\begin{aligned} a_1 &= B_1 \\ b_1 &= A_1 \end{aligned} \tag{5.36}$$

In Section 5.3.1.5 we will develop the force and moment expressions for the main rotor in full generality, i.e. leaving in the flapping dynamics, which can be neglected later by zeroing all $\dot{a}_0$, $\dot{a}_1$ and $\dot{b}_1$ terms.

5.3.1.5 Main Rotor Forces and Moments

We now calculate the force and moment vectors resulting from the aerodynamic forces acting on the main rotor. We first develop the fully general expressions then simplify down to a hover model.

The main rotor thrust T_{mr} and counter-torque Q_{mr} respectively defined as the net body-vertical force and counter-clockwise moment in the body-horizontal plane are evaluated from

$$\begin{aligned} T_{mr} &= \frac{N_b}{2\pi}\int_0^{2\pi}\int_0^R dF^\perp \cos\beta \, d\psi \\ Q_{mr} &= \frac{N_b}{2\pi}\int_0^{2\pi}\int_0^R l \, dF^\parallel \, d\psi \end{aligned}$$

where $N_b = 2$ is the number of blades and $dF^\perp$, $dF^\parallel$ are the perpendicular and parallel aerodynamic forces acting on a blade section given by (5.21) in Section 5.3.1.2. We will also calculate X_{mr}, Y_{mr}, the in-plane force parallel to the x_b and y_b axes given by

$$\begin{aligned} X_{mr} &= \frac{N_b}{2\pi}\int_0^{2\pi}\left(\int_0^R dF^\perp \sin\beta\cos\psi - \int_0^R dF^\parallel \sin\psi\right) d\psi \\ Y_{mr} &= \frac{N_b}{2\pi}\int_0^{2\pi}\left(\int_0^R dF^\perp \sin\beta\sin\psi + \int_0^R dF^\parallel \cos\psi\right) d\psi \end{aligned}$$

as well as L_{mr}, M_{mr}, the moments at the main rotor blade hub in aligned with the x_b and y_b axis directions:

$$L_{mr} = \frac{N_b}{2\pi}\int_0^{2\pi}\left(\int_0^R l\, dF^{\perp} + k_\beta\beta\right)\sin\psi\, d\psi$$
$$M_{mr} = \frac{-N_b}{2\pi}\int_0^{2\pi}\left(\int_0^R l\, dF^{\perp} + k_\beta\beta\right)\cos\psi\, d\psi$$

By assumption from Section 5.3.1 we take the flapping angle β as small such that $\cos\beta \approx 1$ in T and $\sin\beta \approx \beta$ in X_{mr} and Y_{mr} above. The U_T and U_P expressions in (5.27) simplify to

$$U_T = \Omega l + u\sin\psi - v\cos\psi$$
$$U_P = v_i - w + u\beta\cos\psi + v\beta\sin\psi + \dot{\beta}l + pl\sin\psi - ql\cos\psi$$

The $dF^{\perp}$, $dF^{\parallel}$ expressions in (5.21) as well as Θ, β and $\dot{\beta}$ in (5.22), (5.30) and (5.31) are repeated here for convenience:

$$dF^{\perp} = \frac{1}{2}\rho ac\left(\Theta U_T^2 - U_T U_P\right)dl$$
$$dF^{\parallel} = \frac{1}{2}\rho ac\left(\Theta U_T U_P - U_P^2\right)dl + \frac{1}{2}\rho c C_D U_T^2 dl$$
$$\Theta = A_0 + A_1\cos\psi + B_1\sin\psi$$
$$\beta = a_0 - a_1\cos\psi + b_1\sin\psi$$
$$\dot{\beta} = \dot{a}_0 + (b_1\Omega - \dot{a}_1)\cos\psi + (a_1\Omega + \dot{b}_1)\sin\psi$$

Using the expressions above we first evaluate the T_{mr} integral:

$$T_{mr} = \frac{\rho acRN_b}{24}\Bigg\{\Big[4(R\Omega)^2 + 6(u^2+v^2)\Big]A_0 + 6R\Omega\Big[w - v_i - vA_1 + uB_1\Big] - 3R\Big[u(p+\dot{b}_1) + v(q+\dot{a}_1)\Big] - 4R^2\Omega\dot{a}_0\Bigg\}$$

The $p, \dot{b}_1$ and $q, \dot{a}_1$ terms physically represent the lateral and longitudinal angular velocity of the rotor disc, respectively. From Section 5.3.1.1 we know $v_i = v_i(T_{mr})$ and so T_{mr} is a transcendental equation which is typically solved numerically using the Newton-Rhapson method over a few iterations, e.g. [72, p. 129], [65, p. 18], [59, p. 35]. Since the transcendental equation is quartic it can be solved analytically as [21, p. 63], however this still does not provide an explicit T_{mr} expression due to the requirement of selecting one of four possible solutions.

In hover with translational velocities, angular rates and flapping dynamics identically zero, the T_{mr} expression reduces to

$$T_{mr}^h = \frac{\rho acRN_b}{12}\Bigg\{2(R\Omega)^2 A_0 - 3R\Omega v_i^h\Bigg\} \tag{5.37}$$

where from Section 5.3.1.1

$$T_{mr}^h = 2(v_i^h)^2\rho\pi R^2 \Longrightarrow v_i^h = \sqrt{\frac{T_{mr}^h}{2\rho\pi R^2}} \tag{5.38}$$

We can obtain an explicit equation for T^h_{mr} by substituting (5.38) into (5.37), which gives

$$T^h_{mr} = \frac{\rho acR^3 N_b \Omega^2}{6} A_0 - \frac{acRN_b\Omega\sqrt{\rho}}{4\sqrt{2\pi}}\sqrt{T^h_{mr}} := C^T_{mr} A_0 - D^T_{mr}\sqrt{T^h_{mr}}$$

where by inspection C^T_{mr}, D^T_{mr} are positive constants. By defining $x = \sqrt{T^h_{mr}}$ we can solve the above using the quadratic formula:

$$\sqrt{T^h_{mr}} = \frac{-D^T_{mr} + \sqrt{(D^T_{mr})^2 + 4C^T_{mr}A_0}}{2} \text{ or } \sqrt{T^h_{mr}} = \frac{-D^T_{mr} - \sqrt{(D^T_{mr})^2 + 4C^T_{mr}A_0}}{2}$$

Squaring both sides gives

$$T^h_{mr} = C^T_{mr}A_0 + \frac{(D^T_{mr})^2}{2} \pm D^T_{mr}\sqrt{C^T_{mr}A_0 + \frac{(D^T_{mr})^2}{4}}$$

In order to pick a single solution consider $A_0 = 0$ for which

$$T^h_{mr} = (D^T_{mr})^2 \quad \text{or} \quad T^h_{mr} = 0$$

but since zero collective pitch is known to produce zero thrust the "minus" solution is the correct one:

$$T^h_{mr} = C^T_{mr}A_0 + \frac{(D^T_{mr})^2}{2} - D^T_{mr}\sqrt{C^T_{mr}A_0 + \frac{(D^T_{mr})^2}{4}} \tag{5.39}$$

Equation (5.39) is an explicit equation for hover thrust T^h_{mr} as a function of the collective pitch angle A_0 where C^T_{mr}, D^T_{mr} are constant parameters defined above.

A simplified expression for T^h_{mr} can be obtained by taking $T^h_{mr} = mg$ in (5.38); this assumes zero acceleration along the z_b axis[3]. In this case (5.37) becomes

$$T^h_{mr} \approx \frac{\rho acR^3 N_b \Omega^2}{6} A_0 - \frac{acRN_b\Omega}{4}\sqrt{\frac{mg\rho}{2\pi}} \Longrightarrow T^h_{mr} \approx C^T_{mr}A_0 - D^T_{mr}\sqrt{mg}$$

The assumption of zero z_b axis acceleration is poor due to the constant adjustments of the collective input required to maintain hover; for this reason T^h_{mr} should be computed using (5.39).

[3]This also assumes the helicopter is level, however this is reasonable since $mg\cos\phi\cos\theta \approx mg$ for small angles.

The Q_{mr} counter-torque expression evaluates to

$$
\begin{aligned}
Q_{mr} = \frac{-\rho acR^2N_b}{96}\Big\{ & 6(p^2+q^2)R^2 + 24(w-v_i)^2 - 16R\Big[qu-pv\Big]a_0 + 12\Big[u^2+v^2\Big]a_0^2 \\
& + 4\Big[6u(w-v_i) + 4vR\Omega + 3pR^2\Omega\Big]a_1 + 3\Big[3u^2+v^2+2(R\Omega)^2\Big]a_1^2 - 12uva_1b_1 \\
& - 4\Big[6v(w-v_i) + 4uR\Omega + 3qR^2\Omega\Big]b_1 + 3\Big[u^2+3v^2+2(R\Omega)^2\Big]b_1^2 \\
& + 4R\Big[-8w - 4ua_1 + 4vb_1 + 8v_i + 3R\dot{a}_0 - 3R\Omega A_0 + 2vA_1 - 2uB_1\Big]\dot{a}_0 \\
& + 2R\Big[6qR - 8ua_0 - 6R\Omega b_1 + 3R\dot{a}_1 - 4vA_0 + 3R\Omega A_1\Big]\dot{a}_1 \\
& + 2R\Big[6pR + 8va_0 + 6R\Omega a_1 + 3R\dot{b}_1 - 4uA_0 - 3R\Omega B_1\Big]\dot{b}_1 \\
& + 8R\Big[-pu - qv + 2w\Omega - 2\Omega v_i\Big]A_0 \\
& + \Big[-12v(w-v_i) + 6qR^2\Omega - 8uR\Omega a_0 - 3(u^2-v^2)b_1 - 6(R\Omega)^2b_1 - 6uva_1\Big]A_1 \\
& + \Big[12u(w-v_i) - 6pR^2\Omega - 8vR\Omega a_0 + 3(u^2-v^2)a_1 - 6(R\Omega)^2a_1 - 6uvb_1\Big]B_1\Big\} \\
& + \frac{\rho cR^2C_DN_b}{8}\Big\{(R\Omega)^2 + u^2 + v^2\Big\}
\end{aligned}
$$

In hover with zero translational and rotational velocities and zero flapping dynamics, the above reduces to

$$
\begin{aligned}
Q^h_{mr} = \frac{-\rho acR^2N_b}{96}\Big\{ & 24(-v_i^h)^2 + 3\Big[2(R\Omega)^2\Big]a_1^2 + 3\Big[2(R\Omega)^2\Big]b_1^2 + 8R\Big[-2\Omega v_i^h\Big]A_0 \\
& + \Big[-6(R\Omega)^2b_1\Big]A_1 + \Big[-6(R\Omega)^2a_1\Big]B_1\Big\} + \frac{\rho cR^2C_DN_b}{8}\Big\{(R\Omega)^2\Big\}
\end{aligned}
$$

In hover (5.36) gives $a_1 = B_1$ and $b_1 = A_1$ and so Q^h_{mr} becomes

$$
\begin{aligned}
Q^h_{mr} &= \frac{-\rho acR^2N_b}{96}\Big\{24(v_i^h)^2 + 6(R\Omega)^2a_1^2 + 6(R\Omega)^2b_1^2 - 16R\Omega v_i^hA_0 \\
&\quad - 6(R\Omega)^2b_1^2 - 6(R\Omega)^2a_1^2\Big\} + \frac{\rho cR^2C_DN_b}{8}\Big\{(R\Omega)^2\Big\} \\
&= \frac{\rho acR^2N_bv_i^h}{12R\Omega}\Big\{-3R\Omega v_i^h + 2(R\Omega)^2A_0\Big\} + \frac{\rho cR^4\Omega^2C_DN_b}{8} \\
&= \frac{T^h_{mr}R}{R\Omega}\sqrt{\frac{T^h_{mr}}{2\rho\pi R^2}} + \frac{\rho cR^4\Omega^2C_DN_b}{8} := C^Q_{mr}\left(T^h_{mr}\right)^{3/2} + D^Q_{mr} \qquad (5.40)
\end{aligned}
$$

where v_i^h was taken from (5.38), T^h_{mr} is calculated by (5.39) and C^Q_{mr}, D^Q_{mr} are constants whose notation has been chosen to match [79, Sec. 2.2].

We now return to the X_{mr} and Y_{mr} force expressions, which evaluate to

$$\begin{aligned}
X_{mr} = \frac{-\rho acRN_b}{96}\Big\{ & 24Rp(w-v_i) \\
& + 4\Big[18v(w-v_i) - 2qR^2\Omega + 3uR\Omega a_0 + 12uva_1 - 12v^2b_1 + 2(R\Omega)^2 b_1\Big]a_0 \\
& + 3R\Big[pu - 5qv + 12\Omega(w-v_i) + 4\Omega u a_1\Big]a_1 - 12vR\Omega a_1 b_1 + 3R\Big[qu - 7pv\Big]b_1 \\
& - 4R\Big[4pR + 9va_0 + 6R\Omega a_1 - 3uA_0 - 2R\Omega B_1 + 4R\dot{b}_1\Big]\dot{a}_0 \\
& - R\Big[8R\Omega a_0 + 15va_1 - 3ub_1 + 3uA_1 - 3vB_1\Big]\dot{a}_1 \\
& + R\Big[24(w-v_i) + 3ua_1 - 21vb_1 + 8R\Omega A_0 - 3vA_1 + 9uB_1\Big]\dot{b}_1 \\
& + 4\Big[-6u(w-v_i) + 2pR^2\Omega + 9vR\Omega a_0 + 6v^2a_1 + 4(R\Omega)^2 a_1 + 6uvb_1\Big]A_0 \\
& - \Big[3R(qu+pv) + 24v^2a_0 + 8(R\Omega)^2 a_0 + 24vR\Omega a_1\Big]A_1 \\
& + 3\Big[3Rpu + Rqv - 4R\Omega(w-v_i) + 8uva_0 + 4uR\Omega a_1 + 4vR\Omega b_1\Big]B_1\Big\} \\
& - \frac{\rho cR^2\Omega N_b}{4}uC_D
\end{aligned}$$

and

$$\begin{aligned}
Y_{mr} = \frac{-\rho acRN_b}{96}\Big\{ & 24Rq(w-v_i) \\
& + 4\Big[-18u(w-v_i) + 2pR^2\Omega + 3vR\Omega a_0 - 12u^2a_1 + 2(R\Omega)^2 a_1 + 12uvb_1\Big]a_0 \\
& - 3R\Big[pv - 7qu\Big]a_1 - 12uR\Omega a_1 b_1 + 3R\Big[5pu - qv - 12\Omega(w-v_i) + 4\Omega v b_1\Big]b_1 \\
& - 4R\Big[4qR - 9ua_0 - 6R\Omega b_1 - 3vA_0 + 2R\Omega A_1 + 4R\dot{a}_1\Big]\dot{a}_0 \\
& + R\Big[24(w-v_i) + 21ua_1 - 3vb_1 + 8R\Omega A_0 - 9vA_1 + 3uB_1\Big]\dot{a}_1 \\
& + R\Big[8R\Omega a_0 - 3va_1 + 15ub_1 - 3uA_1 + 3vB_1\Big]\dot{b}_1 \\
& - 4\Big[6v(w-v_i) - 2qR^2\Omega + 9uR\Omega a_0 + 6uva_1 + 6u^2b_1 + 4(R\Omega)^2 b_1\Big]A_0 \\
& + 3\Big[-Rpu - 3Rqv + 4R\Omega(w-v_i) + 8uva_0 + 4uR\Omega a_1 + 4vR\Omega b_1\Big]A_1 \\
& + \Big[3R(qu+pv) - 24u^2a_0 - 8(R\Omega)^2 a_0 - 24uR\Omega b_1\Big]B_1\Big\} - \frac{\rho cR^2\Omega N_b}{4}vC_D
\end{aligned}$$

While the X_{mr}, Y_{mr} terms are complicated, this is normal as evidenced by the expressions found in e.g. [41, pp. 7-8]; [113, pp. 108-111]; [21, pp. 234-238]. In hover with $u = v = w = 0$, $p = q = 0$ and $\dot{a}_0 = \dot{a}_1 = \dot{b}_1 = 0$, the X_{mr} and Y_{mr} expressions

simplify to

$$X^h_{mr} = \frac{-\rho acRN_b}{96}\Big\{\Big[8(R\Omega)^2 b_1\Big]a_0 - \Big[36R\Omega v_i^h\Big]a_1 + \Big[16(R\Omega)^2 a_1\Big]A_0 - \Big[8(R\Omega)^2 a_0\Big]A_1 + \Big[12R\Omega v_i^h\Big]B_1\Big\}$$

$$Y^h_{mr} = \frac{-\rho acRN_b}{96}\Big\{\Big[8(R\Omega)^2 a_1\Big]a_0 + \Big[36R\Omega v_i^h\Big]b_1 - \Big[16(R\Omega)^2 b_1\Big]A_0 - \Big[12R\Omega v_i^h\Big]A_1 - \Big[8(R\Omega)^2 a_0\Big]B_1\Big\}$$

Using $a_1 = B_1$ and $b_1 = A_1$ from (5.36) we get

$$\begin{aligned} X^h_{mr} &= \frac{-\rho acRN_b}{96}\Big\{ - \Big[24R\Omega v_i^h\Big]a_1 + \Big[16(R\Omega)^2 a_1\Big]A_0\Big\} \\ &= \frac{-\rho acRN_b}{12}\Big\{2(R\Omega)^2 A_0 - 3R\Omega v_i^h\Big\}a_1 \\ Y^h_{mr} &= \frac{-\rho acRN_b}{96}\Big\{\Big[24R\Omega v_i^h\Big]b_1 - \Big[16(R\Omega)^2 b_1\Big]A_0\Big\} \\ &= \frac{\rho acRN_b}{12}\Big\{2(R\Omega)^2 A_0 - 3R\Omega v_i^h\Big\}b_1 \end{aligned}$$

and using (5.37) we have

$$\begin{aligned} X^h_{mr} &= -T^h_{mr}a_1 \\ Y^h_{mr} &= T^h_{mr}b_1 \end{aligned}$$

which is validated by the flapping sign convention shown in Figure 5.1.

The final set of calculations involve hub moment expressions L_{mr}, M_{mr}, which turn out to have a simpler form than Q_{mr}, X_{mr} and Y_{mr} above:

$$\begin{aligned} L_{mr} = \frac{-\rho acR^2N_b}{96}\Big\{ &- 12uw + 12uv_i + 6pR^2\Omega + 8Rv\Omega a_0 \\ &+ 3\Big[-u^2 + v^2 + 2(R\Omega)^2\Big]a_1 + 6uvb_1 + 8Ru\dot{a}_0 + 6R^2\Omega\dot{b}_1 \\ &- 16uR\Omega A_0 + 6uvA_1 - \Big[9u^2 + 3v^2 + 6(R\Omega)^2\Big]B_1\Big\} + \frac{k_\beta b_1 N_b}{2} \\ M_{mr} = \frac{-\rho acR^2N_b}{96}\Big\{ &- 12vw + 12vv_i + 6qR^2\Omega - 8Ru\Omega a_0 - 6uva_1 \\ &- 3\Big[u^2 - v^2 + 2(R\Omega)^2\Big]b_1 + 8Rv\dot{a}_0 + 6R^2\Omega\dot{a}_1 \\ &- 16vR\Omega A_0 + \Big[3u^2 + 9v^2 + 6(R\Omega)^2\Big]A_1 - 6uvB_1\Big\} + \frac{k_\beta a_1 N_b}{2} \end{aligned}$$

At hover this reduces to

$$L^h_{mr} = \frac{-\rho acR^2N_b}{96}\Big\{3\Big[2(R\Omega)^2\Big]a_1 - \Big[6(R\Omega)^2\Big]B_1\Big\} + \frac{k_\beta b_1 N_b}{2} = \frac{k_\beta b_1 N_b}{2} = k_\beta b_1$$

$$M^h_{mr} = \frac{-\rho acR^2N_b}{96}\Big\{ - 3\Big[2(R\Omega)^2\Big]b_1 + \Big[6(R\Omega)^2\Big]A_1\Big\} + \frac{k_\beta a_1 N_b}{2} = \frac{k_\beta a_1 N_b}{2} = k_\beta a_1$$

where the second equality is due to $a_1 = B_1$ and $b_1 = A_1$ from (5.36) and the third from $N_b = 2$. The final result is validated by Figure 5.1 as well.

5.3.1.6 Main Rotor Contributions

The main rotor forces T_{mr}, X_{mr} and Y_{mr} create a moment around the helicopter's CM which is added to the moments Q_{mr}, L_{mr} and M_{mr}. The main rotor's force and moment contributions along the helicopter's body-fixed axes are given by

$$\begin{aligned} X_{mr} &= X_{mr} \\ Y_{mr} &= Y_{mr} \\ Z_{mr} &= -T_{mr} \\ L_{mr} &= h_{mr} Y_{mr} + L_{mr} \\ M_{mr} &= -h_{mr} X_{mr} + M_{mr} \\ N_{mr} &= -Q_{mr} \end{aligned}$$

where h_{mr} is the height of the main rotor hub above the center of mass, measured directly using the identified CM position, c.f. Figure 5.3 in Section 5.2. The center of mass is placed directly under the hub by moving the avionics box fore and aft in its T-slot rails attachment system. In hover the force and moment contributions become

$$\begin{aligned} X_{mr}^h &= -T_{mr}^h a_1 \\ Y_{mr}^h &= T_{mr}^h b_1 \\ Z_{mr}^h &= -T_{mr}^h \\ L_{mr}^h &= h_{mr} T_{mr}^h b_1 + k_\beta b_1 \\ M_{mr}^h &= h_{mr} T_{mr}^h a_1 + k_\beta a_1 \\ N_{mr}^h &= -C_{mr}^Q \left(T_{mr}^h \right)^{3/2} - D_{mr}^Q \end{aligned}$$

where by (5.39)

$$T_{mr}^h = C_{mr}^T A_0 + \frac{(D_{mr}^T)^2}{2} - D_{mr}^T \sqrt{C_{mr}^T A_0 + \frac{(D_{mr}^T)^2}{4}}$$

and where we defined

$$\begin{aligned} C_{mr}^T &:= \frac{\rho a c R^3 N_b \Omega^2}{6} & D_{mr}^T &:= \frac{a c R N_b \Omega \sqrt{\rho}}{4\sqrt{2\pi}} \\ C_{mr}^Q &:= \frac{1}{R\Omega\sqrt{2\rho\pi}} & D_{mr}^Q &:= \frac{\rho c R^4 N_b \Omega^2 C_D}{8} \end{aligned}$$

The k_β term was used in Sections 5.3.1.3 and 5.3.1.5 and represents a lumped-parameter torsional spring model of the blade's elasticity and the elastomeric flapping restraint within the blade grip. This parameter is experimentally identified by attaching a set of masses m on the main rotor blade and measuring the resulting linear deflection of the attachment point. A picture of the experiment is shown in Figure 5.15, where the deflections are measured w.r.t. the ground with the zero-mass distance used as the datum for subsequent deflection measurements d. The data is converted to torque $\tau = mgl_m$ versus flapping angle $\beta = d/l_m$ where l_m is the constant length from the main rotor shaft to the mass attachment point on the blade. Plotting τ versus β and using a least-squares linear fit provides k_β as the slope of the line, also shown in Figure 5.15. Remark the linear fit is good over a range of values which confirms that a linear torsional spring model for the main blades is accurate.

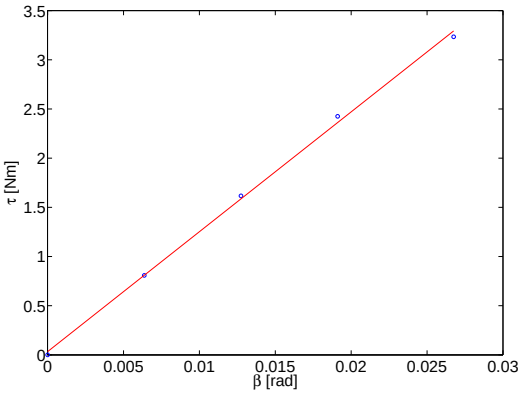

Figure 5.15: Main rotor k_β identification: experiment setup; restoring torque τ versus flapping angle β

5.3.2 Rotor Head

The rotor head system controls the main blade pitch Θ through a series of linkages. The input to this subsystem is a swashplate which can be tilted in a plane as well as raised/lowered through another set of linkages connected to the roll, pitch and collective servos. The rotor head includes a Bell-Hiller system for stability augmentation. The design is shown schematically in Figure 5.16 for $\psi = 0$. Note the swashplate consists of two parts, both tilting but only the upper one rotating.

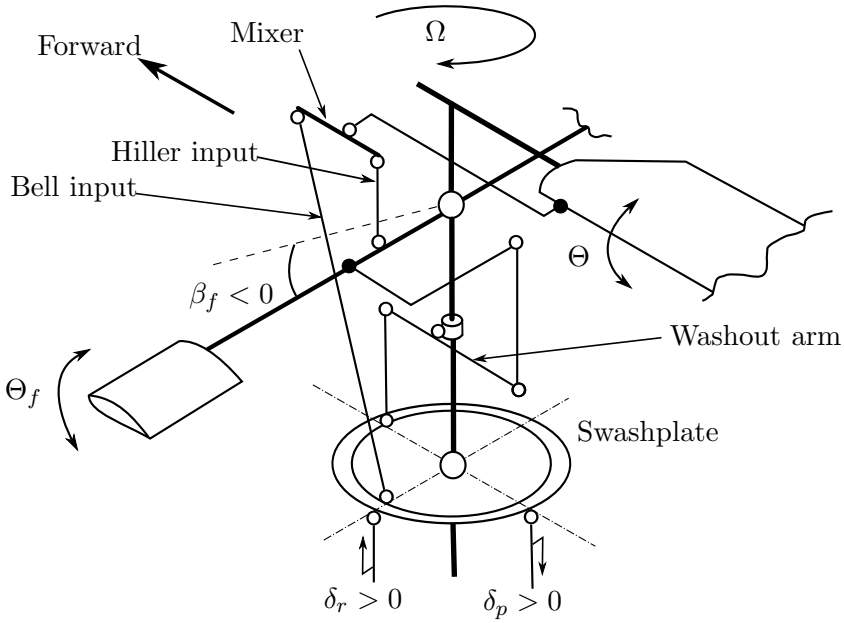

Figure 5.16: Bell-Hiller system schematic [76] for $\psi = 0$, $\psi_f = 90°$; δ_c omitted for clarity.

Let $\delta_c \in [0, 1]$ denote the normalized vertical swashplate position such that $\delta_c = 0$ and $\delta_c = 1$ denote the lowest and highest position reachable corresponding to collective stick fully down and fully up, respectively. Also let $\delta_r \in [-1, 1]$ and

$\delta_p \in [-1, 1]$ denote the normalized swashplate tilt about the helicopter roll and pitch axes, respectively. The sign convention is shown in Figure 5.16 with $\delta_r = 0$, $\delta_p = 0$ denoting the swashplate is level in the roll and pitch axis or the roll and pitch sticks are centered, respectively. The limits $\delta_r = -1$ and $\delta_r = 1$ represent maximum left and right swashplate tilt or roll stick fully left and fully right, respectively. Similarly $\delta_p = -1$ and $\delta_p = 1$ represent maximum forward and backward swashplate tilt or pitch stick fully front and fully back, respectively. Using δ_c, δ_r and δ_p as inputs allows the math model to handle different types of swashplate layouts, e.g. the 90° control setup on the Bergen Industrial Twin or a 120° CCPM control used on the Mini-Titan electric heli; the mapping from δ to servo commands will be discussed in Section 5.3.5.

The Bell-Hiller system consists of a flybar with small airfoils attached to its ends, mounted at 90° to the main blades and rotating about a teetering hinge inside the main rotor shaft. The washout arm moves together with the swashplate such that the input δ_c does not affect the pitch Θ_f of the flybar airfoils but only the collective component of the main rotor blade pitch Θ (5.22):

$$A_0 = C_c \delta_c + D_c \tag{5.41}$$

where C_c and D_c are constants which depend on the mechanical link setup and pilot settings on the transmitter. Physically these are identified by moving the collective stick from $\delta_c = 0$ to $\delta_c = 1$ and measuring the range of Θ and its value at $\delta_c = 0$, respectively, with $D_c < 0$ being typical. The flybar pitch Θ_f is a periodic function of the swashplate tilt as

$$\Theta_f = (K_H \delta_r) \cos \psi_f + (K_H \delta_p) \sin \psi_f \tag{5.42}$$

where K_H is the Hiller input ratio of flybar cyclic pitch amplitude to swashplate tilt; remark the flybar paddle with pitch Θ_f shown in Figure 5.16 is at azimuth station $\psi_f = 90°$. The 2π-periodic flybar pitch function (5.42) will cause the flybar to flap with the approximate profile

$$\beta_f(t, \psi) \approx -a_{1f}(t) \cos \psi_f + b_{1f}(t) \sin \psi_f \tag{5.43}$$

where the sign convention has been chosen identical to (5.30). The dynamics of a_{1f} and b_{1f} will be analyzed in Section 5.3.2.1; remark that (5.43) has no coning component because the flybar is a teetering rotor. Using the Mixer arm shown in Figure 5.16 the cyclic amplitudes A_1, B_1 of the main rotor pitch (5.22) $\Theta = A_0 + A_1 \cos \psi + B_1 \sin \psi$ are controlled by a mix of swashplate tilt and flybar flapping angles as

$$\begin{aligned} A_1 &= K_B \delta_r + K_F b_{1f} \\ B_1 &= K_B \delta_p + K_F a_{1f} \end{aligned} \tag{5.44}$$

where K_B is the Bell input ratio of main rotor cyclic pitch amplitude to swashplate tilt, and K_F is known as the flybar ratio[4] of main rotor pitch to flybar flapping angle. The three ratios above are functions of mechanical linkage setup.

The Bell and Hiller input ratios K_B and K_H can be measured as follows: tilt the swashplate by moving the roll or pitch transmitter stick to one of its limits and

[4]This is standard terminology in RC helicopters. Typical flybar ratios range from .5 : 1 to 1 : 1; this is further discussed at the end of Section 5.3.2.1

hold it there. Using a pitch gauge measure $\max(\Theta)$, $\min(\Theta)$ as well as $\max(\Theta_f)$, $\min(\Theta_f)$ over a complete 360° main rotor revolution; the input ratios are then given by

$$K_B = \frac{\max(\Theta) - \min(\Theta)}{2}, \qquad K_H = \frac{\max(\Theta_f) - \min(\Theta_f)}{2}$$

Remark this assumes the roll or pitch stick center position $\delta = 0$ corresponds to a perfectly level swashplate, and so it is important to zero out any trims on these sticks for this procedure.

The flybar ratio K_F is computed by tilting the flybar to a given angle β_f with respect to the horizontal and measuring the resulting main rotor blade pitch Θ using a pitch gauge. The experimental setup is shown in Figure 5.17; the tilt angle β_f is measured using a digital inclinometer. We obtain a set of (β_f, Θ) pairs which are plotted to obtain K_F as the slope of least-squares linear fit to the data, also shown in Figure 5.17. Computing the slope of the line we find $K_F = 0.66$ i.e. a flybar ratio of .66 : 1.

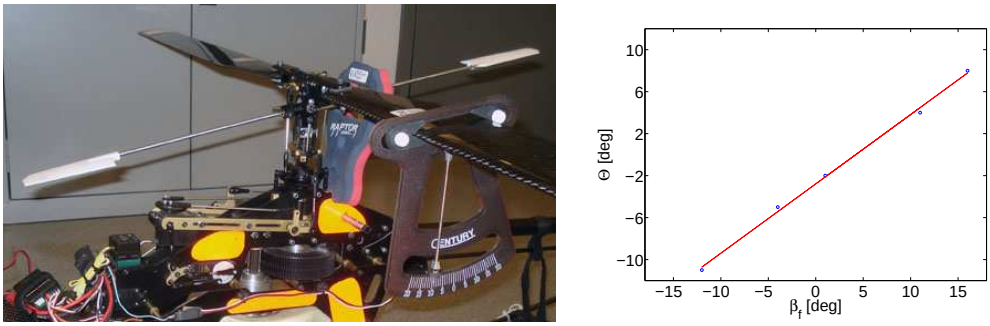

Figure 5.17: Flybar ratio K_F identification: experiment setup; blade pitch Θ versus flybar tilt β_f

5.3.2.1 Flybar Flapping Dynamics

A schematic of the flybar is shown in Figure 5.18. The flybar consists of a uniform rod hinged at the center of the main rotor with two paddle airfoils attached to its ends. The flybar is free to teeter about its pivot and its flapping angle β_f is measured upwards from the horizontal plane. The $\boldsymbol{ijk}$ frame is fixed to the flybar's centre of mass so the moment balance is governed by the standard Euler equation (5.10) rather than its "extended" version (5.18) which was employed in Section 5.3.1.3. The outer radius of the flybar is denoted R_f and the radial distance to each paddle's inner edge is $\varepsilon_f R_f$ where by construction $0 < \varepsilon_f < 1$.

The flybar paddles are symmetric however they are tapered in shape, have a sharp leading edge and their maximum thickness occurs at the midpoint $x_f/c_f = 0.5$. The average paddle chord is $c_f = 50$ mm and maximum thickness is $t_f = 4.4$ mm such that $t_f/c_f = 0.09$. The paddle is classified as the modified four-digit airfoil [8, p. 117] NACA 0009-05, where the first four digits function as before, the fifth digit indicates relative magnitude of the leading edge radius with 0 denoting a sharp edge (a 6 denotes the standard curvature of NACA four-digit series airfoils), and the sixth digit indicates the maximum thickness position with 5 indicating mid-chord.

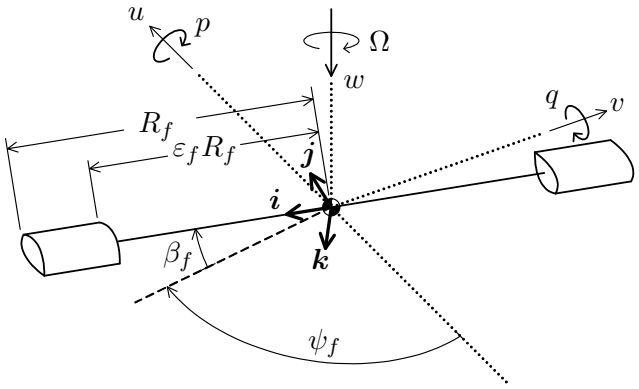

Figure 5.18: Flybar Kinematics

This geometry is used in JavaFoil to compute the paddle lift curve slope a_f using Reynolds number (5.20) with $V_f = \Omega R_f$.

Denoting the flybar's angular velocity vector as $[p^f \quad q^f \quad r^f]^T$, the dynamics of β_f are obtained from a moment balance about the $\boldsymbol{j}$ axis (5.11)

$$J^f_{yy}\dot{q}^f + p^f r^f (J^f_{xx} - J^f_{zz}) = M^f$$

where M^f is the net external moment about the $\boldsymbol{j}$ axis. The flybar is modeled as a slender rod of mass m_r and length $2R_f$ with point masses m_p on each end representing the paddles where by direct measurement $m_r = 0.043$ kg, $R_f = 0.306$ m and $m_p = 0.025$ kg. Using the CM-fixed frame illustrated in Figure 5.18 we have by [100, p. 713]

$$\begin{aligned} J^f_{xx} &\approx 0 \\ J^f_{yy} &= \frac{1}{12} m_r (2R_f^2) + 2 m_p R_f^2 \\ J^f_{zz} &= \frac{1}{12} m_r (2R_f^2) + 2 m_p R_f^2 = J^f_{yy} \end{aligned}$$

and thus $J^f_{xx} - J^f_{zz} = -J^f_{yy} := -J_f$ and the previous equation above becomes

$$J_f(\dot{q}^f - p^f r^f) = M^f \tag{5.45}$$

The angular velocity components in (5.45) can be obtained by inspection of Figure 5.18:

$$\begin{aligned} p^f &= -p\cos\psi_f \cos\beta_f - q\sin\psi_f \cos\beta_f - \Omega \sin\beta_f \\ q^f &= p\sin\psi_f - q\cos\psi_f + \dot{\beta}_f \\ r^f &= -p\cos\psi_f \sin\beta_f - q\sin\psi_f \sin\beta_f + \Omega\cos\beta_f \end{aligned}$$

which is exactly analogous to the main blade flapping analysis in Section 5.3.1.3 due to ψ_f being measured from the same datum as ψ. We directly compute

$$\dot{q}^f = \dot{p}\sin\psi_f + p\Omega\cos\psi_f - \dot{q}\cos\psi_f + q\Omega\sin\psi_f + \ddot{\beta}_f$$

and substituting the above into (5.45) then using the small-angle approximations $\cos\beta_f \approx 1$, $\sin\beta_f \approx \beta_f$, $\beta_f^2 \approx 0$ as well as $p^2 \approx 0$, $q^2 \approx 0$, $pq \approx 0$ due to $p, q \ll \Omega$ we

get

$$p^f r^f = -p\Omega\cos\psi_f - q\Omega\sin\psi_f - \Omega^2\beta_f,$$
$$J_f(\dot{q}^f - p^f r^f) = J_f\big(\ddot{\beta}_f + \dot{p}\sin\psi_f - \dot{q}\cos\psi_f + 2p\Omega\cos\psi_f + 2q\Omega\sin\psi_f + \Omega^2\beta_f\big) \tag{5.46}$$

which is analogous to (5.26). The moment about the central hinge M^f in (5.45) comes *only* from aerodynamic lift, due to the weight moment canceling itself out on the two sides and the absence of a restoring spring term. The tangential and perpendicular flow components U_T, U_P on the advancing paddle at distance l from the central hinge are obtained by inspection of Figure 5.18 or by analogy from (5.27):

$$U_T^a = \Omega l\cos\beta_f + u\sin\psi_f - v\cos\psi_f$$
$$U_P^a = (v_i - w)\cos\beta_f + u\sin\beta_f\cos\psi_f + v\sin\beta_f\sin\psi_f + \dot{\beta}_f l + pl\sin\psi_f - ql\cos\psi_f$$

On the retreating paddle, $\psi_f^r = \psi_f + \pi$ hence $\sin\psi_f^r = -\sin\psi_f$, $\cos\psi_f^r = -\cos\psi_f$ and $\beta_f^r = -\beta_f$, $\dot{\beta}_f^r = -\dot{\beta}_f$, $\ddot{\beta}_f^r = -\ddot{\beta}_f$:

$$U_T^r = \Omega l\cos\beta_f - u\sin\psi_f + v\cos\psi_f$$
$$U_P^r = (v_i - w)\cos\beta_f + u\sin\beta_f\cos\psi_f + v\sin\beta_f\sin\psi_f - \dot{\beta}_f l - pl\sin\psi_f + ql\cos\psi_f$$

From (5.42) the advancing paddle's pitch angle is the period function

$$\Theta_f = (K_H\delta_r)\cos\psi_f + (K_H\delta_p)\sin\psi_f := A_f\cos\psi_f + B_f\sin\psi_f$$

and it follows the retreating paddle has the pitch angle

$$\Theta_f^r = -A_f\cos\psi_f - B_f\sin\psi_f = -\Theta_f$$

As in Section 5.3.1.3 the moment created by aerodynamic lift on the advancing paddle is

$$M^a(\psi_f) = \int_{\varepsilon_f R_f}^{R_f} l dF^{\perp} = \frac{\rho a_f c_f}{2}\int_{\varepsilon_f R_f}^{R_f} l\left[\Theta_f(U_T^a)^2 - U_T^a U_P^a\right] dl$$

The retreating paddle creates the moment

$$M^r(\psi_f) = -\int_{\varepsilon_f R_f}^{R_f} l dF^{\perp,r} = -\frac{\rho a_f c_f}{2}\int_{\varepsilon_f R_f}^{R_f} l\left[-\Theta_f(U_T^r)^2 - U_T^r U_P^r\right] dl$$

where the -1 factor is due to positive (upwards) lift on the retreating paddle creating a negative contribution to M^f. The total aerodynamic lift moment $M^f = M^a + M^r$ is then

$$M^f = \frac{1}{2}\rho a_f c_f\int_{\varepsilon_f R_f}^{R_f} l\Big\{(A_f\cos\psi_f + B_f\sin\psi_f)\left[(U_T^a)^2 + (U_T^r)^2\right] - U_T^a U_P^a + U_T^r U_P^r\Big\} dl$$

which evaluates to

$$\begin{aligned} M^f = \frac{1}{4}\rho a_f c_f R_f^2(1-\varepsilon_f^2)\Big\{&\Big[u^2 + v^2 + (1+\varepsilon_f^2)(R_f\Omega)^2 - (u^2 - v^2)\cos 2\psi_f \\ &- 2uv\sin 2\psi_f\Big](A_f\cos\psi_f + B_f\sin\psi_f) + \Big[2v(v_i - w) + q(1+\varepsilon_f^2)R_f^2\Omega\Big]\cos\psi_f \\ &+ 2uv\beta_f\cos 2\psi_f - \Big[2u(v_i - w) + p(1+\varepsilon_f^2)R_f^2\Omega\Big]\sin\psi_f \\ &- (u^2 - v^2)\beta_f\sin 2\psi_f - (1+\varepsilon_f^2)R_f^2\Omega\dot{\beta}_f\Big\} \end{aligned}$$

and which is substituted into (5.45) along with (5.46) to yield

$$\ddot{\beta}_f + \left\{\frac{\rho a_f c_f R_f^4(1-\varepsilon_f^4)\Omega}{4J_f}\right\}\dot{\beta}_f + \left\{\Omega^2 + \frac{\rho a_f c_f R_f^2(1-\varepsilon_f^2)}{4J_f}\Big[(u^2-v^2)\sin 2\psi_f \right.$$
$$\left. - 2uv\cos 2\psi_f\Big]\right\}\beta_f = -\dot{p}\sin\psi_f + \dot{q}\cos\psi_f - 2p\Omega\cos\psi_f - 2q\Omega\sin\psi_f$$
$$+ \frac{\rho a_f c_f R_f^2(1-\varepsilon_f^2)}{4J_f}\Big\{\Big[u^2+v^2+(1+\varepsilon_f^2)(R_f\Omega)^2 - (u^2-v^2)\cos 2\psi_f$$
$$- 2uv\sin 2\psi_f\Big](A_f\cos\psi_f + B_f\sin\psi_f) + \Big[2v(v_i-w) + q(1+\varepsilon_f^2)R_f^2\Omega\Big]\cos\psi_f$$
$$- \Big[2u(v_i-w) + p(1+\varepsilon_f^2)R_f^2\Omega\Big]\sin\psi_f\Big\} \tag{5.47}$$

The coefficient group $\rho a_f c_f R_f^4(1-\varepsilon_f^4)/J_f$ in (5.47) is similar to the Lock number γ introduced in Section 5.3.1.3. Let $J_f = 2J_{\beta_f}$ where J_{β_f} measures the mass moment of inertia of one-half of the flybar about its flapping hinge[5]. The term $R_f^4(1-\varepsilon_f^4) = R_f^4 - (\varepsilon_f R_f)^4$ measures the length of the half-flybar's lifting surface i.e. the width of an individual paddle. We thus define the flybar Lock number

$$\gamma_f := \frac{\rho a_f c_f R_f^4(1-\varepsilon_f^4)}{J_{\beta_f}}$$

which is introduced into (5.47). The assumed flybar flapping profile (5.43) is differentiated twice w.r.t. time giving

$$\begin{aligned}
\beta_f &= -a_{1f}\cos\psi_f + b_{1f}\sin\psi_f \\
\dot{\beta}_f &= (-\dot{a}_{1f} + b_{1f}\Omega)\cos\psi_f + (a_{1f}\Omega + \dot{b}_{1f})\sin\psi_f \\
\ddot{\beta}_f &= (-\ddot{a}_{1f} + a_{1f}\Omega^2 + 2\dot{b}_{1f}\Omega)\cos\psi_f + (2\dot{a}_{1f}\Omega + \ddot{b}_{1f} - b_{1f}\Omega^2)\sin\psi_f
\end{aligned} \tag{5.48}$$

analogously to (5.31) and (5.32). Substituting the above into (5.47) and matching coefficients of $\cos\psi_f$ and $\sin\psi_f$ gives a set of coupled second-order linear differential equations for the flapping angles a_{1f} and b_{1f}. As in Section 5.3.1.3 we pre-simplify by numerically computing $\gamma_f = 0.93$ using the identified values listed in Section 5.5. Since $\gamma_f < \gamma$ is very small, we are able to disregard the translational velocity effects by setting $u = v = 0$ in (5.47) which simplifies to

$$\ddot{\beta}_f + \frac{\gamma_f\Omega}{8}\dot{\beta}_f + \Omega^2\beta_f = -\dot{p}\sin\psi_f + \dot{q}\cos\psi_f - 2p\Omega\cos\psi_f - 2q\Omega\sin\psi_f$$
$$+ \frac{\gamma_f\Omega^2}{8}(A_f\cos\psi_f + B_f\sin\psi_f) + \frac{\gamma_f\Omega}{8}(q\cos\psi_f - p\sin\psi_f)$$

Substituting (5.48) into the above and matching coefficients of $\cos\psi_f$ and $\sin\psi_f$

[5]This by analogy to J_β in Section 5.3.1.3 which measures the mass moment of inertia of a single blade about its flapping axis

gives

$$\begin{aligned}
-\ddot{a}_{1f} + a_{1f}\Omega^2 + 2\dot{b}_{1f}\Omega + \frac{\gamma_f\Omega}{8}(-\dot{a}_{1f} + b_{1f}\Omega) - \Omega^2 a_{1f} \\
&= \dot{q} - 2p\Omega + \frac{\gamma_f\Omega^2}{8}A_f + \frac{\gamma_f\Omega}{8}q \\
2\dot{a}_{1f}\Omega + \ddot{b}_{1f} - b_{1f}\Omega^2 + \frac{\gamma_f\Omega}{8}(a_{1f}\Omega + \dot{b}_{1f}) + \Omega^2 b_{1f} \\
&= -\dot{p} - 2q\Omega + \frac{\gamma_f\Omega^2}{8}B_f - \frac{\gamma_f\Omega}{8}p
\end{aligned} \tag{5.49}$$

The above is a set of coupled linear differential equations which govern the flybar flapping dynamics. They are rewritten in modal form $\ddot{x} + D\dot{x} + Kx = F$ as

$$\begin{bmatrix} \ddot{a}_{1f} \\ \ddot{b}_{1f} \end{bmatrix} + \begin{bmatrix} \frac{\gamma_f\Omega}{8} & -2\Omega \\ 2\Omega & \frac{\gamma_f\Omega}{8} \end{bmatrix} \begin{bmatrix} \dot{a}_{1f} \\ \dot{b}_{1f} \end{bmatrix} + \begin{bmatrix} 0 & -\frac{\gamma_f\Omega^2}{8} \\ \frac{\gamma_f\Omega^2}{8} & 0 \end{bmatrix} \begin{bmatrix} a_{1f} \\ b_{1f} \end{bmatrix} = \begin{bmatrix} -\dot{q} + 2p\Omega - \frac{\gamma_f\Omega}{8}q - \frac{\gamma_f\Omega^2}{8}A_f \\ -\dot{p} - 2q\Omega - \frac{\gamma_f\Omega}{8}p + \frac{\gamma_f\Omega^2}{8}B_f \end{bmatrix} \tag{5.50}$$

As in Section 5.3.1.3 we perform a complex modal analysis. The homogenous version of (5.50) is written in state-space form $\dot{y} = Ay$ where $y = [y_1 \quad y_2]^T := [x \quad \dot{x}]^T$ such that

$$\begin{bmatrix} \dot{y}_1 \\ \dot{y}_2 \end{bmatrix} = \begin{bmatrix} 0 & I \\ -K & -D \end{bmatrix} \begin{bmatrix} y_1 \\ y_2 \end{bmatrix}$$

The eigenvalues of A are two complex-conjugate pairs λ_1 and λ_2 which govern the natural frequencies and damping ratios of each vibration mode. By direct computation we find

$$\lambda_1 = -\frac{\gamma_f\Omega}{16} \pm \frac{j\Omega}{16}\sqrt{512 - \gamma_f^2 + 32\sqrt{256 - \gamma_f^2}}$$
$$\lambda_2 = -\frac{\gamma_f\Omega}{16} \pm \frac{j\Omega}{16}\sqrt{512 - \gamma_f^2 - 32\sqrt{256 - \gamma_f^2}}$$

and the natural frequency and damping ratio of each mode are given by

$$\omega_i = \sqrt{\mathrm{Re}\{\lambda_i\}^2 + \mathrm{Im}\{\lambda_i\}^2} \qquad \text{and} \qquad \zeta_i = \frac{-\mathrm{Re}\{\lambda_i\}}{\sqrt{\mathrm{Re}\{\lambda_i\}^2 + \mathrm{Im}\{\lambda_i\}^2}}$$

which gives

$$\omega_1 = \Omega\left(2 + \sqrt{4 - \left(\frac{\gamma_f}{8}\right)^2}\right)^{1/2} \qquad \zeta_1 = \frac{\gamma_f\Omega}{16\omega_1}$$
$$\omega_2 = \Omega\left(2 - \sqrt{4 - \left(\frac{\gamma_f}{8}\right)^2}\right)^{1/2} \qquad \zeta_2 = \frac{\gamma_f\Omega}{16\omega_2}$$

The eigenvalues γ_1 and γ_2 represent the advancing and regressing flybar flapping modes, respectively. By inspection of the last result above, for a "small" γ_f we have $4 \gg (\gamma_f/8)^2$ and thus $\omega_1 \approx 2\Omega$, such that the advancing flybar flapping mode is much faster than the rigid-body motions and can be neglected. By contrast the regressing mode frequency ω_2 will be very low.

Using the numerical values $\gamma_f = 0.67$ and $\Omega = 55\pi$ rad/s from Section 5.5 we compute

$$\omega_1 = 345.50 \text{ rad/s} = 54.99 \text{ Hz} \qquad \zeta_1 = 0.0208$$
$$\omega_2 = 7.18 \text{ rad/s} = 1.14 \text{ Hz} \qquad \zeta_2 = 0.9998$$

which confirms the regressing flybar flapping mode's natural frequency is sufficiently low, or equivalently the 5% step input settling time $t_s = 3/(\zeta_2\omega_2) = 0.418$ s is sufficiently long to noticeably impact the helicopter's dynamics. The regressing mode's near-critical damping ratio means it can be approximated as a first-order system by setting $\ddot{a}_{1f} = \ddot{b}_{1f} = 0$ in (5.49) as well as setting $\dot{p} = \dot{q} = 0$ exactly as in Section 5.3.1.3. The regressing flapping dynamics of the flybar become

$$2\dot{b}_{1f}\Omega + \frac{\gamma_f\Omega}{8}(-\dot{a}_{1f} + b_{1f}\Omega) = -2p\Omega + \frac{\gamma_f\Omega^2}{8}A_f + \frac{\gamma_f\Omega}{8}q$$
$$2\dot{a}_{1f}\Omega + \frac{\gamma_f\Omega}{8}(a_{1f}\Omega + \dot{b}_{1f}) = -2q\Omega + \frac{\gamma_f\Omega^2}{8}B_f - \frac{\gamma_f\Omega}{8}p$$

We assume the control links from the swashplate to the flybar are phased to decouple the flapping response, i.e. the roll cyclic $A_f = K_H\delta_r$ affects only the lateral flapping b_{1f} and the pitch cyclic $B_f = K_H\delta_p$ only the longitudinal flapping a_{1f}. This is done by dropping respectively $\dot{a}_{1f}$ and $\dot{b}_{1f}$ from the first and second equation above. Normalizing the coefficients of A_f and B_f gives

$$\frac{16}{\gamma_f\Omega}\dot{a}_{1f} + a_{1f} = -\frac{16}{\gamma_f\Omega}q - \frac{1}{\Omega}p + B_f$$
$$\frac{16}{\gamma_f\Omega}\dot{b}_{1f} + b_{1f} = -\frac{16}{\gamma_f\Omega}p + \frac{1}{\Omega}q + A_f$$

where $B_f = K_H\delta_p$ and $A_f = K_H\delta_r$ are inputs from the swashplate. Finally, evaluating the coefficients $16/(\gamma_f\Omega) = 0.1392$ and $(1/\Omega) = 0.0058$ we see the on-axis effect of q on a_{1f} and p on b_{1f} dominate the off-axis effects and the above can be simplified to

$$\begin{aligned}\frac{16}{\gamma_f\Omega}\dot{a}_{1f} + a_{1f} &= -\frac{16}{\gamma_f\Omega}q + K_H\delta_p \\ \frac{16}{\gamma_f\Omega}\dot{b}_{1f} + b_{1f} &= -\frac{16}{\gamma_f\Omega}p + K_H\delta_r\end{aligned} \tag{5.51}$$

where $16/(\gamma_f\Omega) := \tau_f$ is the time constant of the simplified flybar flapping dynamics (5.51).

As discussed in Section 5.3.2 the flybar flapping angles enter the main rotor cyclic pitch amplitudes A_1, B_1 as (5.44)

$$A_1 = K_B\delta_r + K_F b_{1f}$$
$$B_1 = K_B\delta_p + K_F a_{1f}$$

and A_1 and B_1 in turn map to main rotor flapping angles by (5.36)

$$b_1 = A_1$$
$$a_1 = B_1$$

This last relationship was obtained in Section 5.3.1.4 by neglecting the main rotor flapping dynamics due to their fast time constant. The flybar performs two functions: first, it slows down the main rotor flapping response to swashplate tilt since $\delta_p \to a_{1f} \to B_1 \to a_1$ and $\delta_r \to b_{1f} \to A_1 \to b_1$ provide a partial rate limit on a_1 and b_1 due to the first-order dynamics of a_{1f} and b_{1f}. Second, the flybar dynamics (5.51)

contain negative feedback terms $-\tau_f q$ and $-\tau_f p$ which provide derivative action in the pitch and roll channels of the helicopter which damps the response to external disturbances such as wind gusts.

The flybar can be summarized in control diagram form as shown in Figure 5.19 for the roll channel; the pitch channel has the same diagram with $(\delta_r, b_{1f}, A_1, b_1, p)$ replaced by $(\delta_p, a_{1f}, B_1, a_1, q)$. The Roll Dynamics block represents $\dot{p} = qr(J_{yy} - J_{zz})/J_{xx} + L/J_{xx}$ from (5.11) where $L \approx L^h_{mr} = (h_{mr}T^h_{mr} + k_\beta)b_1$, i.e. we use the roll moment expression in hover developed in Section 5.3.1.5 instead of $L = h_{mr}Y_{mr} + L_{mr}$ due to the complexity of the Y_{mr} and L_{mr} expressions; the key point of this block is that a $b_1 > 0$ rotor disc tilt provides a $p > 0$ roll response. Increasing the flybar ratio K_F increases the derivative feedback action, making the helicopter more resistant to disturbances such as wind gusts but also slowing down input step responses; indeed higher flybar ratios are better for beginning pilots as well as helicopter competitions which demand stable hover and resistance to wind conditions, while lower flybar ratios are better for 3D flying which require very nimble handling of the helicopter. The derivative feedback action can also be boosted by increasing $\tau_f = 16/(\gamma_f \Omega)$ which by the definition of γ_f is equivalent to reducing a_f, c_f, R_f and augmenting ε_f, J_{β_f}. This is why using heavier, shorter paddles makes the helicopter more stable, while using longer flybars with lightweight, wide paddles (whose larger aspect ratio $(R_f - \varepsilon_f R_f)/c$ provides higher a values) is preferred for 3D flight.

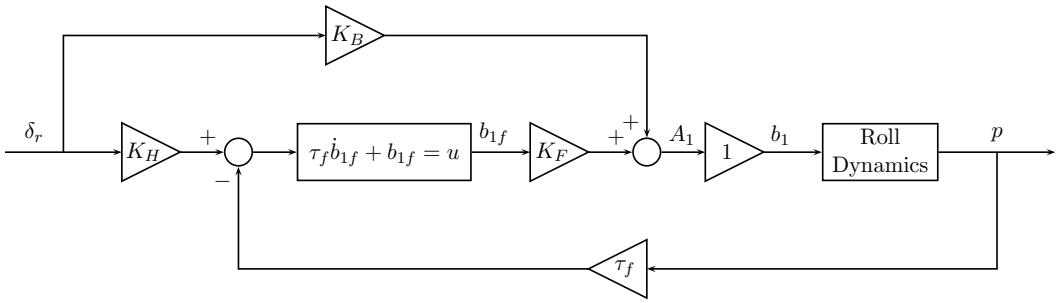

Figure 5.19: Rotor head system diagram — roll channel

5.3.3 Tail Rotor

The tail rotor uses a fixed-pitch design, similar to an airplane propeller. We use the tail blade pitch Θ_t as the input term as in Section 5.3.1.5. Due to the fixed pitch design the tail rotor does not exhibit flapping. The tail rotor is geared to rotate counter-clockwise as viewed from the right side of the helicopter at the rate $\Omega_t = K_t \Omega$ where $K_t > 1$ is the tail to main rotor gearing ratio. We define $\Theta_t > 0$ as the pitch which creates tail rotor thrust T_{tr} in the positive y_b direction and take the tail blade azimuth position $\psi_t = 0$ as the blade's rear-most position. This is illustrated in Figure 5.20. The tail rotor blades are symmetric with $c_t = 32.5$ mm and maximum thickness $t_t = 3.9$ mm at $x_t = 10$ mm from the leading edge, giving $t_t/c_t = 0.12$, $x_t/c_t = 0.31$ which classifies them as NACA 0012 airfoils. We obtain a_t, $C_{D,t}$ as in Section 5.3.1.2 using $V_t = \Omega_t R_t$ (where R_t is the tail rotor disc radius) to compute the Reynolds number (5.20).

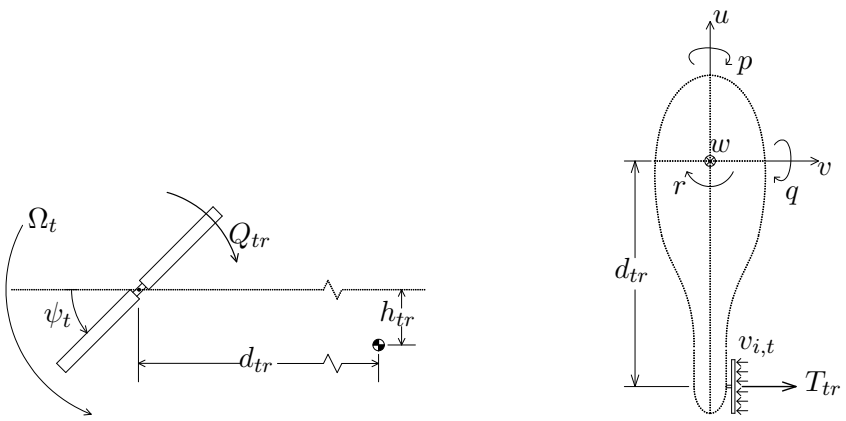

Figure 5.20: Helicopter tail: Side view (left), Overhead view (right)

By inspection of Figure 5.20, the tail blade airfoil section at distance l from the rotor shaft is subject to tangential and perpendicular flow components

$$U_T = \Omega_t l + u \sin\psi_t + w \cos\psi_t + q(d_{tr} + l\cos\psi_t)$$
$$U_P = v_{i,t} + v + p(h_{tr} - l\sin\psi_t) - r(d_{tr} + l\cos\psi_t)$$

where d_{tr} and h_{tr} are the longitudinal distance and height of the tail rotor axis w.r.t. the helicopter's CM. The tail rotor induced velocity $v_{i,t}$ is assumed constant across the rotor disc as in Section 5.3.1. Using (5.21) in Section 5.3.1.2 the infinitesimal force components perpendicular and parallel to the vertical plane are

$$dF^{\perp} = \frac{1}{2}\rho a_t c_t \left(\Theta_t U_T^2 - U_T U_P\right) dl$$
$$dF^{\parallel} = \frac{1}{2}\rho a_t c_t \left(\Theta U_T U_P - U_P^2\right) dl + \frac{1}{2}\rho c_t C_{D,t} U_T^2 dl$$

The tail rotor thrust and counter-torque are evaluated from

$$T_{tr} = \frac{N_{bt}}{2\pi}\int_0^{2\pi}\int_0^{R_t} dF^{\perp}\, d\psi_t$$
$$Q_{tr} = \frac{N_{bt}}{2\pi}\int_0^{2\pi}\int_0^{R_t} l\, dF^{\parallel}\, d\psi_t$$

where $N_{bt} = 2$ is the number of tail rotor blades. The in-plane forces X_{tr}, Y_{tr} and moments L_{tr}, M_{tr} are neglected as small, which is justified due to the size of the tail rotor as compared to the main one. The T_{tr} expression evaluates to

$$\begin{aligned} T_{tr} = \frac{\rho a_t c_t R_t N_{bt}}{24}\Big\{ &\Big[4(R_t\Omega_t)^2 + 6(u^2+w^2) + 6qR_t(w + 2d_{tr}\Omega_t) \\ &+ 2q^2(R_t^2 + 6d_{tr}^2)\Big]\Theta_t + 2qrR_t^2 + 3R_t(pu + rw) \\ &- 6(R_t\Omega_t + 2qd_{tr})(v + v_{i,t} + ph_{tr} - rd_{tr})\Big\} \end{aligned} \tag{5.52}$$

The tail rotor induced velocity $v_{i,t}$ is computed as in Section 5.3.1.1. We assume the main rotor's downwash is sufficiently far to not affect the tail rotor inflow due to the

Bergen Industrial Twin's extended tail boom (c.f. Figure 5.23 in Section 5.3.7.1). Note that for a smaller helicopter where the rotor disc overhangs the tail this assumption would not hold, e.g. [59, p. 49]. Since the tail rotor disc is vertical, the general flight inflow equation (5.19) becomes

$$v_{i,t} = \frac{T_{tr}}{2\rho\pi R_t^2\sqrt{u^2 + (w + qd_{tr})^2 + (v + ph_{tr} - rd_{tr} + v_{i,t})^2}}$$

which gives a transcendental equation for T_{tr} when substituted into (5.52), just as for the main rotor in Section 5.3.1.5. At hover, the tail thrust (5.52) reduces to

$$T_{tr}^h = \frac{\rho a_t c_t R_t N_{bt}}{12}\left\{2(R_t\Omega_t)^2\Theta_t - 3R_t\Omega_t v_{i,t}^h\right\} \tag{5.53}$$

where

$$v_{i,t}^h = \sqrt{\frac{T_{tr}^h}{2\rho\pi R_t^2}} \tag{5.54}$$

We obtain an explicit $T_{tr}^h = T_{tr}^h(\Theta_t)$ expression by substituting (5.54) into (5.53) and solving a quadratic equation as in Section 5.3.1.5. The substitution gives

$$T_{tr}^h = \frac{\rho a_t c_t R_t^3 N_{bt}\Omega_t^2}{6}\Theta_t - \frac{ac_t R_t N_{bt}\Omega_t\sqrt{\rho}}{4\sqrt{2\pi}}\sqrt{T_{tr}^h} := C_{tr}^T\Theta_t - D_{tr}^T\sqrt{T_{tr}^h}$$

with C_{tr}^T, D_{tr}^T positive constants. The solution to the above is exactly analogous to (5.39)

$$T_{tr}^h = C_{tr}^T\Theta_t + \frac{(D_{tr}^T)^2}{2} - D_{tr}^T\sqrt{C_{tr}^T\Theta_t + \frac{(D_{tr}^T)^2}{4}} \tag{5.55}$$

where we have chosen the solution for which $\Theta_t = 0 \Longrightarrow T_{tr}^h = 0$. A simpler version of (5.55) can be obtained by employing $T_{tr}^h = Q_{mr}^h/d_{tr} \approx C_{mr}^Q(mg)^{3/2} + D_{mr}^Q$ in (5.53) which gives

$$T_{tr}^h \approx C_{tr}^T\Theta_t - \left(D_{tr}^T\sqrt{C_{mr}^Q(mg)^{3/2} + D_{mr}^Q}\right)$$

but which requires $\dot{w} = \dot{r} = 0$, i.e. zero heave acceleration and zero yaw angular acceleration, making it much worse than (5.55).

Returning above, the Q_{tr} expression is

$$\begin{aligned}
Q_{tr} = &-\frac{\rho a_t c_t R_t^2 N_{bt}}{48}\Big\{\Big[3qrR_t^2 + 4R_t(pu + rw) - 4(2R_t\Omega_t + 3qd_{tr}) \\
&(v + v_{i,t} + ph_{tr} - rd_{tr})\Big]\Theta_t + 3(p^2 + r^2)R_t^2 + 12(v + v_{i,t} + ph_{tr} - rd_{tr})^2\Big\} \\
&+ \frac{\rho c_t R_t^2 C_{D,t} N_{bt}}{48}\Big\{6(R_t\Omega_t)^2 + 6(u^2 + w^2) + 8qR_t(w + 2d_{tr}\Omega) + 3q^2(R_t^2 + 4d_{tr}^2)\Big\}
\end{aligned}$$

and at hover this simplifies to

$$\begin{aligned}
Q_{tr}^h &= -\frac{\rho a_t c_t R_t^2 N_{bt}}{48}\left\{\Big[-4(2R_t\Omega_t)v_{i,t}^h\Big]\Theta_t + 12(v_{i,t}^h)^2\right\} + \frac{\rho c_t R_t^2 C_{D,t} N_{bt}}{48}\left\{6(R_t\Omega_t)^2\right\} \\
&= \frac{\rho a_t c_t R_t^2 N_{bt} v_{i,t}^h}{24 R_t\Omega_t}\left\{4(R_t\Omega_t)^2\Theta_t - 6R_t\Omega_t v_{i,t}^h\right\} + \frac{\rho c_t R_t^4\Omega_t^2 C_{D,t} N_{bt}}{8} \\
&= \frac{T_{tr}^h R_t}{R_t\Omega_t}\sqrt{\frac{T_{tr}^h}{2\rho\pi R_t^2}} + \frac{\rho c_t R_t^4\Omega_t^2 C_{D,t} N_{bt}}{8} := C_{tr}^Q\left(T_{tr}^h\right)^{3/2} + D_{tr}^Q
\end{aligned} \tag{5.56}$$

where by inspection C_{tr}^Q and D_{tr}^Q are constants.

5.3.3.1 Tail Rotor Contributions

The tail rotor's thrust and counter-torque T_{tr} and Q_{tr} generate the following force and moment components along the helicopter's body-fixed axes:

$$\begin{aligned}
X_{tr} &= 0 \\
Y_{tr} &= T_{tr} \\
Z_{tr} &= 0 \\
L_{tr} &= h_{tr} T_{tr} \\
M_{tr} &= -Q_{tr} \\
N_{tr} &= -d_{tr} T_{tr}
\end{aligned}$$

where h_{tr} and d_{tr} are the height and longitudinal distance, respectively, of the tail rotor hub w.r.t. the center of mass as illustrated in Figure 5.20; as in Section 5.3.1.6 these are directly measured c.f. Figure 5.3 in Section 5.2. In hover this becomes

$$\begin{aligned}
X_{tr}^h &= 0 \\
Y_{tr}^h &= T_{tr}^h \\
Z_{tr}^h &= 0 \\
L_{tr}^h &= h_{tr} T_{tr}^h \\
M_{tr}^h &= -C_{tr}^Q\left(T_{tr}^h\right)^{3/2} - D_{tr}^Q \\
N_{tr}^h &= -d_{tr} T_{tr}^h
\end{aligned}$$

where by (5.55)

$$T_{tr}^h = C_{tr}^T\Theta_t + \frac{(D_{tr}^T)^2}{2} - D_{tr}^T\sqrt{C_{tr}^T\Theta_t + \frac{(D_{tr}^T)^2}{4}}$$

and where

$$\begin{aligned}
C_{tr}^T &:= \frac{\rho a_t c_t R_t^3 N_{bt}(K_t\Omega)^2}{6} & D_{tr}^T &:= \frac{a c_t R_t N_{bt} K_t\Omega\sqrt{\rho}}{4\sqrt{2\pi}} \\
C_{tr}^Q &:= \frac{1}{R_t K_t\Omega\sqrt{2\rho\pi}} & D_{tr}^Q &:= \frac{\rho c_t R_t^4 N_{bt} C_{D,t}(K_t\Omega)^2}{8}
\end{aligned}$$

5.3.3.2 Tail Gyro

As seen in Section 5.3.1.5 the main rotor's counter-torque on the helicopter body Q_{mr} is a function of thrust T_{mr}, e.g. $Q^h_{mr} = C^Q_{mr}\left(T^h_{mr}\right)^{3/2} + D^Q_{mr}$ in hover, such that changes in collective input require adjustments to the tail input in order to cancel the counter-torque. On full-sized helicopters this is done manually by the pilot by adjusting the tail pedal inputs [121, p. 43]. RC helicopters such as the Bergen Industrial Twin have relatively small J_{zz} mass moment of inertias and high thrust-to-weight ratios, which make manual compensation of counter-torque too taxing for the pilot. For this reason tail rotor control is augmented with an electronic gyro which provides closed-loop control of the tail input using the sensed yaw rate r.

The ANCL helicopter employs the popular Futaba GY401 tail gyro [58] which provides two modes of operation: a Normal mode which stabilizes the sensed yaw rate r using the tail pitch servo and thus provides damping in the yaw channel; and a Heading Hold[6] mode which provides tracking control of r using tail stick deflections for r_{ref} and a PI control action on the error signal. For zero tail stick deflection, Heading Hold mode can thus maintain a steady heading angle ψ in the presence of exogenous inputs (changes in Q_{mr}, wind gusts), while Normal mode will remove yaw velocity r but exhibit a steady-state error in ψ. The GY401 manual [58] calls this the weathervane effect, where a helicopter hovering in wind under Normal mode will eventually align itself along the wind vector due to its tail stabilizers, whereas in the same situation Heading Hold mode is able to maintain a prescribed heading angle.

The GY401 unit uses two inputs from the on-board receiver, the tail channel and gyro sensitivity channel, and one output to the tail servo which directly controls the blade pitch Θ_t used in Section 5.3.3. In Normal mode, the tail input is added to a gain on the sensed r and passed directly to the tail servo, whereas in Heading Hold mode this input is used as r_{ref} where $r_{ref} = 0$ is taken as the tail input level at initialization. The gyro sensitivity input is interpreted as follows: for a "neutral" signal from the receiver (PWM with $T_{\text{ON}} = 1.5$ ms, c.f. Section 5.3.5) the gyro gain is set to zero. For PWM signals above neutral i.e. 1.5 ms $< T_{\text{ON}} <$ 2.0 ms the gyro operates in Heading Hold mode with the P and I gain values increasing from 0 to 100% of their maximum values. Conversely for signals below neutral the gyro operates in Normal mode with 1.5 ms $> T_{\text{ON}} >$ 1.0 ms mapping to a P gain from 0 to 100% of its maximum value. In this way the GY401 can be switched in-flight between Normal and Heading Hold modes, and the feedback gains adjusted to fine-tune the overall performance. Heading Hold mode is useful for hovering and forward flight while Normal mode is better for turns as well as certain 3D maneuvers.

The exact relationship between gyro sensitivity input and gain values in Normal and Heading Hold modes is not available from Futaba and thus requires experimental identification. The GY401 contains a "Control Delay" trimmer whose setting is adjustable from 0 to 100%. The exact function of this feature is not explained although we speculate it acts as a rate limit on the output control signal to the tail servo; this must be confirmed in experiment and the exact relationship between this setting and resulting rate limit needs to be identified. Heading Hold mode appears to implement an integrator reset function, although this is not stated in the manual,

[6] Futaba calls this the Angular Vector Control System (AVCS) mode

and the reset error threshold requires experimental identification as well.

Based on the above paragraph we can model the tail gyro unit in one of the following ways, listed in order of increasing difficulty:

1. Use Heading Hold mode and assume the input sensitivity is properly tuned such that the yaw channel is stabilized and $r = r_{ref}$, i.e. discard the $\dot{r}$ dynamics.

2. Turn off the tail gyro by setting the gyro sensitivity input to neutral ($T_{\text{ON}} = 1.5$ ms). The $\dot{r}$ dynamics remain and Q_{mr}, T_{tr} terms are computed as in Sections 5.3.1.5 and 5.3.3, respectively.

3. Include an identified model of the tail gyro as in e.g. [22].

Define $\delta_t \in [-1, 1]$ as the normalized tail input where $\delta_t = -1$ denotes tail stick fully left and $\delta_t = 1$ fully right. The map from δ_t to the helicopter model has three possible forms corresponding to the above:

1. $r = r_{ref} = \kappa_t \delta_t$ where κ_t is identified in flight by commanding a maximum tail stick deflection and measuring the resulting yaw rate r^{max} using the avionics box, such that $\kappa_t = |r^{max}|$.

2. $\Theta_t = C_t \delta_t + D_t$ where $C_t = [\Theta_t(\delta_t = 1) - \Theta_t(\delta_t = -1)]/2$, $D_t = \Theta_t(\delta_t = 0)$ are measured using a pitch gauge[7]. We have $C_t, D_t < 0$ because a positive yaw turn ($\delta_t > 0$) requires $\Theta_t < 0$ by sign convention of Section 5.3.3.

3. $r_{ref} = \kappa_t \delta_t$ as in 1, then compute $e_r = r_{ref} - r$ and $\Theta_t = \kappa_P e_r + \kappa_I \int e_r$ where κ_P, κ_I are the identified gains of the tail gyro; also include the "control delay" and integrator reset into the calculation.

For option 1, T_{tr} still appears in the Y_{tr} and L_{tr} terms summarized in Section 5.3.3.1 and must be computed from

$$T_{tr} = -Q_{mr} d_{tr}$$

where Q_{mr} is given in Section 5.3.1.5 and $T_{tr} < 0$ compensates for $Q_{mr} > 0$ by sign convention in Section 5.3.3.

5.3.4 Rotor Speed and Engine

The dynamics of Ω are governed by a moment balance on the main rotor shaft,

$$\dot{\Omega} = \dot{r} + \frac{1}{J_{mr}}(K_e Q_e - Q_{mr} - K_t Q_{tr}),$$

where J_{mr} is the rotational inertia of the main blades and rotor head, $K_e > 1$ is the engine to main rotor gearing ratio, Q_e is the torque generated by the engine, Q_{mr}, Q_{tr} are the counter-torques from the main and tail rotors available respectively from Sections 5.3.1.5 and 5.3.3, and $K_t > 1$ is the tail to main rotor gearing ratio. The engine input is a fuel throttle controlled by a dedicated servo. Let $\delta_e \in [0, 1]$ denote the normalized fuel throttle input with $\delta_e = 0$ and $\delta_e = 1$ denoting fully closed and

[7] The Θ_t offset term D_t models the design of the tail servo linkage.

fully open fuel inputs, respectively. Following [59, p. 44] we model the engine output power P_e and subsequently output torque as

$$P_e = P_e^{max}\delta_e \Longrightarrow Q_e = \frac{P_e}{K_e\Omega}$$

where P_e^{max} is the engine's maximum output power. The δ_e to Q_e model is assumed instantaneous since the time constants associated to fuel flow, air intake and combustion are much faster than the vehicle's dynamics [59, p. 44].

Internal combustion engines operate most efficiently in a narrow RPM band, hence maintaining a constant Ω is desirable. This is accomplished using either an engine governor, which maintains a target Ω by controlling δ_e using a PI control structure, or through a throttle-pitch curve, a nonlinear map from δ_c to δ_e programmed on the RC transmitter and tuned by the pilot. The current ANCL helicopter uses the latter solution, with two different versions of the curve used for no-payload ("stock") and full-payload flights. For illustration purposes the two curves are plotted in Figure 5.21; the values come from a lookup table, which is either built from servo inputs logged by the on-board avionics box or downloaded directly from the transmitter's flash memory card.

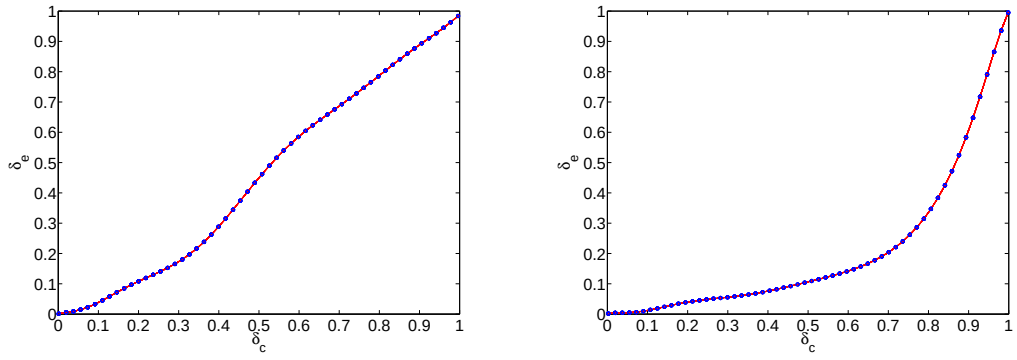

Figure 5.21: Throttle-pitch curves: Stock (left), Full-payload (right)

Based on the above discussion, we will ignore rotor speed dynamics and take Ω as constant, assuming a well-tuned curve or by physically adding a governor to the helicopter. The dynamics of Ω are important in autorotations [4]; in this case, the engine and tail rotors are disengaged through a centrifugal clutch, such that $\dot{\Omega}$ is a function of Q_{mr} only.

5.3.5 Servo Commands

The swashplate normalized vertical position δ_c and tilt angles δ_r, δ_p introduced in Section 5.3.2 are physically controlled by the collective, roll and pitch servos through a set of mechanical linkages. Similarly the tail rotor pitch Θ_t in Section 5.3.3 and the fuel throttle in Section 5.3.4 are controlled by their corresponding servos. The servos themselves are controlled by PWM signals coming from either the on-board Futaba R149DP radio receiver or generated by the avionics's Measurement Computing CTR10HD card, except for the tail servo which is controlled by PWM signals generated by the tail gyro unit as discussed in Section 5.3.3.2.

The servo reacts by rotating an output wheel, where the output rotation is mechanically limited to a $[-45°, 45°]$ range where 0 is the servo's neutral position. The input PWM signal to the servo is a square wave with period $T_{\text{PWM}} = 1/70$ s $\approx$ 14.3 ms and pulse width of T_{ON} where pulse widths of $T_{\text{ON}} = 1.0$ ms, $T_{\text{ON}} = 1.5$ ms and $T_{\text{ON}} = 2.0$ ms command output rotations of $-45°$, 0 and $45°$, respectively [75, p. 11]. The same signal type is used for the inputs to the tail gyro discussed in Section 5.3.3.2 where the above pulse widths are interpreted as "min", "neutral" and "max" signals, respectively.

The PWM duty cycle Δ is defined as

$$\Delta = \frac{T_{\text{ON}}}{T_{\text{PWM}}}$$

such that for $T_{\text{PWM}} = 1/70$ s we have $\Delta = 70T_{\text{ON}}$ and $0.070 \leq \Delta \leq 0.140$ for the above servo logic. The duty cycle Δ is the numerical value either logged or output by the avionics box via its CTR10HD card. For instance generating a "neutral" signal on the gyro sensitivity channel (c.f. Section 5.3.3.2) corresponds to setting $\Delta = 0.105$ on the appropriate CTR10HD PWM output channel.

Since the servo output rotations are converted to linear motion by a set of mechanical linkages, the full $[-45°, 45°]$ output range is typically not used, and in fact the extreme ranges may cause jamming or breaking of the linkages. For this reason the normalized system inputs δ are used, which respect the servo limits programmed by the pilot into the transmitter unit. We then need to identify the mapping from δ to Δ, such that the avionics box can mimic the signal limits programmed into the transmitter.

The identification process is made using the avionics box's receiver logging functionality. For collective, roll, pitch and tail inputs we propose the linear maps

$$\begin{aligned} \Delta_c &= m_c\delta_c + b_c \\ \Delta_r &= m_r\delta_r + b_r \\ \Delta_p &= m_p\delta_p + b_p \\ \Delta_t &= m_t\delta_t + b_t \end{aligned} \tag{5.57}$$

where

$$\left.\begin{aligned} m_s &= \Delta_{\delta_s=1} - \Delta_{\delta_s=0} \\ b_s &= \Delta_{\delta_s=0} \end{aligned}\right\} \qquad s = \{c, r, p, t\}$$

The identified values of the m and b parameters in (5.57) are listed in Section 5.5. The duty cycles were logged using the "Bergen-02" transmitter programming employed for full-payload flight, c.f. Section 5.3.4; sample plots for the collective and roll channels are shown in Figure 5.22 where the corresponding pilot sticks are swept through their full range of motion. Observe that the collective duty uses a larger portion of its maximum $0.070 \leq \Delta_c \leq 0.140$ range than does Δ_r. As expected the roll stick neutral position $\delta_r = 0$ provides a duty of $\Delta_r \approx 0.105$ corresponding to neutral servo output. We identify $m_c < 0$ and $m_r < 0$ from the plots due to the mechanical linkage setup between servo output wheel and swashplate.

The Δ_e duty cycle input to the engine throttle servo can be stored as a look-up table as discussed in Section 5.3.4, and is not required if an engine governor is installed. Finally Δ_g, the duty cycle input to the gyro sensitivity channel is typically

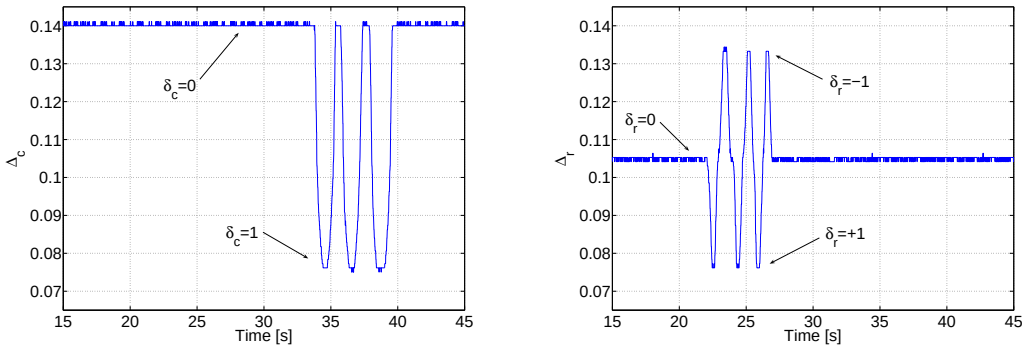

Figure 5.22: Duty Cycles Δ_c, Δ_r for collective and roll stick sweeps

set to $\Delta_g = 0.105$ in order to disable the tail gyro for autonomous control purposes, as discussed in Section 5.3.3.2. Remark the maps (5.57) do not apply to a CCPM (Cyclic/Collective Pitch Mixing) setup where the collective, roll and pitch pilot stick each control more than one servo simultaneously, however this is a moot point since the Bergen Industrial Twin does not employ a CCPM setup.

The servos do not move instantaneously. The ANCL helicopter employs JR-DS8311 digital servos. A comprehensive identification study [73] proposes to model these as a combination of a rate limit of $274°/\text{s} = 4.782$ rad/s together with a PT_4-Block transfer function

$$G(s) = \frac{1}{(1 + 0.0093s)^4}$$

where 0.0093 s is the identified time constant when the system is inside its rate limits. Since the servo time constant is on the order of the main rotor regressing flapping time constant calculated in Section 5.3.1.4, and the latter dynamics were approximated as being instantaneous, the servo dynamics can be neglected as well. By observation of a human pilot the stick movements required for hover and smooth flight are small in amplitude and gradual, meaning the servo rate limits are also a negligible effect for our system.

5.3.6 Fuselage Drag

The fuselage generates a drag force on the helicopter due to velocity drag plus deflection of the downwash from the main rotor. As in Section 5.3.1.2 the drag force F_D on a three-dimensional object in airflow is

$$F_D = \frac{1}{2}\rho U^2 C_D A$$

where ρ is the air density, U is the magnitude of airflow velocity, A is the cross-sectional area exposed to the flow, and C_D is the coefficient of drag, which is a function of the object's geometry but can be assumed constant with U for subsonic flow. The typical order of magnitude of the drag coefficient for non-streamlined bodies is $C_D \approx 1$ as compared with $C_D \approx 0.01$ for blade airfoils.

In forward or sideways flight, the main rotor downwash is deflected by the fuselage, creating a drag force along the x_b and y_b axes additional to the velocity-induced

drag force. To model this effect we adapt the drag model from [59, p. 47]:

$$\begin{aligned} U &= \sqrt{u^2 + v^2 + (w - v_i)^2} \\ X_{fus} &= -\frac{1}{2}\rho A_x C_{D,fus}\, u|U| \\ Y_{fus} &= -\frac{1}{2}\rho A_y C_{D,fus}\, v|U| \\ Z_{fus} &= -\frac{1}{2}\rho A_z C_{D,fus}\, (w - v_i)|U| \end{aligned}$$

where A_x, A_y, A_z are the cross-sectional areas of the helicopter normal to the body-fixed axes and $C_{D,fus}$ is the (constant) coefficient of drag. We model the helicopter as a box with vertices parallel to the body-fixed axes and enclosing the helicopter body forward of the tail boom, for which $C_{D,fus} = 1.05$ [104, p. 612] and A_x, A_y and A_z are the measured areas of the box faces. We neglect the generation of moments by the fuselage since its centre of pressure is close to the CM of the helicopter.

In hover with $u = v = w = 0$ we have $U^h = v_i^h$ and $Z_{fus}^h = (1/2)\rho A_z C_{D,fus}\, (v_i^h)^2$ where by (5.38) $v_i^h = \sqrt{T_{mr}^h/(2\rho\pi R^2)}$. Substituting the latter into the former and using the parameters in Section 5.5 we compute

$$Z_{fus}^h = \left(\frac{A_z C_{D,fus}}{4\pi R^2}\right) T_{mr}^h = 0.019\, T_{mr}^h$$

i.e. $Z_{fus}^h \ll T_{mr}^h$ and thus fuselage drag can be omitted from the hover model.

5.3.7 Tail Stabilizers

Horizontal and vertical stabilizer fins mounted on the tail of the helicopter increase forward flight stability by providing restoring moments in the pitch and yaw axes, respectively. For aerodynamic analysis the stabilizers are modeled as thin plates whose surface areas A_{hs} and A_{vs} can be directly measured.

Just like a symmetric airfoil, a thin plate in axial flow generates a lift force L_p proportional to its angle of attack α [13, p. 328] such that (c.f. Section 5.3.1.2)

$$L_p = \frac{1}{2}\rho U^2 a_p \alpha A_p,$$

where $U^2 = U_T^2 + U_P^2$ is the (squared) flow velocity, A_p is the surface area of the plate and a_p is the slope of the lift curve, where for a thin airfoil or plate this value can be computed analytically [13, Sec. 4.7] to be $a_p = 2\pi$. Based on experimental testing of thin plates in subsonic flow [106, p. 76], maximum lift is achieved at approximately $\alpha \approx 9°$ then gradually decreases until stall at $\alpha \approx 15°$ although the change of slope of C_L versus α is gentle around $C_{L,max}$. Unlike the main rotor blades in Section 5.3.1.2 where $U_T \gg U_P$ essentially guarantees the blades remain in the pre-stall region, tail fin stall is common and must be modeled [65, p. 17]. We proceed as follows: $\alpha = \arctan(U_P/U_T) \approx U_P/U_T$ in the pre-stall region and lift force is

$$L_p = \frac{1}{2}\rho(U_T^2 + U_P^2) a_p \frac{U_P}{U_T} A_p = \frac{1}{2}\rho A_p \left(a_p U_T U_P + U_P^2 a_p \frac{U_P}{U_T}\right).$$

The U_T denominator term would create numerical issues in low-speed forward flight. We revert to $U_P/U_T = \alpha$ and thus $a_p U_P/U_T = C_{L,p}$, the coefficient of lift of a thin plate. Based on experimental data for a thin plate in subsonic flow [106, p. 79] $C_{L,p} \approx 1$ for $5^\circ \leq \alpha \leq 15^\circ$, while for $\alpha < 5^\circ$ we have $U_P \ll 1 \implies U_P^2 \approx 0$ which cancels out the term using the (now incorrect) $C_{L,p} \approx 1$ assumption[8]. We therefore approximate pre-stall tail stabilizer fin lift as

$$L_p \approx \frac{1}{2}\rho A_p \left(a_p U_T U_P + U_P^2\right) \tag{5.58}$$

which agrees with [59, p. 47] where it is provided without explanation. Post-stall lift is calculated using the Bernoulli Equation which holds since the fluid acts incompressible (Mach number < 0.3). The dynamic pressure at each tail fin is $(1/2)\rho U^2$ and so the maximum lift force is

$$|L_p^{max}| = \frac{1}{2}\rho(U_T^2 + U_P^2)A_p \tag{5.59}$$

The tail stabilizer lift force L_p is calculated using (5.58) and saturated to (5.59) if $|L_p| > |L_p^{max}|$ as suggested by [65, p. 21] and [59, p. 48]. We neglect drag contributions as being accounted for by the fuselage model in Section 5.3.6.

5.3.7.1 Tail Stabilizer Force and Moment Contributions

As shown in Figure 5.23, the horizontal stabilizer is exposed to the main rotor inflow velocity v_i while the vertical is exposed to $v_{i,t}$. Denote the longitudinal distance and height of each stabilizer's geometric centre w.r.t. the CM as (d_{hs}, h_{hs}) and (d_{vs}, h_{vs}), respectively, which are measured directly c.f. Figure 5.3 in Section 5.2. The surface areas of the stabilizers are denoted A_{hs}, A_{vs} and were calculated by removing the fins, tracing their shapes on paper and manually computing the surface area. The numerical values are listed in Section 5.5.

Figure 5.23: Tail zoom-in; note main blades overhang horizontal stabilizer

Using Figure 5.20 in Section 5.3.3 with $(d_{tr}, h_{tr}) \mapsto (d_{hs}, h_{hs})$, the horizontal stabilizer is exposed to tangential and perpendicular flow components

$$U_T^{hs} = \sqrt{u^2 + v^2 + (p\, h_{hs})^2 + (r\, d_{hs})^2}$$
$$U_P^{hs} = v_i - w - q\, d_{hs}$$

[8] Remark $U_T \gg U_P$ would invalidate this argument, however this is a moot point since for the tail stabilizers $U_T \approx U_P$ from an order-of-magnitude point of view.

which by (5.58) give the vertical force

$$F_{hs} = \frac{1}{2}\rho A_{hs}\Big(a_p U_P^{hs}|U_T^{hs}| + U_P^{hs}|U_P^{hs}|\Big)$$

with $F_{hs} > 0$ denoting a downwards force as shown in Figure 5.1. The force and moment contribution to the rigid-body dynamics (5.11) is

$$\begin{aligned} X_{hs} &= 0 \\ Y_{hs} &= 0 \\ Z_{hs} &= F_{hs} \\ L_{hs} &= 0 \\ M_{hs} &= d_{hs} F_{hs} \\ N_{hs} &= 0 \end{aligned}$$

In hover $U_T^{hs,h} = 0$, $U_P^{hs,h} = v_i^h$ and so $F_{hs}^h = (1/2)\rho A_{hs}(v_i^h)^2$. From (5.38) $v_i^h = \sqrt{T_{mr}^h/(2\rho\pi R^2)}$ and so

$$F_{hs}^h = \frac{A_{hs}}{4\pi R^2} T_{mr}^h = 0.0015\, T_{mr}^h$$

where we used numerical parameters from Section 5.5; we see $F_{hs}^h \ll T_{mr}^h$ and can be neglected.

Now using Figure 5.20 with $(d_{tr}, h_{tr}) \mapsto (d_{vs}, h_{vs})$ the vertical stabilizer is exposed to the flow components

$$\begin{aligned} U_T^{vs} &= \sqrt{u^2 + w^2 + (d_{vs} q)^2} \\ U_P^{vs} &= v + v_{i,t} + h_{vs} p - d_{vs} r \end{aligned}$$

which by (5.58) give the horizontal force

$$F_{vs} = \frac{1}{2}\rho A_{vs}\Big(a_p U_P^{vs}|U_T^{vs}| + U_P^{vs}|U_P^{vs}|\Big)$$

and $F_{vs} > 0$ denotes a force in the $-y_b$ direction as shown in Figure 5.1. The contribution of F_{vs} to (5.11) is

$$\begin{aligned} X_{vs} &= 0 \\ Y_{vs} &= -F_{vs} \\ Z_{vs} &= 0 \\ L_{vs} &= -h_{vs} F_{vs} \\ M_{vs} &= 0 \\ N_{vs} &= d_{vs} F_{vs} \end{aligned}$$

In hover $U_T^{vs,h} = 0$ and $U_P^{vs,h} = v_{i,t}^h \implies F_{vs}^h = (1/2)\rho A_{vs} v_{i,t}^h |v_{i,t}^h|$. Using (5.54) $v_{i,t}^h = \sqrt{T_{tr}^h/(2\rho\pi R_t^2)}$ we have

$$F_{vs}^h = \frac{A_{vs}}{4\pi R_t^2} T_{tr}^h = 0.048\, T_{tr}^h$$

using the parameters in Section 5.5. Since F_{vs}^h is less than 5% of T_{tr}^h we take $F_{vs}^h \approx 0$, although this approximation is weaker than $F_{hs}^h \approx 0$ above.

5.4 Dynamics Model Summary

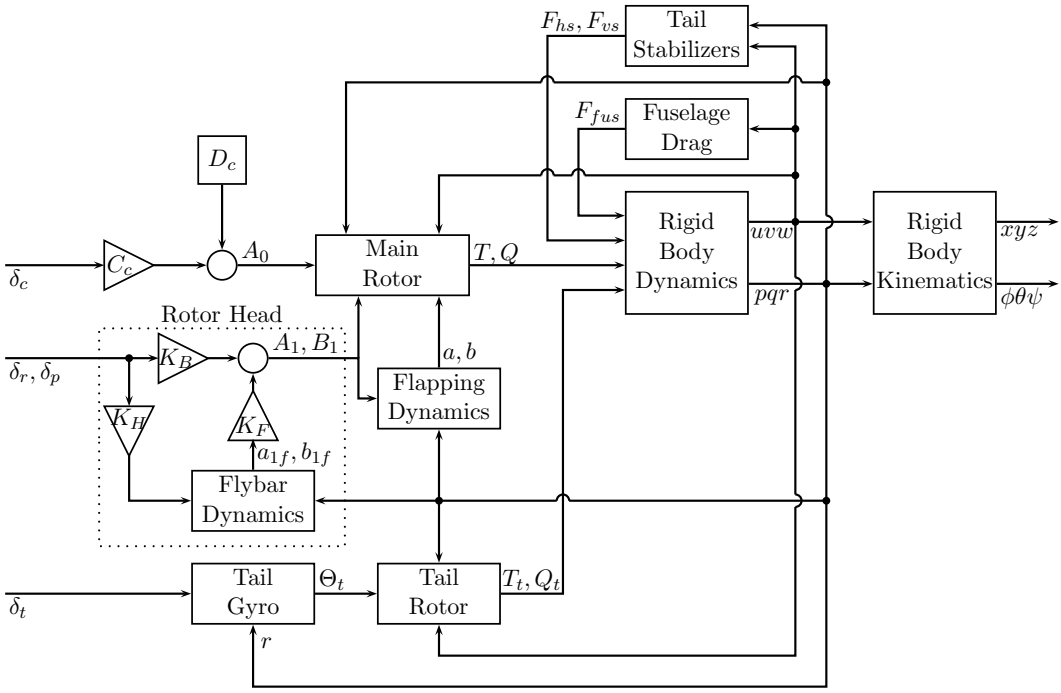

Figure 5.24: Topology of helicopter dynamics model

The general (non-hover) helicopter dynamics model is shown as a block diagram in Figure 5.24. The inputs to the system are $u = [\delta_c \quad \delta_r \quad \delta_p \quad \delta_t]^T$. We have

- Collective input $\delta_c \in [0, 1]$ where $\delta_c = 0$ and $\delta_c = 1$ are respectively collective stick down, swashplate vertically down and collective stick up, swashplate vertically up.

- Roll and pitch inputs $\delta_r, \delta_p \in [-1, 1]$ with $\delta_{r,p} = 0$ for centered sticks and swashplate level in the roll and pitch axes, respectively. The endpoints $\delta_{r,p} = -1$ represent roll stick fully left, pitch stick fully up and maximal swashplate tilt in negative roll, negative pitch axes directions, respectively. Conversely $\delta_{r,p} = 1$ represent roll stick fully right, pitch stick fully down and maximal swashplate tilt along the positive roll and pitch axes.

- Tail input δ_t with $\delta_t = 0$ representing centered tail stick and zero tail pitch Θ_t, while $\delta_t = -1$ and $\delta_t = 1$ represent respectively full left and full right on the tail stick, positive and negative yaw angular velocities $r > 0$, $r < 0$ and $\Theta_t < 0$ and $\Theta_t > 0$ by sign convention in Section 5.3.3.

The δ inputs are converted to servo commands using (5.57). We take main rotor speed Ω as constant as discussed in Section 5.3.4 and neglect servo dynamics based on Section 5.3.5.

5.4.1 Hover Model

The model is made up of the flybar dynamics (5.51)

$$\tau_f \dot{a}_{1f} + a_{1f} = -\tau_f q + K_H \delta_p$$
$$\tau_f \dot{b}_{1f} + b_{1f} = -\tau_f p + K_H \delta_r$$

with flybar time constant

$$\tau_f := \frac{16}{\gamma_f \Omega} = \frac{16 J_{\beta_f}}{\rho a_f c_f R_f^4 (1 - \varepsilon_f^4)\Omega} \tag{5.60}$$

The main rotor cyclic amplitudes (5.44)

$$A_1 = K_B \delta_r + K_F b_{1f}$$
$$B_1 = K_B \delta_p + K_F a_{1f}$$

The main rotor flapping angles (5.36)

$$a_1 = B_1$$
$$b_1 = A_1$$

The main rotor collective pitch amplitude (5.41)

$$A_0 = C_c \delta_c + D_c$$

The main rotor thrust and counter-torque (5.39), (5.40)

$$T_{mr}^h = C_{mr}^T A_0 + \frac{(D_{mr}^T)^2}{2} - D_{mr}^T \sqrt{C_{mr}^T A_0 + \frac{(D_{mr}^T)^2}{4}}$$
$$Q_{mr}^h = C_{mr}^Q \left(T_{mr}^h\right)^{3/2} + D_{mr}^Q$$

with constants

$$C_{mr}^T = \frac{\rho a c R^3 N_b \Omega^2}{6} \qquad D_{mr}^T = \frac{a c R N_b \Omega \sqrt{\rho}}{4\sqrt{2\pi}}$$
$$C_{mr}^Q = \frac{1}{R\Omega\sqrt{2\rho\pi}} \qquad D_{mr}^Q = \frac{\rho c R^4 N_b \Omega^2 C_D}{8} \tag{5.61}$$

The tail rotor pitch with tail gyro turned off for control purposes (option 2 in Section 5.3.3.2)

$$\Theta_t = C_t \delta_t + D_t$$

And the tail rotor thrust and counter-torque (5.55), (5.56)

$$T_{tr}^h = C_{tr}^T \Theta_t + \frac{(D_{tr}^T)^2}{2} - D_{tr}^T \sqrt{C_{tr}^T \Theta_t + \frac{(D_{tr}^T)^2}{4}}$$
$$Q_{tr}^h = C_{tr}^Q \left(T_{tr}^h\right)^{3/2} + D_{tr}^Q$$

with

$$
\begin{aligned}
C_{tr}^{T} &= \frac{\rho a_t c_t R_t^3 N_{bt} (K_t \Omega)^2}{6} & D_{tr}^{T} &= \frac{a c_t R_t N_{bt} K_t \Omega \sqrt{\rho}}{4\sqrt{2\pi}} \\
C_{tr}^{Q} &= \frac{1}{R_t K_t \Omega \sqrt{2\rho\pi}} & D_{tr}^{Q} &= \frac{\rho c_t R_t^4 N_{bt} C_{D,t} (K_t \Omega)^2}{8}
\end{aligned}
\tag{5.62}
$$

At hover the fuselage (Section 5.3.6) and tail stabilizers (Section 5.3.7) can be neglected. The force and moment contributions to the helicopter dynamics come from main rotor and tail rotor with components (c.f. Sections 5.3.1.6 and 5.3.3.1)

$$
\begin{aligned}
X^h &= -T_{mr}^h a_1 \\
Y^h &= T_{mr}^h b_1 + T_{tr}^h \\
Z^h &= -T_{mr}^h \\
L^h &= h_{mr} T_{mr}^h b_1 + k_\beta b_1 + h_{tr} T_{tr}^h \\
M^h &= h_{mr} T_{mr}^h a_1 + k_\beta a_1 - Q_{tr}^h \\
N^h &= -Q_{mr}^h - d_{tr} T_{tr}^h
\end{aligned}
$$

which enter the rigid-body dynamics (5.11) where cross-coupling terms are neglected as small in hover,

$$
\begin{aligned}
\dot{u} &= R_{31} g + X^h / m \\
\dot{v} &= R_{32} g + Y^h / m \\
\dot{w} &= R_{33} g + Z^h / m \\
\dot{p} &= L^h / J_{xx} \\
\dot{q} &= M^h / J_{yy} \\
\dot{r} &= N^h / J_{zz}
\end{aligned}
$$

with rigid-body kinematics (5.12)

$$
\begin{aligned}
\dot{R} &= RS\left([p \quad q \quad r]^T\right) \\
\dot{p}^n &= R\,[u \quad v \quad w]^T
\end{aligned}
$$

where $p^n = [p_N \quad p_E \quad p_D]^T$ is the position vector in the navigation frame. The above equations can be summarized in a single $\dot{x} = f(x, u)$ expression as

$$
\begin{aligned}
T^h_{mr} &:= C^T_{mr}(C_c\delta_c + D_c) + \frac{(D^T_{mr})^2}{2} - D^T_{mr}\sqrt{C^T_{mr}(C_c\delta_c + D_c) + \frac{(D^T_{mr})^2}{4}} \\
T^h_{tr} &:= C^T_{tr}(C_t\delta_t + D_t) + \frac{(D^T_{tr})^2}{2} - D^T_{tr}\sqrt{C^T_{tr}(C_t\delta_t + D_t) + \frac{(D^T_{tr})^2}{4}} \\
\dot{a}_{1f} &= -\frac{1}{\tau_f}a_{1f} - q + \frac{K_H}{\tau_f}\delta_p \\
\dot{b}_{1f} &= -\frac{1}{\tau_f}b_{1f} - p + \frac{K_H}{\tau_f}\delta_r \\
\dot{p} &= \frac{1}{J_{xx}}\left((h_{mr}T^h_{mr} + k_\beta)(K_B\delta_r + K_F b_{1f}) + h_{tr}T^h_{tr}\right) \\
\dot{q} &= \frac{1}{J_{yy}}\left((h_{mr}T^h_{mr} + k_\beta)(K_B\delta_p + K_F a_{1f}) - C^Q_{tr}\left(T^h_{tr}\right)^{3/2} - D^Q_{tr}\right) \\
\dot{r} &= \frac{1}{J_{zz}}\left(-C^Q_{mr}\left(T^h_{mr}\right)^{3/2} - D^Q_{mr} - d_{tr}T^h_{tr}\right) \\
\dot{R} &= RS\left([p \quad q \quad r]^T\right) \\
\dot{u} &= R_{31}g + \frac{1}{m}\left(-T^h_{mr}(K_B\delta_p + K_F a_{1f})\right) \\
\dot{v} &= R_{32}g + \frac{1}{m}\left(T^h_{mr}(K_B\delta_r + K_F b_{1f}) + T^h_{tr}\right) \\
\dot{w} &= R_{33}g + \frac{1}{m}\left(-T^h_{mr}\right) \\
\dot{p}^n &= R\,[u \quad v \quad w]^T
\end{aligned}
\tag{5.63}
$$

where the flybar time constant τ_f is provided in (5.60); the $C^{\{T,Q\}}_{mr}, D^{\{T,Q\}}_{mr}$ and $C^{\{T,Q\}}_{tr}, D^{\{T,Q\}}_{tr}$ parameter groups are listed in (5.61) and (5.62), respectively. The model parameters and their identified numerical values are summarized in Section 5.5. Remark the hover dynamics (5.63) are linear except for the attitude dynamics $\dot{R} = RS(\omega)$. The flapping dynamics $\dot{a}_{1f}, \dot{b}_{1f}$ and angular velocity dynamics $\dot{p}, \dot{q}$ are interconnected, which models the coupled rotor/fuselage dynamics characteristic of helicopter UAV's [127, Chap. 15], [101, Chap. 5].

5.5 Identified Parameter Values

The various subsystem models given previously require a number of symbolic constants as well as coefficient groups. The symbols, their identified values and physical meaning are provided below, grouped chronologically by subsystem.

A set of identified values for a Bergen Industrial Twin UAV used by a different research group are provided in [21, App. B]. The identification details are not given and their helicopter is configured differently from ours, e.g. the larger R value indicates longer main rotor blades, which affects other main rotor parameters such as J_β and a. Nevertheless, the numbers provided indicate our identified values are correct from an order-of-magnitude point of view.

Rigid Body Model		
Symbol	Value	Description
m	13.765 kg	Total helicopter dry mass
J_{xx}	0.36 kg m^2	Helicopter x-axis mass moment of inertia
J_{yy}	1.48 kg m^2	Helicopter y-axis mass moment of inertia
J_{zz}	1.21 kg m^2	Helicopter z-axis mass moment of inertia
g	9.81 m/s^2	Acceleration due to gravity

Main Rotor		
Symbol	Value	Description
ρ	1.225 kg/m^3	Density of air
A	2.061 m^2	MR disc area $= \pi R^2$
R	0.810 m	Radius of MR disc
k_β	122 N m/rad	MR blade restoring spring constant
J_β	0.057 kg m^2	MR blade mass moment of inertia about β axis
M_β	0.105 kg m	MR blade first mass moment $= (1/2)(\rho_b R)R$
ρ_b	0.321 kg/m	Linear mass density of MR blade
Ω	55π rad/s	MR angular rotation rate = 1650 RPM
a	6.6	Lift curve slope of MR blade
c	0.066 m	MR blade chord length
C_D	0.016	Coefficient of drag of MR blades
γ	4.03	Lock number of MR blade $= \rho a c R^4 / J_\beta$
N_b	2	Number of blades in MR
h_{mr}	0.32 m	Height of MR hub above CM
K_e	90/13	Engine to main rotor gearing ratio

Rotor Head and Flybar		
Symbol	Value	Description
C_c	0.23 rad	Slope of $A_0 = C_c\delta_c + D_c$ map
D_c	-0.05 rad	Offset of $A_0 = C_c\delta_c + D_c$ map
K_H	0.28 rad	Hiller input ratio (Flybar cyclic pitch to δ_r or δ_p)
K_B	0.09 rad	Bell input ratio (MR cyclic pitch to δ_r or δ_p)
K_F	0.66	Flybar ratio (MR cyclic pitch to a_{1f} or b_{1f})
a_f	5	Lift curve slope of flybar paddle
c_f	0.050 m	Flybar paddle chord length
R_f	0.306 m	Radius of flybar rotor disc
ε_f	0.712	Fractional location of paddle on flybar
J_f	0.006 kg m^2	Flybar mass moment of inertia about β_f axis
J_{β_f}	0.003 kg m^2	Half-flybar mass moment of inertia $= J_f/2$
γ_f	0.67	Lock number of flybar $= \rho a_f c_f R_f^4 (1 - \varepsilon_f^4)/J_{\beta_f}$
τ_f	0.139 s	Flybar flapping time constant $= 16/(\gamma_f \Omega)$

Tail Rotor and Tail Gyro		
Symbol	Value	Description
K_t	70/15	Tail to main rotor gearing ratio
d_{tr}	1.06 m	Longitudinal distance of TR axis to CM
h_{tr}	0.12 m	Height of TR axis above CM
a_t	6.4	Lift curve slope of TR blade
c_t	0.0325 m	TR blade chord length
$C_{D,t}$	0.017	Coefficient of drag of TR blades
R_t	0.163 m	Radius of TR disc
N_{bt}	2	Number of blades in TR
C_t	-0.30 rad	Slope of $\Theta_t = C_t\delta_t + D_t$ map
D_t	-0.07 rad	Offset of $\Theta_t = C_t\delta_t + D_t$ map

Fuselage		
Symbol	Value	Description
A_x	0.125 m^2	Fuselage area normal to x axis
A_y	0.3 m^2	Fuselage area normal to y axis
A_z	0.15 m^2	Fuselage area normal to z axis
$C_{D,fus}$	1.05	Fuselage coefficient of drag

Tail Stabilizers		
Symbol	Value	Description
d_{hs}	0.79 m	Longitudinal distance of horizontal stabilizer to CM
h_{hs}	0.14 m	Height of horizontal stabilizer above CM
d_{vs}	0.99 m	Longitudinal distance of vertical stabilizer to CM
h_{vs}	0.11 m	Height of vertical stabilizer above CM
A_{hs}	0.0120 m^2	Surface area of horizontal stabilizer
A_{vs}	0.0161 m^2	Surface area of vertical stabilizer
a_p	6.3	Lift curve slope of thin plate (tail fins)

Servo Commands		
Symbol	Value	Description
m_c	-0.064	Slope of $\Delta_c = m_c\delta_c + b_c$ map
b_c	0.140	Offset of $\Delta_c = m_c\delta_c + b_c$ map
m_r	-0.028	Slope of $\Delta_r = m_r\delta_r + b_r$ map
b_r	0.104	Offset of $\Delta_r = m_r\delta_r + b_r$ map
m_p	0.020	Slope of $\Delta_p = m_p\delta_p + b_p$ map
b_p	0.103	Offset of $\Delta_p = m_p\delta_p + b_p$ map
m_t	-0.014	Slope of $\Delta_t = m_t\delta_t + b_t$ map
b_t	0.105	Offset of $\Delta_t = m_t\delta_t + b_t$ map

Chapter 6

Conclusions

6.1 Review of Results

The research goals listed in Section 1.1.1 have been successfully achieved. We focus on the results of the three research topics proposed in the Ph.D. Candidacy Report [14] preceding this thesis, namely magnetometer integration into an Aided INS, development of an invariant observer as an alternative to the EKF, and obtaining an identified model of the Bergen Industrial Twin helicopter UAV.

6.1.1 Magnetometer Integration

The novel magnetometer calibration technique in [54] was summarized in Section 2.9 including numerical values of parameters identified from engine-off and engine-on tests of our vehicle. Its integration into the AHRS and Aided INS designs was explained in Section 3.2.2 as part of sensor signal and noise modeling. Finally its importance to overall system performance was experimentally assessed in Section 3.4.2 for engine-off ground tests and in Section 3.4.3 for engine-on flight tests.

The experimental results have validated this technique and demonstrated an improvement in performance over the conventional method known as hard-iron calibration. The deficiencies of the former GPS-only Aided INS design were explained and resolved by the addition of the magnetometer. The importance of magnetometer calibration to the performance of an Aided INS is an important lesson for any experimentally-validated work: consider [59, p. 21] who simply discarded measurements from the on-board magnetometer to get better heading accuracy. The same author pointed out [59, pp. 26–28] the inadequacy of this solution for non-aggressive flight such as prolonged hover, as well as the necessity of calibration. In [88, Sec. V-A] the authors suggest reducing the weighing of the magnetometer w.r.t. the accelerometer due to magnetic field distortions created by the vehicle's motor. In flight experiments [88, Sec. VI] of a tail-sitter UAV, the magnetometer readings are turned off completely and the yaw angle is not estimated.

6.1.2 Invariant Observers

The method of invariant observers was treated throughout Chapter 4. The theoretical foundations of the method were studied in-depth, including its relationship to earlier work on symmetries in systems under state feedback, as well as the three

types of symmetries (body-frame, ground-frame and combined) found in the AHRS and Aided INS examples. Invariant observers were then constructed for each symmetry type in both examples, using the rotation matrix representation of the $SO(3)$ manifold instead of unit quaternions as done in previously published work. The choice of rotation matrices over unit quaternions has profound implications for the validity of global stability analysis of the resulting observers [78, 20, 38]; indeed the nonlinear design for AHRS observer gains in Section 4.8 guaranteeing almost-global asymptotic stability is only possible because the system is written in terms of rotation matrices.

Of course a nonlinear design of observer gains is non-systematic and was not found for the Aided INS case. Motivated by this fact we adapted the Invariant EKF method [23, 29] to our examples, developing an approach which does not require defining invariant noise terms and works for systems whose manifold M and symmetry group G are not necessarily the same, c.f. Section 4.9.1. The Invariant EKF provides a fully systematic approach to observer gain selection, and we performed the calculations for both the AHRS and Aided INS examples. The resulting nonlinear observers were then successfully validated in simulation as well as experiment. Comparing the nonlinear gain design versus the Invariant EKF for the AHRS, we saw the former is able to perform as well or better than the linearization-based Invariant EKF design, in addition to being dramatically less computationally expensive and amenable to global stability analysis. For this reason, a nonlinear design for the invariant Aided INS observer is of great interest for future research in this area. Early steps have recently been carried out in [31, 24].

6.1.3 Modeling and Identification

Chapter 5 contains a complete first-principles derivation of a nonlinear dynamics model for the helicopter UAV and the experimental identification of its parameters. As discussed in Section 1.1.1 such a model was required to bridge the gap between the variety of nonlinear approaches developed for helicopter UAV flight control and their actual implementation in experiment. This gap has been pointed out by other authors e.g. [59, p. 56] in reference to the work of [55]:

> For the simplified model used, the method was theoretically proved to provide tracking controllers for a wide class of trajectories, including aggressive trajectories involving extreme attitude angles. The mathematical model used for design and evaluation of this controller relied on a number of unrealistic assumptions: exact knowledge of the tail rotor torque and moments of inertia, and instantaneous application of precisely known control moments. While the design approach in its current state is probably not applicable to a real helicopter, the approach may potentially be modified to yield a practical control design method for tracking aerobatic trajectories.

The proposed model is composed of the 6 DoF rigid-body dynamics (5.11), equations of force and moment contributions of the main rotor, tail rotor, fuselage drag and tail stabilizers, plus dynamics of the main rotor and flybar flapping angles and maps from servo positions to the above subsystems. Using a combination of assumptions and experimentally identified parameter values, we simplified the model whenever

possible, e.g. neglecting the coning and advancing modes of the main rotor flapping dynamics in Section 5.3.1.4. The first-principles modeling approach gave insight into a number of issues which are poorly explained in the existing literature such as: the superiority of the torsional over the trifilar pendulum for mass moment of inertia testing, c.f. Section 5.2; a mathematical model of the Bell-Hiller stabilization action, c.f. Section 5.3.2.1; and the source of the rotor-fuselage coupling obtained in frequency-domain identification results, c.f. Section 5.4.1. The nonlinear model is summarized in Section 5.4 and its identified parameters in Section 5.5.

The general model is complicated by the induced velocity v_i and rotor thrust T forming a set of two transcendental equations in both the main rotor (Section 5.3.1.5) and tail rotor (Section 5.3.3), in addition to the symbolic complexity of the force and moment expressions. The model equations can be greatly simplified by specializing to the case of hover by taking the translational and rotational velocities as identically zero; furthermore, we are then able to analytically solve the coupled v_i and T equations. The result is provided as (5.63) in Section 5.4.1 and should be useful for a first version of model-based control design.

6.2 Future Work

Development and implementation of nonlinear model-based control is the next logical step in the ANCL UAV helicopter project. The research work presented in this thesis was carried out precisely for this purpose, and a number of nonlinear designs are already available in the literature e.g. the control references listed in Section 1.1.1. Based on first-hand experience of developing experimentally-validated designs, this work should be performed in incremental steps, beginning with non-model based (PID-type) control, moving to model-based hover stabilization using (5.63) in Section 5.4.1, and only then employing the complete nonlinear model. The value of the experience gained from the simpler designs cannot be overstated. In addition, the Sections below list specific research tasks which build directly on the work presented in this thesis.

6.2.1 Engine-on Noise Characteristics

The Aided INS engine-on flight experiments in Sections 3.4.3 and 4.11.3.2 required ad-hoc tuning of the filter parameters, in contrast to the engine-off experiments in Sections 3.4.2 and 4.11.3.1 which employed identified parameters from Section 3.2.2 without modification; the identified parameters were also used as-is by the AHRS design. To remedy this situation, more accurate sensor modeling is needed for the engine-on case, in particular choice of bias model and identification of its parameters. The Allan Variance method [12] employed by [75, Chap. 4] to obtain the parameters listed in Table 3.1 required logging approximately 14 hours of sensor data, which is impossible due to the fuel limit and overheating issues of the helicopter's engine. This time length may be reduced by either accepting a larger estimation error (set to 10% for the engine-off identification [75, p. 58]) or employing a different identification method.

6.2.2 Nonlinear Gain Design for Invariant Aided INS Observer

As discussed in Section 4.8, a nonlinear gain design for the invariant Aided INS observer remains an open problem. In the AHRS case such a design was found, and based on simulation and experimental testing in respectively Sections 4.10.2 and 4.10.3, it provides performance which is equivalent or superior to the Invariant EKF while requiring significantly less computational power. Such a design also enables a formal analysis of the region of attraction and the capability of finding gains which provide almost-global stability, making it interesting from a theoretical point of view. Of course such an analysis is non-systematic and an almost-global design may not exist, although proving this fact would be a significant theoretical contribution as well. References [31, 24] as well as [69, 118] listed in Section 4.8 may provide insight into the method of attack for this problem. Theorem 4 in Section 4.6.3 guarantees a reduced-order form of the invariant observer's estimation dynamics, which will simplify the analysis over the general case.

6.2.3 Experimental Testing of Nonlinear Model

The model developed in Chapter 5 requires experimental testing under flight conditions. As mentioned in Section 5.1 the model's nominal parameter values are expected to require adjustments in order to match the model's predictions with experimental data. The recommended approach is to obtain a log of experimental data consisting of pilot inputs and estimated helicopter states collected while the pilot executes a series of step inputs on each of the sticks — collective δ_c, roll δ_r, pitch δ_p and tail δ_t — returning to hover in-between each. From the hover model (5.63) the dynamics in each axis are decoupled from each other and the collected data could be used with a least-squares formulation to identify the C and D parameters (5.61), (5.62) whose reliance on aerodynamic parameters makes them the most sensitive to model uncertainty. For the forward flight regime, the fuselage drag parameters A_x, A_y, A_z in Section 5.3.6 and tail stabilizer parameters A_{hs}, A_{vs} should be experimentally tuned, ideally using wind-tunnel testing to directly measure the drag forces experienced by the helicopter. The resulting experimentally-tuned model would provide better performance of any model-based control. Of course closed-loop control provides robustness against model uncertainty, meaning that even a poorly-identified model should still achieve satisfactory performance in experimental autonomous flight.

Bibliography

[1] Department of Defense World Geodetic System 1984 - its definition and relationships with local geodetic systems. Technical Report 8350.2, Third Edition, Amendment 1, National Imagery and Mapping Agency, Bethesda, MD, January 2000.

[2] International Geomagnetic Reference Field: the eleventh generation. *Geophysical Journal International*, 183(3):1216–1230, December 2010.

[3] Pieter Abbeel. *Apprenticeship Learning and Reinforcement Learing with Application to Robotic Control*. PhD thesis, Stanford University, August 2008.

[4] Pieter Abbeel, Adam Coates, Timothy Hunter, and Andrew Y. Ng. Autonomous autorotation of an RC helicopter. In Oussama Khatib, Vijay Kumar, and George J. Pappas, editors, *The Eleventh International Symposium on Experimental Robotics*, volume 54 of *Springer Tracts in Advanced Robotics*, pages 385–394. Springer, 2009.

[5] Pieter Abbeel, Adam Coates, and Andrew Y. Ng. Autonomous helicopter aerobatics through apprenticeship learning. *The International Journal of Robotics Research*, 29(13):1608–1639, November 2010.

[6] Pieter Abbeel, Adam Coates, Morgan Quigley, and Andrew Y. Ng. An application of reinforcement learning to aerobatic helicopter flight. In Bernhard Schölkopf, John Platt, and Thomas Hofmann, editors, *Advances in Neural Information Processing Systems*, volume 19, pages 1–8. MIT Press, September 2007.

[7] Pieter Abbeel, Varun Ganapathi, and Andrew Y. Ng. Learning vehicular dynamics, with application to modeling helicopters. In Yair Weiss, Bernhard Schölkopf, and John Platt, editors, *Advances in Neural Information Processing Systems*, volume 18, pages 1–8. MIT Press, May 2006.

[8] Ira H. Abbott and Albert E. Von Doenhoff. *Theory of Wing Sections*. Dover Publications, 1958.

[9] Federal Aviation Administration. *Instrument Flying Handbook*. Oklahoma City, OK, 2008. FAA-H-8083-15A.

[10] Nasradine Aghannan and Pierre Rouchon. On invariant asymptotic observers. In *Proceedings of the 41st IEEE Conference on Decision and Control*, pages 1479–1484, Las Vegas, NV, December 2002.

[11] Nasradine Aghannan and Pierre Rouchon. An intrinsic observer for a class of lagrangian systems. *IEEE Transactions On Automatic Control*, 48(6):936–945, June 2003.

[12] David W. Allan. Statistics of atomic frequency standards. *Proceedings of the IEEE*, 54(2):221–230, February 1966.

[13] John D. Anderson, Jr. *Fundamentals of Aerodynamics*. McGraw–Hill, fourth edition, 2007.

[14] Martin Barczyk. Candidacy examination thesis status report. Ph.D. candidacy report, Department of ECE, University of Alberta, May 2009.

[15] Martin Barczyk, Michael Jost, David R. Kastelan, Alan F. Lynch, and Kim D. Listmann. An experimental validation of magnetometer integration into a GPS-aided helicopter UAV navigation system. In *Proceedings of the 2010 American Control Conference*, pages 4439–4444, Baltimore, MD, July 2010.

[16] Martin Barczyk and Alan F. Lynch. An attitude and heading reference system design for indoor UAV testing. In *Proceedings of the 23rd Canadian Congress of Applied Mechanics*, Vancouver, BC, June 2011.

[17] Martin Barczyk and Alan F. Lynch. Integration of a triaxial magnetometer into a helicopter UAV GPS-aided INS. *IEEE Transactions on Aerospace and Electronic Systems*, 2011. In press.

[18] Martin Barczyk and Alan F. Lynch. Invariant Extended Kalman Filter design for a magnetometer-plus-GPS aided inertial navigation system. In *Proceedings of the Joint 50th IEEE Conference on Decision and Control and European Control Conference*, pages 5389–5394, Orlando, FL, December 2011.

[19] Martin Barczyk and Alan F. Lynch. Invariant Extended Kalman Filter design for an attitude and heading reference system. *IEEE Transactions on Control Systems Technology*, June 2011. Submitted.

[20] Sanjay P. Bhat and Dennis S. Bernstein. A topological obstruction to continuous global stabilization of rotational motion and the unwinding phenomenon. *Systems & Control Letters*, 39(1):63–70, January 2000.

[21] Morten Bisgaard. *Modeling, Estimation, and Control of Helicopter Slung Load System*. PhD thesis, Aalborg University, November 2007.

[22] Morten Bisgaard and Anders la Cour-Harbo. *AAU HeliSim*. Aalborg University Autonomous Vehicles Group, Denmark, April 2009. `http://uavlab.org`.

[23] Silvère Bonnabel. Left-invariant extended Kalman filter and attitude estimation. In *Proceedings of the 46th IEEE Conference on Decision and Control*, pages 1027–1032, New Orleans, LA, December 2007.

[24] Silvère Bonnabel, Jean-Emmanuel Deschaud, and Erwan Salaün. A simple nonlinear filter for low-cost ground vehicle localization system. In *Proceedings of the Joint 50th IEEE Conference on Decision and Control and European Control Conference*, pages 3270–3275, Orlando, FL, December 2011.

[25] Silvère Bonnabel, Philippe Martin, and Pierre Rouchon. A non-linear symmetry-preserving observer for velocity-aided intertial navigation. In *Proceedings of the 2006 American Control Conference*, pages 2910–2914, Minneapolis, MN, June 2006.

[26] Silvère Bonnabel, Philippe Martin, and Pierre Rouchon. Non-linear observer on Lie groups for left-invariant dynamics with right-left equivariant output. In *Proceedings of the IFAC 17th World Congress*, pages 8594–8598, Seoul, Korea, July 2008.

[27] Silvère Bonnabel, Philippe Martin, and Pierre Rouchon. Symmetry-preserving observers. *IEEE Transactions On Automatic Control*, 53(11):2514–2526, December 2008.

[28] Silvère Bonnabel, Philippe Martin, and Pierre Rouchon. Non-linear symmetry-preserving observers on Lie groups. *IEEE Transactions On Automatic Control*, 54(7):1709–1713, July 2009.

[29] Silvère Bonnabel, Philippe Martin, and Erwan Salaün. Invariant Extended Kalman Filter: theory and application to a velocity-aided attitude estimation problem. In *Proceedings of the Joint 48th IEEE Conference on Decision and Control and 28th Chinese Control Conference*, pages 1297–1304, Shanghai, P.R. China, December 2009.

[30] Silvère Bonnabel and Pierre Rouchon. On invariant observers. In Thomas Meurer, Knut Graichen, and Ernst Dieter Gilles, editors, *Control and Observer Design for Nonlinear Finite and Infinite Dimensional Systems*, volume 322 of *Lecture Notes in Control and Information Sciences*, pages 53–65. Springer, Berlin, 2005.

[31] Silvère Bonnabel and Erwan Salaün. Design and prototyping of a low-cost vehicle localization system with guaranteed convergence properties. *Control Engineering Practice*, 19(6):591–601, June 2011.

[32] B. R. Bowring. The accuracy of geodetic latitude and height equations. *Survey Review*, 28(218):202–206, October 1985.

[33] A.R.S. Bramwell, George Done, and David Balmford. *Bramwell's Helicopter Dynamics*. AIAA, second edition, 2001.

[34] Robert Grover Brown and Patrick Y.C. Hwang. *Introduction to Random Signals and Applied Kalman Filtering*. John Wiley & Sons, third edition, 1997.

[35] Richard L. Burden and J. Douglas Faires. *Numerical Analysis*. Brooks/Cole, sixth edition, 1997.

[36] Guowei Cai, Ben M. Chen, and Tong Heng Lee. *Unmanned Rotorcraft Systems*. Springer, 2011.

[37] Pedro Castillo, Rogelio Lozano, and Alejandro E. Dzul. *Modelling and Control of Mini-Flying Machines*. Springer, 2005.

[38] Nalin A. Chaturvedi, Amit K. Sanyal, and N. Harris McClamroch. Rigid-body attitude control: Using rotation matrices for continuous, singularity-free control laws. *IEEE Control Systems Magazine*, 31(3):30–51, June 2011.

[39] Chi-Tsong Chen. *Introduction to Linear System Theory*. Holt, Rinehart and Winston, Inc., 1970.

[40] Chi-Tsong Chen. *Linear System Theory and Design*. Oxford University Press, third edition, 1999.

[41] Robert T. N. Chen. A simplified rotor system mathematical model for piloted flight dynamics simulation. Technical Memorandum 78575, NASA, Ames Research Center, Moffett Field, CA, May 1979.

[42] Robert T. N. Chen. Effects of primary rotor parameters on flapping dynamics. Technical Paper 1431, NASA, Ames Research Center, Moffett Field, CA, January 1980.

[43] Robert T. N. Chen, J. Victor Lebacqz, Edwin W. Aiken, and Mark B Tischler. Helicopter mathematical models and control law development for handling qualities research. In *NASA/Army Rotorcraft Technology Conference*, volume 2: Materials and Structures, Propulsion and Drive Systems, Flight Dynamics and Control, and Acoustics, pages 837–899, Moffett Field, CA, March 1987.

[44] James R. Chiles. *The God Machine: From Boomerangs to Black Hawks, The Story of the Helicopter*. Bantam Books, 2007.

[45] Marco La Civita. *Integrated Modeling and Robust Control for Full-Envelope Flight of Robotic Helicopters*. PhD thesis, Carnegie Mellon University, December 2002.

[46] Marco La Civita, George Papageorgiou, William C. Messner, and Takeo Kanade. Design and flight testing of an $\mathcal{H}_\infty$ controller for a robotic helicopter. *Journal of Guidance, Control, and Dynamics*, 29(2):485–494, March-April 2006.

[47] Carsten Collon and Joachim Rudolph. Invariant tracking control design via integrator backstepping. *Proceedings in Applied Mathematics and Mechanics*, 10(1):603–604, December 2010.

[48] John L. Crassidis and John L. Junkins. *Optimal Estimation of Dynamic Systems*. Chapman & Hall/CRC, 2004.

[49] John L. Crassidis, F. Landis Markley, and Yang Cheng. Survey of nonlinear attitude estimation methods. *Journal Of Guidance, Control, And Dynamics*, 30(1):12–28, January-February 2007.

[50] Joerg S. Dittrich. Design and integration of an unmanned aerial vehicle navigation system. Master's thesis, Georgia Institute of Technology, May 2002.

[51] Jay A. Farrell. *Aided Navigation: GPS with High Rate Sensors*. McGraw Hill, 2008.

[52] Mark Fels and Peter J. Olver. Moving coframes: II. regularization and theoretical foundations. *Acta Applicandae Mathematicae*, 55(2):127–208, January 1999.

[53] Romeo Tatsambon Fomena and Nikos I. Vitzilaios. Determining moments of inertia of MiniTitan and Bergen helicopters using the trifilar pendulum method. Technical report, Applied Nonlinear Controls Lab, University of Alberta, October 2011.

[54] Christopher C. Foster and Gabriel Hugh Elkaim. Extension of a two-step calibration methodology to include nonorthogonal sensor axes. *IEEE Transactions On Aerospace And Electronic Systems*, 44(3):1070–1078, July 2008.

[55] Emilio Frazzoli. *Robust Hybrid Control for Autonomous Vehicle Motion Planning*. PhD thesis, Massachusetts Institute of Technology, June 2001.

[56] Emilio Frazzoli, Munther A. Dahleh, and Eric Feron. Trajectory tracking control design for autonomous helicopters using a backstepping algorithm. In *Proceedings of the 2000 American Control Conference*, pages 4102–4107, Chicago, IL, June 2000.

[57] Emilio Frazzoli, Munther A. Dahleh, and Eric Feron. Maneuver-based motion planning for nonlinear systems with symmetries. *IEEE Transactions on Robotics*, 21(6):1077–1091, December 2005.

[58] Futaba Corporation, Chiba, Japan. *GY401 AVCS Rate Gyro Instruction Manual*, July 2000.

[59] Vladislav Gavrilets. *Autonomous Aerobatic Maneuvering of Miniature Helicopters*. PhD thesis, Massachusetts Institute of Technology, May 2003.

[60] Vladislav Gavrilets, Bernard Mettler, and Eric Feron. Nonlinear model for a small-size acrobatic helicopter. In *AIAA Guidance, Navigation and Control Conference and Exhibit*, Montreal, QC, August 2001. AIAA 2001-4333.

[61] Alfred Gessow and Garry C. Myers, Jr. *Aerodynamics of the Helicopter*. Macmillan Company, 1952.

[62] Hermann Glauert. A general theory of the autogyro. Reports and Memoranda 1111, Aeronautical Research Committee, November 1926.

[63] Jessy W. Grizzle and Steven I. Marcus. The structure of nonlinear control systems possessing symmetries. *IEEE Transactions On Automatic Control*, 30(3):248–258, March 1985.

[64] Denis Guillaume and Pierre Rouchon. Observation and control of a simplified car. In *IFAC International Workshop on Motion Control*, pages 63–67, Grenoble, France, September 1998.

[65] Robert K. Heffley and Marc A. Mnich. Minimum-complexity helicopter simulation math model. NASA Contractor Report 177476, Ames Research Center, Moffett Field, CA, April 1988.

[66] Gabriel M. Hoffmann, Haomiao Huang, Steven L. Waslander, and Claire J. Tomlin. Precision flight control for a multi-vehicle quadrotor helicopter testbed. *Control Engineering Practice*, 19(9):1023–1036, September 2011.

[67] Roger A. Horn and Charles R. Johnson. *Matrix analysis*. Cambridge University Press, 1985.

[68] Jonathan P. How, Brett Bethke, Adrian Frank, Daniel Dale, and John Vian. Real-time indoor autonomous vehicle test environment. *IEEE Control Systems Magazine*, 28(2):51–64, April 2008.

[69] Minh-Duc Hua. Attitude estimation for accelerated vehicles using GPS/INS measurements. *Control Engineering Practice*, 18(7):723–732, July 2010.

[70] Daniel J. Inman. *Engineering Vibration*. Prentice–Hall, second edition, 2001.

[71] Alberto Isidori, Lorenzo Marconi, and Andrea Serrani. Robust nonlinear motion control of a helicopter. *IEEE Transactions On Automatic Control*, 48(3):413–426, March 2003.

[72] Wayne Johnson. *Helicopter Theory*. Dover Publications, 1980.

[73] Michael Jost. Regelung eines Modellhelikopters. Studienarbeit, Technische Universität Darmstadt, June 2009.

[74] Aaron D. Kahn. The design and development of a modular avionics system. Master's thesis, Georgia Institute of Technology, April 2001.

[75] David R. Kastelan. Design and implementation of a GPS-aided inertial navigation system for a helicopter UAV. Master's thesis, University of Alberta, 2009.

[76] Sung K. Kim. *Modeling, Identification, and Trajectory Planning for a Model-Scale helicopter*. PhD thesis, University of Michigan, 2001.

[77] Knife Edge Software, Corvallis, OR. *RealFlight R/C Flight Simulator G3.5*, 2006.

[78] Daniel E. Koditschek. Application of a new lyapunov function to global adaptive attitude tracking. In *Proceedings of the 27th IEEE Conference on Decision and Control*, pages 63–68, Austin, TX, December 1988.

[79] T. John Koo and Shankar Sastry. Output tracking control design of a helicopter model based on approximate linearization. In *Proceedings of the 37th IEEE Conference on Decision and Control*, pages 3635–3640, Tampa, FL, December 1998.

[80] T. John Koo and Shankar Sastry. Differential flatness based full authority helicopter control design. In *Proceedings of the 38th IEEE Conference on Decision and Control*, pages 1982–1987, Phoenix, AZ, December 1999.

[81] Marco La Civita, William Messner, and Takeo Kanade. Modeling of small-scale helicopters with integrated first-principles and system-identification techniques. In *Proceedings of the 58th Forum of the American Helicopter Society*, pages 2505–2516, Montreal, QC, June 2002.

[82] B.P. Lathi. *Signal Processing and Linear Systems*. Oxford University Press, 1998.

[83] John M. Lee. *Smooth Manifolds*, volume 218 of *Graduate Texts in Mathematics*. Springer, 2003.

[84] Eugene J. Lefferts, F. Landis Markley, and Malcolm D. Shuster. Kalman filtering for spacecraft attitude estimation. *Journal of Guidance*, 5(5):417–429, Sep-Oct 1982.

[85] Alan F. Lynch. Inspection system for electrical transmission lines using an unmanned aerial vehicle (UAV). NSERC Strategic Project Grant, April 2010.

[86] Robert Mahony and Tarek Hamel. Robust trajectory tracking for a scale model autonomous helicopter. *International Journal of Robust and Nonlinear Control*, 14(12):1035–1059, August 2004.

[87] Robert Mahony, Tarek Hamel, and Alejandro E. Dzul. Hover control via Lyapunov control for an autonomous model helicopter. In *Proceedings of the 38th IEEE Conference on Decision and Control*, pages 3490–3495, Phoenix, AZ, December 1999.

[88] Robert Mahony, Tarek Hamel, and Jean-Michel Pflimlin. Nonlinear complementary filters on the special orthogonal group. *IEEE Transactions On Automatic Control*, 53(5):1203–1218, June 2008.

[89] Lorenzo Marconi and Roberto Naldi. Robust full degree-of-freedom tracking control of a helicopter. *Automatica*, 43(11):1909–1920, November 2007.

[90] Philippe Martin, Pierre Rouchon, and Joachim Rudolph. Invariant tracking. *ESAIM: Control, Optimisation and Calculus of Variations*, 10(1):1–13, January 2004.

[91] Philippe Martin and Erwan Salaün. Invariant observers for attitude and heading estimation from low-cost inertial and magnetic sensors. In *Proceedings of the 46th IEEE Conference on Decision and Control*, pages 1039–1045, New Orleans, LA, December 2007.

[92] Philippe Martin and Erwan Salaün. Design and implementation of a low-cost aided attitude and heading reference system. In *AIAA Guidance, Navigation and Control Conference and Exhibit*, Honolulu, HI, August 2008. AIAA 2008-7169.

[93] Philippe Martin and Erwan Salaün. A general symmetry-preserving observer for aided attitude heading reference systems. In *Proceedings of the 47th IEEE Conference on Decision and Control*, pages 2294–2301, Cancun, Mexico, December 2008.

[94] Philippe Martin and Erwan Salaün. An embedded attitude and heading reference system based on a nonlinear filter. In Juan Andrade-Cetto, Jean-Louis Ferrier, and Joaquim Filipe, editors, *Informatics in Control, Automation and Robotics*, volume 37 of *Lecture Notes in Electrical Engineering*, pages 267–281. Springer, 2009.

[95] Philippe Martin and Erwan Salaün. Design and implementation of a low-cost observer-based attitude and heading reference system. *Control Engineering Practice*, 18(7):712–722, July 2010.

[96] Philippe Martin and Erwan Salaün. Generalized Multiplicative Extended Kalman Filter for aided attitude and heading reference system. In *AIAA Guidance, Navigation, and Control Conference*, Toronto, Canada, August 2010. AIAA 2010-8300.

[97] Leonard A. McGee and Stanley F. Schmidt. Discovery of the Kalman Filter as a practical tool for aerospace and industry. NASA Technical Memorandum 86847, Ames Research Center, Moffett Field, CA, November 1985.

[98] Susan McLean, Susan Macmillan, Stefan Maus, Vincent Lesur, David Dater, and Alan Thomson. The US/UK world magnetic model for 2005–2010. Technical Report NESDIS/NGDC-1, NOAA National Geophysical Data Center, Boulder, CO, December 2004.

[99] James L. Meriam. *Dynamics*. John Wiley & Sons, second edition, 1971.

[100] James L. Meriam and L. Glenn Kraige. *Engineering Mechanics: Dynamics*. John Wiley & Sons, fourth edition, 1998.

[101] Bernard Mettler. *Identification Modeling and Characteristics of Miniature Rotorcraft*. Kluwer Academic Publishers, 2003.

[102] Nathan Michael, Daniel Mellinger, Quentin Lindsey, and Vijay Kumar. The GRASP multiple micro-UAV test bed. *IEEE Robotics & Automation Magazine*, 17(3):56–65, September 2010.

[103] Pablo Monzón. On necessary conditions for almost global stability. *IEEE Transactions On Automatic Control*, 48(4):631–634, April 2003.

[104] Bruce R. Munson, Donald F. Young, and Theodore H. Okiishi. *Fundamentals of Fluid Mechanics*. John Wiley & Sons, third edition, 1998.

[105] Richard M. Murray, Zexiang Li, and S. Shankar Sastry. *A Mathematical Introduction to Robotic Manipulation*. CRC Press, 1994.

[106] Yasuki Nakayama, editor. *Visualized flow: fluid motion in basic and engineering situations*. Pergamon Press, 1988.

[107] Henk Nijmeijer and Arjan van der Schaft. *Nonlinear Dynamical Control Systems*. Springer, 1990.

[108] NovAtel Inc. *OEM4 Family of Receivers - Command and Log Reference Manual*, June 2005.

[109] Katsuhiko Ogata. *Modern Control Engineering*. Prentice–Hall, fourth edition, 2002.

[110] Peter J. Olver. *Applications of Lie Groups to Differential Equations*, volume 107 of *Graduate Texts in Mathematics*. Springer, second edition, 1993.

[111] Peter J. Olver. *Equivalence, Invariants, and Symmetry*. Cambridge University Press, 1995.

[112] Peter J. Olver. *Classical Invariant Theory*, volume 44 of *London Mathematical Society Student Texts*. Cambridge University Press, 1999.

[113] Gareth D. Padfield. *Helicopter Flight Dynamics: The Theory and Application of Flying Qualities and Simulation Modeling*. Blackwell Science, 1996.

[114] Allan G. Piersol and Thomas L. Paez, editors. *Harris' Shock and Vibration Handbook*. McGraw-Hill, sixth edition, 2010.

[115] Raymond W. Prouty. *Helicopter Performance, Stability and Control*. Krieger Publishing Company, 1986.

[116] Ioannis A. Raptis and Kimon P. Valavanis. *Linear and Nonlinear Control of Small-Scale Unmanned Helicopters*. Springer, 2011.

[117] Ihnsoek Rhee, Mamoun F. Abdel-Hafez, and Jason L. Speyer. Observability of an integrated GPS/INS during maneuvers. *IEEE Transactions On Aerospace and Electronic Systems*, 40(2):526–535, April 2004.

[118] Andrew Roberts and Abdelhamid Tayebi. On the attitude estimation of accelerating rigid-bodies using GPS and IMU measurements. In *Proceedings of the Joint 50th IEEE Conference on Decision and Control and European Control Conference*, pages 8088–8093, Orlando, FL, December 2011.

[119] Robert M. Rogers. *Applied Mathematics in Integrated Navigation Systems*. AIAA, second edition, 2003.

[120] Pierre Rouchon and Joachim Rudolph. Invariant tracking and stabilization: problem formulation and examples. In Dirk Aeyels, Françoise Lamnabhi-Lagarrigue, and Arjan van der Schaft, editors, *Stability and Stabilization of Nonlinear Systems*, volume 246 of *Lecture Notes in Control and Information Sciences*, chapter 14, pages 261–273. Springer, London, 1999.

[121] Dieter Schlüter. *Schlüter's Radio Controlled Helicopter Manual*. Argus Books, second edition, 1986.

[122] Hyunchul Shim. *Hierarchical Flight Control System Synthesis for Rotorcraft-based Unmanned Aerial Vehicles*. PhD thesis, University of California, Berkely, 2000.

[123] Dan Simon. *Optimal State Estimation*. Wiley, 2006.

[124] Yongkyu Song and Jessy W. Grizzle. The extended kalman filter as a local asymptotic observer for discrete-time nonlinear systems. *Journal of Mathematical Systems, Estimation, and Control*, 5(1):59–78, 1995.

[125] John Stuelpnagel. On the parametrization of the three-dimensional rotation group. *SIAM Review*, 6(4):422–430, October 1964.

[126] Peter D. Talbot, Bruce E. Tinling, William A. Decker, and Robert T. N. Chen. A mathematical model of a single main rotor helicopter for piloted simulation. NASA Technical Memorandum 84281, Ames Research Center, Moffett Field, CA, September 1982.

[127] Mark B. Tischler and Robert K. Remple. *Aircraft and Rotorcraft System Identification: Engineering Methods with Flight-Test Examples*. AIAA, 2006.

[128] Janos Toth and Adelana Gilpin-Jackson. Smart view for a smart grid – unmanned aerial vehicles for transmission lines. In *2010 1st International Conference on Applied Robotics for the Power Industry*, Montreal, QC, October 2010.

[129] Arjan van der Schaft. Symmetries and conservation laws for Hamiltonian systems with inputs and outputs: A generalization of Noether's theorem. *Systems & Control Letters*, 1(2):108–115, August 1981.

[130] Charles F. Van Loan. Computing integrals involving the matrix exponential. *IEEE Transactions On Automatic Control*, 23(3):395–404, June 1978.

[131] Juan-Carlos Avila Vilchis, Bernard Brogliato, Alejandro Dzul, and Rogelio Lozano. Nonlinear modelling and control of helicopters. *Automatica*, 39(9):1583–1596, September 2003.

[132] David Vissiere. *Guidance, Navigation, And Control Solutions For Unmanned Heterogeneous Vehicles In A Collaborative Mission*. PhD thesis, Ecole Nationale Superieure des Mines de Paris, July 2008.

[133] Bruce Woodley, Chad Jennings, Andrew Conway, and Steven Rock. A contestant in the 1995 aerial robotics competition. In *Proceedings Manual, AUVS '95 technical papers*, pages 669–676, Washington, DC, July 1995.

[134] Xilin Yang. *Automatic Landing of a Rotary-Wing UAV in Rough Seas*. PhD thesis, University of New South Wales, November 2010.

[135] Yunchun Yang and Jay A. Farrell. Two antennas GPS-aided INS for attitude determination. *IEEE Transactions On Control Systems Technology*, 11(6):905–918, November 2003.